2012-11-26

Microfabrication, Characterization, and Application of Carbon Nanotube Templated Thin Layer Chromatography Plates, and Functionalization of Porous Graphitic Carbon

David S. Jensen
Brigham Young University - Provo

BYU ScholarsArchive Citation

Jensen, David S., "Microfabrication, Characterization, and Application of Carbon Nanotube Templated Thin Layer Chromatography Plates, and Functionalization of Porous Graphitic Carbon" (2012). *All Theses and Dissertations*. 3862.
https://scholarsarchive.byu.edu/etd/3862

Microfabrication, Characterization, and Application of Carbon Nanotube Templated Thin Layer Chromatography Plates, and Functionalization of Porous Graphitic Carbon

David Scott Jensen

A dissertation submitted to the faculty of
Brigham Young University
in partial fulfillment of the requirements for the degree of

Doctor of Philosophy

Matthew R. Linford, Chair
Daniel E. Austin
Steven L. Castle
Robert C. Davis
Milton L. Lee

Department of Chemistry and Biochemistry

Brigham Young University

November 2012

ABSTRACT

Microfabrication, Characterization, and Application of Carbon Nanotube Templated Thin Layer Chromatography Plates, and Functionalization of Porous Graphitic Carbon

David Scott Jensen
Department of Chemistry and Biochemistry, BYU
Doctor of Philosophy

This dissertation contains the following sections. Chapter 1 contains a detailed description of the theory of thin layer chromatography (TLC). Chapter 2 describes the benefits and practical considerations of elevated temperatures in liquid chromatography (LC). The porous graphitic carbon (PGC) I modified as part of my work is often used in elevated temperature LC. Chapter 3 shows a thermodynamic analysis of chromatographic retention at elevated temperature, and Chapter 4 contains a closer look at the van 't Hoff equation in LC and how it can be used in retention modeling. In Chapter 5, I describe a new procedure for microfabricating TLC plates that avoids the volume/feature distortions that occurred in our first microfabrication. The primary advance of this work was the priming of the carbon nanotube (CNT) forests with chemical vapor deposition (CVD) carbon and atomic layer deposition (ALD) alumina, which permitted effective ALD-like deposition of SiO_2. Chapter 6 describes advancements in the microfabrication process of TLC, which excluded the use of the CVD carbon and Al_2O_3 coating as described in Chapter 5. The use of ozone, to lightly oxidize the CNT surface, primed the material for direct ALD deposition. Chapter 7 gives a detailed surface analysis of the microfabrication process up to and including the CNT forest. It was noticed that a channeling effect was present during Rutherford backscattering analysis of the CNTs. Additionally, characterization of CNTs using time-of-flight secondary ion mass spectrometry in the negative ion mode showed an odd-even effect for a homologous series of carbon, where the even moieties had a stronger signal. Chapter 8 describes the functionalization of PGC with di-tert-amyl peroxide (DTAP) and its effect on increasing the chromatographic performance as seen by a reduction in the tailing factors of test analytes. Chapter 9 – 13 are detailed X-ray photoelectron analyses of the thin films and CNTs used in producing microfabricated TLC plates.

Keywords: Carbon nanotubes, atomic layer deposition, chemical vapor deposition, thin layer chromatography, liquid chromatography, elevated temperature chromatography, van 't Hoff

ACKNOWLEDGEMENTS

I am grateful for the mentorship, insightful discussions, and encouragement from Dr. Matthew R. Linford. I am thankful to have worked under his direction during my graduate studies.

I acknowledge and appreciate the suggestions and insight given from my committee members, Dr. Robert C. Davis, Dr. Steven L. Castle, Dr. Daniel E. Austin and Dr. Milton L. Lee.

I acknowledge and am grateful for all the members and friends in the Linford group: Dr. Li Yang, Dr. Guarav Saini, Dr. Feng Zhang, Dr. Lei Pei, Landon A. Wiest, Nitesh Madaan, Chuan-Hsi Hung, Supriya S. Kanyal, and Bhupinder Singh.

I thank Diamond Analytics, a US Synthetic company for rendered financial support throughout my graduate study tenure. I thank Andrew E. Dadson, Dr. Michael A. Vail and Andrew J. Miles for their suggestions and insight.

I thank the Department of Chemistry and Biochemistry at Brigham Young University for the opportunity to earn my doctoral degree in analytical chemistry.

Finally, I am grateful for the love and support of my family, personal friends, and especially my wife, Amber Jensen.

TABLE OF CONTENTS

LIST OF TABLES

LIST OF FIGURES

Chapter 1: Introduction to Thin Layer Chromatographic Theory and Modern Technology

1.1. Introduction to Chromatography

According to the International Union of Pure and Applied Chemistry (IUPAC) the definition of chromatography is "… a physical method of separation in which the components to be separated are distributed between two phases, one of which is stationary (stationary phase) while the other (the mobile phase) moves in a definite direction." As such, chromatography is a technique used to separate chemical mixtures into their individual components for qualification and quantification. As further defined by IUPAC the stationary phase is "…one of the two phases forming a chromatographic system. It may be a solid, a gel or a liquid. If a liquid, it may be distributed on a solid. This solid may or may not contribute to the separation process. The liquid may also be chemically bonded to the solid (Bonded Phase) or immobilized onto it (Immobilized Phase)."[1] Of course the mobile phase may be a liquid, a gas, or a supercritical fluid.

In a simplistic form, the degree of interaction (adsorption, partition, and/or size exclusion) between the analyte, mobile phase, and stationary phase is dependent upon the chemical and physical natures of all three components. Adsorption chromatography is defined by IUPAC as a "separation [that] is based mainly on differences between the adsorption affinities of the sample components for the surface of an active solid."[1] A variety of techniques are categorized under adsorption chromatography including: affinity, argentation, charge transfer, complexation, hydrophobic interaction, ion-exchange, ion, ion-pair, ligand exchange, and metal chelate chromatography.[2] Partition chromatography is a "separation based mainly on differences between the solubilities of the sample components in the stationary phase (gas chromatography), or on differences between the solubilities of the components in the mobile and stationary phases (liquid chromatography)."[1] The techniques that fall under this definition are: capillary gas, countercurrent, centrifugal, gas, liquid, micellar liquid, normal-phase, reserved-phase, subcritical fluid, supercritical fluid, and solvating gas chromatography.[2] Exclusion chromatography is defined as a separation "…based mainly on exclusion effects, such as differences in molecular size and/or shape or in charge. The term 'Size-Exclusion Chromatography' may also be used when separation is based on molecular size. The terms 'Gel Filtration' and 'Gel-Permeation Chromatography' (GPC) were used earlier to describe this process when the stationary phase is a swollen gel. The term 'Ion-Exclusion Chromatography' is specifically used for the separation of ions in an aqueous phase."[1] The following are examples of exclusion chromatography: size exclusion, gel, gel filtration, gel permeation, and hydrodynamic chromatography.[2]

A stationary phase can either be placed/packed into a tube or cast across a surface. These two different methods of using the stationary phase are classified as either column chromatography or planar chromatography, respectively. Column chromatography uses a stationary phase that is enclosed in a column and the mobile phase is forced through the column under applied pressure or gravity flow. Planar chromatography uses a solid stationary phase support that is adhered to a planar surface and the liquid mobile phase moves through the stationary phase via capillary action or gravity. Both of these methods operate under similar chromatographic retention mechanisms. As such, the degree of chemical and physical interactions that occur between stationary and mobile phases allows analytes to be separated, i.e., if analyte A interacts to a greater degree with the stationary phase than analyte B, they may be separable.

1.2. Retention Mechanism in Chromatography

In either adsorption or partition chromatography, whether the mobile phase is a liquid, supercritical fluid, or gas, separation of analytes can be viewed as a simple equilibrum between the analyte in the stationary phase and mobile phase as follows:

$$A_{mobile} \rightleftharpoons A_{stationary} \tag{1}$$

This equilibrium is governed by an equilibrium constant, K, and written as:

$$K = \frac{[A]_s}{[A]_m} \tag{2}$$

where $[A]_s$ is the concentration of analyte A in the stationary phase and $[A]_m$ is its concentration in the mobile phase. A brief look at Eq. 2 suggests that if an analyte has a large value of K it has a greater affinity for the stationary phase and as such the analyte will have a significant retention time in column chromatography, or in planar chromatography it will not travel very far (low R_{F} value, vide infra). In column chromatography the value assigned to the degree of affinity between the stationary phase and the mobile phase is the retention factor, k, which is directly proportional to K. In planar chromatography, or thin layer chromatography (TLC), the migration distance of an analyte is given a value termed the retardation factor, R_{F}, and is defined as:

$$R_{\mathrm{F}} = \frac{length\ of\ spot\ migration, z_x}{solvent\ front, z_f - application\ zone, z_o} \tag{3}$$

where z_f and z_0 are measured from the bottom of the plate and z_S is measured from the point of application. As shown by Eq. 3, the R_F gives a numerical value of the chromatographic spot position and provides the chromatographer a limited idea of the chromatographic process and results. The R_F value does not give information on other 'limiting' factors that are produced during chromatography and as such a true value for K cannot be obtained.[3] In contrast with the R_F value, the 'thermodynamic R_F' value or R_F', which is based upon the equilibrium constant, K, allows the chromatographer to relate the chemical separation process to K (Eq. 2),[4-5] where the retention is viewed as the amount of time (t) the analyte experiences in the mobile (m) and stationary phases (s), as follows:

$$R_{\mathrm{F}}' = \frac{t_m}{t_m + t_s} \tag{4}$$

Eq. 4 can be further expressed in molar concentrations (c) of the analyte in both the mobile and stationary phases as:

$$R_{\mathrm{F}}' = \frac{mol_m}{mol_m + mol_s} = \frac{c_m V_m}{c_m V_m + c_s V_s} = \frac{1}{1 + (c_s/c_m)(V_s/V_m)} \tag{5}$$

Thus, Eq. 5 allows the chromatographer to relate the position of the analyte spot to the distribution of the analyte in the mobile and stationary phases. Of course, the (c_s/c_m) term in Eq. 5 is the equilibrium constant, K, and the (V_s/V_m) term is the phase ratio, ϕ. Accordingly, Eq. 5 can be rewritten as:

$$R'_{\mathrm{F}} = \frac{1}{1 + K\phi} \tag{6}$$

Eq. 6 now allows the retention factor, k, defined as $k = K\phi$, to be determined, although in spite of its common occurrence in HPLC, k is seldom seen in the TLC literature.[6] Eq. 6 can be solved for k ($K\phi$) as follows:

$$k = \frac{1}{R'_{\mathrm{F}}} - 1 \tag{7}$$

Eq. 6 also allows for the union of K with the R'_{F} through the established thermodynamic equilibrium value, which can be further expressed as:

$$\ln K = \frac{\Delta\mu_p^o}{RT} \tag{8}$$

where $\Delta\mu_p^o$ is the standard chemical potential for partition.[5] This analysis of thermodynamic behavior allows the chromatographer to relate the separation process back to a basic equilibrium process.

Nevertheless, the conditions that need to be met to relate R_{F} values with R_{F}' values are as follows: (a) the phase ratio is constant along the chromatographic layer, (b) the chemical nature of the stationary phase is homogenous, (c) the solvent front velocity equals the solvent velocity at the location of the analyte, and (d) the material is not preconditioned with the mobile phase so as not to alter the stationary phase.[4] These conditions, especially (c) and often (d) are difficult to meet in practice, so R'_{F} is little used in practice.

1.3. Contributions to Band Broadening

Understanding chromatographic equilibrium does not provide an understanding of the efficiency of a separation. Chromatographic bands, under ideal conditions, are nearly Gaussian, and plate height, *H*, a measure of efficiency, is based on the spatial variance of the chromatographic spot per unit length over the separation path.

$$H = \frac{\sigma_t^2}{z_S} \tag{9}$$

where σ_t^2 is the total variance of the peak and z_s is the length over which chromatography occurred – the migration distance of the band. Contributions to 'zone broadening' or 'band broadening' during chromatography are based on the *A*, *B*, and *C* terms of the van Deemter or Knox equation. When these terms are summed together they produce the total zone broadening seen in chromatography:

$$\sigma_t^2 = \sigma_A^2 + \sigma_B^2 + \sigma_C^2 \tag{10}$$

However, Guiochon and Siouffi determined that the Knox equation better described the slower liquid chromatographic process of TLC as to the van Deemter equation:

$$(H_{loc})_{TLC} = d_p(Av^{1/3} + {}^{B}/_{v} + Cv) \tag{11}$$

where $v = u\frac{d_p}{D_M}$, with u being the flow velocity, d_p the particle diameter and D_M the diffusion coefficient of the analyte in the mobile phase. These A, B, and C terms are dimensionless Knox constants that describe the packing quality (eddy diffusion, A), diffusion in the mobile phase (B), and the resistance to mass transfer (C), respectively.[7-14]

The A term can be described as a representation of the heterogeneity of the chromatographic bed. In a heterogeneous TLC stationary phase, an analyte may experience different bed densities, particle sizes, particle shapes, particle packing, and amounts of binder or fluorescence indicator. These irregularities may result in different flow velocities this will contribute to the band broadening process, or stagnant areas where the mobile phase may pool and allow diffusion to occur. Thus, regular particle size and packing is important for reduction of the A term. Guiochon et al. were able to adapt the Eddy diffusion term in the Knox equation, A, for the slow process of TLC as follows:[8]

$$\sigma_A^2 = Ad_p\left(\frac{d_p}{D_M R_{\mathrm{F}} t}\right)^{1/3} \tag{12}$$

where d_p is the particle diameter, D_M is the diffusion coefficient of the analyte in the mobile phase, R_{F} is the retardation factor, and t is the time the analyte spends in the mobile phase.

The B term arises from the diffusion of the analyte in the mobile phase. That is, over time a substance will diffuse in all directions to a certain extent as defined by its diffusion coefficient. Zone broadening by diffusion can be expressed as:

$$\sigma_B^2 = 2D_M t \tag{13}$$

where D_M is the diffusion coefficient in the mobile phase (cm^2/s) and t is the time it takes for the analyte to diffuse a distance of ca. σ_B. Eq. 13 can be corrected for liquid chromatographic conditions by including a tortuosity factor, γ, and R_F:

$$\sigma_B^2 = 2D_M\gamma_m R_F t = BD_M R_F t \tag{14}$$

where B is the Knox constant that takes γ into account. As a result, the B term in the Knox equation is inversely proportional to the mobile phase velocity, which decreases with increasing migration in TLC – this is an obvious and important difference between HPLC and TLC. Thus, the B term contribution only becomes noticeable for large migration distances.

The dimensionless Knox constant, C, takes into account the particle size diameter and can be written for TLC as follows:

$$\sigma_C^2 = C\frac{d_p^2}{D_M R_F t} \tag{15}$$

This term obviously favors smaller particles because it goes as the square of the particle diameter. However, there is a limit in useful particle size in TLC because, as the particle diameter is reduced, capillary action decreases. Finally, it should be noted that all of the contributions to zone broadening contain an R_F value.

The R_F value can be further related to the mobile phase velocity, u, as follows:

$$R_F t = \frac{z_S}{u} \tag{16}$$

As stated in Eq. 10 the plate height, *H*, is the summation of all contributions to the zone broadening and by substituting the equations for *A* (Eq. 12), *B* (Eq. 13 – 14), and *C* (Eq. 15) into Eq. 11 the Knox Equation is obtained.[15]

$$H = Ad_p \left(\frac{d_p}{D_M} u \right)^{1/3} + \frac{BD_M}{u} + C \frac{d_p^2}{D_M} u \tag{17}$$

To determine chromatographic efficiency one usually plots the mobile phase velocity vs. *H*. In column chromatography this plot allows the determination of the optimum flow velocity. However, the flow velocity in TLC is not constant and calculating H_{min} is complicated. In TLC *H* is dependent on the R_F of the analyte. To calculate H_{min} for the TLC process the following equation can be used:

$$\bar{H}_{min} = \frac{1}{\int_{z_o}^{z_f} dz_f} \int_{z_o}^{z_f} Hz_f = \frac{1}{z_f - z_o} \int_{z_o}^{z_f} \left(Ad_p \left(\frac{d_p}{D_M} u \right)^{1/3} + \frac{BD_M}{u} + C \frac{d_p^2}{D_M} u \right) dz_f \tag{18}$$

where z_o is the distance from the bottom of the TLC plate where the sample is applied, and z_f is the distance the solvent front travels. Eq. 18 can be solved if the local flow velocity, Eq. 21 (vide infra), is substituted into it, which gives the following:[8, 10-13, 16]

$$\bar{H}_M = \frac{3}{2} A \left(\frac{d_p^4 \kappa}{2D_M} \right)^{1/3} \frac{z_f^{2/3} - z_o^{2/3}}{z_f - z_o} + \frac{BD_M}{\kappa} (z_f + z_o) + \frac{C\kappa d_p^2}{2D_M (z_f - z_o)} \ln \frac{z_f}{z_o} \tag{19}$$

A closer look at this equation underscores the idea of a decrease in both the A and C terms by reducing the particle diameter. Nevertheless, this approach to determine $\overline{H}_{min}$, produced by Guiochon, does not fully take into account the dependence of $\overline{H}_{min}$ on z_o when z_o is below its optimum value (meaning that Eq. 19 does not give good fits when the value of z_o is small).[16] As an example, when the sample is spotted near the edge of the TLC plate (low value of z_o) the velocity of the solvent front is high, which increases $\overline{H}_{min}$ due to an increase in resistance to mass transfer (C term dependency). If the sample is spotted at a higher place (high value of z_o) the velocity of the solvent front, once it reaches the application zone, is low, forcing $\overline{H}_{min}$ to be limited by diffusion (B term dependency). As stated earlier, theoretically determining the right spotting distance (z_o) has yet to be described. However, the optimum spotting distance has been shown empirically for TLC and high-performance (HP) TLC plates to be 10 – 12 mm and 6 – 7 mm, respectively.[16]

As discussed earlier, Eq. 9 addresses how plate heights can be calculated in TLC. To include the influence of diffusion upon migration of the sample spot, Eq. 9 can be modified to include this parameter and further adjusted to only be influenced by the variance from chromatography (σ^2_{chrom}) itself:

$$H_{obs} = \frac{\sigma^2_{chrom}}{R_\mathrm{F}(z_f - z_o)} \tag{20}$$

Obviously H_{obs} varies with R_F, so if two systems are to be compared their R_F values must be the same. Additionally, H_{obs} for an unretained compound ($R_\mathrm{F} = 1$) is a hypothetical value because this corresponds to an analyte moving with the solvent front (the analyte does not have any attractive interactions with the stationary phase). This value is an inflated value or upper chromatographic limit of the system.[17]

There are two other effects on H_{obs} other than the influence of migration/chromatography (σ^2_{chrom}). The next few equations, as originally presented by Poole et al., can be used to calculations TLC efficiencies.[17] Because the sample is applied to the stationary phase with a given width (σ^2_{SA}) this ultimately influences the final band width of the analyte after chromatography. Also the effect of sample detection (σ^2_{INS}) needs to be considered. That is, all three contribute to band broadening in TLC are combined to create the observed variance in chromatography (σ^2_{obs}):[17]

$$\sigma^2_{obs} = \sigma^2_{chrom} + \sigma^2_{SA} + \sigma^2_{INS} \tag{21}$$

Using these contributions one can calculate (H_{obs}).

At least two processes occur as the mobile phase first travels over the applied analyte spot.[17] First, the material at the bottom of the spot begins to migrate before than at the top causing a focusing of the band. However, dissolution of the analytes may not be immediate and this delay may cause band broadening. For these reasons, the width of the applied band may not be a good estimate for σ^2_{SA}, although it is often used as such. A more sophisticated treatment of this problem was by Kaiser[17] who suggested that band widths (full-width at half maxima, FWHM, as measured by a densitometer) be plotted as a function of R_F to obtain the following equation:

$$b_s = b_o + mR_F(z_f - z_o) \tag{22}$$

where b_s is the peak width at FWHM, and b_o is the rest diffusion value (application width of band) of the sample application zone as calculated by linear regression. From Eq. 22 the real chromatographic efficiency, $H_{real,}$ can be calculated as follows:

$$H_{real} = \frac{(b_s - b_o)^2}{5.54R_{\mathrm{F}}(z_f - z_o)} \tag{23}$$

with b_s being a continuous function of R_{F}.

So far three different methods to calculate H have been discussed, and one may ask which method produces the correct value for the system. Poole made the following comments regarding this issue. First, "The location of the minimum plate heights on the migration distance axis is roughly the same in each case." Second, he noted the importance of always using the same equation to calculate H (either Equation 9, 20, or 23). Finally, he stated that "Since it cannot be established that any of the three methods is correct in its calculation of the true plate height a general recommendation cannot be made."[17]

1.4. Capillary Flow in Thin Layer Chromatography

The above discussion of zone broadening using the Knox equation does not allow the chromatographer to understand the flow process of TLC via capillary action. The adsorbent layer of a TLC plate can be modeled as a collection of interconnected capillaries. Thus, capillary action is the main mechanism for solvent flow. Capillary action is based on the reduction of surface free energy of the mobile phase/stationary phase as the mobile phase enters a porous medium. The velocity of the mobile phase in TLC through a bed of particles obeys a quadratic relationship when the vapor phase is in equilibrium with the adsorbent surface.[18-21] Therefore, the position of the solvent front at any particular time can be calculated by:

$$(z_f)^2=\kappa t \tag{24}$$

After differentiation of Eq. 24 the solvent front velocity (u_f) can be calculated by:

$$dz_f/dt = u_f=\kappa/2z_f \tag{25}$$

where z_f is the distance the solvent front has traveled from the solvent level and κ is the velocity constant (cm^2/s), which is given by:

$$\kappa = 2K_o d_p(\gamma/\eta)\cos\theta \tag{26}$$

where K_o is a dimensionless permeability constant of the adsorbent layer that takes into account (a) the external pore size distribution, (b) the role of the porosity on the permeability of the adsorbent layer, and (c) how the bulk mobile phase velocity relates to the solvent front velocity, d_p is the average particle diameter, γ is the surface tension of the mobile phase, and η is the mobile phase viscosity.[22] For normal phase separations, θ, the contact angle, is close to zero, especially if the adsorbent layer is polar, e.g., silica, which has a high free energy surface.

A brief look at Eq. 26 reveals that an increase in d_p will result in an increase in the mobile phase velocity leading to a reduction in the analysis time. However, an increase in d_p also results in an increase in the resistance to mass transfer term (*C*) in the Knox equation (Eq. 17), thus degrading the quality of a separation. In a classical, particle-based TLC separation, the trade-offs are obvious: one can have a rapid separation with fewer theoretical plates (decreased efficiency) or a slower separation with higher efficiency. Of course with smaller particles, an option is to simply develop over a shorter distance, leading to a fair number of theoretical plates and a shorter development time. Nevertheless, with particle-based TLC plates the dilemma is still in force – it is not possible to increase theoretical plate numbers and decrease development times in the same separation by changing the particle size. Of course, two other modes of TLC that have been used to overcome these limitations are ignored: forced-flow development and multiple development. However, the corresponding development apparatuses are not common and the techniques have not caught on to a great extent. In summary, there is a theoretical barrier in TLC to changing both particle size and fluid velocity to achieve both rapid and efficient separations.

1.5. Computer Simulation for Ordered Chromatographic Media

To achieve higher efficiencies it is imperative to have control over the dimensions of the adsorbent material, i.e., particles size, particle size homogeneity, capillary width, and porosity. If one could control these dimensions independently one might produce a chromatographic material for TLC that is superior to current technology. Recent computer simulations of separations on perfectly arranged cylindrical pillars in two dimensions, as shown in Figure 1.1, have shown a decrease in plate height with increasing bed homogeneity due to a major reduction in eddy diffusion, i.e., the *A* term in the van Deemter equation.[23-29]

This reduction in the *A* term is not surprising as it underscores the importance of constructing uniform support materials for chromatography. Furthermore, it was reported that this cylindrical pillar geometry may not be optimal. A review article by Desmet states that an arrayed media that is based upon a parallel plate geometry (cf. Figure 1.2) would give optimal performance due to the following reasons (a) this type of geometry gives the lowest calculated flow resistance, (b) it allows for the most uniform flow field, (c) it also allows for a minimal mass-transfer distance between chromatographic supports.[30] Desmet goes on to say that this parallel plate geometry would give optimal performance if the intraporosity of the medium was below 90%.[31] Before how to prepare such a material, a brief overview of the state of the art of TLC will be given.

Figure 1.1 ‘Schematic representation of a 2-D ordered porous pillar column.’ From Ref. 29 with permission.

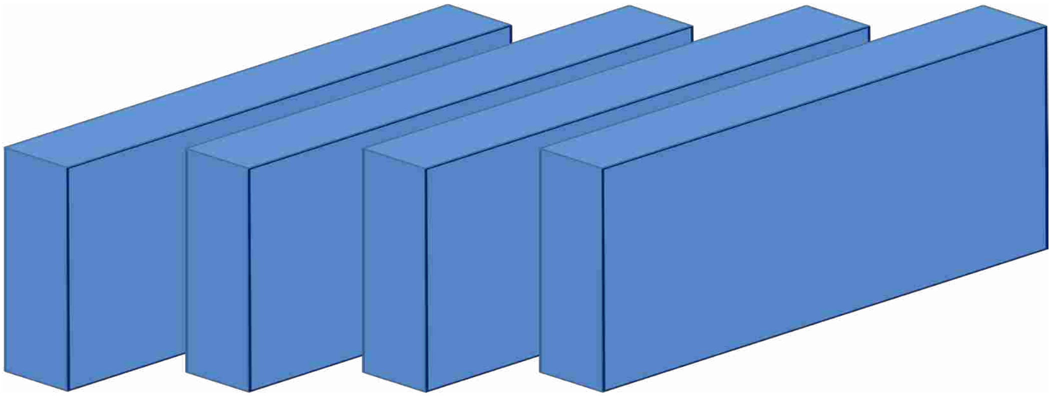

Figure 1.2 Schematic representation of a 2-D ordered porous pillar parallel plate geometry.

1.6. Current Thin Layer Chromatography Technology

1.6.1 Traditional TLC adsorbents

Thin-layer chromatography (TLC) was introduced in the 1950s[18, 32-33] and has subsequently been widely used in organic and inorganic chemistry laboratories, life and environmental sciences, and natural product and pharmaceutical industries.[18, 33] The advantages of TLC lie in its simplicity and speed, and, as such, it is used ubiquitously in organic chemistry laboratories to provide a straightforward means to obtain/monitor reaction progress and purity of targeted products. For quantitative analyses on TLC plates a densitometer can be employed. Even though, TLC is considered an inexpensive analysis and the plate is usually discarded after chromatography, it can be used as an archival device since all of the separated components are adsorbed on the media. TLC also allows for several samples to be separated in parallel thus increasing sample throughput.[22, 34] A review by Sherma gives an excellent overview of the types of separations done on silica-based TLC media.[35]

TLC usually employs an adsorbent layer comprised of micron sized amorphous or spherical silicon dioxide particles. These particles are cast onto aluminum, plastic, or glass backings and the adsorbent layer will be adhered to itself and to the backing material through a small amount of binder. These binders are typically low molecular weight polymers such as poly(acrylic acid) or inorganic materials such as gypsum (calcium sulfate). A less intrusive binder, nanosilica particles, has also been proposed.[36] It should be noted that silica materials may contain nonhydrogen bonded silanols, also referred to as isolated silanols. If the silica based material contains a large number of isolated silanols this will result in poor chromatography for basic analytes due to strong interactions that lead to peak tailing.[37]

In addition, to these possible surface chemistry inhomogeneities, i.e., isolated silanols, silica based TLC plates may contain some type of fluorescent indicator, usually a manganese-doped zinc silicate which fluoresces green under 254 nm light.[38] The fluorescent indicator is used to detect conjugated π-electron systems, e.g., aromatics, through quenching mechanisms.[37] It is usually assumed that the fluorescent indicator is benign and does not affect the chromatographic properties because of its low concentration in the TLC media.

As noted, TLC uses either spherical or amorphous particles that come in a variety of sizes and size distributions. Accordingly, these materials will be placed into one of two groups, i.e., particles for TLC or those for high-performance TLC (HPTLC). Conventional TLC plates typically employ porous, amorphous particles with mean particle sizes of 10 – 12 μm, and particle size distributions of 5 – 20 μm. These adsorbent layers are typically ca. 250 μm thick. With these dimensions plate heights of 35 – 45 μm can be achieved.[19-22, 32] High-performance TLC (HPTLC) made its début in the 1970s, and uses smaller particles with more uniform size distributions. HPTLC employs a mean particle size of 5 – 6 μm with a size distribution of 4 – 8 μm. The typical thickness of the adsorbent layer is ca. 200 um. The reductions in these dimensions (particle size and size distribution) result in shorter migration distances. More efficient separations are also achieved with shorter separation distances because of the improvements in the chromatographic efficiencies of smaller particles and more uniform particle size distribution. These improvements effectively influence the *A* and *C* terms in the van Deemter equation by decreasing Eddy diffusion and improving the mass transfer of the analyte, respectively. The ability to do separations over a shorter distance allows for lower solvent consumption, making it a greener approach. A typical HPTLC separation shows plate heights of approximately 12 μm.[19-22, 32]

1.6.2 Adsorption and Partition Effects in TLC

TLC can be divided into two different retention-type categories: (1) adsorption chromatography (liquid-solid) and (2) partition chromatography (liquid-liquid). Typically, adsorption chromatography is characterized as a method of separating analytes on nonmodified silica, whereas, partition chromatography uses a phase that is bonded to the silica surface.

1.6.2.1 Adsorption Chromatography

Because silica is composed of silicon and oxygen bonded in a tetrahedral configuration, with the surface being terminated in silanol groups (SiOH), the retention mechanism for unmodified silica is adsorption (liquid-solid chromatography). The surface of silica, in its fully hydrated state, has ca. 8 μmol/m^2 (ca. 4.6/nm^2) of SiOH groups.[39-40] These surface silanols function as adsorptive sites whereby molecules interact through hydrogen bonding, dipole-dipole interactions, and/or dispersion interactions.[3] Because the silica surface in adsorption chromatography is polar, the mobile phase is comparatively less polar, and this type of liquid chromatography is termed normal phase chromatography.

1.6.2.2 Partition Chromatography

Silica is the traditional material to which a bonded phase is created and as such it is used for partition chromatography. Partition chromatography exploits the effects of different solubilities of various analytes between the mobile and stationary phases. That is, if the analyte has a high solubility in the stationary phase then the analyte will have a low R_F value, likewise, if the analyte has a high solubility in the mobile phase it will have a large R_F value.

1.6.3 Bonded Phases in TLC

Fried and Sherma have written extensively about sample preparation and stationary phases used in TLC. The following discussion of analytes and stationary phases highlights the work by Fried and Sherma,[3, 41] and Poole.[42] Most phases in liquid chromatography are bonded phases that use silanes with different functional groups covalently attached to the surface via silanol groups. These bonded phases typically come in degrees of polarity with silica being the most polar (nonbonded) and C_{18} being the least polar. The general trend in polarity of the following commercially available phases is as follows: silica > amino (NH_2) > diol > cyano (CN) > > C_2 > C_4 > C_8 > C_{18} 50% > C_{18} wettable (W) > C_{18} 100%.

1.6.3.1 Nonpolar Phases in TLC

A variety of nonpolar (hydrocarbon) phases have been used to separate analytes under reversed-phase conditions. These bonded ligands can range in chain length from C_1 to C_{18}. The typical use for a C_2 phase is to separate water-soluble polar organic molecules under reversed-phase conditions. The C_8 phase is used for both weak acids and bases under ion suppression reversed-phase conditions, and the C_{18} phase is used for strong acids and bases under ion suppression conditions, and nonpolar and polycyclic aromatic types of compounds.[42]

Coating silica with paraffin oil, squalane, silicone oil, octanol, or oleyl alcohol was a once practiced process for coating TLC media with a nonpolar material, e.g., to reverse the phase polarity.[40, 43] Today, a commercially available TLC plate is still produced by Analtech that uses a nonpolar liquid that is similarly adsorbed in a noncovalent fashion to the chromatographic support, although this technique does not appear to be commonly practiced anymore.[40] This approach allows for a highly aqueous mobile phase to be used because the surface is still wettable due to nonbonded (and presumably somewhat exposed) silanol groups. However, the drawback is that the adsorbed stationary phase cannot tolerate nonpolar organic mobile phases.

C_{18} is regarded as the traditional reversed-phase material and is mostly used in high-pressure liquid chromatography, but it does have its niche in TLC. A variety of different compounds can be separated on a C_{18} bonded phase. Different steroids (classes of estrogens, cholesterols, and corticosteroids) have been separated on RPTLC plates using either methanol or acetonitrile as the organic modifier.[44-46] Other mobile phases that have been used to separate steroids include different ethers and n-alcohols.[47-50] Oleszek et al. have discussed a variety of approaches to separate polyphenolic compounds (saponins).[51-52] An assortment of dyes and food dyes have been successfully separated under various conditions.[40, 53-61] Separation of lipids has been performed on C_{18} modified silica.[62] However, a pure C_{18} material does have its limitations because nonpolar materials are not easily wet by highly polar mobile phases. To circumvent this issue of wettability, bonded phases that are characterized as wettable C_{18} (C_{18}W) or C_{18} 50% have been developed.

As just stated, to alleviate the problem of wettability and/or lack of solvent front migration on a C_{18} functionalized plate the degree of silanization can be decreased, which in turn increases the number of polar, non-bonded silanol groups. Accordingly, if the degree of surface functionalization is controlled, the TLC medium could exhibit both normal- and reversed-phase characteristics. The separation of pesticides and herbicides has been reported using a C_{18}W phase.[63] Another method to increase mobile phase wettability on reversed-phase materials is to add ca. 3% NaCl to the mobile phase.[40]

Bhushan and Martens[40] discussed work done by Lepri et al. who used reversed-phase materials in the separations of peptides and proteins with varying stationary phase hydrophobicity (C_2, C_8, and C_{18}). It was discussed that a host of closely related peptides was separated on C_2 silanized TLC plates that were impregnated with N-dodecylpyridinium chloride.[64] TLC plates that were silanized with either C_2, C_9, or C_{18} ligands and further impregnated with dodecylbenzenesulphonic acid were used to separate various amino acids and dipeptides.[65-67] Other work showed the separation of peptides on reversed-phase TLC plates that had been impregnated with anionic and cationic surfactants.[68] Lepri further looked at the C_{18} 50% phase to separate amino acid derivatives, peptides, and typtamine derivatives, comparing these separations to TLC media that were impregnated with ammonium tungstophosphate.[69]

1.6.3.2 Polar Phases in TLC

As stated earlier, the amino, cyano, and diol phases are hydrophilic. Obviously these layers are wettable with pure to partially aqueous mobile phases. In addition, these hydrophilic phases exhibit multimodal properties that allow different analyte classes to be separated.

The amino bonded phase is less polar than silica but is more polar than the cyano-bonded phase. Because the amino group is ionizable it can act as a weakly basic ion exchanger to separate anionic species including nucleotides and/or sulfonic acids.[40] Poole showed that this phase performed under both normal-phase (via hydrogen-bond interactions) and ion-exchange (under acidic conditions) mechanisms but is limited in retention under reversed phased conditions.[42] A sampling of the numerous analytes that have been separated on this phase include: barbiturates and steroids,[70-71] carbohydrates,[72-74] phenols and xanthin derivatives,[75] benzodiazepine,[76] food pigments,[77] and purines and pyrimidines.[78-79] The amino phase has the useful and interesting property that upon heating it yields fluorescent, and therefore easily detectable, adducts with a variety of compounds including carbohydrates and catecholamines,[40, 80-83] mycotoxin sterigmatocystin,[84] steroid hormones,[85] glucosamine,[86] and creatine.[82]

The diol phase is another moderately hydrophilic bonded phase that is more retentive than the amino phase.[42] This phase can be used under both normal- and reversed-phase conditions because the bonded phase contains both polar and nonpolar sections. A typical retention mechanism under normal-phase conditions is through both hydrogen bonding and dipole-dipole interactions.[42] Poole discusses retention on diol phases and states that it is similar to short chain alkylsiloxane-bonded phases under normal-phase conditions, but the selectivity for hydrogen-bonding species is different.[42] Under reversed-phase conditions containing triethylamine Poole et al. separated a series of estrogens.[87] A few steroids were separated using different ratios of chloroform–acetone–petroleum ether.[88] A series of benzodiazapines were also separated on a diol TLC plate.[76] This phase was further used to identify 2-hydroxycinnamaldehyde in commercial cinnamons,[89] sugars in foods using automated multiple development,[42, 90] and food pigments in chili powder.[77] A complex mixture of fermented carbohydrates was separated using a 15-step automated multi-development technique.[91-92] Flavonol glycosides have been successfully separated.[93] In a study by Vaccari et al. a diol phase was used to separate a series of oligosaccharides in sugar products, where they chose the diol phase because it gave better selectivity and used less water with respect to either an amino or normal phase medium.[94]

The cyano phase is another mildly hydrophilic stationary phase that can be created from a cyanopropyl silane. Since this phase contains both hydrophilic (cyano) and hydrophobic (propyl) groups it can also be used in either reversed- or normal-phase separations,[42] e.g., it has been used to separate progesterones under both normal- and reversed-phase conditions.[40] It has been reported that the cyano phase has similar properties to short-chain alkyl ligand bonded phases and has no selectivity for dipole-type interactions.[42] Because the cyano phase can be used under both normal- and reversed-phase conditions, it can be used advantageously in 2D separations. Accordingly, a variety of sulfonamides have been separated.[95] The following classes of compounds have also been separated on cyano-bonded phase: analgesics,[95] antibiotics,[95] benzodiazepines,[76, 96] carboxylic acids,[97] carotenoids,[98] pesticides,[99] phenols,[100-101] food pigments,[77] and steroids.[102]

1.6.4 Nontraditional TLC Adsorbents

Next to silica, alumina-based adsorbents are the most common type of TLC phase. Alumina materials for TLC are made from calcining alumina hydroxide at ca. 500 °C.[15, 103] The surface chemical moieties on alumina are hydroxyl groups, oxide (O^{2-}) ions, and alumina cations.[104] Alumina can be obtained at three different degrees of activity, e.g., acidic (pH 4.0 – 4.5), neutral (7.0 – 8.0 pH), and basic (9.0 – 10.0 pH). These varying degrees of activity show different chromatographic properties. Similar to silica, alumina separates analytes according to polarity through hydrogen bonding and dipole-dipole interactions. Acidic alumina is used to separate neutral and acidic lipophilic analytes. In addition, it interacts strongly with basic analytes and, conversely, basic alumina interacts strongly with acidic analytes. Aromatic analytes interact to a higher degree with alumina than silica therefore aromatic analytes are more strongly retained on alumina.[41] Other classes of compounds that can be separated on alumina include: herbicides,[105] hydrazines,[106] insecticides,[107] metal ions,[108] and fat-soluble vitamins.[40, 109] However, the drawback of alumina is its ability to catalytically degrade labile analytes.[41] Ahmad had reviewed TLC analyses of inorganic and organometallic compounds on alumina.[110]

Zirconium oxide (zirconia) is another metal oxide that has been used somewhat as a nontraditional TLC adsorbent, where the preparation of this material may use zirconium (IV) propoxide as a precursor.[111-115] Zirconia has been used as a ion exchange TLC medium to separate Bi(III) from a ternary and quaternary mixture of metal ions.[116] It has also been used in normal phase separations, e.g., of dyes.[117] Various publications have noted that the surface of zirconia is composed of both Lewis acid and Lewis base sites, which makes surface interactions during chromatography difficult to describe.[118-120]

Florisil is a TLC medium that is produced from the coprecipitation of silica with magnesia. TLC of pesticide residues was optimized on Florisil under five different solvent systems.[121] Florisil has also been used to separate phenols, derivatives of aniline, quinoline bases, and polyaromatic hydrocarbons.[122] Compared to silica and alumina Florisil generally tends to be intermediate in its activity. Florisil has a reduced tendency to catalytically degrade labile analytes.[123]

Perlite, a natural by occurring volcanic glass that is produce from hydrating obsidian (ca. 70% SiO_2), has been used to separate dyes in commercially available inks, amino acids, carboxylic acids, mono- and disaccharides, and halide ions.[37, 124] A few other types of naturally occurring TLC adsorbents are zeolites and diatomaceous earth (known as Kieselguhr, when it is purified). Diatomaceous earth was used to separate ink components after calcination and reflux with acid.[125] It also has been used as a TLC adsorbent for the separation of polar compounds: chlorophyll and prophyrins,[126] carbohydrates,[127] desacetyl lanatosides and lanatosides,[128] sugars,[129] and other highly hydrophilic sunstances.[130] With zeolites, other colorants have been separated under a metal cation-organic cation type retention mechanism.[131]

1.6.5 Current Research TLC Absorbents

In the early 2000s Merck introduced ultrathin layer chromatography (UTLC).[132-133] This type of TLC employs a thin, monolithic silica layer that is coated onto a glass backing.[134] The adsorbent layer is ca. 10 µm thick with 1 – 2 µm macropores and 3 – 4 nm mesopores.[135] This reduced layer thickness (10 µm) almost always offers lower detection limits.[134] However, UTLC is limited by the migration distances that are achievable, with a maximum possible migration of ca. 3 cm due to a reduction in capillary action with Z_f. UTLC plates also suffer from reduced sample capacity because of the limited surface area of the thin adsorbent layer.

A variety of different nonsilica-based monolithic TLC plates have been produced and studied in the literature in an attempt to increase the separation efficiencies and detection of large molecules.[34, 136] These monolithic devices are based upon poly(butyl acrylate-*co*-ethylene dimethacrylate) that was polymerized onto glass backings, and were constructed specifically for MALDI-MS detection.

Other recent developments in UTLC include a technique known as glancing-angle deposition (GLAD) that was used to produce plates with 1 – 7 µm silica adsorbent layers.[137] These plates showed reasonable resolution and efficiencies under short developing distances. However, solvent front migration is relatively slow.

Another new type of UTLC plate is based on electrospun, nanofibrous polymers, e.g., polyacrylonitrile.[138] Even though this technology produces more than a sufficient number of theoretical plates for efficient separations, the ultimate value of these plates to the community is questionable for the following reasons. (a) The adsorbent is polymeric, and polymers may swell or even dissolve in organic solvents. Thus, an understanding of the retention mechanism of a separation may be complicated by selective absorption of one or more of the components of the mobile phase. (b) A fairly long time seems to be required to electrospin the fibers for each TLC plate, although it may be that these materials could be produced more rapidly if they were manufactured commercially. (c) Most chromatographers are not familiar with the properties of polymeric stationary phases; it would be preferable if the material were silica. If this were the case, it would be much easier to transfer the plethora of methods that have been developed on silica to these new plates.

Another study by the Olesik group used electrospun polymers (SU-8 2100 photoresist) that were subsequently carbonized at various temperatures (600 – 1000 °C) to form a glassy carbon stationary phase, which may have similar chromatographic properties to commercially available porous graphitic carbon.[139-140] These carbonized fibers were used as a TLC medium with a mat thickness of ca. 15 μm to separate a set of laser dyes and some FITC-labeled amino acids.[140] In this separation it proved easier to separate the analytes than to detect them because the stationary phase strongly absorbs light. For detection, the plates were sprayed with acetone to reduce the fluorescence quenching of the glassy carbon.

In the Linford group at BYU, a microfabricated TLC plate that is based on carbon nanotube (CNT) templated microfabrication has been reported.[141] These novel TLC plates are constructed using patterned carbon nanotubes (CNTs) as a template for the assembly of porous, silica-based TLC plates. This technique allows for the precise collocation of the adsorbent material. That is, CNTs are grown from ethylene and hydrogen feed stocks on a photolithographically patterned substrate onto which iron has been deposited by physical vapor depostion. After CNT growth, they are infiltrated with silicon via a low-pressure chemical vapor deposition (LPCVD) of silane (SiH_4). Once the CNT forest is coated with a thin film of silicon, the resulting material is subjected to a dry oxidation (air at elevated temperature) to remove (burn out) the CNTs and convert the silicon to silica. This process produces a silica-based TLC plate that contains no binder, and that is mechanically more robust than traditional TLC or HPTLC adsorbent layers. The precise placement of features in these new TLC plates appears to reduce the *A* term in the van Deemter equation. A reduction in the *C* term in the van Deemter equation will be realized by reducing the dimensions of the features, thus improving mass transfer.

Unfortunately, there are at least three problems associated with LPCVD of silicon. The first, which would be manageable if it were the only problem, is that LPCVD of elemental silicon is fairly slow. The second, which is more substantial, is that LPCVD silicon must be oxidized at high temperatures, ca. 1000°C, which limits the substrate materials that can be used. Third, and most significantly, oxidation of LPCVD silicon results in a volume expansion of the material that warps patterned features on TLC plates – the features that were placed so perfectly through lithography become distorted, resulting in conditions that are far from ideal. Thus, oxidation of LPCVD silicon is problematic for a variety of reasons:

(i) Warped/deformed features lead to irregular solvent fronts in developing TLC plates. Thus, R_f values may not remain constant from track to track, making a direct visual comparison of zones on different tracks challenging. This situation is probably unacceptable to most users.

(ii) Warped features raise the *A* term in the van Deemter equation; warped features clearly lead to a lack of uniformity across a plate and along its tracks, which lowers chromatographic performance.

(iii) A fabrication process involving warped features is difficult to control. In our experience it has been difficult, if not impossible, to predict the degree and direction of warping, as the degree and direction of warping seems to depend on even small differences in the amount of silicon deposited across the plate by LPCVD, where this degree of LPCVD deposition appears to be affected by variables like the position of the substrate in the deposition oven and/or temperature gradients in the deposition oven.

(iv) Volume expansions of features make it difficult to control the widths of channels. In some cases this can cause channels to close off.

(v) There appears to be at least a small difference between the widths of features in many locations including near their bases, at the substrate, where they are pinned, and at the top of the features. As a result, the channel width is not constant in the direction perpendicular to the plane of the substrate.

However, much was learned from these early efforts. They demonstrated that the process of using CNT templates for the production of microfabricated TLC plates has merit, and can even produce plates with improved chromatographic efficiencies. Nevertheless, in order to avoid expansion/distortion of the features during the oxidation process, another method of coating CNTs with a chromatographic material has been developed. This process requires several deposition processes to create a material that does not expand upon the removal of the CNTs at high temperatures.

In brief, the first attempt was to directly deposit SiO_2 onto CNTs via a pseudo-atomic layer deposition (ALD) process.[142] However, it quickly became apparent that depositing metal oxides, via ALD, directly onto CNTs was futile. Many studies have shown that because of their inertness it requires some type of priming/adhesion layer for successful ALD deposition onto

CNTs.[143-146] In our case, a thin film of CVD carbon was applied followed by ALD of Al_2O_3 to promote adhesion of the subsequently deposited SiO_2 layer. Interestingly, both films were required to produce a stable microfabricated TLC plate. This process ultimately produced a chromatographic material with efficiencies up to 225,000 N/m. Nevertheless, producing TLC plates via CVD of carbon and ALD of Al_2O_3 was quite cumbersome and required high temperatures and multiple, long depositions. Thus, this process most likely would not be industrially viable. However, further characterization of the carbon coated CNTs, via XPS, revealed that the material contained ca. 1 atom% oxygen. This oxygen appeared to allow for the nucleation of the ALD precursors thus facilitating ALD film growth.

To increase the amount of oxygen on CNT forests, ozone was used as the oxidant to prime the CNTs[147-148] for subsequent ALD. The advantage of ozonation is that it allows one to circumvent/replace the CVD of carbon and ALD of Al_2O_3. In addition, this ozone process allows for lower processing temperatures, thereby permitting the use of other substrate materials such as high temperature glass. TLC plates were constructed using this ozone priming procedure and the final chromatographic outcome was a TLC plate producing ca. 400,000 N/m on a weakly retained compound. An unretained compound produced in excess of 1,000,000 N/m.

These increases in chromatographic efficiency are possibly due to the highly ordered material. Also, as the number of processing steps was reduced, the number of theoretical plates increased, which suggests a reduction in the variability of the plates. In this dissertation, the process of creating a highly ordered chromatographic material based upon templated CNT forests will be discussed in detail.

1.7 References

1. Lettre, L. S., *Pure & Appl., Chem.* **1993,** *65* (4), 819-872.

2. Lee, M. L., *Fundamentals of Analytical Separations*. BYU Academic Publishing: Provo, 2010.

3. Sherma, J.; Fried, B., *Handbook of Thin-Layer Chromatography*. 3rd ed.; Taylor & Francis: New York, 2003; Vol. 89.

4. Geiss, F., *Fundamentals of thin layer chromatography (planar chromatography)*. Mitterwger Werksatz GmbH: Plankstadt, 1987.

5. Wojciech, P.; Teresa, K., TLC: Theory and Mechanism. In *Encyclopedia of Chromatography, Third Edition*, Taylor & Francis: 2009; pp 2332-2335.

6. Fair, J. D.; Kormos, C. M., *J. Chromatogr., A* **2008,** *1211* (1–2), 49-54.

7. Spangenberg, B.; Poole, C. F.; Wiens, C., *Quantitative Thin-Layer Chromatography: A Practical Survey*. Springer: New York, 2011.

8. Siouffi, A. M.; Bressolle, F.; Guiochon, G., *J. Chromatogr., A* **1981,** *209* (2), 129-147.

9. Guiochon, G.; Siouffi, A. M., *J. Chromatogr., A* **1982,** *245* (1), 1-20.

10. Guiochon, G.; Siouffi, A.-M., *J. Chromatogr. Sci.* **1978,** *16*, 470-481.

11. Guiochon, G.; Bressolle, F.; Siouffi, A.-M., *J. Chromatogr. Sci.* **1979,** *17*, 368-386.

12. Guiochon, G.; Siouffi, A.-M.; Engelhardt, H.; Halaz, I., *J. Chromatogr. Sci.* **1978,** *16*, 152-157.

13. Guiochon, G.; Siouffi, A.-M., *J. Chromatogr. Sci.* **1978,** *16*, 324-329.

14. Guiochon, G.; Korosi, G.; Siouffi, A.-M., *J. Chromatogr. Sci.* **1980,** *18*, 324-329.

15. *High-Perfomrance Liquid Chromatography Advances and Perspectives*. Academic Press: New York, 1980; Vol. 2.

16. Cavalli, E.; Guinchard, C., *Chromatographia* **1993,** *37* (1), 107-109.

17. Poole, S. K.; Poole, C. F., *J. Chromatogr. A* **2011,** *1218* (19), 2648-2660.

18. Siouffi, A. M., *Sep. Purif. Rev.* **2005,** *34* (2), 155-180.

19. Colin F, P., *J. Chromatogr., A* **2003,** *1000* (1–2), 963-984.

20. Poole, C. F.; Poole, S. K., *J. Chromatogr., A* **1995,** *703* (1–2), 573-612.

21. Poole, C. F.; Poole, S. K., *Anal. Chem.* **1989,** *61* (22), 1257A-1269A.

22. Poole, C. F., The Essence of Chromatography. Elsevier Science B.V.: Amsterdam, 2003; pp 499-567.

23. Malsche, W. D.; Gardeniers, H.; Desmet, G., *Anal. Chem.* **2008,** *80* (14), 5391-5400.

24. De Smet, J.; Gzil, P.; Baron, G. V.; Desmet, G., *J. Chromatogr., A* **2007,** *1154* (1–2), 189-197.

25. De Smet, J.; Gzil, P.; Vervoort, N.; Verelst, H.; Baron, G. V.; Desmet, G., *J. Chromatogr., A* **2005,** *1073* (1–2), 43-51.

26. Desmet, G.; Cabooter, D.; Gzil, P.; Verelst, H.; Mangelings, D.; Heyden, Y. V.; Clicq, D., *J. Chromatogr., A* **2006,** *1130* (1), 158-166.

27. Yan, X.; Wang, Q.; Bau, H. H., *J. Chromatogr., A* **2010,** *1217* (8), 1332-1342.

28. Gzil, P.; Vervoort, N.; Baron, G. V.; Desmet, G., *Anal. Chem.* **2004,** *76* (22), 6707-6718.

29. Gzil, P.; Vervoort, N.; Baron, G. V.; Desmet, G., *Anal. Chem.* **2003,** *75* (22), 6244-6250.

30. Billen, J.; Desmet, G., *J. Chromatogr. A* **2007,** *1168* (1-2), 73-99.

31. De Smet, J.; Gzil, P.; Vervoort, N.; Verelst, H.; Baron, G. V.; Desmet, G., *Anal. Chem.* **2004,** *76* (13), 3716-3726.

32. Colin F, P., *J. Chromatogr., A* **1999,** *856* (1–2), 399-427.

33. Sherma, J., *Anal. Chem.* **2010,** *82* (12), 4895-4910.

34. Han, Y.; Levkin, P.; Abarientos, I.; Liu, H.; Svec, F.; Fréchet, J. M. J., *Anal. Chem.* **2010,** *82* (6), 2520-2528.

35. Sherma, J., *J. Chromatogr., A* **2000,** *880* (1–2), 129-147.

36. Handbook of Thin-Layer Chromatography. 2nd Ed. ed.; Marcel Dekker, Inc: New York, 1996; p 1104.

37. Gocan, S., *J. Chromatogr. Sci.* **2002,** *40* (10), 538-549.

38. Tsai, M.-T.; Lu, Y.-F.; Wang, Y.-K., *J. Alloys Compd.* **2010,** *505* (2), 818-823.

39. Bergna, H. E., Colloid Chemistry of Silica: An Overview. In *Colloidal Silica Fundamentals and Applications*, Bergna, H. E.; Roberts, W. O., Eds. Taylor & Francis Group: Boca Raton, 2006; Vol. 131, pp 9-35.

40. Sherma, J., *Handbook of Thin-Layer Chromarography*. 2nd Ed. ed.; Marcel Dekker, Inc.: New York, 1996; Vol. 71.

41. Fried, B.; Sherma, J., *Thin-Layer Chromatography*. 4th Ed. ed.; Marcel Dekker, Inc.: New York, 1999.

42. Poole, C. F.; Dias, N. C., *J. Chromatogr., A* **2000,** *892* (1–2), 123-142.

43. Stahl, E., In *Thin Layer Chromatography*, Stahl, E., Ed. Springer-Verlag: New York, 1969; pp 48-52.

44. Lamparczyk, H.; Ochocka, R.; Zarzycki, P.; Zielinski, *J. Planar Chromatogr.* **1990,** *3*, 34.

45. Fuchs, B.; Süß, R.; Teuber, K.; Eibisch, M.; Schiller, J., *J. Chromatogr., A* **2011,** *1218* (19), 2754-2774.

46. Abidi, S. L., *J. Chromatogr., A* **2001,** *935* (1–2), 173-201.

47. Lamparczyk, H.; Ochocka, R.; Zarzycki, P., *Chromatographia* **1989,** *27* (11), 565-568.

48. Okamoto, M., *Chromatographia* **1988,** *26* (1), 145-148.

49. Dinan, L.; Harmatha, J.; Lafont, R., *J. Chromatogr., A* **2001,** *935* (1–2), 105-123.

50. Halaweish, F. T.; Tallamy, D. W., *J. Liq. Chromatogr. Relat. Technol.* **1993,** *16* (2), 497-511.

51. Oleszek, W.; Bialy, Z., *J. Chromatogr., A* **2006,** *1112* (1–2), 78-91.

52. Oleszek, W. A., *J. Chromatogr., A* **2002,** *967* (1), 147-162.

53. Perenich, T. A., *Textile Chem. Color* **1982,** *14*, 60.

54. Perenich, T. A. Natl. Tech. Cong., AATCC, 1982; p 173.

55. Oka, H.; Ikai, Y.; Kawamura, N.; Yamada, M.; Inoue, H.; Ohno, T.; Inagaki, K.; Kuno, A.; Yamamoto, N., *J. Chromatogr. A* **1987,** *411* (0), 437-444.

56. Yin, P.; Qin, P.; Liu, Q., *Supu* **1989,** *7*, 313.

57. Janjic, T. J.; Milojkovic, D. M.; Arbutina, Z. J.; Celap, M. B., *J. Serb. Chem. Soc.* **1991,** *56*, 33.

58. Koerner, A., *J. Planar Chromatogr. Mod. TLC* **1993,** *6*, 138.

59. Yin, P. Y.; Li, H. N.; Yan, C. T., *Fenxi Huaxue* **1993,** *21*, 365.

60. Oka, H.; Ikaia, Y.; Ohno, T.; Kawamura, N.; Hayakawa, J.; Harada, K.-i.; Suzuki, M., *J. Chromatogr., A* **1994,** *674* (1–2), 301-307.

61. Cserháti, T.; Forgács, E., *J. Chromatogr., A* **2001,** *936* (1–2), 119-137.

62. Komsta, Ł.; Skibiński, R.; Berecka, A.; Gumieniczek, A.; Radkiewicz, B.; Radoń, M., *J. Pharm. Biomed. Anal.* **2010,** *53* (4), 911-918.

63. Tuzimski, T.; Soczewiński, E., *J. Chromatogr., A* **2002,** *961* (2), 277-283.

64. Lepri, L.; Desideri, P. G.; Heimler, D., *J. Chromatogr., A* **1981,** *211* (1), 29-37.

65. Lepri, L.; Desideri, P. G.; Heimler, D., *J. Chromatogr., A* **1981,** *207* (3), 412-420.

66. Lepri, L.; Desideri, P. G.; Heimler, D., *J. Chromatogr., A* **1981,** *209* (2), 312-315.

67. Lepri, L.; Desideri, P. G.; Heimler, D., *J. Chromatogr., A* **1980,** *195* (1), 65-73.

68. Lepri, L.; Desideri, P. G.; Heimler, D., *J. Chromatogr., A* **1980,** *195* (2), 187-195.

69. Lepri, L.; Desideri, P. G.; Heimler, D., *J. Chromatogr., A* **1983,** *268* (0), 493-501.

70. Grassini-Strazza, G.; Nicoletti, I., *J. Chromatogr., A* **1985,** *322* (0), 149-158.

71. Zlatanov, L.; Gonnet, C.; Marichy, M., *Chromatographia* **1986,** *21* (6), 331-334.

72. John L, M., *Anal. Biochem.* **1985,** *150* (1), 13-17.

73. Patzsch, K.; Netz, S.; Funk, W., *J. Planar Chromatogr.* **1988,** *1*, 39.

74. Patzsch, K.; Netz, S.; Funk, W., *J. Planar Chromatogr.* **1988,** *1*, 177.

75. Jost, W.; Hauck, H. E., *J. Chromatogr., A* **1983,** *261* (0), 235-244.

76. Cserháti, T.; Hauck, H. E., *J. Chromatogr., A* **1990,** *514* (0), 45-55.

77. Cserháti, T.; Forgács, E.; Morais, H.; Mota, T., *J. Biochem. Biophys. Methods* **2000,** *45* (2), 221-229.

78. Gunther, H. O., *Merch Spectrum (Darmstadt)* **1992,** *3*, 30.

79. Jost, W.; Hauck, H. E., *Anal. Biochem.* **1983,** *135* (1), 120-127.

80. Klaus, R.; Fischer, W.; Hauck, H., *Chromatographia* **1989,** *28* (7), 364-366.

81. Klaus, R.; Fischer, W.; Hauck, H., *Chromatographia* **1990,** *29* (9), 467-472.

82. Klaus, R.; Fischer, W.; Hauck, H., *Chromatographia* **1991,** *32* (7), 307-316.

83. Klaus, R.; Fischer, W.; Hauck, H., *Chromatographia* **1993,** *37* (3), 133-143.

84. Stroka, J.; Dasko, L.; Spangenberg, B.; Anklam, E., *J. Liq. Chromatogr. Relat. Technol.* **2004,** *27* (13), 2101-2111.

85. Klaus, R.; Fischer, W.; Hauck, H., *Chromatographia* **1994,** *39* (1), 97-102.

86. Bleichert, M.; Eckhardt, H.-S.; K-F., K.; Spangenberg, B., *J. Planar Chromatogr.* **2008,** *21*, 55-59.

87. Poole, S. K.; Baley, M. T.; Poole, C. F., *J. Planar Chromatogr.* **1992,** *5*, 16.

88. Cimpoiu, C.; Hosu, A.; Hodisan, S., *J. Pharm. Biomed. Anal.* **2006,** *41* (2), 633-637.

89. Kiridena, W.; Miller, K. G.; Poole, C. F., *J. Planar Chromatogr. Mod. TLC* **1995,** *10*, 31.

90. Lodi, G.; Bighi, V.; Brandolini, E., *J. Planar Chromatogr. Mod. TLC* **1997,** *10*, 31.

91. Bernardi, T.; Tamburini, E., *J. Planar Chromatogr. Mod. TLC* **2009,** *22* (5), 321-325.

92. Ferenczi-Fodor, K.; Végh, Z.; Renger, B., *J. Chromatogr., A* **2011,** *1218* (19), 2722-2731.

93. Miserez, F.; Potterat, O.; Marston, A.; Mungai, G. M.; Hostettmann, K., *Phytochem.* **1996,** *43* (1), 283-286.

94. Vaccari, G.; Lodi, G.; Tamburini, E.; Bernardi, T.; Tosi, S., *Food Chem.* **2001,** *74* (1), 99-110.

95. Van Poucke, L. V.; Rousseau, D.; Van Peteghem, C.; De spiegeleer, B. M. J., *J. Planar Chromatogr.* **1989,** *2*, 395.

96. Cserháti, T.; Olajos, S.; Jacob, K.; Egeler, E.; Luppa, P.; Birwé, H.; Hesse, A.; Specht, D.; Meese, C. O.; Ratge, D.; Eichelbaum, M.; Wisser, H.; Englmaier, P.; Krauss, G. J.; Friebe, S.; Nitsche, H.; Parviainen, M. T.; Kokko, H.; Mononen, I.; Pikkarainen, P.; Röhler, S. B.; Wolf, C.; Schmid, R. W.; Schertel, B.; Eichler, W., *Fresenius' J. Anal. Chem.* **1990,** *337* (1), 60-72.

97. Tomkinson, G. P.; Wilson, I. D.; Ruane, R. J., *J. Planar Chromatogr.* **1990,** *3*, 491.

98. Daurade-Le Vagueresse, M.; Bounias, M., *Chromatographia* **1991,** *31* (1), 5-10.

99. Hauck, H. E.; Mack, M.; Reuke, S.; Herber, H., *J. Planar Chromatogr.* **1989,** *2*, 268.

100. Hoffman, A.; Funk, W., *GIT suppl.* **1988,** *3*, 70.

101. Hawrył, M. A.; Waksmundzka-Hajnos, M., *J. Chromatogr., A* **2011,** *1218* (19), 2812-2819.

102. Jost, W.; Hauck, H.; Fischer, W., *Chromatographia* **1986,** *21* (7), 375-378.

103. Baithsolts, A. D.; Ardell, R. E., *J. Chromatogr., A* **1967,** *30* (0), 493-501.

104. Gocan, S., Stationary Phases in Thin-Layer Chromatography In *Modern Thin-Layer Chromatography*, Grinberg, N., Ed. Marcel Dekker: New York, 1991.

105. Caissie, G. E.; Mallet, V. N., *J. Chromatogr., A* **1976,** *117* (1), 129-136.

106. Schmeltz, I.; Wenger, A.; Hoffmann, D., *Thin-Layer Chromatography*. John Wiley: New York, 1980.

107. Kovac, M. F., *J. Assoc. Off. Agric. Chem.* **1963,** *46*, 884.

108. Ajmal, M.; Mohammad, A.; Fatima, N.; Ahmad, J., *J. Planar Chromatogr.* **1988,** *1*, 239.

109. Seher, A., *Mikrochim. Acta* **1961,** *1*, 308.

110. Ahmad, J., *J. Planar Chromatogr.* **1996,** *9*, 236-46.

111. Rigney, M. P.; Funkenbusch, E. F.; Carr, P. W., *J. Chromatogr., A* **1990,** *499* (0), 291-304.

112. Annen, M. J.; Kizhappali, R.; Carr, P. W.; McCormick, A., *J. Mater. Sci.* **1994,** *29* (23), 6123-6130.

113. Rigney, M. P.; Weber, T. P.; Carr, P. W., *J. Chromatogr., A* **1989,** *484* (0), 273-291.

114. Carr, P. W.; Funkenbusch, E. F.; Rigney, M. P.; Coleman, P. L.; Hanggi, W. A. S. High stability porous zirconium oxide spherules. 1991.

115. Yan, B.; McNeff, C. V.; Carr, P. W.; McCormick, A. V., *J. Am. Ceram. Soc.* **2005,** *88* (3), 707-713.

116. Senl, A. K.; Das, S. B.; Ghosh, U. C., *J. Liquid Chromatogr.* **1985,** *8* (16), 2999-3008.

117. Danielson, N. D.; Katon, J. E.; Bouffard, S. P.; Zhu, Z., *Anal. Chem.* **1992,** *64* (18), 2183-2186.

118. Nawrocki, J.; Dunlap, C. J.; Carr, P. W.; Blackwell, J. A., *Biotechnol. Prog.* **1994,** *10* (6), 561-573.

119. Blackwell, J. A.; Carr, P. W., *J. Liquid Chromatogr.* **1991,** *14* (15), 2875-2889.

120. *Encyclopedia of Chromatography 2004 Update Supplement*. Marcel Dekker: New York, 2004.

121. Hamilton, D. J.; Simpson, B. W., *J. Chromatogr., A* **1969,** *39* (0), 186-194.

122. Waksmundzka-Hajnos, M.; Wrońska, B., *Chromatographia* **1996,** *43* (7), 405-412.

123. *Modern Thin-Layer Chromatography*. Marcel Dekker, Inc.: New York, 1990; Vol. 52.

124. Karakas, R.; Yuksel, U., *Journal of Chromatographic Science* **1998,** *36* (10), 499-504.

125. Erg; uuml; l, S.; Kadan, m.; Savac, a.; l, S., *Journal of Chromatographic Science* **2005,** *43* (8), 394-400.

126. Strain, H. H., *Chromatography*. 1967.

127. John L, G., *J. Chromatogr., A* **1964,** *15* (0), 90-92.

128. Weiler, E. W., *Planta Med.* **1979,** *35*, 162.

129. Stahl, E.; Kaltenbach, U., *J. Chromatogr., A* **1961,** *5* (0), 351-355.

130. Waldi, D., *Thin-Layer Chromatography: Laboratory Handbook*. Academic Press: New York, 1965.

131. Măruţoiu, C.; Bădescu, M.; Pătruţ, A.; Tecoanţă, A.; Dascălu, M., *Acta Chromatographica* **1998,** *8*, 32-38.

132. Stevenson, R., Journal of Chromatography Library. Elsevier: 2004; pp 469-518.

133. Hauck, H. E.; Schulz, M., *J. Chromatogr. Sci.* **2002,** *40* (10), 550-552.

134. Hauck, H.; Schulz, M., *Chromatographia* **2003,** *57* (0), S313-S315.

135. Hauck, H.; Bund, O.; Fischer, W.; Schulz, M., *J. Planar Chromatogr.--Mod. TLC* **2001,** *14* (4), 234-236.

136. Bakry, R.; Bonn, G. K.; Mair, D.; Svec, F., *Anal. Chem.* **2006,** *79* (2), 486-493.

137. Bezuidenhout, L. W.; Brett, M. J., *J. Chromatogr., A* **2008,** *1183* (1–2), 179-185.

138. Clark, J. E.; Olesik, S. V., *Anal. Chem.* **2009,** *81* (10), 4121-4129.

139. Zewe, J. W.; Steach, J. K.; Olesik, S. V., *Anal. Chem.* **2010,** *82* (12), 5341-5348.

140. Clark, J. E.; Olesik, S. V., *J. Chromatogr., A* **2010,** *1217* (27), 4655-4662.

141. Song, J.; Jensen, D. S.; Hutchison, D. N.; Turner, B.; Wood, T.; Dadson, A.; Vail, M. A.; Linford, M. R.; Vanfleet, R. R.; Davis, R. C., *Adv. Funct. Mater.* **2011,** *21* (6), 1132-1139.

142. Hausmann, D.; Becker, J.; Wang, S.; Gordon, R. G., *Science* **2002,** *298* (5592), 402-406.

143. Cavanagh, A. S.; Wilson, C. A.; Weimer, A. W.; George, S. M., *Nanotechnol.* **2009,** *20* (25), 255602.

144. Herrmann, C. F.; Fabreguette, F. H.; Finch, D. S.; Geiss, R.; George, S. M., *Appl. Phys. Lett.* **2005,** *87* (12), 2053358-2053360.

145. Farmer, D. B.; Gordon, R. G., *Electrochem. Solid-State Lett.* **2005,** *8* (4), G89-G91.

146. Farmer, D. B.; Gordon, R. G., *Nano Lett.* **2006,** *6* (4), 699-703.

147. Li, M.; Boggs, M.; Beebe, T. P.; Huang, C. P., *Carbon* **2008,** *46* (3), 466-475.

148. Peng, K.; Liu, L.-Q.; Li, H.; Meyer, H.; Zhang, Z., *Carbon* **2011,** *49* (1), 70-76.

Chapter 2: Elevated Temperatures in Liquid Chromatography I: Benefits and Practical Considerations*

2.1. Overview

Elevated temperature separations are an important current topic in liquid chromatography because they offer significant benefits over those performed at ambient temperature. Here twelve such benefits are discussed, and then describe some practical considerations for implementation of elevated temperature LC.

2.2. Benefits of Elevated Temperature LC

Some of the frequently cited advantages of elevated temperature separations are as follows.

i) Because solvent viscosity is a strong function of temperature, *elevated temperatures decrease mobile phase viscosities,* which leads to *lower column back pressures and faster separations*. The dependence of viscosity on temperature is exponential and is given by:

$$\eta = 10^{a+\frac{b}{T+c}} \qquad (1)$$

where η is the viscosity, *a, b,* and *c* are coefficients that are specific to a solvent, and *T* is the temperature in Kelvin.[1] Accordingly, noticeable reductions in viscosity, and therefore backpressure, are observed in systems running even at relatively low temperatures. For example, the viscosity of water decreases from 0.890 centipoise (cp) to 0.547 cp and that of acetonitrile from 0.369 cp to 0.284 cp at 25 and 50 °C, respectively.[2] This advantage only

---

*This chapter is reproduced with permission from (David S. Jensen, Thorsten Teutenberg, Jody Clark, and Matthew R. Linford) *LCGC North Am.* **2012**, *30* (9), 850-862. Copyright 2012 **Advanstar Communications, Inc.**

increases with increasing temperature: a 20-fold improvement in analysis time can be realized when working at 150 - 200 °C.[3-5]

ii) With the reduction in mobile phase viscosity with increasing temperature, *less toxic and 'greener', but inherently more viscous, organic modifiers can be contemplated*, e.g., ethanol. Separation of eighteen fat and water soluble UV filters for cosmetic formulations was achieved using ethanol as an organic modifier under gradient conditions at 45 °C.[6] Ethanol and water were also used to separate various phthalates at 35 °C.[7]

iii) Column temperatures exceeding the normal boiling points of the typical solvents used in LC can be employed in elevated temperature LC because a relatively inexpensive backpressure regulator can be installed at the end of the system, e.g., after the UV detector, to suppress boiling of the mobile phase in the column. The typical pressure range for a backpressure regulator is 20 – 70 bar.

The increase in solvent boiling point with external pressure follows from the integrated Clausius-Clapeyron equation:[8]

$$p = p^{*}e^{-\chi} \tag{2}$$

$$\chi = \frac{\Delta_{\text{vap}}H}{R}\left(\frac{1}{T} - \frac{1}{T^{*}}\right) \tag{3}$$

in these equations, p^* is the vapor pressure of the liquid at a temperature of T^*, p is the vapor pressure at the temperature T, $\Delta_{\text{vap}}H$ is enthalpy of vaporization of the liquid, and R is the gas constant. Values of $\Delta_{\text{vap}}H$ for various solvents of importance in chromatography are given in Table 2.1. Because a liquid boils when its vapor pressure exceeds the pressure acting on it, it is clear that the column pressure must be kept above the vapor pressure of the mobile phase to prevent it from boiling. A backpressure regulator of ca. 30 bar is usually sufficient to keep typical mobile phases from boiling.[9]

iv) As temperature increases, water's static permittivity decreases, so water behaves increasingly like an organic solvent. *Thus, at elevated temperature, water is increasingly able to dissolve non-polar species,*[10] *and separations using more aqueous mobile phases can mimic those using more organic modifiers at lower temperatures*. For neutral compounds on silica- and zirconica-based columns, an increase in 4 - 5 °C affects retention like a 1% increase in organic modifier.[11-13] More specifically, a temperature increase of 3.75 °C had a similar elution strength change as a 1% increase in methanol,[14] and a 5 °C increase in temperature was comparable to a 1% increase in acetonitrile.[11] Figure 2.1 shows this effect graphically – how heated water can mimic the elution strengths (dielectric constants) of water/methanol and/or water/acetonitrile mixtures. For example, to replace a separation that uses 40:60 H_2O/ethanol with a pure aqueous mobile phase the chromatographer would operate near 130 °C.

Some applications have employed pure aqueous mobile phases at temperatures exceeding 100 °C, which they term "superheated water chromatography," "subcritical water chromatography" or "chromatography in very hot water."[13] Figure 2.2 shows the separation of several steroids at various temperatures using a superheated water mobile phase.[15] The separation performed at 120 °C was far from ideal. As the temperature was increased to 140 and then 185 °C the analysis time was reduced tremendously, from 30 min to 18 min to 5.5 min. Notice that the degree of tailing decreased with increasing temperature, which can be attributed to a decrease in the number and/or effectiveness of secondary interactions.

Table 2.1 Enthalpy of vaporization (Δ_vap H) for various solvents.[2] Note that enthalpies are generally fairly constant with temperature.

	$\Delta_{vap}H(25\ °C)$ (kJ/mol)
Tetrahydrofuran	31.99
Acetonitrile	32.94
Methanol	37.43
Ethanol	42.32
Water	43.98
Isopropanol	45.39

The van Deemter equation (eq. 4) sheds light on some of the benefits of elevated temperature LC:

$$H = A + \frac{B}{u} + c \cdot u \tag{4}$$

where H is the height equivalent of a theoretical plate, A is the eddy diffusion coefficient, which depends on the quality of the column packing and the size of the particles in the packed bed, but is otherwise unaffected by temperature, B is the longitudinal diffusion term, C is the mass transfer coefficient, and u is the linear velocity of the mobile phase. A simplistic breakdown of the B and C terms shows that both depend on the analyte diffusion coefficient, D_m, as follows:[1]

$$B \propto D_m \tag{5}$$

$$C \propto \frac{1}{D_m} \tag{6}$$

D_m is strongly temperature dependent (as is η – see Eq. 1),[1] and depends on T and η:

$$D_m \propto \frac{T}{\eta} \tag{7}$$

Hence, $B \propto \frac{T}{\eta}$ and $C \propto \frac{\eta}{T}$, so as T increases, B increases and C decreases. As a result, an increase in temperature will increase the degree to which longitudinal diffusion occurs (the B term), unfavorably raising plate heights and broadening bands. However, elevated temperatures lead to more efficient solute/mass transfer between the mobile and stationary phases, and diffusion is accelerated within the mobile phase itself,[20, 21] which reduces the resistance to mass transfer of the analyte (the C term), and lowers plate height and is favorable.

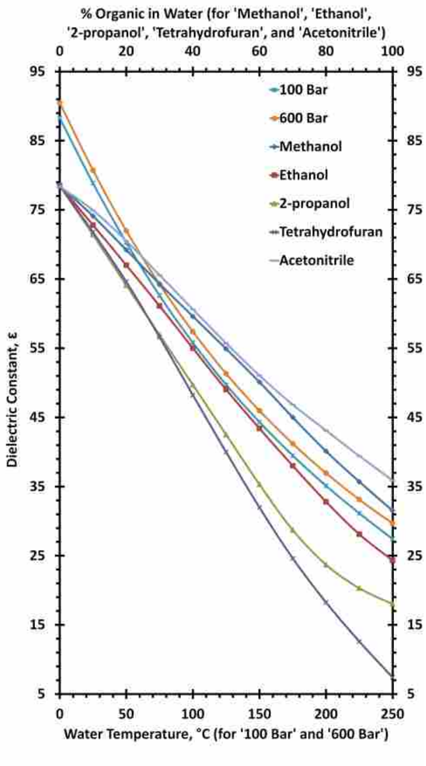

Figure 2.1 Change in polarity (dielectric constant) of water with changing temperature at 100 and 600 bar (bottom x-axis),16 compared to the effect of mixing an organic modifier into water at 25 °C and ambient pressure (top x-axis). Lables are: * 100 Bar (water), ● 600 bar (water), ♦ methanol, ■ ethanol, ▲2-propanol, x tetrahydrofuran, - acetonitrile.[17, 18] Lines are guides to the eye.

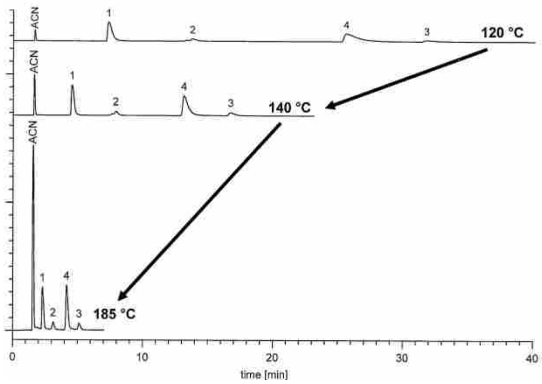

Figure 2.2 ‘Isocratic and isothermal separation of a mixture containing four steroids on a polybutadiene-coated zirconium dioxide column (ZirChrom-PBD; 4.6 x 150 mm ID; 3 μm, 300 Å). Chromatographic conditions: temp.: 120, 140 and 185 °C; flow rate: 1 mL/min; mobile phase: deionized water; detection: UV at 200 nm. Peaks: 1) estriol; 2) androstaiendione; 3) dehydroepiandrosterone; and 4) estrone.’ From Ref. 19 with permission.

Two important consequences of these effects are that as temperature increases (i) the minimum in the van Deemter equation (H_{min}) shifts to higher values of u[21, 22] and (ii) van Deemter curves flatten (see Figure 2.3). Thus, elevated temperatures allow for *faster separations with little or no loss of efficiency*. Note that in general, H_{min} stays roughly constant with increasing temperature, so efficiencies do not change significantly with changing temperature as long as the linear velocity for the separation is near the optimum.

An empirical demonstration that higher flow rates do not strongly affect the quality of a separation at elevated temperature (185 °C) is shown in Figure 2.4. At 1 mL/min four steroids were separated in under 5.5 min.[19] Under identical conditions, the same separation was then performed in under 1.5 min using a flow rate of 5 mL/min.[15] Even at this greatly increased flow rate, the steroids were still baseline separated.

v) *Temperature is an instrumental variable, not a chemical variable*, so with proper equipment it is often easier to change the temperature of a separation than to explore a chemical change in the mobile or stationary phase.

vi) *Changes in analyte selectivity with temperature can sometimes be substantial*, and reversal of elution order of certain analytes with increasing temperature may be observed.[25] For example, while a decrease in retention times of analytes is usually found with increasing temperature in reversed-phase LC, McCalley demonstrated an increase in retention times of various bases with increasing temperature.[26] This increase in retention could be attributed to a temperature dependency of the pK_a of the ionizable portion of the base.

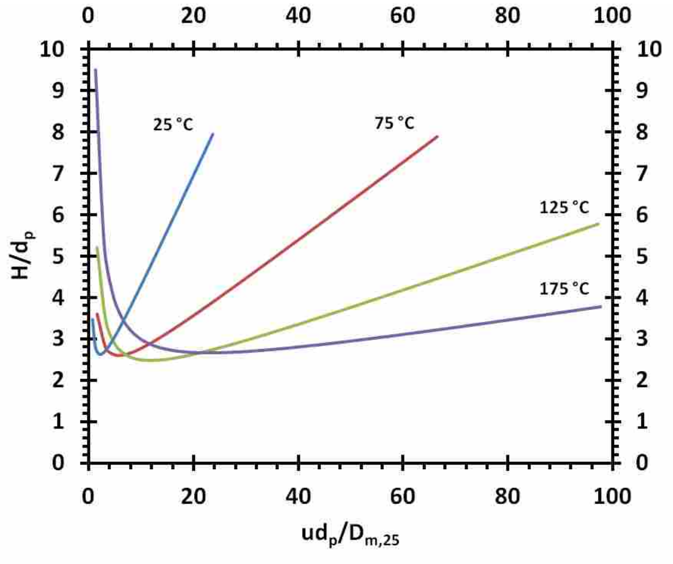

Figure 2.3 'Plots of the reduced plate height [the plate height, *H*, divided by the particle diameter, d_p] *versus* the reduced velocity [linear velocity, *u*, multiplied by the particle diameter, d_p, divided by the diffusion coefficient for the analyte] scaled to $D_{m,25}$ [the diffusion coefficient of the analyte at 25 °C] with the temperature as the parameter. Conditions: totally porous particles, rapid sorption kinetics, $D_{m,25} = 6 \times 10^{-7}$ and $d_p = 3$ µm. Plate height versus linear velocity at various temperatures.'[23] Figure 2.adapted from Ref. (23). The same trends are observed in plots of *H* vs. *u*.[22] As temperature increases: (i) the minimum value of *H* stays roughly constant, (ii) B increases, and (iii) C decreases, which leads to the expected flattening of the van Deemter curve. (As noted, in the classical expression for the van Deemter equation, the *A* term does not depend on temperature.[21] However, there is at least some suggestion that the higher analyte diffusion coefficients at elevated temperatures reduce the effects of multiple paths for analytes in a column and may lead to some improvement in *A*.[24])

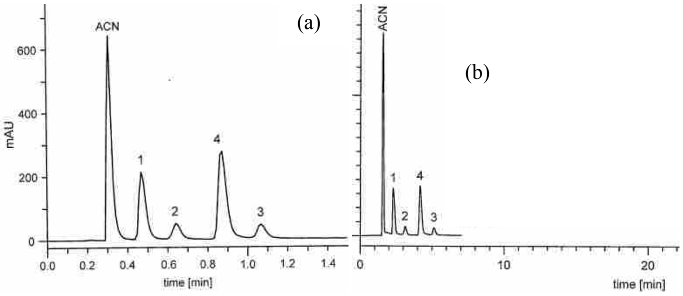

Figure 2.4 'Isocratic and isothermal separation of a mixture containing four steroids on a polybutadiene-coated zirconium dioxide column (ZirChrom-PBD; 4.6 x 150 mm ID; 3 µm, 300 Å). Chromatographic conditions: temp.: … 185 °C; … mobile phase: deionized water; detection: UV at 200 nm. Peaks: 1) estriol; 2) androstaiendione; 3) dehydroepiandrosterone; and 4) estrone.' (19). Separations are identical except (a) was done at 5.0 mL/min and (b) was done at 1.0 mL/min. From Refs. (18 and 19) with permission.

vii) Elevated temperature LC raises the possibility of performing *retention modeling over a range of temperatures, i.e.*, predicting and optimizing the retentions of analytes with input from relatively few experiments.[27-32] Because plots of ln k vs. $1/T$ are often linear, and because elevated temperature LC is increasingly practiced, this advantage is becoming particularly important.[33]

viii) There is an option of *direct extraction of thermodynamic data through van 't Hoff plots*, which are plots of ln k vs. $1/T$, where k is the retention factor and T is the temperature in Kelvin. This information can serve both to characterize a column and also to allow its comparison to others.[34, 35]

ix) In general, thermostatting (see page 13) a column at a temperature above room temperature is a very good idea *to avoid the daily fluctuations in temperature that take place in most laboratories* and that can change analyte retention. Analyte retention typically changes by ca. 2% for each 1 °C change, so a daily or day-to-day change in laboratory temperature of ± 5 °C or more, which can occur in many laboratories, can substantially change analyte retentions.[20, 36-38]

x) *The equipment needed for elevated temperature separations is readily available*; relatively inexpensive column ovens are commercially available, and provide temperature control and the necessary precolumn heating and postcolumn cooling of the mobile phase.[36, 39] [40-42] Many HPLC and UHPLC systems sold today come with column ovens.

xi) *Analyte decomposition in elevated temperature LC is not generally an issue*, as most analytes possess good thermal stability, even at relatively high temperatures, during their short dwell times in a column.[3] However, in the case that a thermally labile compound may be part of a separation, or a reaction may be possible between the mobile phase and an analyte, the questions presented by Thompson et al.[3] may help the chromatographer decide whether elevated temperature chromatography will be desirable: (1) Does working at elevated temperature reduce the dependability 'of the analytical calibration curve?' (2) Does elevated temperature chromatography 'induce a significant intercept in the calibration curve?' (3) Does temperature 'significantly diminish the sensitivity?' (4) If present, do 'on-column reactions distort … peak shape?' (5) Does elevated temperature chromatography 'introduce new peaks that interfere with the resolution/quantitation of the analyte or impurities?' (6) 'Pursuant to an impurity analysis, does a high-temperature mobile phase cause chemical reactions that alter the concentration or produce products that would interfere with quantitation of the impurity?' If the answers to these questions is 'no', then elevated temperature chromatography should be a viable option.

2.3. Practical Considerations for Elevated Temperature LC

In order to realize the advantages of elevated temperature HPLC, the mobile phase flow rate must increase and the column oven must be equipped with an efficient, low volume means of properly adjusting the mobile phase temperature.[4] That is, the mobile phase needs to be preheated before entering the chromatographic column to avoid thermal mismatch between the column and the incoming mobile phase. If such thermal mismatch exists, then band broadening of the peak may result, producing less than optimal chromatography. This thermal mismatch should be kept to less than 5 °C.[3] Many systems come equipped with column preheaters that can be thermostatted independently of the column oven. Figure 2.5 shows a diagram of a typical elevated temperature apparatus. As with most systems, the solvents are mixed after the pumps and before the injector. The incoming solvent is preheated. The column is thermostated (Figure

2.5) at a particular temperature via a column oven, the effluent is cooled before it enters the detector, and the column is maintained under a certain pressure via a backpressure regulator that is placed inline after the detector and before waste.

Figure 2.6 demonstates how band broadening may occur if the mobile phase is not properly preheated. In situation (a) the temperature of the incoming mobile phase matches the temperature of the column. When the temperatures of the mobile phase and column match, peak distortion resulting from thermal gradients is avoided. In situation (b) the incoming mobile phase is cooler than the column, which leads to radial thermal gradients, i.e., the center of the column will be cooler than the outer portion of the column. This type of thermal mismatch between the column and mobile phase will result in broader peaks and less than optimal chromatography. In situation (c) frictional heating is present. Frictional heating becomes a problem at high pressures due to friction between the mobile phase and the stationary phase/support. Frictional heating may lead to axial (along the length of the column) and radial thermal gradients. Axial thermal gradients also result in band broadening and a loss of efficiency. Situation (d) shows that one may compensate for frictional heating by introducing the mobile phase at a reduced temperature.

A chromatographic demonstration of the thermal mismatch diagrammed in Figure 2.6 is shown in Figure 2.7. Figure 2.7(a) shows an ideal chromatogram, obtained by preheating the mobile phase to the temperature of the column. Figure 2.7(b) shows a chromatogram with the incoming mobile phase cooler than the column. This thermal mismatch produces two effects: (1) the retention times of peaks C, D, E F, and G are changed when compared to chromatogram 7(a) –they are longer because the temperature of the mobile phase is lower, and (2) peaks F and G are broader and distorted, which is attributed to thermal gradients in the column.[43, 44] Figure 2.7(c) also shows a thermal mismatch between the entering mobile phase and the column, where in this case these temperatures were adjusted to produce the same retention times as in the ideal chromatogram of 7(a). However, peaks C, F, and G are still distorted, and peaks F and G are noticeably split. These less than desirable effects are again attributed to axial and thermal gradients in the column.

As a final practical consideration, one must be aware of the temperature limits of any columns that might be contemplated for use in elevated temperature chromatography. Many stationary phases/supports, especially those based on silica, degrade quickly at elevated temperatures. These effects are exacerbated at extremes of pH. However, there are also some materials based on silica that exhibit excellent stability even at temperatures above 100 °C.[45]

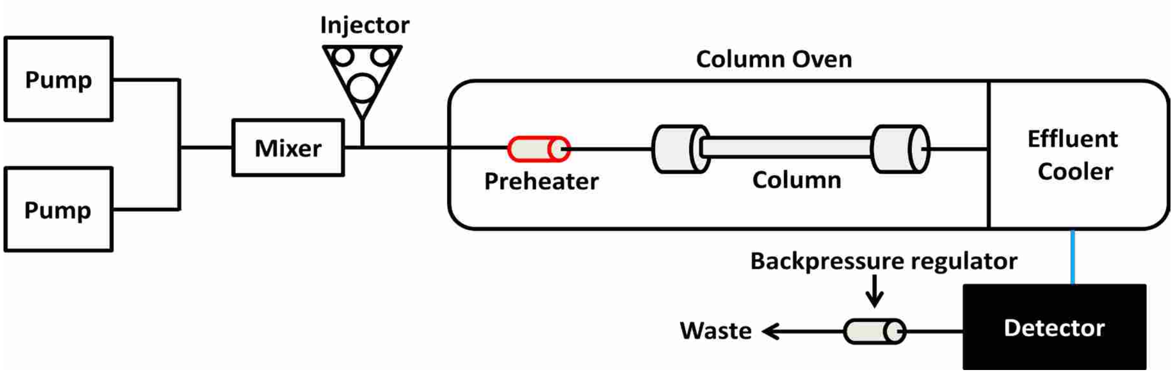

Figure 2.5 Typical apparatus for elevated temperature LC with preheater, which can be temperature controlled independent of the column oven, post effluent cooler, and backpressure regulator.

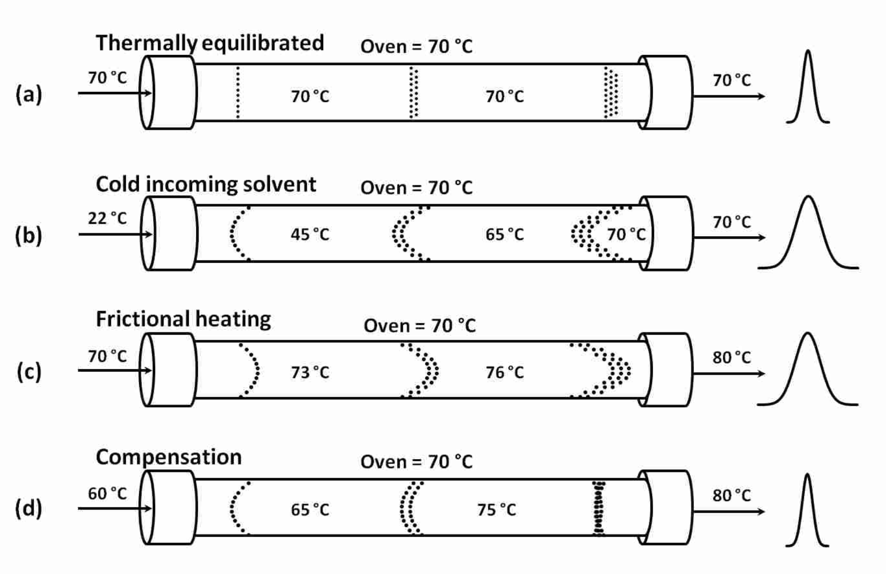

Figure 2.6 'Band broadening due to thermal effects. (a) Ideal case, no thermal effects; (b) effect of incoming mobile phase that is at a lower temperature than the column; (c) effect of frictional heating; (d) combined effects of cold incoming mobile phase and frictional heating. An oven temperature of 70 °C is assumed. Number shown inside column suggest plausible solvent temperatures at column center.' Figure adapted from Ref. 43.

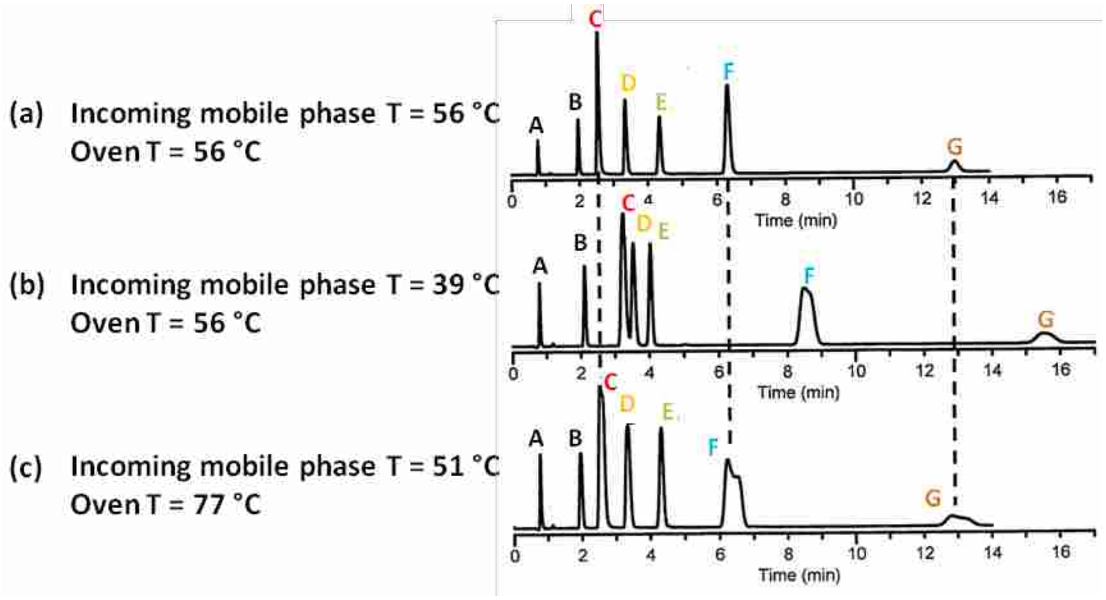

Figure 2.7 ‘Effect of the inlet solvent temperature on separation. Flow rate is 2.0 mL/min, incoming and oven temperatures shown the in figure.’ Adapted from Ref. 43.

2.4. Acknowledgments

T.T. and J.C aided in technical questions. D.J. and M.L. wrote the manuscript.

2.5. References

1. Giegold, S.; Teutenberg, T.; Tuerk, J.; Kiffmeyer, T.; Wenclawiak, B., *J. Sep. Sci.* **2008,** *31* (20), 3497-3502.

2. *CRC Handbook of Chemistry and Physics*. 85th ed.; CRC Press: Boca Raton, 2004.

3. Thompson, J. D.; Carr, P. W., *Anal. Chem.* **2002,** *74* (5), 1017-1023.

4. D. Antia, F.; Horváth, C., *J. Chromatogr. A* **1988,** *435*, 1-15.

5. Teutenberg, T.; Wiese, S.; Wagner, P.; Gmehling, J., *J. Chromatogr. A* **2009,** *1216* (48), 8470-8479.

6. Salvador, A.; Chisvert, A., *Anal. Chim. Acta* **2005,** *537* (1-2), 15-24.

7. Orsi, D. D.; Gagliardi, L.; Porrà, R.; Berri, S.; Chimenti, P.; Granese, A.; Carpani, I.; Tonelli, D., *Anal. Chim. Acta* **2006,** *555* (2), 238-241.

8. Atkins, P.; De Paula, J., *Atkins' Physical Chemistry*. 8th ed.; W.H. Freeman and Company: New York, 2006.

9. McNeff, C. V.; Yan, B.; Stoll, D. R.; Henry, R. A., *J. Sep. Sci.* **2007,** *30* (11), 1672-1685.

10. Edge, A. M.; Shillingford, S.; Smith, C.; Payne, R.; Wilson, I. D., *J. Chromatogr., A* **2006,** *1132* (1-2), 206-210.

11. Michelle Hong, C.; Horváth, C., *J. Chromatogr., A* **1997,** *788* (1-2), 51-61.

12. Tran, J. V.; Molander, P.; Greibrokk, T.; Lundanes, E., *J. Sep. Sci.* **2001,** *24* (12), 930-940.

13. Heinisch, S.; Rocca, J.-L., *J. Chromatogr., A* **2009,** *1216* (4), 642-658.

14. Bowermast, J.; McNair, H. M., *J. Chromatogr. Sci.* **1984,** *22*, 165-170.

15. Teutenberg, T.; Goetze, H. J.; Tuerk, J.; Ploeger, J.; Kiffmeyer, T. K.; Schmidt, K. G.; Kohorst, W. g.; Rohe, T.; Jansen, H. D.; Weber, H., *J. Chromatogr., A* **2006,** *1114* (1), 89-96.

16. Meyer, C. A., *ASME steam tables : thermodynamic and transport properties of steam : comprising tables and charts for steam and water, calculated using the 1967 IFC formulation for industrial use in conformity with the 1963 international skeleton tables, as adopted by the Sixth International Conference on the Properties of Steam*. American Society of Mechanical Engineers: New York, 1983.

17. Gagliardi, L. G.; Castells, C. B.; Ràfols, C.; Rosés, M.; Bosch, E., *J. Chem. Eng. Data* **2007,** *52* (3), 1103-1107.

18. Akerlof, G., *J. Am. Chem. Soc.* **1932,** *54* (11), 4125-4139.

19. Teutenberg, T., *High-Temperature Liquid Chromatography A User's Guide for Method Development*. RSC Publishing: Cambridge, 2010.

20. Vanhoenacker, G.; David, F.; Sandra, P., *Chromatogr. Today* **2010,** *3* (3), 14-16.

21. Xiang, Y.; Yan, B.; Yue, B.; McNeff, C. V.; Carr, P. W.; Lee, M. L., *J. Chromatogr., A* **2003,** *983* (1-2), 83-89.

22. Vanhoenacker, G.; Sandra, P., *Anal. Bioanal. Chem.* **2008,** *390* (1), 245-248.

23. D. Antia, F.; Horváth, C., *J. Chromatogr., A* **1988,** *435* (0), 1-15.

24. Li, J.; Carr, P. W., *Anal. Chem.* **1997,** *69* (5), 837-843.

25. Edge, A. M.; Shillingford, S.; Smith, C.; Payne, R.; Wilson, I. D., *J. Chromatogr. A* **2006,** *1132* (1-2), 206-210.

26. Buckenmaier, S. M. C.; McCalley, D. V.; Euerby, M. R., *J. Chromatogr. A* **2004,** *1060* (1-2), 117-126.

27. Dolan, J. W., *J. Chromatogr. A* **2002,** *965* (1-2), 195-205.

28. Dolan, J. W.; Snyder, L. R.; Djordjevic, N. M.; Hill, D. W.; Saunders, D. L.; Van Heukelem, L.; Waeghe, T. J., *J. Chromatogr. A* **1998,** *803* (1-2), 1-31.

29. Dolan, J. W.; Snyder, L. R.; Saunders, D. L.; Van Heukelem, L., *J. Chromatogr. A* **1998,** *803* (1-2), 33-50.

30. Dolan, J. W.; Snyder, L. R.; Djordjevic, N. M.; Hill, D. W.; Waeghe, T. J., *J. Chromatogr. A* **1999,** *857* (1-2), 1-20.

31. Dolan, J. W.; Snyder, L. R.; Djordjevic, N. M.; Hill, D. W.; Waeghe, T. J., *j. chromatogr. A* **1999,** *857* (1-2), 21-39.

32. Dolan, J. W.; Snyder, L. R.; Wolcott, R. G.; Haber, P.; Baczek, T.; Kaliszan, R.; Sander, L. C., *J. Chromatogr. A* **1999,** *857* (1-2), 41-68.

33. Wiese, S.; Teutenberg, T.; Schmidt, T. C., *Anal. Chem.* **2011,** *83* (6), 2227-2233.

34. Cole, L. A.; Dorsey, J. G.; Dill, K. A., *Anal. Chem.* **1992,** *64* (13), 1324-1327.

35. Cole, L. A.; Dorsey, J. G., *Anal. Chem.* **1992,** *64* (13), 1317-1323.

36. Heinisch, S.; Rocca, J.-L., *J. Chromatogr. A* **2009,** *1216* (4), 642-658.

37. Gritti, F.; Guiochon, G., *J. Chromatogr., A* **2005,** *1099* (1-2), 1-42.

38. Dolan, J. W., *LCGC North Am.* **2003,** *21* (3), 262-266.

39. Wolcott, R. G.; Dolan, J. W.; Snyder, L. R.; Bakalyar, S. R.; Arnold, M. A.; Nichols, J. A., *J. Chromatogr. A* **2000,** *869* (1-2), 211-230.

40. Teutenberg, T.; Goetze, H. J.; Tuerk, J.; Ploeger, J.; Kiffmeyer, T. K.; Schmidt, K. G.; Kohorst, W. g.; Rohe, T.; Jansen, H. D.; Weber, H., *J. Chromatogr. A* **2006,** *1114* (1), 89-96.

41. Selerity Technologies, Inc. http://www.selerity.com/main/main_products_hplc_9000.html.

42. Scientific Instruments Manufacturer GmbH. http://www.sim-gmbh.de/index.php?option=com_content&task=view&id=64&Itemid=502&lang=en.

43. Wolcott, R. G.; Dolan, J. W.; Snyder, L. R.; Bakalyar, S. R.; Arnold, M. A.; Nichols, J. A., *J. Chromatogr., A* **2000,** *869* (1-2), 211-230.

44. Guillarme, D.; Heinisch, S.; Rocca, J. L., *J. Chromatogr. A* **2004,** *1052* (1-2), 39-51.

45. Teutenberg, T.; Hollebekkers, K.; Wiese, S.; Boergers, A., *J. Sep. Sci.* **2009,** *32* (9), 1262-1274.

Chapter 3: Elevated Temperatures in Liquid Chromatography II: Basic Thermodynamics of Elevated Temperature LC, Including the van ’t Hoff Relationship*

3.1. Introduction

In the previous article various advantages and practical considerations of performing elevated temperature separations were discussed.[1] Here a continuation of this topic, exploring some basic thermodynamic relationships, including the derivation and use of the van ’t Hoff equation is discussed. It is believed that an improved understanding of basic thermodynamics, including the van ’t Hoff relationship, will better help the chromatographer do elevated temperature liquid chromatography.

3.2. Basic Thermodynamic Relationships

a) The *enthalpy* of transfer (ΔH^0) of an analyte in a chromatographic separation is the change in enthalpy that occurs when it moves from the mobile phase to the stationary phase. Enthalpy is defined as $H = E + PV$, where E is the internal energy, P is the pressure, and V is the volume. Thus, for the nearly constant pressures and volumes that are present in analyte transfer in liquid chromatography, $\Delta H \approx \Delta E$. And at constant pressure, which again is closely approximated in liquid chromatography, $\Delta H = q$, where q is the heat transferred in the process. Thus, the enthalpy of transfer provides a measure of the difference between the bonding interactions, *e.g.*, London dispersion, dipole-induced dipole, dipole-dipole, hydrogen bonding, *etc.*, of the analyte with the mobile phase compared to its interactions with the stationary phase. The presence of retention in a chromatographic separation implies that the analyte has at least some affinity for the stationary phase. This further implies that, in general, the *enthalpy* of

---

*This chapter is reproduced with permission from (David S. Jensen, Thorsten Teutenberg, Jody Clark, and Matthew R. Linford) *LCGC North Am.* **2012**, *30*, 992-998.

transfer of the analyte from the mobile phase to the stationary phase is favorable, which is signified by a negative ΔH^0 value. (Positive values of ΔH^0 are unfavorable.)

b) The *entropy of transfer* (ΔS^0) of the analyte from the mobile phase to the stationary phase in a chromatographic separation is the change in entropy that occurs when the analyte moves from the mobile phase to the stationary phase. Entropy can be viewed as a measure of the change in the randomness/mobility/ability to diffuse of the analyte, or put more formally, as the change in the number of available states of a system. In general, as an analyte moves from the mobile to the stationary phase its mobility is restricted, which causes the entropy of transfer to be unfavorable. This is signified by a negative ΔS^0 value. (Unlike changes in enthalpy, positive values of ΔS^0 are generally favorable.)

The view presented above for the change in enthalpy or entropy in analyte transfer from the mobile to the stationary phase is admittedly simplistic. Nevertheless, in many cases it will capture a significant fraction of the thermodynamics of the problem, providing at least a starting point for thinking about the problem. Of course, to fully understand these parameters, one would need to consider all interactions in the system, including those of the solvent with itself, and any that may come as a result of the analyte replacing solvent molecules that may be adsorbed on the stationary phase.

c) The *Gibbs' free energy* (ΔG^0) predicts whether an *overall* process is favored (indicated by a negative value of ΔG^0) or disfavored (signified by a positive value of ΔG^0). ΔG^0 has a contribution from the change in enthalpy, ΔH^0, a contribution from the change in entropy, ΔS^0, and it depends on the absolute temperate in Kelvin, T, as follows:

(1) $\Delta G^0 = \Delta H^0 - \mathrm{T}\Delta S^0$

Figure 3.1 shows how the values of ΔH^0 and ΔS^0 in a typical reversed-phase (RP) separation (negative and favored for ΔH^0 and negative and unfavored for ΔS^0) interact with temperature in the Gibbs equation (Equation 1). This relationship helps us understand the typically observed phenomenon of the retention factor, *k*, decreasing with temperature. As illustrated in Figure 1, at lower temperatures ΔH^0 is dominant and negative so ΔG^0 is negative – lower temperatures favor retention. However, as the temperature increases, the "– $T\Delta S^0$" part of Equation 1 causes ΔG^0 to become less negative (because, again, ΔS^0 is negative in our case) and at some point, ΔG^0 becomes positive. That is, as temperature increases, adsorption (retention) is increasingly disfavored.

This same analysis provides an even more straightforward explanation for retention in gas chromatography (GC), where decreases in retention occur with increases in temperature. ΔH^0 will definitely be negative (favored) for analyte adsorption/partitioning into the stationary phase from the mobile phase in GC because one is comparing essentially no chemical bonding interactions in the gas phase to, at a minimum, London dispersion forces upon adsorption. Furthermore, there will be a substantial decrease in the entropy of the system upon adsorption/partitioning because of the high entropies of gas phase species compared to the lower entropies of the same species in a condensed phase.

Thus, a relatively simple thermodynamic analysis helps us understand why retention in some of the most important forms of chromatography will, in general, decrease with temperature. Of course there are some underlying assumptions here, one of which is that ΔH^0 and ΔS^0 are independent of temperature, and another is that the stationary phase and mobile phase remain unchanged with temperature. These assumptions, which in many cases are reasonable, are discussed in greater detail below and in a subsequent article.

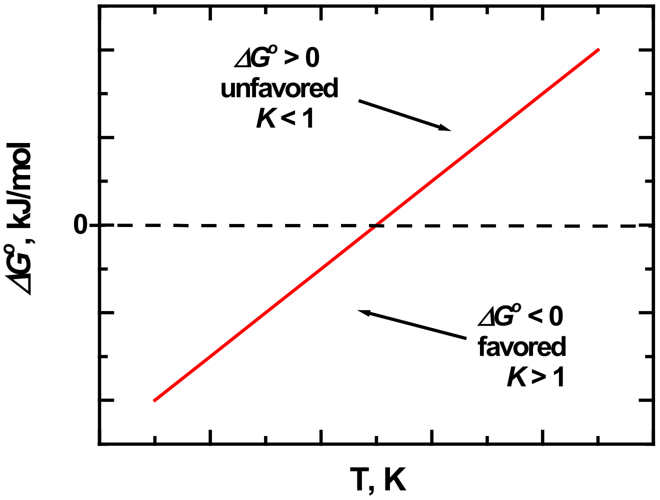

Figure 3.1 ΔG^0 plotted as a function of temperature in $\Delta G^0 = \Delta H^0 - T\Delta S^0$ for ΔH^0 negative (favored) and constant, and also ΔS^0 negative (unfavored) and constant, which are good approximations for a typical reversed-phase separation. At lower temperatures, ΔG^0 is negative (favored), which leads to higher values of the equilibrium constant, K, and larger values of the retention factor, *k*. At higher temperatures, ΔG^0 is positive (disfavored), which leads to lower values of the equilibrium constant, K, and smaller values of *k*.

d) The *equilibrium constant*, K, for the transfer of an analyte from the mobile phase to the stationary phase is:

$$(2)\quad K = \frac{[A]_S}{[A]_M},$$

where $[A]_S$ is the concentration of the analyte in the stationary phase and $[A]_M$ is the concentration of the analyte in the mobile phase.

Now, in general, K is not easily measured in a chromatographic separation. However, using the definition of concentration as moles solute per unit volume, K can be expressed in terms of the retention factor, *k* (see below), which is an easily measured parameter, as follows:

$$(3)\quad K = \frac{[A]_S}{[A]_M} = \frac{\left(\frac{mol_s}{V_s}\right)}{\left(\frac{mol_M}{V_M}\right)} = \left(\frac{mol_S}{mol_M}\right)\left(\frac{V_M}{V_S}\right)$$

where mol_S and mol_M are the number of moles of the analyte A in the stationary phase and mobile phase, respectively, and V_S and V_M are the volumes of the stationary and mobile phases, respectively.

e) *The retention factor, k*, is the ratio of the time the analyte spends in the stationary phase divided by the time it spends in the mobile phase:

$$(4)\quad k = \frac{(t_r - t_o)}{t_o} = \frac{\text{time analyte spent in stationary phase}}{\text{time analyte spent in mobile phase}}$$

where t_r is the retention time of the analyte and t_0 is the mobile phase hold-up time or dead time. (A variety of approaches can be taken to determine the thermodynamic dead-time of a column, which include the disturbance peak (unretained components in the analyte mixture) or the use of isotopically labeled eluent components.[2, 3])

Basic chromatographic theory also teaches us that during a separation, *k* equals the number of moles of analyte in the stationary phase divided by the number of moles of analyte in the mobile phase:

(5) $k = \frac{(t_r - t_o)}{t_o} = \frac{mol_S}{mol_M}$

f) The ratio of the volume of the mobile phase to the volume of the stationary phase is known as the *phase ratio, or phase volume ratio, β*:

(6) $\beta = V_M/V_S$

So Equations 3, 5, and 6 can be combined to obtain the following relationship for K

(7) $K = k\beta$

Thus it is seen that K is directly proportional to *k*. As noted, this equation is important because it relates K to something that is measured easily – the retention factor, *k*.

g) A well-known expression relates ΔG^0 to K through the gas constant, R, and the absolute temperature:

(8) $\Delta G^0 = -RT \ln K$

From Equation 8 it is seen that a change in ΔG^0 has a direct impact on the equilibrium constant, and therefore retention factor: if $\Delta G^0 = 0$ then $K = 1$, if $\Delta G^0 > 0$ then $K < 1$, and if $\Delta G^0 < 0$ then $K > 1$.

3.3. The van ’t Hoff Relationship

The van ’t Hoff equation is closely tied to the thermodynamics of the transfer of the analyte from the mobile phase to the stationary phase. To obtain the van ’t Hoff equation combine equations (1) and (8):

(9) $-RT \ln K = \Delta H^0 - T\Delta S^0$

Then isolate ln K:

(10) $\ln K = -\Delta H^0/RT + \Delta S^0/R$

and substitute Equation 7 into Equation 9:

(11) $\ln k\beta = -\Delta H^0/RT + \Delta S^0/R$

and with a little more algebra obtain the van ’t Hoff equation, as it is typically seen in liquid chromatography:

(12) $\ln k = -\Delta H^0/RT + \Delta S^0/R - \ln \beta$

Now compare Equation 12 to the basic equation for a straight line:

(13) $y = mx + b$

where m is the slope of the line and b is its y-intercept. Thus, y corresponds to ln k, x corresponds to 1/T, m corresponds to $-\Delta H^0/R$, and b corresponds to $\Delta S^0/R - \ln \beta$. Hence, if ln k vs. 1/T are plotted, and then take the slope and intercept of this line, this can directly obtain the enthalpy of transfer of the analyte from the mobile phase to the stationary phase as $\Delta H^0 = -mR$, and the entropy of transfer from the intercept of the line, provided the phase ratio, β, is known, where an assumption that the plot produces a straight line, which it often does.

So, in a straightforward way the van ’t Hoff equation was derived, which allows information about two key thermodynamic parameters to be obtained through some direct chromatographic measurements, i.e., we simply measure the retention factor of an analyte in two or more different chromatograms at different temperatures under otherwise identical conditions, and then plot and analyze ln k vs. 1/T.

Figure 3.2 is a mock (synthesized data) example of a van ’t Hoff plot for two different hypothetical analytes. The slopes of the two fit lines are different, where the steepest slope (Analyte 2) corresponds to the largest value of ΔH^0, while the largest value of ΔS^0 will come from the curve with the largest intercept (Analyte 1). Note that because 1/T is plotted on the x-axis, temperature increases from right to left, and not left to right, which is typical. Consistent with the plot of Gibbs free energy (Figure 3.1), the van ’t Hoff plot (Figure 3.2) shows the usual RP-HPLC behavior of an increase in temperature resulting in a decrease in retention. With this information separation conditions may be chosen to optimize resolution and analysis time.

3.4. Prelude to the Next Installment on High Temperature Liquid Chromatography

In our next installment of this series on ‘Elevated Temperatures in Liquid Chromatography’ we will discuss the van ’t Hoff equation in greater detail as follows: (a) the van ’t Hoff equation and retention mapping,[4, 5] (b) thermodynamics of linear van ’t Hoff plots,[6] (c) nonlinearities in van ’t Hoff plots due to phase transitions,[7-9] (d) irregularities in van ’t Hoff plots due to pH effects,[10, 11] (e) confirmation of the linearity of van ’t Hoff plots and evaluating changes in entropy,[12] and (f) concerns about the van ’t Hoff equation.[13, 14]

3.5. Conclusions

We have introduced some of the basic thermodynamics of liquid chromatography, leading to the van ’t Hoff equation. The next installment in this series will describe examples from the literature and important considerations for the van ’t Hoff equation.

3.6. Acknowledgments

T.T. and J.C aided in technical questions. D.J. and M.L. wrote the manuscript.

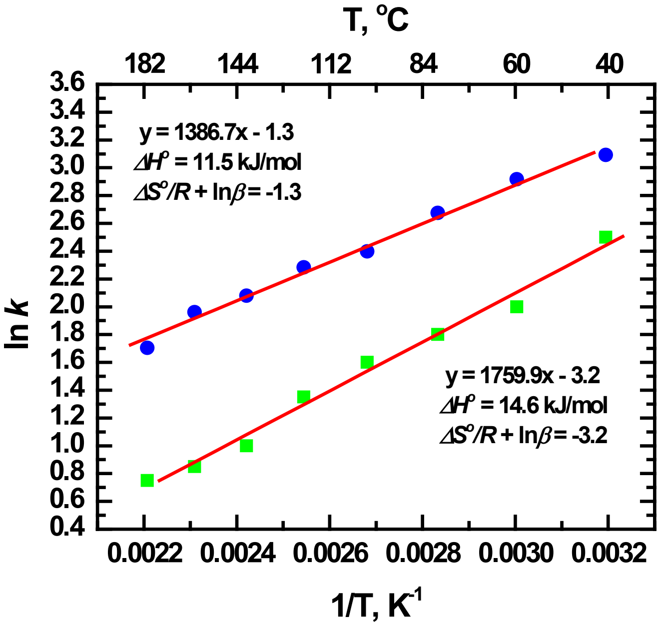

Figure 3.2 Plot of ln *k* vs. 1/T (van ’t Hoff plot), for two analytes (mock/synthesized data). Analytes ‘1’ and ‘2’ correspond to the circles (top) and squares (bottom), respectively.

3.7. References

1. Jensen, D. S.; Teutenberg, T.; Clark, J.; Linford, M. R., *LCGC North Am.* **2012,** *30* (9), 850-862.

2. Kazakevich, Y. V.; McNair, H. M., *J. Chromatogr. Sci.* **1993,** *31* (8), 317-322.

3. Knox, J. H.; Kaliszan, R., *J. Chromatogr. A* **1985,** *349* (2), 211-234.

4. Dolan, J. W., *J. Chromatogr., A* **2002,** *965* (1-2), 195-205.

5. Snyder, L. R.; Kirkland, J. J.; Dolan, J. W., *Introduction to Modern Liquid Chromatography*. 3rd ed.; Wiley: 2010.

6. Liu, Y.; Grinberg, N.; Thompson, K. C.; Wenslow, R. M.; Neue, U. D.; Morrison, D.; Walter, T. H.; O'Gara, J. E.; Wyndham, K. D., *Anal. Chim. Acta* **2005,** *554* (1-2), 144-151.

7. Sentell, K. B.; Henderson, A. N., *Anal. Chim. Acta* **1991,** *246* (1), 139-149.

8. Heinisch, S.; Rocca, J.-L., *J. Chromatogr., A* **2009,** *1216* (4), 642-658.

9. Wheeler, J. F.; Beck, T. L.; Klatte, S. J.; Cole, L. A.; Dorsey, J. G., *J. Chromatogr., A* **1993,** *656* (1-2), 317-333.

10. Thorsten, T., *Anal. Chim. Acta* **2009,** *643* (1-2), 1-12.

11. Pous-Torres, S.; Torres-Lapasió, J. R.; Baeza-Baeza, J. J.; García-Álvarez-Coque, M. C., *J. Chromatogr., A* **2007,** *1163* (1-2), 49-62.

12. Chester, T. L.; Coym, J. W., *J. Chromatogr., A* **2003,** *1003* (1-2), 101-111.

13. Gritti, F.; Guiochon, G., *J. Chromatogr., A* **2005,** *1099* (1-2), 1-42.

14. Gritti, F.; Guiochon, G., *Anal. Chem.* **2006,** *78* (13), 4642-4653.

Chapter 4: Elevated Temperatures in Liquid Chromatography III: A Closer Look at the van ’t Hoff Equation*

4.1. Introduction

In the first installment in this series,[1] we discussed some of the advantages of and practical considerations for elevated temperature separations in liquid chromatography. In the second installment,[2] we reviewed some of the basic thermodynamics of chromatography and for elevated temperature separations, which included a brief derivation and discussion of the van ’t Hoff equation. We now continue our exploration of elevated temperatures in liquid chromatography with a more detailed discussion of the van ’t Hoff equation, exploring its usefulness and relevance using various examples from the literature.

4.2. Review of Advantages of Elevated Temperature Separations[1]

Elevated temperatures offer a number of benefits in liquid chromatography. Some are: (a) elevated temperatures facilitate retention mapping in which k, the retention factor, is measured at a few temperatures so that the values of k over a range of temperatures can be predicted;[3, 4] retention mapping, which can also include the probing and predicting of k at different mobile phase compositions, is widely used in method development;[3, 5, 6] (b) selectivity (α) may change with temperature, which is also important for retention mapping and is another parameter that can be considered in method development;[3, 5, 6] (c) increasing temperatures can improve sample throughput because they shift van Deemter minima to higher flow rates, i.e., the optimal efficiency for a separation shifts to a high mobile phase velocity;[7-9] and (d) a decrease in organic modifier is possible due to a change in water’s polarity with increasing temperatures, i.e., water

---

*This chapter is reproduced with permission from (David S. Jensen, Thorsten Teutenberg, Jody Clark, and Matthew R. Linford) *LCGC North Am.* **2012**, *30*, 1052-1057. Copyright 2012 **Advanstar Communications, Inc.**

behaves more like an organic solvent at elevated temperatures, and a more aqueous mobile phase is considered 'greener' due to a reduction in the amount of organic modifier needed.[10-14] Clearly there are good reasons for considering the use of elevated temperatures in liquid chromatography. We will now discuss various aspects of high temperature separations in the context of the van 't Hoff equation.

4.3. Review of the van 't Hoff Equation [2]

The van 't Hoff equation is derived from the following two basic thermodynamic equations:

$$\Delta G^0 = \Delta H^0 - \mathrm{T}\Delta S^0 \qquad (1)$$

and

$$\Delta G^0 = -\mathrm{RT} \ln \mathrm{K} \qquad (2)$$

When we set these two equations equal to each other and solve for ln K we achieve the van 't Hoff equation:

$$\ln \mathrm{K} = -\Delta H^0/\mathrm{RT} + \Delta S^0/\mathrm{R} \qquad (3)$$

As discussed in the previous article,[2] $\ln \mathrm{K} = \ln k\beta$, where k is the retention factor and β is the phase ratio (V_M/V_S) – the ratio of the mobile phase volume and stationary phase volume. By substituting $k\beta$ for K in Equation 3 we obtain the van 't Hoff equation as it is commonly encountered in liquid chromatography:

$$\ln k = -\Delta H^0/RT + \Delta S^0/R - \ln \beta \qquad (4)$$

Note that sometimes Φ is used instead of β, where $\Phi = 1/\beta = V_S/V_M$. Thus, an equivalent form of Equation 4 is:

$$\ln k = -\Delta H^0/RT + \Delta S^0/R + \ln \Phi \qquad (5)$$

Unfortunately, both β and Φ are referred to as the ‘phase ratio’.

4.4. The van ’t Hoff Equation in Retention Mapping

Van ’t Hoff plots are often linear, which makes them useful in retention mapping. For this purpose, a simpler, but mathematically equivalent, version of Equation 4 can be used:[3, 15]

$$\log k = A + B/T \qquad (6)$$

where plots of log *k* vs. 1/T are generated under isocratic conditions.[6, 16-18] While to some degree this semi-empirical equation conceals the underlying thermodynamics, in most cases this is not of primary concern. Of course retention mapping may be conveniently performed using commercially available software.

When using temperature as a variable to optimize a separation, the chromatographer can create a series of van ’t Hoff plots for various analytes to determine the best temperature for the separation. To demonstrate this optimization process, Figure 4.1 shows a series of van ’t Hoff plots for various drugs. In this example, some of the drugs, e.g., the circled lines in the plot, show different slopes and change elution order (reverse selectivity) where their lines cross.

Obviously, the temperature at this crossing point would be a very poor choice for separation conditions because the peaks would coelute, i.e., $\alpha = k_2/k_1 = 1$ here. Thus, in a separation involving multiple analytes, a series of van ’t Hoff plots can be used to optimize the separation.

4.5. Thermodynamics of Linear van ’t Hoff Plots

Linear van ’t Hoff plots, such as those in Figure 4.1, suggest that the retention mechanisms for the analytes are constant, i.e., the values for ΔH^0, ΔS^0, and β for the analytes, are constant over the temperature range under consideration. (Of course there is the possibility that ΔH^0, ΔS^0, and β are mutually changing so that the net effect is a linear relationship, but this will be dealt with below.) If the retention mechanism *is* constant with temperature it may be possible to compare the enthalpies (ΔH^0) and entropies (ΔS^0) of similar analytes on the same column, or of a single analyte on different columns. It should be noted again[2] that ΔH^0 of transfer of the analyte from the mobile phase to the stationary phase can be derived from the slope of its van ’t Hoff plot (see Equation 4). When ΔH^0 is negative, which is the typical case in reversed-phase (RP) chromatography, transfer of the analyte from the mobile phase to the stationary phase is favored and exothermic. Clearly the more negative ΔH^0 is, the more favorable the interaction between the analyte and the stationary phase, which generally leads to larger values of *k*. For example, in RP chromatography, the ΔH^0 values for a homologous series of increasingly hydrophobic analytes, *e.g.*, the alkyl benzenes with longer and longer alkyl chains, should steadily become more negative (exothermic). This effect is shown in Figure 4.2; the alkyl benzenes with longer alkyl chain lengths (more hydrophobic) have larger slopes than those with shorter chain lengths (less hydrophobic).[19]

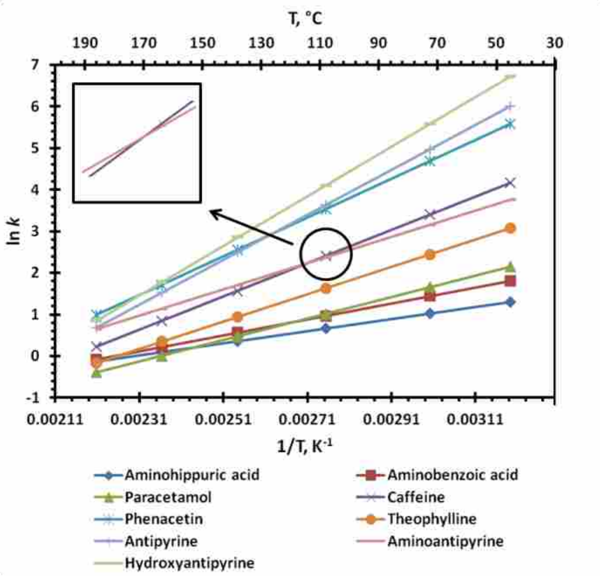

Figure 4.1 van 't Hoff plots for test probes showing linear relationships between the natural logs of the retention factors vs. 1/T for these compounds. 'The inset shows the point at which the elution is reversed for aminoantipyrine and caffeine.' From left to right, the data points correspond to 180, 150, 120, 90, 60, and 40 °C. Figure adapted from the slopes and intercepts given for the analytes in Ref. 10.

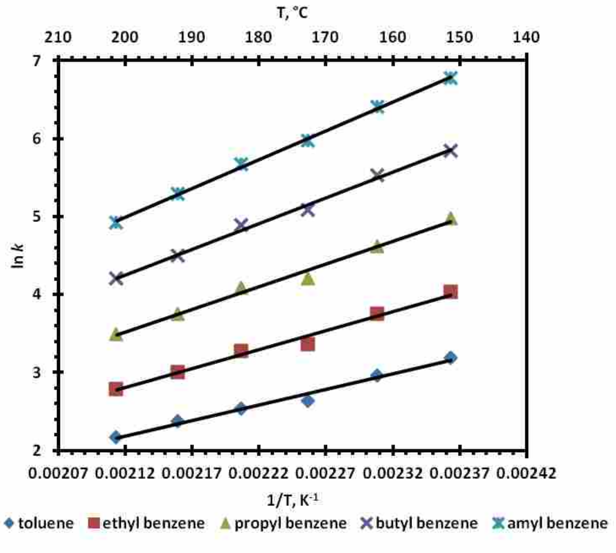

Figure 4.2 'van 't Hoff plots for a homologous series of alkyl benzenes.' Increase in alkyl character results in larger slope values indicating more negative ΔH^0 values. From left to right, the data points correspond to 200, 190, 180, 170, 160, and 150 °C. Figure adapted from Ref 19.

4.6. Nonlinearities in van 't Hoff Plots due to Phase Transitions

As a corollary to the previous statements, a nonlinear van 't Hoff plot shows that ΔH^0, ΔS^0, and/or β is changing, *i.e.*, the retention mechanism for the analyte is *not* constant over the temperature range under consideration. A possible explanation for a nonlinear van 't Hoff plot is a phase transition in the stationary phase; at lower temperatures the stationary phase will generally be in a solid-like conformation and at higher temperatures it will adopt a more liquid-like conformation,[13, 20, 21] i.e., a nonlinear van 't Hoff plot may indicate that the thermodynamic interactions between the analyte and stationary phase change when the stationary phase undergoes a phase transition. For silica-based C_{18} stationary phases, this phase transition may occur in the range of 20 - 50 °C,[22-24] which seems reasonable because long chain hydrocarbons have melting points in this range, e.g., the melting point of octadecane is ca. 28 °C. Of course, the melting transition of a C_{18} stationary phase is much more complicated than the simple melting of a pure hydrocarbon because of the tethering of the chains in the stationary phase, the density/packing of the chains, the presence of other chemical groups in the film, endcapping agents, etc.

Other phase transitions at higher temperatures have also been reported. For example, a phase transition around 100 °C was found for a silica based hybrid C_{18} column (Figure 4.3). This transition was attributed to a change in the conformation of the stationary phase *in the presence of the mobile phase* as a function of temperature.[19] This idea was substantiated by solid state NMR, which showed, over a temperature range of 30 – 150 °C, that the dry stationary phase did not undergo any conformational changes. Differential scanning calorimetry (DSC) was also performed on the stationary phase under conditions that mimicked typical LC mobile phase conditions. DSC showed thermal desorption of the mobile phase (70:30 H_2O:ACN) from the stationary phase around the phase transition point (ca. 97 °C), suggesting a change in the conformation of the stationary phase when the mobile phase was present.

The phase transition in Figure 4.3 produces two linear van ’t Hoff plots: ‘Region I’ at lower temperatures (32 – 97.3 °C) and ‘Region II’ at higher temperatures (97.3 to 200 °C). Interestingly, ΔH^0 in Region II is ca. twice that of Region I. Coym and Dorsey discussed this possibility of an increase in ΔH^0 following a phase transition stating: “It may seem odd that the enthalpy of transfer (retention) at high temperature is more favorable than at low temperature, because retention is greater at low temperature. The thermodynamic quantity that governs retention is the free energy [ΔG^0], which has an entropy component [ΔS^0]. Because of the change in hydrogen bond structure of water with temperature, the entropy change associated with retention changes with temperature. At lower temperatures, where the mobile phase is hydrogen bonded, there is a favorable entropy change upon retention. This is commonly referred to as the ‘hydrophobic effect’. However, at high temperatures, where there is little or no hydrogen bonding, the entropy change would be expected to be much less. As a result, although the enthalpy [ΔH^0] of retention is more favorable at high temperature, it is outweighed by the entropic [ΔS^0] contribution.”[25]

4.7. Irregularities in van ’t Hoff Plots due to pH Effects

Unusual van ’t Hoff plots may be observed in the separation of polar acid/base compounds[26] because a change in the temperature, and therefore polarity, of the mobile phase can affect the pK_a/pK_b values of weak acids/bases. Obviously, a change in ionization state of an analyte or buffer in a mobile phase can alter retention,[27] and selectivity changes associated with temperature changes are larger for polar and ionizable analytes than for nonpolar analytes.[28-32] In particular, an analyte’s pK_a value can shift ca. -0.03 pK_a units per °C.[33, 34]

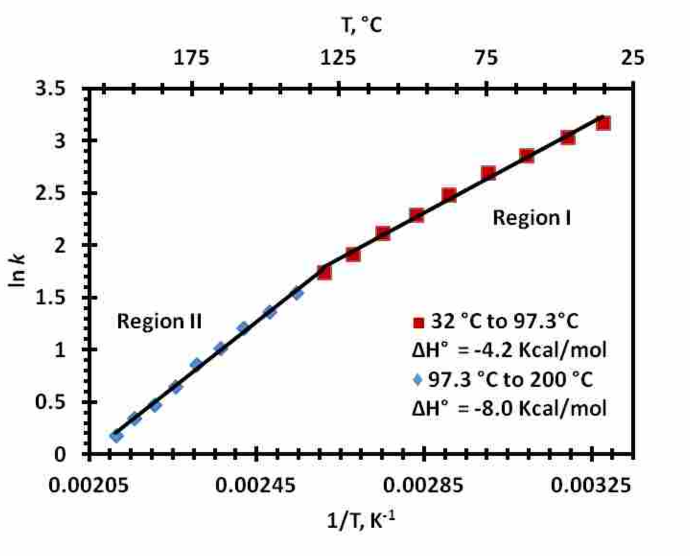

Figure 4.3 'van 't Hoff plot for toluene' demonstrating curvilinear behavior around 100 °C. Adapted from Ref.19.

These effects are complex, and are typically most strongly manifest when pH ≈ pK_a, i.e., where both the weak acid and conjugate base have appreciable concentrations.[29] The success of these types of separations depends on the nature of the buffer and analyte.[30] Two examples follow. Figure 4.4 shows an *increase* in retention of protriptyline, a tricyclic antidepressant, with increasing temperature on two different columns. Figure 4.5 also shows analytes that exhibit (unusual) negative slopes in their van ’t Hoff plots. As a side note, temperature can also affect large molecules, e.g., proteins may undergo conformation changes with temperature.[31]

4.8. Confirming the Linearity of van ’t Hoff Plots and Evaluating Changes in Entropy

Chester and Coym explored the possibility of β changing during a van ’t Hoff analysis, and noted that, at least in theory, a change in β could compensate for changes in ΔH^0 and/or ΔS^0, leading to an (apparently) linear van ’t Hoff relationship.[35] (This statement is consistent with some of the concerns raised by Gritti and Guichon,[36, 37] *i.e.*, different compensating/canceling factors may lead to the linearity often observed in van ’t Hoff plots.) In order to eliminate this possibility, Chester and Coym noted a slightly more advanced use of van ’t Hoff analysis in which one plots ln α vs. 1/T, where α is the selectivity (k_2/k_1) between two analytes. This relationship is obtained from Equation 4 by subtracting the van ’t Hoff relationship for the second analyte from the van ’t Hoff relationship for the first, leading to:

$$\ln k_2 - \ln k_1 = \ln(k_2/k_1) = \ln \alpha = -(1/RT)(\Delta H^0{}_2 - \Delta H^0{}_1) + (1/R)(\Delta S^0{}_2 - \Delta S^0{}_1) \qquad (7)$$

which can also be expressed as:

$$\ln \alpha = -(1/RT)\,\Delta\Delta H^0{}_{2,1} + (1/R)\,\Delta\Delta S^0{}_{2,1} \qquad (8)$$

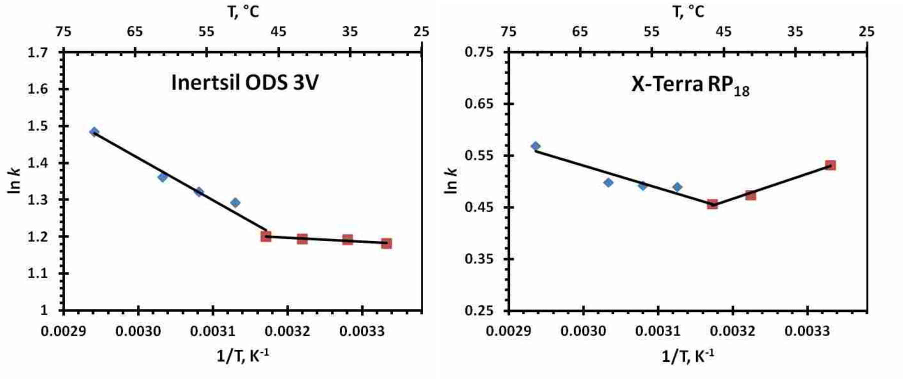

Figure 4.4 Van ’t Hoff plots of protriptyline obtained at pH 7.8. Flow rate: 1.0 ml/min. Temperature increases from right to left. Adapted from Ref. 33.

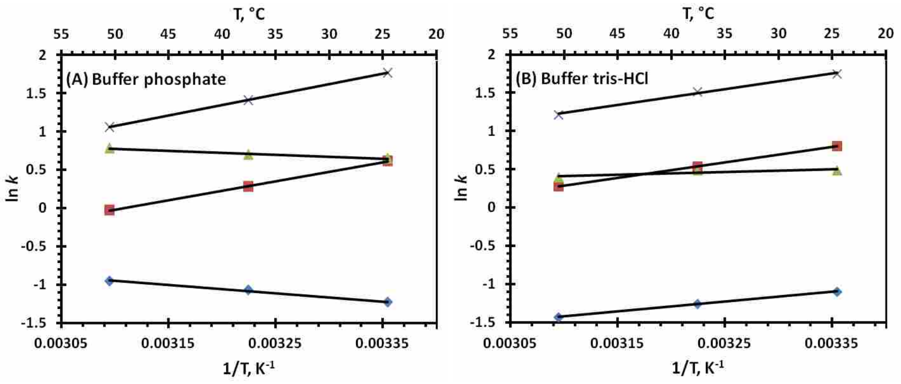

Figure 4.5 'van 't Hoff plots of acidic and basics analytes. (A) Phosphate buffer pH (25 °C) = 8.10, and (B) tris + HCl buffer pH (25 °C) = 8.09; mobile phase contains 50% (v/v) methanol. Analytes: (x) 2,4-dichlorophenol; (■) 2,6-dichlorophenol; (♦) benzylamine; (▲) benzyldimethylamine.' Adapted from Ref. 29.

If the individual van ’t Hoff relationships for the first and second analytes are linear, and the van’t Hoff relationship in Equations 7 or 8 for their selectivity is also linear, then there is a higher probability that ΔH^0, ΔS^0, and β are constant (or at least not substantially changing) over the temperature range in question. Thus, if one wishes to use a van ’t Hoff analysis to extract ΔH^0 and ΔS^0 values for an analyte, it would probably be advisable to apply this additional check on the data. If the resulting plot of Equation 7 or 8 is linear, it would add credence to any claim that meaningful thermodynamic information could be extracted from the analysis. In addition, if the plot of ln α vs. 1/T is nonlinear then the stationary phase may undergo a conformational change in the temperature range studied.[38-41]

As a corollary to these last points, using $b_1 = \Delta S^0{}_1/R - \ln \beta$ for the first analyte and $b_2 = \Delta S^0{}_2/R - \ln \beta$ for the second analyte under the same conditions/same column, we can calculate the difference in entropies of transfer for the two analytes as $\Delta\Delta S^0{}_{21} = \Delta S^0{}_2 - \Delta S^0{}_1 = R(b_2 - b_1)$, where this latter term is the gas constant multiplied by the difference between the y-intercepts of the two van ’t Hoff plots for the two analytes. Note that the phase ratio, which we often do not know, has canceled, leaving us with the difference between the two entropies of transfer. This analysis can be useful on a series of compounds, where they are all compared to one member of the series.

4.9. Concerns about the van ’t Hoff Equation

A careful study of the van ’t Hoff equation and its use in elevated temperature liquid chromatography suggests that there is some question regarding its fundamental accuracy.[36, 37] For example, the van ’t Hoff relationship assumes that the stationary phase is homogeneous, which it clearly is not. In general, a stationary phase will contain different types of sites, which will have different affinities for a given analyte. The van ’t Hoff equation also assumes that both the stationary phase and the mobile phase remain constant as a function of temperature. Neither will be entirely true. The adsorption and absorption (partitioning) of mobile phase components in the stationary phase, which will alter the properties of the stationary phase, will vary with temperature, and the mobile phase will also change with temperature, e.g., the static permittivity (dielectric constant) of water will change with temperature. Perhaps a measured view of these concerns is to acknowledge their validity, while also noting that in many circumstances it appears that these effects are not so extreme that useful information can be obtained by van ’t Hoff analysis.

4.10. Conclusions

Van ’t Hoff plots can be a useful and interesting part of data analysis for high temperature liquid chromatography. They are valuable in an empirical sense for retention modeling. Thermodynamic data may be extracted from them. They can reveal phase transitions in stationary phases, and the changes in pK_a values of analytes with temperature. Plots of ln α vs. 1/T can help confirm that ΔH^0 and ΔS^0 are constant with temperature. It should be understood that the underlying assumptions of the van ’t Hoff equation are not entirely correct.

4.11. Acknowledgments

T.T. and J.C aided in technical questions. D.J. and M.L. wrote the manuscript.

4.12. References

1. Jensen, D. S.; Teutenberg, T.; Clark, J.; Linford, M. R., *LCGC North Am.* **2012,** *30* (9), 850-862.

2. Jensen, D. S.; Teutenberg, T.; Clark, J.; Linford, M. R., *LCGC North Am.* **2012,** *In Press*.

3. Dolan, J. W., *J. Chromatogr., A* **2002,** *965* (1-2), 195-205.

4. Wiese, S.; Teutenberg, T.; Schmidt, T. C., *J. Chromatogr., A* **2011,** *1218* (39), 6898-6906.

5. Dolan, J. W.; Snyder, L. R.; Djordjevic, N. M.; Hill, D. W.; Saunders, D. L.; Van Heukelem, L.; Waeghe, T. J., *J. Chromatogr., A* **1998,** *803* (1-2), 1-31.

6. Wolcott, R. G.; Dolan, J. W.; Snyder, L. R., *J. Chromatogr., A* **2000,** *869* (1-2), 3-25.

7. Vanhoenacker, G.; David, F.; Sandra, P., *Chromatogr. Today* **2010,** *3* (3), 14-16.

8. Xiang, Y.; Yan, B.; Yue, B.; McNeff, C. V.; Carr, P. W.; Lee, M. L., *J. Chromatogr., A* **2003,** *983* (1-2), 83-89.

9. Vanhoenacker, G.; Sandra, P., *Anal. Bioanal. Chem.* **2008,** *390* (1), 245-248.

10. Edge, A. M.; Shillingford, S.; Smith, C.; Payne, R.; Wilson, I. D., *J. Chromatogr., A* **2006,** *1132* (1-2), 206-210.

11. Michelle Hong, C.; Horváth, C., *J. Chromatogr., A* **1997,** *788* (1-2), 51-61.

12. Tran, J. V.; Molander, P.; Greibrokk, T.; Lundanes, E., *J. Sep. Sci.* **2001,** *24* (12), 930-940.

13. Heinisch, S.; Rocca, J.-L., *J. Chromatogr., A* **2009,** *1216* (4), 642-658.

14. Bowermast, J.; McNair, H. M., *J. Chromatogr. Sci.* **1984,** *22*, 165-170.

15. Snyder, L. R.; Kirkland, J. J.; Dolan, J. W., *Introduction to Modern Liquid Chromatography*. 3rd ed.; Wiley: 2010.

16. Zhu, P. L.; Snyder, L. R.; Dolan, J. W.; Djordjevic, N. M.; Hill, D. W.; Sander, L. C.; Waeghe, T. J., *J. Chromatogr., A* **1996,** *756* (1-2), 21-39.

17. Zhu, P. L.; Dolan, J. W.; Snyder, L. R., *J. Chromatogr., A* **1996,** *756* (1-2), 41-50.

18. Wolcott, R. G.; Dolan, J. W.; Snyder, L. R.; Bakalyar, S. R.; Arnold, M. A.; Nichols, J. A., *J. Chromatogr., A* **2000,** *869* (1-2), 211-230.

19. Liu, Y.; Grinberg, N.; Thompson, K. C.; Wenslow, R. M.; Neue, U. D.; Morrison, D.; Walter, T. H.; O'Gara, J. E.; Wyndham, K. D., *Anal. Chim. Acta* **2005,** *554* (1-2), 144-151.

20. Wheeler, J. F.; Beck, T. L.; Klatte, S. J.; Cole, L. A.; Dorsey, J. G., *J. Chromatogr., A* **1993,** *656* (1-2), 317-333.

21. Sentell, K. B.; Henderson, A. N., *Anal. Chim. Acta* **1991,** *246* (1), 139-149.

22. Cole, L. A.; Dorsey, J. G., *Anal. Chem.* **1992,** *64* (13), 1317-1323.

23. Cole, L. A.; Dorsey, J. G.; Dill, K. A., *Anal. Chem.* **1992,** *64* (13), 1324-1327.

24. Morel, D.; Serpinet, J., *J. Chromatogr., A* **1981,** *214* (2), 202-208.

25. Coym, J. W.; Dorsey, J. G., *J. Chromatogr., A* **2004,** *1035* (1), 23-29.

26. Teutenberg, T., *Anal. Chim. Acta* **2009,** *643* (1-2), 1-12.

27. Hemmateenejad, B., *J. Chemom.* **2005,** *19* (11-12), 657-667.

28. Pous-Torres, S.; Torres-Lapasió, J. R.; Baeza-Baeza, J. J.; García-Álvarez-Coque, M. C., *J. Chromatogr., A* **2007,** *1163* (1-2), 49-62.

29. Castells, C. B.; Gagliardi, L. G.; Ràfols, C.; Rosés, M.; Bosch, E., *J. Chromatogr., A* **2004,** *1042* (1-2), 23-36.

30. Gagliardi, L. G.; Castells, C. B.; Ràfols, C.; Rosés, M.; Bosch, E., *J. Chromatogr., A* **2005,** *1077* (2), 159-169.

31. Chloupek, R. C.; Hancock, W. S.; Marchylo, B. A.; Kirkland, J. J.; Boyes, B. E.; Snyder, L. R., *J. Chromatogr., A* **1994,** *686* (1), 45-59.

32. Gagliardi, L. G.; Castells, C. B.; Ràfols, C.; Rosés, M.; Bosch, E., *Anal. Chem.* **2006,** *78* (16), 5858-5867.

33. Buckenmaier, S. M. C.; McCalley, D. V.; Euerby, M. R., *J. Chromatogr., A* **2004,** *1060* (1-2), 117-126.

34. Buckenmaier, S. M. C.; McCalley, D. V.; Euerby, M. R., *J. Chromatogr., A* **2004,** *1026* (1-2), 251-259.

35. Chester, T. L.; Coym, J. W., *J. Chromatogr. A* **2003,** *1003* (1-2), 101-111.

36. Gritti, F.; Guiochon, G., *J. Chromatogr., A* **2005,** *1099* (1-2), 1-42.

37. Gritti, F.; Guiochon, G., *Anal. Chem.* **2006,** *78* (13), 4642-4653.

38. Wang, F.; O’Brien, T.; Dowling, T.; Bicker, G.; Wyvratt, J., *J. Chromatogr., A* **2002,** *958* (1-2), 69-77.

39. O'Brien, T.; Crocker, L.; Thompson, R.; Thompson, K.; Toma, P. H.; Conlon, D. A.; Feibush, B.; Moeder, C.; Bicker, G.; Grinberg, N., *Anal. Chem.* **1997,** *69* (11), 1999-2007.

40. Papadopoulou-Mourkidou, E., *Anal. Chem.* **1989,** *61* (10), 1149-1151.

41. Gilpin, R. K.; Ehtesham, S. E.; Gregory, R. B., *Anal. Chem.* **1991,** *63* (24), 2825-2828.

Chapter 5: Stable, Microfabricated Thin Layer Chromatography Plates without Volume Distortion on Patterned, Amorphous Carbon-Primed Carbon Nanotube Forests*

5.1. Abstract

Recently fabrication of thin layer chromatography (TLC) plates was described that was formed from patterned carbon nanotube (CNT) forests via direct infiltration/coating of the CNTs by low pressure chemical vapor deposition (LPCVD) of silicon from SiH_4, followed by high temperature oxidation of the CNTs and Si. Herein is presented an improved microfabrication process for the preparation of these TLC plates. First, a few nanometers of carbon and/or a layer of atomic layer deposition (ALD) of Al_2O_3 is deposited on the CNTs. This method of priming the CNTs for subsequent depositions appears to be new. X-ray photoelectron spectroscopy confirms the presence of additional oxygen after carbon deposition. After priming, the plates are coated by rapid, conformal deposition of an inorganic material that does not require subsequent oxidation, i.e., by fast pseudo (ψ)-ALD growth of SiO_2 via alumina catalyzed deposition of tris(*tert*-butoxy)silanol. Unlike devices described previously, faithful reproduction of the features in the masks was still observed after oxidation. A bonded, amino phase on the resulting plates showed fast, highly efficient separations of fluorescent dyes (plate heights in the range of 1.6 – 7.7 μm). Extensive characterization of the new materials by TEM, SEM, EDAX, DRIFT, and XPS is reported. A substantially lower process temperature for the removal of the CNT scaffold is possible as a result of the already oxidized materials used.

*This chapter is reproduced with permission from (David S. Jensen, Supriya S. Kanyal, Vipul Gupta, Michael A. Vail, Andrew E. Dadson, Mark Engelhard, Richard Vanfleet, Robert C. Davis, and Matthew R. Linford) *J. Chromatogr., A* **2012**, *1257*, 195-203. Copyright 2012 Elsevier B.V.

5.2. Introduction

Recently, various reports have highlighted the use of new materials in thin layer chromatography. In the early 2000s Merck introduced the UTLC (ultrathin layer chromatography) plate.[1] This device employed a thin (ca. 10 μm), monolithic silica layer with 1 – 2 μm macropores and 3 – 4 nm mesopores on a glass backing.[2, 3] However, these plates showed limited migration distances (up to ca. 3 cm) due to reduced capillary action. They also suffered from reduced sample capacity because of the limited surface area of the thin adsorbent layer. Perhaps for some of these reasons, Merck has recently stopped manufacturing these materials. Another development is the use of glancing-angle deposition (GLAD) to produce 1 – 7 μm adsorbent layers of silica.[4] This plate showed reasonable resolution and efficiencies under short development distances. Thin layer chromatography (TLC) plates based on electrospinning of nanofibrous polymers have also been described.[5] Later this same group demonstrated carbonization of electrospun polymers to form a glassy-carbon stationary phase,[6] which is similar to the commercially available porous graphitic carbon chromatographic adsorbent. Other nonsilica-based monolithic TLC plates have also been produced in an attempt to increase the separation efficiencies of large molecules.[7-9]

We recently reported a microfabrication of thin TLC plates that consisted of growth of patterned carbon nanotube forests and their subsequent infiltration with silicon via conformal, low-pressure chemical vapor deposition (LPCVD) of silane (SiH_4).[10] This study was an application to separations science of Davis and Vanfleet's seminal work on infiltrated carbon nanotube forests.[11, 12] TLC plates made in this fashion separated a test dye mixture under normal phase conditions. However, subsequent follow up studies revealed a few disadvantages to this approach. First, oxidation/conversion of silicon to silica appeared to expand and distort the features in the patterned chromatographic bed, which removed some of the advantages we had hoped to gain through microfabrication. Such inhomogeneities in the chromatographic bed should reduce chromatographic performance by increasing the A-term in the van Deemter equation[13, 14] – although the van Deemter equation assumes a constant flow velocity, which clearly does not exist in the upward, capillary driven flow of a typical TLC separation, one may interpret TLC results through it.[15] Also, to the degree that feature sizes are unacceptably increased, the C-term of the van Deemter equation would also increase. However, because the mobile phase slows as it ascends a TLC plate, the main contribution to band broadening in TLC is due to the B-term in the van Deemter equation. In a few extreme cases, the fissures and channels that develop upon oxidation in the plates along the flow direction would also detrimentally affect the B-term by allowing increased diffusion, thus increasing the tortuosity factor of the B-term. In some cases, most likely as a result of these issues, irregular solvent fronts on the microfabricated TLC plates were observed. Clearly there are significant advantages to a faithful rendering/reproduction of a photolithographic mask's features in microfabrication.

Another concern with our previous study was the high temperature, ca. 850 – 1000 °C, needed to convert the LPCVD silicon to silica, which limited our choice of substrates. At elevated temperatures (above 200 °C) surface silanols (SiOH) begin to condense into siloxanes (Si-O-Si linkages), which subsequently requires their repopulation for good chromatography.[16, 17] Of course, concomitant to the oxidation of Si to SiO_2 was the desirable removal of the carbon nanotube framework, which resulted in a white TLC adsorbant material.

To overcome these issues, we developed a process that first builds on the strengths of the previous work, where advantages included: (i) the straightforward photolithographic patterning of the surface, (ii) the ease of growth of high aspect ratio, vertically aligned carbon nanotube forests, (iii) the conformal coating of these materials with an inorganic material, and (iv) the removal of carbon nanotube templates by air oxidation. However, we explore other deposition techniques to create robust, coated, CNT forests, which upon lower temperature oxidation of the CNT framework show no distortion of features and where the resulting materials are suitable for TLC (see overview of microfabrication process in Figure 5.1).

In particular, we focus on the priming of the CNTs with carbon and/or alumina to allow direct deposition of silica using a pseudo atomic layer deposition (ψ-ALD) process.[18] To the best of our knowledge the use of carbon as a priming layer on CNTs is new, although more extensive carbon infiltration of CNT forests has previously been reported.[19-21] Other researchers have previously attempted to prime CNTs for ALD growth, including the adsorption of NO_2 and TMA.[22] However, this approach required many NO_2 and TMA cycles prior to deposition of Al_2O_3. ALD of alumina from water and trimethylaluminum (TMA), is a straightforward and reliable ALD reaction.[22-24] The inorganic material that is finally deposited on the CNTs is already oxidized so a lower temperature can be used to burn out the underlying CNTs. An amino silane is deposited on this material, creating a bonded phase that results in rapid development times and high efficiencies for various analytes.[25] The literature contains other examples of the use of carbon nanotubes in analytical chemistry.[26, 27]

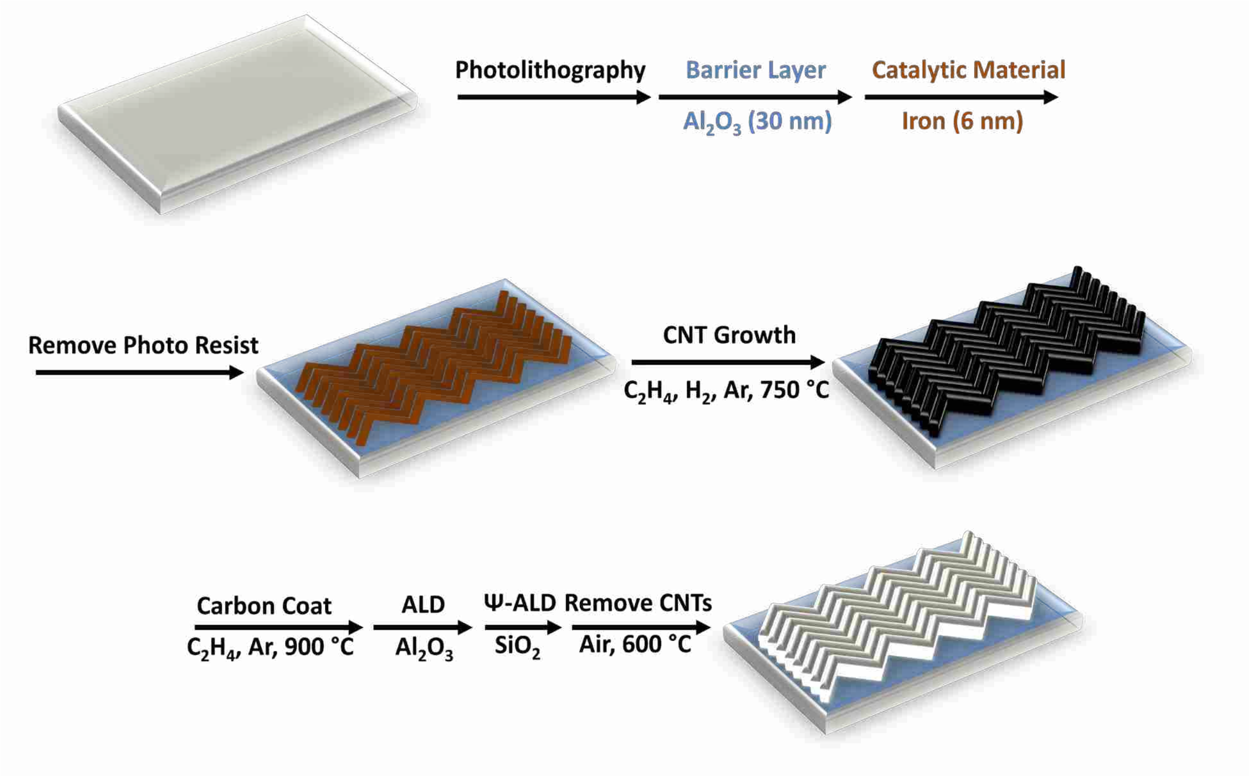

Figure 5.1 Overview of the microfabrication process. Surfaces are photolithographically patterned. Al_2O_3 and Fe are deposited sequentially. The devices then undergo lift-off, leaving a pattern of Fe on Al_2O_3, CNT growth, coating with carbon, ALD of Al_2O_3 and pseudo-ALD of SiO_5. The material is finally heated to 600°C to remove the CNT framework.

5.3. Experimental

5.3.1. Photolithography

5.3.1.1. Dimensions of Photolithographic Features

The mask for photolithography contained patterns for four different TLC plates, all based on zig-zag geometries, 100 µm flow channels, and 90° angles between channels. Out of these four possibilities, two types of plates were used in this study: (i) a plate with 3 µm hedges and 5.65 µm flow channels, or (ii) a plate with 4 µm hedges and 4.95 µm flow channels. Both plates (i) and (ii) were used under normal phase conditions. Plate (i) was used to separate the fluorescent dyes.

5.3.1.2. Lithography and Catalytic Material Depositions

Silicon wafers (University Wafers, South Boston, MA), 4" diameter, <100>, were used as the backing material in our process. Accordingly, a thin film of photoresist, AZ-3312-F (AZ Electronic Materials USA Corp, Somerville, NJ), was spin coated onto a wafer. The resulting wafer was patterned with photolithography (Karl Suss Mask Aligner, Vermont, USA), followed by e-beam evaporation (Benton Vacuum E-beam Evaporator, Moorestown, NJ) of a thin barrier layer of alumina (35 nm), and thermal evaporation (home-built apparatus) of a few nanometers of iron (6 nm). The iron deposition was monitored using a quartz crystal device. The photoresist was then lifted off with a resist stripper (Micropsoit 1165, MicroChem, Newton, MA), leaving a pattern of Al_2O_3/Fe at the surface.

5.3.2. Microfabrication of the Thin Layer Chromatography Plate

5.3.2.1. Carbon Nanotube Growth

The photolithographically patterned wafer was loaded into a fused silica tube (22 mm ID), preheated to 200 °C in a Lindberg/Blue M tube furnace (Thermo Electron Corporation, Marietta, OH), and heated to 400 °C under flow of argon. The temperature was then raised from 400 °C to 750 ˚C in an atmosphere of hydrogen (6.67 x 10^{-6} m^3/s), where this process reduces iron to its elemental form and simultaneously produces iron nanoparticles.[28, 29] CNTs were grown for 2 min at 750 ˚C to a height of ca. 50 µm with ethylene (Grade 5.0, 99.999% from Air Gas) at 1.67 x 10^{-5} m^3/s and hydrogen (Air Gas), at 6.67 x 10^{-6} m^3/s. The material was cooled under argon to 200 °C.

5.3.2.2. Amorphous Carbon Deposition

To improve/facilitate deposition on the CNTs, they were primed with a thin layer (4 nm) of carbon. Accordingly, the CNTs were placed in the same tube furnace used for CNT growth and the temperature was raised to 900 °C under an argon atmosphere. Carbon was then deposited at 900 °C from ethylene (5.50 x 10^{-6} m^3/s) and argon (5.00 x 10^{-6} m^3/s) for 45 s (deposition rate ca. 5 nm/min). After this chemical vapor deposition (CVD) of carbon the plates were cooled to 200 ˚C under argon. The thickness of the carbon was also determined on planar (100) silicon witness substrates by spectroscopic ellipsometry (M-2000D, J.A. Woollam Co., Lincoln, NE). In addition to determining the deposition rate, the deposition profile of the furnace was measured to ensure that the carbon was deposited in a uniform fashion over a uniform area (see Figure 5.2).

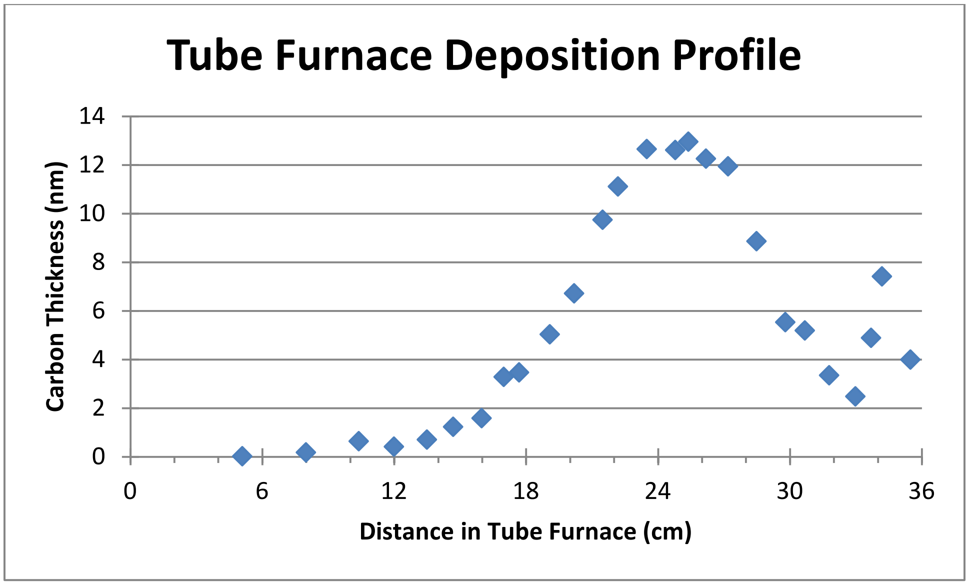

Figure 5.2 Profile for carbon deposition in our tube furnace. Deposition time was 45 s. The film thickness was determined by spectroscopic ellipsometry.

5.3.2.3. Atomic Layer Deposition (ALD) of Al_2O_3

ALD of Al_2O_3 was performed using a Cambridge Fiji F200 system (Cambridge NanoTech, Cambridge, MA) from trimethylaluminum (97%, Sigma-Aldrich) and water that were cycled in an ABAB type fashion. The deposition was performed at 250 °C. Either 70 or 105 AB cycles were performed to produce film thicknesses of either 7 or 10.5 nm, respectively. Film thicknesses were monitored via spectroscopic ellipsometry with film growth of ca. 0.1 nm/cycle.

5.3.2.4. Pseudo Atomic Layer Deposition (ψ-ALD) of SiO2

ψ-ALD of SiO_2 was also done with a Cambridge Fiji F200 system using trimethylaluminum (97%, Sigma-Aldrich) and tris(*tert*-butoxy)silanol (99.999%, Sigma-Aldrich) as precursors that were cycled in an ABAB type fashion. The deposition was performed at 235 °C. Eight AB cycles at a rate of ca. 13 nm/cycle were preformed to produce the final Al-doped SiO_2 film. Film thicknesses were monitored by spectroscopic ellipsometry.

5.3.2.5. Removal of CNTs

To produce a white material for chromatography the CNTs were removed via air oxidation. The silica coated CNTs were placed in a preheated (200°C) bench top furnace (Thermolyne 6000 Furnace, Dubuque, IA) and heated to 600 °C at 1 °C/min. The material was held at 600 °C for 17.33 h, for a total processing time of 24 h. The furnace was then cooled to 200 °C.

5.3.3. Surface modification

5.3.3.1. Rehydration of SiO_2

Because the SiO_2 material was subjected to temperatures above 200 °C, the surface needed to be repopulated with silanols.[30, 31] Surface silanol repopulation was performed with a pH 10 NH_4OH etching solution at room temperature for 18 h. After 18 h the material was removed from solution and rinsed with deionized water to neutrality. It was dried at 120 °C prior to chromatography or APTES deposition.

5.3.3.2. Amino-Functionalization

A TLC plate was placed in a freshly prepared solution of 1% (v/v) 3-aminopropyltriethoxysilane (APTES) (≥ 98%, Sigma-Aldrich) in water-saturated toluene (≥ 99.8%, Sigma-Aldrich) and heated to 70 °C. The solution was held at this temperature for 10 min after which the TLC plate was removed and rinsed three times with methanol (≥ 99%, Sigma-Aldrich). The optical properties of Si wafers (terminated with native oxide), APTES-coated Si wafers, and carbon-coated silicon wafers were determined by variable angle spectroscopic ellipsometry (VASE) using an M-2000D instrument (J.A. Woollam Co., Lincoln, NE), which gives values of Δ and ψ from ca. 200 – 1000 nm. Ellisometric data were taken at 70° and 75° and fitted using the WVASE 32 instrument software, Version 3.635. All of the ultrathin films (the native oxide, the APTES, and the CVD carbon) were modeled using the optical constants of SiO_2 from the instrument software (sio5.jaw).

5.3.4. Material Characterization via X-ray Photoelectron Spectroscopy (XPS) and Diffuse Reflectance Infrared Fourier Transform Spectroscopy (DRIFTS)

XPS was performed on two separate instruments. XPS analysis of CNTs (n = 2) was done on a Physical Electronics Quantera Scanning X-ray Microprobe (Chanhassen, MN) at Pacific Northwest National Laboratory (PNNL) in the Environmental Molecular Sciences Laboratory (EMSL). This system uses a focused, monochromatic Al Kα X-ray (1486.7 eV) source for excitation and a spherical section analyzer. The instrument has a 32 element multichannel detection system. A 98 W X-ray beam focused to 100 μm was rastered over a 1.3 mm x 0.1 mm rectangle on the sample. Further XPS analyses were performed using a Surface Science SSX-100 X-ray photoelectron spectrometer (serviced by Service Physics, Bend, OR) with a monochromatic Al K_α source, a hemispherical analyzer, and a take-off angle of 35°. Survey and narrow scans were recorded with an 800 μm × 800 μm spot size. The XP spectra from the SSX-100 instrument were analyzed using the ESCA Data Analysis Application software (Version: Analysis 25 V.01.02). DRIFTS was performed using a Thermo Scientific Nicolet 6700 FT-IR. Both the microfabricated material (scraped from microfabricated TLC plates) and commercially available silica (Sepax HP-Silica, 3 μm, 120 Å, Sepax Technologies, Delaware) were scanned 128 times with a resolution of 4 cm^{-1}. The spectra were analyzed using the instrument OMNIC 8.1.11 software.

5.3.5. Chromatography

5.3.5.1. Spot Application and Pre-equilibration of Thin Layer Chromatography Plate

A predetermined volume of an analyte or mixture of analytes was applied as a 3 x 0.7-0.8 mm band at the bottom of the TLC plate using a Linomat 5 spotter (CAMAG, Muttenz, Switzerland). The band was applied 5 mm from the bottom of the plate. The plate was then placed in a 10 x 10 cm twin trough chamber (CAMAG, Muttenz, Switzerland) and pre-equilibrated with the vapors of the mobile phase. After the pre-equilibration, 3 mL of the mobile phase was introduced at the bottom of the plate to commence chromatography. The TLC plate was developed over a 30 mm distance.

5.3.5.2. Separation of a Test Dye Mixture

Test dye mixture III solution in toluene from CAMAG (Muttenz, Switzerland) containing indophenol, ariabel red, Sudan blue II, Sudan IV, and dimethylaminoazobenzene was diluted in hexanes to produce a 1% v/v solution. A 1 μL or 3 μL volume of this diluted solution was applied to a plate, where the mobile phase was toluene (99.8%, Sigma-Aldrich), with or without 0.1% v/v triethylamine (99.5%, Sigma-Aldrich) as modifier.

5.3.5.3 Separation of Two Fluorescent Dyes

Eosin Y disodium salt (~85%, Sigma-Aldrich) and sulforhodamine B (75%, Sigma-Aldrich) were dissolved together in methanol to concentrations of ca. 5 x 10^{-7} M. A 0.5 μL of this solution was applied and a 1:100 LiCl/methanol (LiCl, >99%, EMD, Gibbstwon, NJ) solution was used as the mobile phase.[32]

5.3.5.4 Separation of Four Fluorescent Dyes

Eosin Y disodium salt (~85%, Sigma-Aldrich), sulforhodamine B (75%, Sigma-Aldrich), rhodamine 6G (~95%, Sigma-Aldrich), and fluorescein sodium salt (98%, Sigma-Aldrich) were dissolved in methanol at concentrations of ca. 5 x 10^{-7} M. 0.5 μL of this solution was applied and 1:70:30 LiCl/methanol/isopropanol (isopropanol, ≥ 99%, Sigma-Aldrich) was used as the mobile phase.

5.3.6. Visualization of Separated Dyes and Calculation of R_F, N, and H_{obs}

Imaging of the separated dyes was performed with a digital camera (Canon PowerShot S95, Canon USA, Lake Success, NY). The TLC plate was exposed to short wavelength UV light

(254 nm) (Model UVG-11 Mineralight Lamp, Ultra-Violet Products, San Gabriel, CA) for fluorescent visualization. All images were processed using ImageJ (ImageJ 1.42q, National Institutes of Health, USA).

Retention factors (R_F) were calculated with the following equation:

$$\boldsymbol{R_F = \frac{Z_o}{Z_f}} \tag{2}$$

where Z_o is the analyte migration distance from the application origin and Z_f is the distance the solvent front traveled, also from the application origin. Chromatographic efficiencies were determined by the number of theoretical plates (N) according to:

$$\boldsymbol{N = 16\left(\frac{Z_f R_f}{W}\right)^2} \tag{3}$$

where W is the width of the chromatographic band.[33] However, these values (N/m) will only be used to compare to those of Song et al.[10] Because the fluid velocity in TLC is dynamic, N is not typically used to determine chromatographic efficiency. Accordingly, observed plate heights (H_{obs}) are reported as follows:[34-38]

$$\boldsymbol{H_{obs} = \frac{\sigma^2_{chrom}}{R_F(Z_f - Z_o)}} \tag{4}$$

The value of σ^2_{chrom} in this equation is calculated from

$$\sigma^2_{\mathrm{obs}} = \sigma^2_{\mathrm{chrom}} + \sigma^2_{\mathrm{SA}} + \sigma^2_{\mathrm{INS}} \tag{5}$$

where σ^2_{obs} is the observed variance of the band after elution, σ^2_{SA} is the variance of the band at the spot application, and σ^2_{INS} is the variance of the densitometric measurement (we are not using a densitometer, so we set $\sigma^2_{INS} = 0$ in Equation 5).[34, 37, 39] The value of σ^2_{SA} was determined from the initial width of the spot at application (0.7 mm), which was taken as $5\sigma_{\mathrm{SA}}$. Thus $\sigma^2_{SA} = 0.019_6$ mm^2 in our calculations.

5.3.7. Microscopy

SEM images were captured with an FEI Helios Nanolab 600 (Hillsboro, OR). TEM images were captured using a FEI Tecnai F20 Analytical STEM (Hillsboro, OR).

5.4. Results and Discussion

5.4.1. Conformal Coating of CNT Scaffolds

An important issue for the future manufacturing of our microfabricated TLC plates is the speed with which ca. 50 – 100 nm of conformal inorganic material can be deposited onto the CNTs. Preferably this material would be silica because silica is of primary importance in modern chromatography, cf. typical materials for TLC, HPTLC, HPLC, and UHPLC. For these reasons, we considered the rapid, pseudo ALD (ψ-ALD) process developed by Hausmann et al. that results in ca. 13 nm of silica (ψ-SiO_2) per cycle using trimethylaluminum (TMA) as a priming/catalytic layer and tris(*tert*-butoxy)silanol ((($(CH_3)_3O)_3SiOH$), (TTBS))) as the silicon dioxide precursor.[18] This deposition rate can be compared to the ca. 0.1 nm per cycle obtained in the more classical ALD deposition of SiO_2 from precursors such as $SiCl_4$ and H_2O.[40]

Accordingly, we attempted to grow ψ-SiO_2 directly onto patterned CNT forests using the Hausmann process, and significant growth was observed. However, the resulting thin ψ-SiO_2 films on CNTs lacked conformality and usually showed a large number of pearl-like features (see Figure 5.3a). This lack of conformal growth was expected to affect the plates’ mechanical stability. Indeed, after removal of the CNTs via air oxidation, the plates were submerged in water and immediate failure/delamination was observed. It seemed unlikely that these devices could act as acceptable substrates for thin layer chromatography.

The pearl-like growth observed in the direct deposition of ψ-SiO_2 from TMA and TTBS appeared to be the result of an insufficient number of nucleation sites on the CNTs, which are quite chemically inert. In this situation an appropriate adhesion promoter, which might increase the number of nucleation sites on the CNTs, might allow more conformal growth to take place. As noted above, there are previous reports of the filling/infiltration of CNT forests with carbon.[19, 20, 41] However, in contrast to these studies, we believed that only a very thin layer, perhaps only a few nanometers, might be sufficient to significantly increase the number of nucleation sites available for subsequent ALD. To the best of our knowledge, this method for chemically activating CNTs is new. We hypothesized that these nucleation sites would be oxygen-containing moieties at defects in the carbon layer. Accordingly, a few nanometers of carbon was deposited onto CNTs using ethylene diluted in argon at 900 °C. The resulting carbon layers showed good conformality and even some measured crystallinity, as indicated by the texture of their transmission electron microscopy (TEM) images (Figure 5.4).

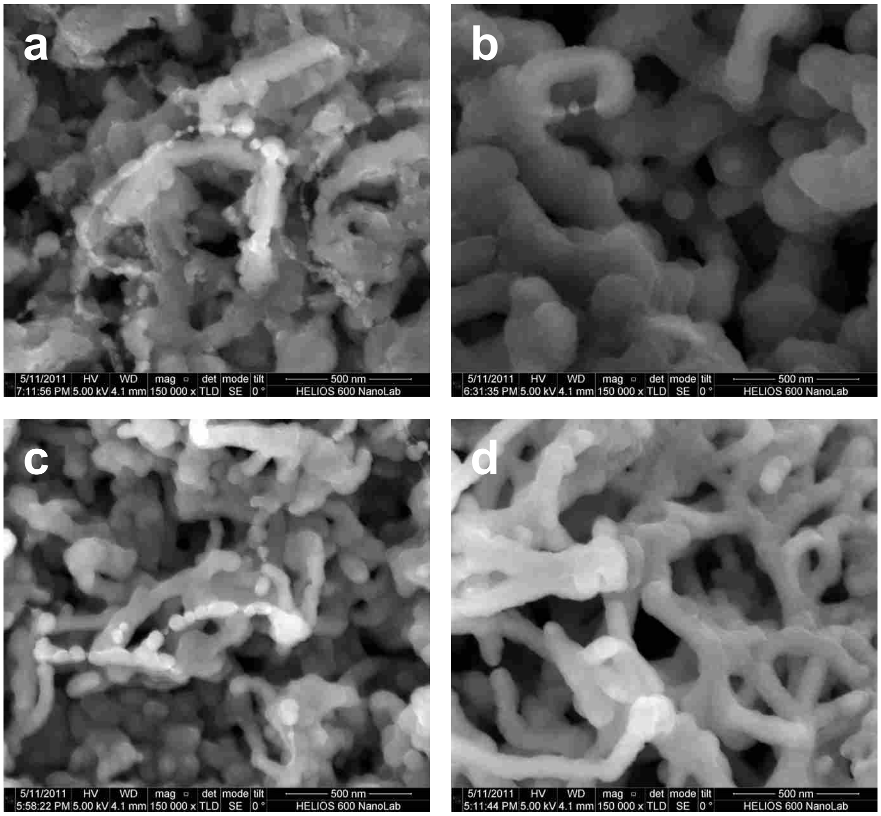

Figure 5.3 Scanning electron micrographs of materials for TLC prepared under various conditions. At least some pearl-like nucleation/growth appears in the first three of the micrographs: (a) CNT-ψ-SiO_2(8), (b) CNT-a-C(4 nm)-ψ-SiO_2(8), (c) CNT-Al_2O_3(70)-ψ-SiO_2(8), and (d) CNT-a-C(4 nm)-Al_2O_3(70)-ψ-SiO_2(8). The unitless numbers in parentheses signify the number of ALD cycles completed.

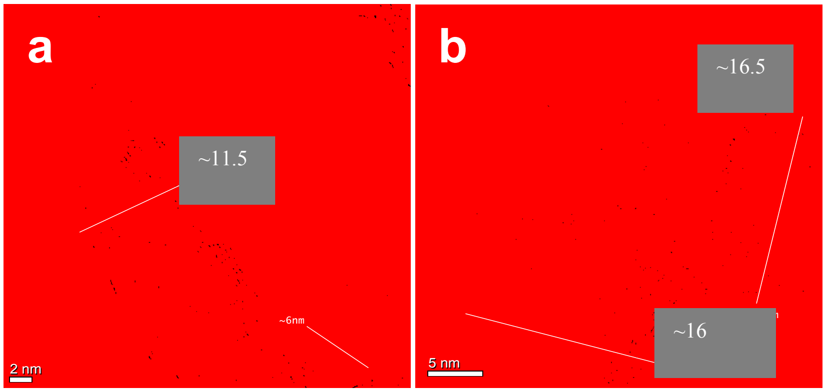

Figure 5.4 (a) TEM image of as-grown CNTs (scale bar 2 nm) (b) TEM image of CNTs coated with amorphous carbon (45 s deposition time) (scale bar 5 nm).

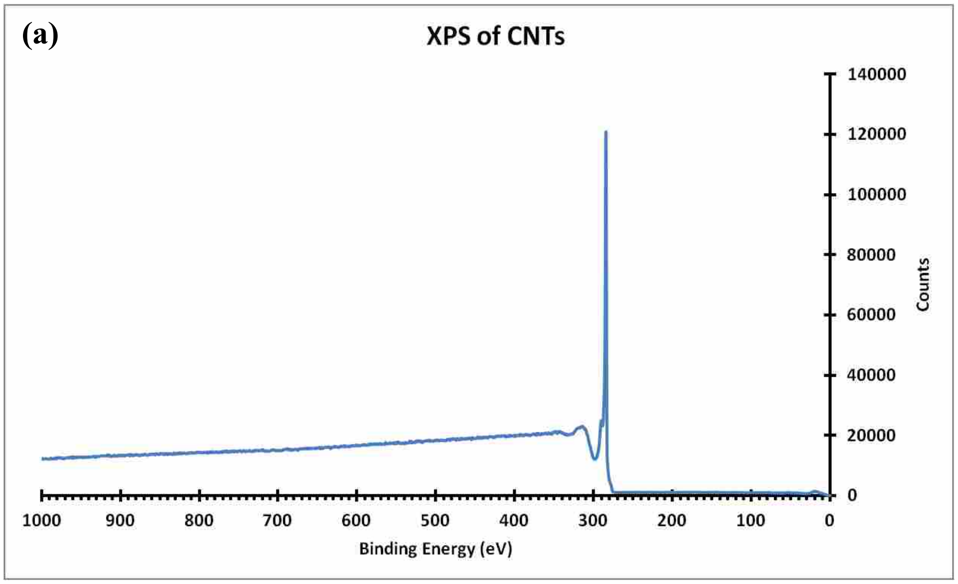

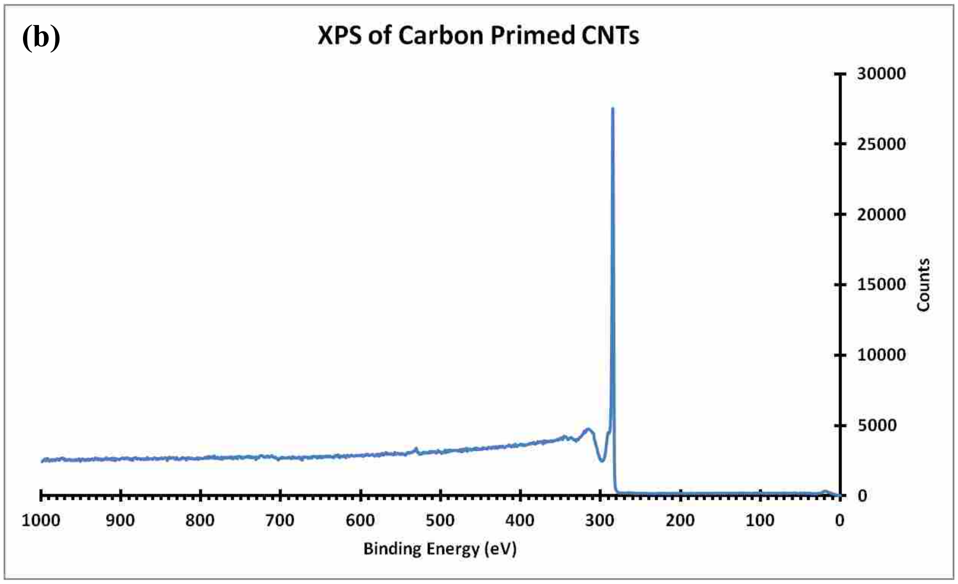

Figure 5.5 (a) XPS survey spectum of as grown CNTs. No element except carbon (at ca. 285 eV) is present. Oxygen would appear at ca. 530 eV. (b) XPS survey spectrum of carbon-primed CNTs. The spectrum shows both carbon at ca. 285 eV and a small oxygen signal at ca. 530 eV.

X-ray photoelectron spectroscopy (XPS) of unprimed and carbon coated CNTs was also performed. Multiple XPS scans of multiple unprimed CNT forests showed the material to be 100% carbon (n=6). In contrast, XPS of carbon coated CNTs showed the presence of oxygen (0.80 ± 0.11 atom% O, 99.20 ± 0.11 atom% C from four scans of four different CNT forests, see Figures 5.4). This increase in oxygen should increase the number of nucleation sites available for ALD, especially given the highly reactive nature of trimethylaluminum. To explore whether these few nanometers of carbon might improve ALD or ψ-ALD on CNTs, and to show that these plates might indeed exhibit the desired stability and chromatographic properties, four types of depositions were performed on patterned CNT forests using different combinations of carbon (C), Al_2O_3 (deposited in a 'true' ALD process), and ψ-SiO_2: (i) CNT-ψ-SiO_2(8), (ii) CNT-C(4 nm)-ψ-SiO_2(8), (iii) CNT-Al_2O_3(70)-ψ-SiO_2(8), and (iv) CNT-C(4 nm)-Al_2O_3(70)-ψ-SiO_2(8), where the number in parentheses after 'Al_2O_3' and 'ψ-SiO_2' refers to the number of ALD or pseudo ALD cycles, one cycle referring to the introduction of both precursors for each process. Both these and also the deposition mentioned below (same as deposition (iv) but with more Al_2O_3 ALD cycles) were made on patterned nanotube forests. Each of these four depositions was performed three times, from start to finish, in separate fabrications.

After deposition of carbon, Al_2O_3, and/or fast (ψ-ALD) deposition of SiO_2, the coated materials were oxidized to remove both the CNT framework and the carbon priming layer. In contrast to our previous work,[10] it was no longer necessary to convert the Si to SiO_2 so the nanotubes and carbon layer could be burned out at a much lower temperature (ca. 600 °C). Finally, the plates were visually inspected for whiteness, where a whiter plate points to a greater deposition of inorganic material, as it hides the darker silicon substrate. As expected, the CNT-ψ-SiO_2(8) plates visually showed the least amount of deposition (they were the darkest) and all of them failed a water immersion test, showing immediate delamination/removal of the layer. The CNT-C(4 nm)-ψ-SiO_2(8) plates (Figure 5.3b) showed more SiO_2 deposition, but ca. 50% of them failed the water immersion test. The CNT-Al_2O_3(70)-ψ-SiO_2(8) plates performed about as well as the CNT-carbon(4 nm)-ψ-SiO_2(8) plates, with one plate completely passing and about half of another plate passing the immersion test (Figure 5.3c). The best performing substrates contained both CVD carbon and Al_2O_3 (Figure 5.3d); they showed the greatest deposition of inorganic material (greatest whiteness) and ca. 2.5 of 3 plates passed the immersion test (only part of one plate failed). This synergistic effect of both carbon and alumina to create a stable structure is attributed to the introduction of oxygen at defect sites on carbon, followed by sufficient growth of Al_2O_3 by ALD at these sites so that strong nucleation would occur in subsequent ψ-SiO_2 growth – note that exposure/deposition of trimethylaluminum is the first setp in ψ-SiO_2 growth. Thus, it appeared that at this point we had a nearly viable process for fabricating TLC plates with features that did not swell or expand upon oxidation. Figure 5.6 shows SEM micrographs of portions of TLC plates prepared with our original method, showing some distortion of the features, and with this newer approach showing straight, undistorted features. More stable materials, which withstood the water immersion test after oxidation, were next prepared by increasing the number of Al_2O_3 ALD layers. TEM/STEM analysis of the resulting CNT-C(4 nm)-Al_2O_3(105)-ψ-SiO_2(8) materials showed the expected sequential encapsulation of the CNTs and carbon with Al_2O_3 and ψ-SiO_2 (see Figure 5.7), (See also Figure 5.8 for other TEM images.)

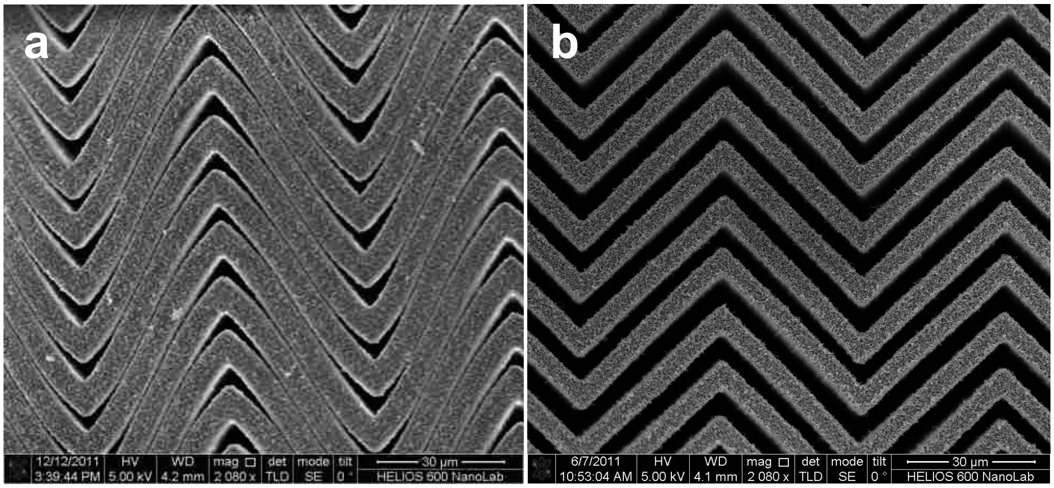

Figure 5.6 SEM images of (a) a TLC plate prepared via the method of Song et al.[10] (b) a TLC plate prepared by the method described within this manuscript. Both plates were made from the same lithography mask, plate (ii). Note that the flow direction for TLC in these devices would be from left to right, or right to left.

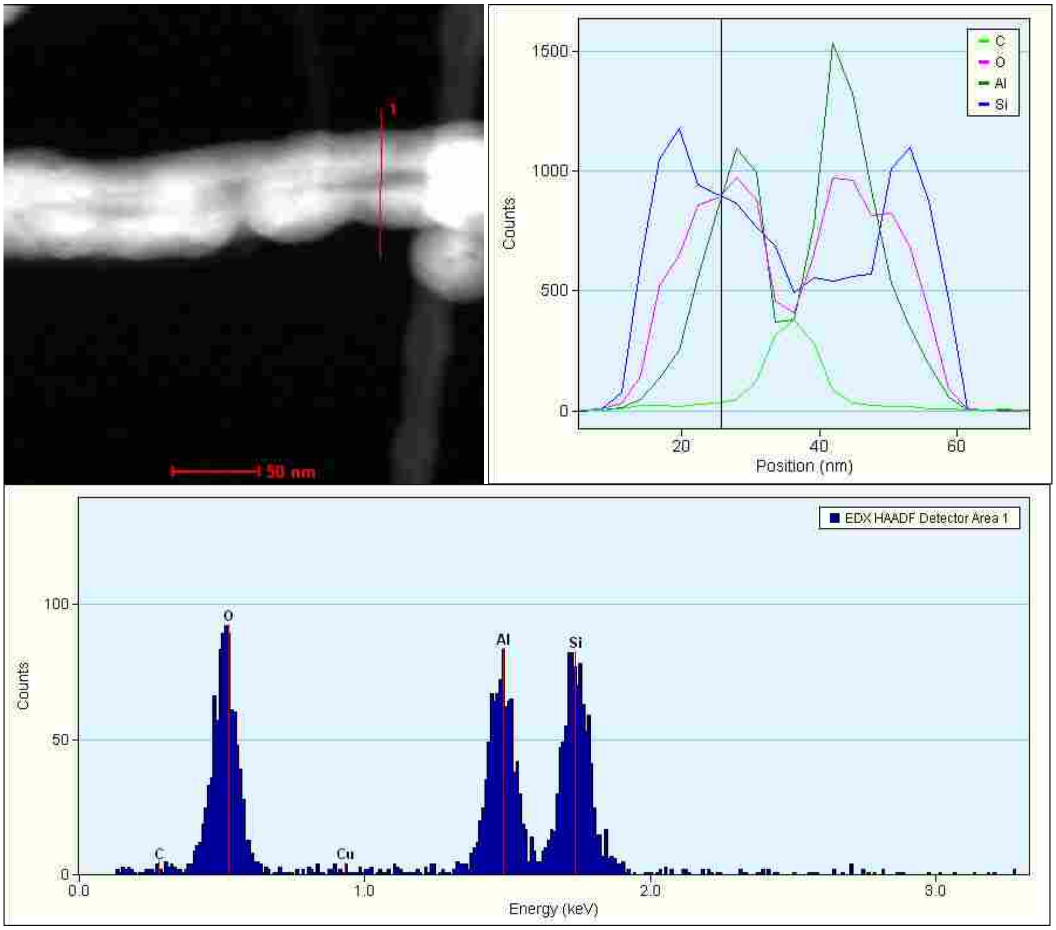

Figure 5.7 STEM of the CNT-C(4nm)-Al_2O_3(105)-ψ-SiO_2(8) assembly. STEM shows the expected presence of carbon, aluminum, oxygen and silicon, with carbon at the center of the assembly, followed by aluminum, and then silicon.

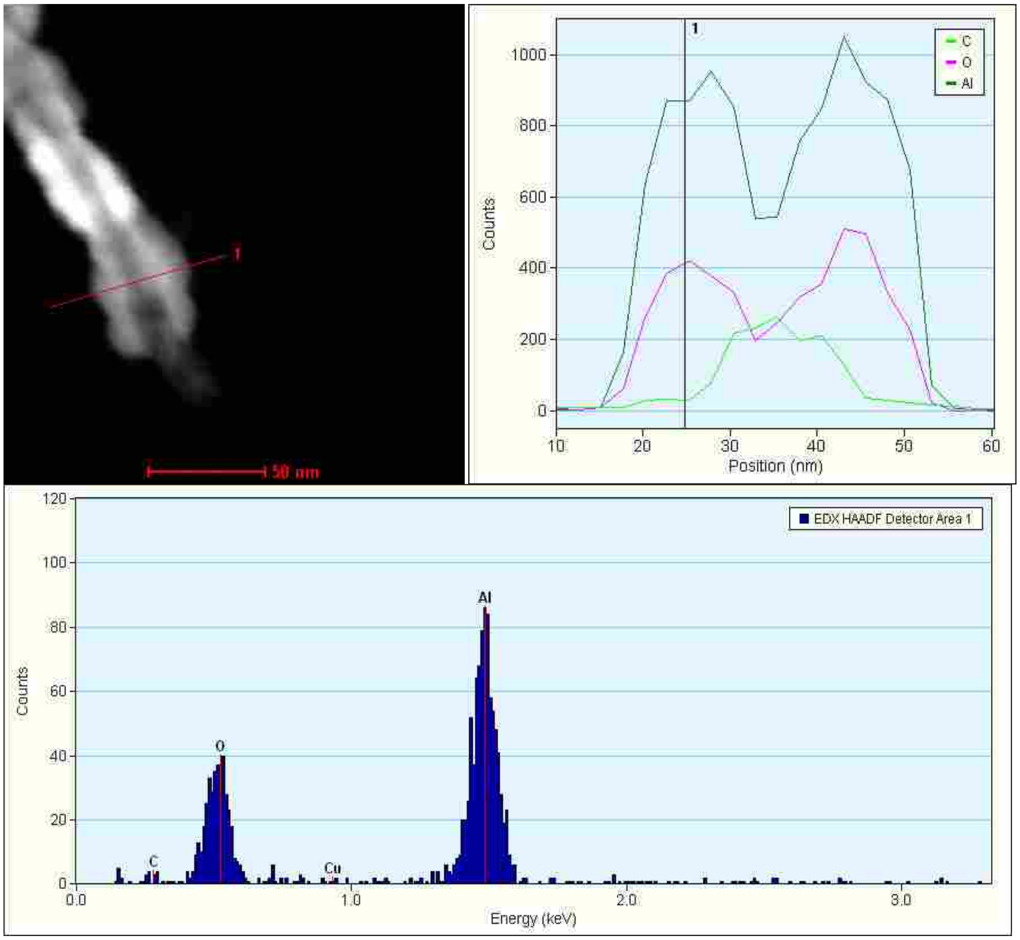

Figure 5.8 STEM of alumina-coated CNT. A carbon coated CNT is located in the center of the feature and is encapsulated with Al_2O_3.

5.4.2 Separations on Microfabricated-Thin Layer Chromatography (M-TLC) Plates

TLC was then performed on the better [CNT-C(4nm)-Al_2O_3(105)-ψ-SiO_2(8)] plates. However, because temperatures as low as 200 °C are known to remove silanol (SiOH) groups from silica,[42] and because appropriate densities of SiOH groups are essential for good chromatography,[31] the plates were first hydrated via a literature method that consisted of (i) immersion in a pH 10 NH_4OH solution for 18 h, and (ii) rinsing with water to neutrality.[31] TLC of a CAMAG test dye mixture was then performed under normal phase conditions with the recommended mobile phase (toluene). The results were mixed. First, the run times for the plates were short, which of course is positive: ca. 30 s development times for 30 mm development distances. Second, all of the analytes in the test mixture generally showed substantial streaking except the fastest moving analyte, which appeared as a tight band, with an observed plate height (H_{obs}) of 4.1 µm [ca. 77 000 theoretical plates per meter (N/m)] for the plate (ii) geometry and H_{obs} of 5.6 µm (ca. 100 000 N/m) for plate (i) at moderate retention factor (R_F) values of ca. 0.6 (See Figure 5.9). These results suggested the presence of strongly adsorbing sites that interact to a greater extent with the more polar (more strongly retained) analytes in the test mixture.

Metal impurities, including aluminum, are well known to create strongly adsorbing sites in silica that deleteriously affect chromatography. Indeed, one of the significant advances in liquid chromatography over the past few decades has been the development of the so-called Type B silica, which, in contrast to the older Type A, has extremely low levels of metal impurities.[43, 44] So while in theory our plates should be entirely covered by silica, one possible source of strongly adsorbing sites could be aluminum from the ψ-ALD deposition of SiO_2, i.e., alumina from $Al(CH_3)_3$ is the catalyst that begins each deposition cycle.

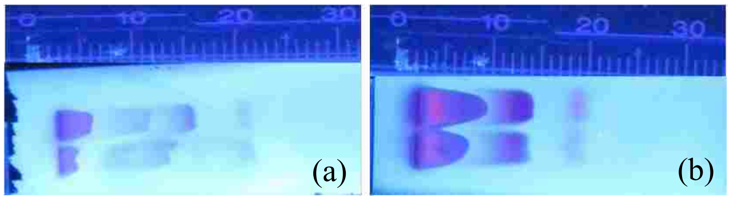

Figure 5.9 Separation of a CAMAG test dye mixture on two microfabricated TLC plates with different geometries. (a) 4 µm hedges and 4.95 µm flow channels (CNT-C(4nm)-Al_2O_3(105)-ψ-SiO_2(8), plate (ii)), and (b) 3 µm hedges with 5.65 µm flow channels (CNT-C(4nm)-Al_2O_3(105)-ψ-SiO_2(8), plate (i)). Both separations were performed over 30 mm with development times of ca. 30 s. Plates were visualized under 254 nm light. For the fastest moving analyte in (a): R_F = 0.63 with an efficiency (H_{obs}) of 5.6 µm (100 000 N/m), and in (b): R_F = 0.55 with an efficiency (H_{obs}) of 4.1 µm (77 000 N/m).

Accordingly, X-ray photoelectron spectroscopy (XPS) was performed on a CNT-C(4 nm)-Al_2O_3(70)-ψ-SiO_2(8) plate to determine whether any aluminum was present in the upper ca. 5 - 10 nm of the SiO_2 film, which is the approximate probe depth of the technique. A negative signal (no Al by XPS) would indicate that the aluminum was entirely covered with a thick layer of silica. A small positive signal would be ambiguous – the Al might be covered with a moderately thick film of SiO_2 or it might be near enough to the surface to create highly acidic/adsorptive sites. XPS showed ca. 2 atom% Al on the TLC material. Interestingly, less Al (0.2 atom%) was found on a planar ψ-SiO_2 film, which suggested that the deposition of ψ-SiO_2 on the curved nanotubes was not quite the same as on a planar substrate, and that this difference in geometry may change the distribution of Al in the plate.

In addition to XPS, diffuse reflectance infrared Fourier transform spectroscopy (DRIFT) was performed on our materials, along with a commercially available standard silica material produced for HPLC. This study was motivated by Köhler et al., who showed that highly adsorptive silicas with highly acidic/isolated silanols that show poor chromatographic performance have peak maxima for silanols at or greater than 3740 cm^{-1}, while silicas that show better chromatographic performance show a maximum below this value, which corresponds to associated/more closely spaced/hydrogen bonded silanols.[31] The DRIFT analysis of our material gave a silanol peak position of 3740.5 cm^{-1}, suggesting the presence of at least some highly adsorptive sites, while the commercial silica standard gave a value of 3739.9 cm^{-1}.

Thus, chromatographic, XPS, and DRIFT analyses suggested that strongly adsorbing sites were present in our stationary phase/support and that these may be due to aluminum. To further probe this issue, a small amount (0.1%) of triethylamine (TEA) was added to the mobile phase. TEA is a well-known modifier to mobile phases for liquid chromatography on the older

Type A silica materials, where its function was to interact strongly with isolated silanols/strongly adsorbing sites.[45-47] TEA had two effects on our TLC separations. First, it changed the chromatographic characteristics of the mobile phase, i.e., it strengthened it, which resulted in higher R_f values for the analytes. Indeed, the analytes largely ran together with R_F values of ca. 0.8. But more importantly, the addition of TEA eliminated streaking on the plates. The results from these experiments are consistent with the presence of strongly adsorbing sites on our plates.

With this information, our next goal was to find a chemical reagent that might permanently bind to/cover up the strongly adsorbing sites on our TLC plates. And because TEA, an amine, seemed to reduce or eliminate the effects of strongly adsorbing sites, hydrated TLC plates were reacted with an amino silane: 3-aminopropyltriethoxysilane (APTES). This is the first demonstration of a bonded phase on one of our microfabricated TLC plates. An advantage of APTES in silane deposition is that, due to its primary amine, it catalyzes its own condensation.[48] APTES deposition was inferred from planar shards of silicon that were placed in the solution, which showed increases in thickness of 1.6 ± 0.1 nm by spectroscopic ellipsometry. The advancing and receding water contact angles on these planar surfaces were 46.3 ± 1.7° and 8.4 ± 1.0°, respectively, which is consistent with literature results.[49, 50] XPS further confirmed APTES deposition, showing a small but noticeable nitrogen signal (N1s:Si2p ratio of 2:25) for APTES-coated TLC plates. No such signal was present on the plate prior to deposition of the silane. TLC of two fluorescent dyes was first attempted on a somewhat defective APTES-functionalized CNT-C(4 nm)-Al_2O_3(70)-ψ-SiO_2(8) plate. Fortunately, both compounds appeared to separate under these conditions, or at least to be separable, albeit with same distortion. A CNT-C(4 nm)-Al_2O_3(105)-ψ-SiO_2(8) plate was then functionalized with APTES, and the separation of the fluorescent dyes was attempted as before. This time a baseline separation of the dyes was observed in 1:08 min over a 30 mm distance (see Figure 5.10). This same separation was performed on a commercially available amino-HPTLC plate under the same conditions. Comparing the solvent front migration times between the two TLC plates (microfabricated vs. HPTLC) our plates ran 3 times faster (amino-HPTLC development time: 3:26 min).

The green spot in Figure 5.11, which is probably most representative of the separation, showed an R_F value of 0.85 with H_{obs} of 7.7 μm (ca. 85,000 N/m). The orange spot, which migrated further and with an R_F of 0.94, was probably focused by the solvent front so the corresponding value of H_{obs} (6.6 μm or 89,000 N/m) may be inflated. This two component separation was promising and was reproduced on three separate TLC plates. It was apparent that surface functionalization with APTES rendered a material that was more suitable for chromatography. Accordingly, we attempted to separate a four-component fluorescent dye mixture: eosin Y disodium salt, sulforhodamine B, rhodamine 6G and fluorescein sodium salt, using a 1:70:30 LiCl/methanol/isopropanol mobile phase. Figure 5.10 shows the separation of these dyes on an APTES-functionalized TLC plate in a rather short period of time (1:52 min) over a 30 mm development distance.

This latest separation showed improved efficiencies over the previous separations, which may be attributed to a reduction in the mobile phase migration rate due to a more viscous mobile phase, and which may have allowed the separation to occur at a better mobile phase velocity. The efficiencies obtained in this separation ranged from 1.6 to 5.8 μm (200,000 to 270,000 N/m) (more specifically H_{obs} of 5.8 μm, 1.6 μm, 1.9 μm, 5.1 μm at R_F values of 0.79, 0.86, 0.89, and 0.94, respectively). The separated dyes appeared as symmetrical bands, which would again be consistent with APTES covering highly adsoptive sites on the ψ-ALD deposited SiO_5.

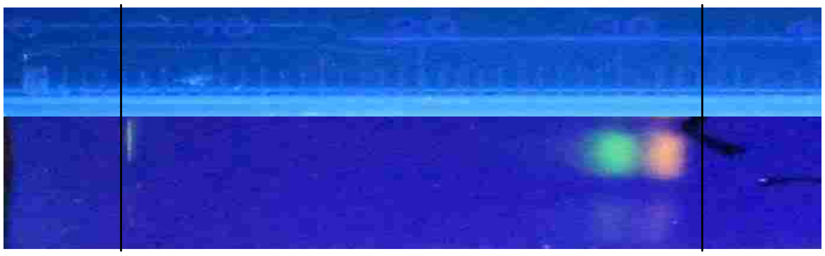

Figure 5.10 Separation of two fluorescent dyes (eosin Y disodium and sulforhodamine B) over a 30 mm run distance using a 1:100 LiCl/methanol mobile phase. The analyte concentration in the lower track is ca. 10% of the concentration of the analytes in the upper track. The fluorescent image was captured under 254 nm light.

Figure 5.11 Separation of four fluorescent dyes (eosin Y disodium salt, sulforhodamine B, rhodamine 6G and fluorescein sodium salt) using a 1:70:30 LiCl/methanol/isopropanol mobile phase. The development occurred over a 30 mm distance in 1:52 minutes. The fluorescent image was captured under 254 nm light.

A comparison of these results to a commercially available amino-phase HPTLC plate showed that these TLC plates were ca. 6 times more efficient and ca. 4 times faster. Thus, microfabricated TLC plates allow for both extremely efficient separations and increased speed of analysis.

The use of ALD type reactions to coat CNTs for the construction of a chromatographic medium has proven to give more efficient chemical separations when compared to the original work done by some of us.[10] The maximum number of theoretical plates per meter (N/m) previously obtained was ca. 75,000 N/m. The process described within this document produced a chromatographic medium that gave a maximum of 270,000 N/m (1.6 μm), a significant improvement.

5.5. Conclusions

Microfabricated TLC plates were constructed from CNT-patterned surfaces. The CNTs were coated with silica, the chromatographic material, via pseudo-atomic layer deposition.[18] The use of an adhesion layer of carbon and ALD of Al_2O_3 allowed for the construction of silica-coated TLC media that were mechanically robust. After surface functionalization with APTES to cover strongly adsorptive sites, two different test dye mixtures were successfully separated. Separations occurred in short periods of time with high efficiencies.

5.6. Acknowledgments

We thank Diamond Analytics, a US Synthetic company (Orem, UT), for funding this study. Part of this research was performed at EMSL, a national scientific user facility sponsored

by the Department of Energy's Office of Biological and Environmental Research and located at Pacific Northwest National Laboratory.

Author contributions: D.J. Concieved the idea of carbon coating CNTs, did the ALD, chromatography and microscopy. S.K. fabricated the devices up to and including CNT growth. V.G. helped with preliminary ALD depositions. M.V. and A.D. helped direct the research. M.L. recognized that a defective carbon surface would end up with adsorbed oxygen that could be used in subsequent depositions. A.D. suggested the use of ALD of Al_2O_3. M.E. performed the XPS analyses. M.L. was the principle investigator of the project. The manuscript was written by D.J. and M.L.

5.7. References

1. Stevenson, R., Chapter 12 Instrumentation. In *Journal of Chromatography Library*, Heftmann, E., Ed. Elsevier: 2004; Vol. Volume 69, pp 469-518.

2. Hauck, H.; Bund, O.; Fischer, W.; Schulz, M., *J. Planar Chromatogr.--Mod. TLC* **2001,** *14* (4), 234-236.

3. Hauck, H.; Schulz, M., *Chromatographia* **2003,** *57* (0), S313-S315.

4. Bezuidenhout, L. W.; Brett, M. J., *J. Chromatogr., A* **2008,** *1183* (1-2), 179-185.

5. Clark, J. E.; Olesik, S. V., *Anal. Chem.* **2009,** *81* (10), 4121-4129.

6. Zewe, J. W.; Steach, J. K.; Olesik, S. V., *Anal. Chem.* **2010,** *82* (12), 5341-5348.

7. Bakry, R.; Bonn, G. K.; Mair, D.; Svec, F., *Anal. Chem.* **2006,** *79* (2), 486-493.

8. Han, Y.; Levkin, P.; Abarientos, I.; Liu, H.; Svec, F.; Fréchet, J. M. J., *Anal. Chem.* **2010,** *82* (6), 2520-2528.

9. Urbanova, I.; Svec, F., *J. Sep. Sci.* **2011,** *34* (16-17), 2345-2351.

10. Song, J.; Jensen, D. S.; Hutchison, D. N.; Turner, B.; Wood, T.; Dadson, A.; Vail, M. A.; Linford, M. R.; Vanfleet, R. R.; Davis, R. C., *Adv. Funct. Mater.* **2011,** *21* (6), 1132-1139.

11. Hutchison, D. N.; Morrill, N. B.; Aten, Q.; Turner, B. W.; Jensen, B. D.; Howell, L. L.; Vanfleet, R. R.; Davis, R. C., *J. Microelectromech. Syst* **2010,** *19* (1), 75-82.

12. Moulton, K.; Morrill, N. B.; Konneker, A. M.; Jensen, B. D.; Vanfleet, R. R.; Allred, D. D.; Davis, R. C., *J. Micromech. Microeng.* **2012,** *22* (5), 055004.

13. Billen, J.; Desmet, G., *J. Chromatogr. A* **2007,** *1168* (1-2), 73-99.

14. John H, K., *J. Chromatogr. A* **1999,** *831* (1), 3-15.

15. Reich, E.; Schibli, A., *High-performance thin-layer chromatography for the analysis of medicinal plants*. Thieme Medical Publishers, Inc.: New York, 2007.

16. Van Le, T.; Ross, E. E.; Velarde, T. R. C.; Legg, M. A.; Wirth, M. J., *Langmuir* **2007,** *23* (16), 8554-8559.

17. Bergna, H. E.; Roberts, W. O., *Colloidal silica: fundamentals and applications*. Taylor & Francis Group: Boca Raton, 2006; Vol. 131.

18. Hausmann, D.; Becker, J.; Wang, S.; Gordon, R. G., *Science* **2002,** *298* (5592), 402-406.

19. Gong, Q.-m.; Li, Z.; Li, D.; Bai, X.-d.; Liang, J., *Solid State Commun.* **2004,** *131* (6), 399-404.

20. Gong, Q.-m.; Li, Z.; Bai, X.-d.; Li, D.; Liang, J., *Compos. Sci. Tochnol.* **2005,** *65* (7-8), 1112-1119.

21. Kleckley, S.; Chai, G. Y.; Zhou, D.; Vanfleet, R.; Chow, L., *Carbon* **2003,** *41* (4), 833-836.

22. Cavanagh, A. S.; Wilson, C. A.; Weimer, A. W.; George, S. M., *Nanotechnol.* **2009,** *20* (25), 255602.

23. Dillon, A. C.; Ott, A. W.; Way, J. D.; George, S. M., *Surf. Sci.* **1995,** *322* (1-3), 230-242.

24. Ott, A. W.; Klaus, J. W.; Johnson, J. M.; George, S. M., *Thin Solid Films* **1997,** *292* (1-2), 135-144.

25. Tleugabulova, D.; Zhang, Z.; Chen, Y.; Brook, M. A.; Brennan, J. D., *Langmuir* **2003,** *20* (3), 848-854.

26. Valcárcel, M.; Cárdenas, S.; Simonet, B. M., *Anal. Chem.* **2007,** *79* (13), 4788-4797.

27. Merkoçi, A., *Microchim. Acta* **2006,** *152* (3), 157-174.

28. Mattevi, C.; Wirth, C. T.; Hofmann, S.; Blume, R.; Cantoro, M.; Ducati, C.; Cepek, C.; Knop-Gericke, A.; Milne, S.; Castellarin-Cudia, C.; Dolafi, S.; Goldoni, A.; Schloegl, R.; Robertson, J., *J. Phys. Chem. C* **2008,** *112* (32), 12207-12213.

29. Esconjauregui, S.; Fouquet, M.; Bayer, B. C.; Ducati, C.; Smajda, R.; Hofmann, S.; Robertson, J., *ACS Nano* **2010,** *4* (12), 7431-7436.

30. Bergna, H. E.; Roberts, W. O., *Colloidal silica: fundamentals and applications*. Taylor & Francis Group: Boca Raton, 2006; Vol. 131.

31. Köhler, J.; Kirkland, J. J., *J. Chromatogr. A* **1987,** *385* (0), 125-150.

32. Wako Pure Chemical Industries Ltd. NH2 Silica Gel 60F254 Plate-Wako. http://www.wako-chem.co.jp/english/labchem/pdf/NH2_TLC_Plate.pdf.

33. Poole, C. F.; Poole, S. K., *Anal. Chem.* **1989,** *61* (22), 1257A-1269A.

34. Poole, S. K.; Poole, C. F., *J. Chromatogr. A* **2011,** *1218* (19), 2648-2660.

35. Poole, C. F., *The Essence of Chromatography*. 2003.

36. Bertsch, W.; Hara, S.; Kaiser, R. E.; Zlatkis, A., *Instrumental HPTLC*. Huethig, 1980.

37. Spangenberg, B.; Poole, C. F.; Wiens, C., *Quantitative Thin-Layer Chromatography: A Practical Survey*. Springer: New York, 2011.

38. Prosek, M.; Golc-Wondra, A.; Vovk, I., *J. Planar Chromatogr.* **2001,** *14*, 100.

39. Poole, C. F., *J. Planar Chromatogr.* **1988,** *1*, 373.

40. Sneh, O.; Wise, M. L.; Ott, A. W.; Okada, L. A.; George, S. M., *Surf. Sci.* **1995,** *334* (1-3), 135-152.

41. Li, X.; Ci, L.; Kar, S.; Soldano, C.; Kilpatrick, S. J.; Ajayan, P. M., *Carbon* **2007,** *45* (4), 847-851.

42. Bergna, H. E., Colloid Chemistry of Silica: An Overview. In *Colloidal Silica Fundamentals and Applications*, Bergna, H. E.; Roberts, W. O., Eds. Taylor & Francis Group: Boca Raton, 2006; Vol. 131, pp 9-35.

43. Kirkland, J. J.; Dilks Jr, C. H.; DeStefano, J. J., *J. Chromatogr. A* **1993,** *635* (1), 19-30.

44. Stella, C.; Rudaz, S.; Veuthey, J.; Tchapla, A., *Chromatographia* **2001,** *53* (0), S113-S131.

45. Park, J.; Ryu, Y.; Lim, H.; Lee, H.; Lee, Y.; Jang, M.; Suh, J.; Carr, P., *Chromatographia* **1999,** *49* (11), 635-642.

46. Hill, D. W.; Kind, A. J., *J. Liq. Chromatogr.* **1993,** *16* (18), 3941-3964.

47. Dolan, J. W., *LCGC Eur.* **2003,** *September*, 2-4.

48. Asenath Smith, E.; Chen, W., *Langmuir* **2008,** *24* (21), 12405-12409.

49. Zeng, X.; Xu, G.; Gao, Y.; An, Y., *J. Phys. Chem. B.* **2010,** *115* (3), 450-454.

50. Zhang, F.; Sautter, K.; Larsen, A. M.; Findley, D. A.; Davis, R. C.; Samha, H.; Linford, M. R., *Langmuir* **2010,** *26* (18), 14648-14654.

Chapter 6: Ozone Priming of Patterned Carbon Nanotube Forests for Subsequent ALD-Like Deposition of SiO_2 for the Preparation of Microfabricated Thin Layer Chromatography Plates*

6.1. Abstract

Herein, is reported the ozonation of patterned, vertically aligned carbon nanotube (CNT) forests as a method for priming them for subsequent pseudo atomic layer deposition (ψ-ALD) of silica to produce CNT-templated thin layer chromatography (TLC) plates. Gas phase ozonation simplifies the deposition scheme by replacing two steps in the previous fabrication process: chemical vapor deposition of carbon and ALD of Al_2O_3, with this much simpler priming step. Ozonation appears to prime/increase the number of nucleation sites on the CNTs by oxidizing them, thereby facilitating conformal growth of silica by ψ-ALD, where some form of priming appears to be necessary for this growth, i.e., as shown before ψ-ALD of SiO_2 onto unprimed CNTs is ineffective and leads to poor quality depositions. CNT oxidation as a function of exposure to ozone is monitored by X-ray photoelectron spectroscopy (XPS). After coating with SiO_2, the CNTs are removed via elevated temperature air oxidation, the SiO_2 is rehydrated, and the plates are coated with 3-aminopropyltriethoxysilane (APTES). The resulting APTES-coated plates separate various fluorescent dyes giving results that are generally at least as good as those we reported previously with our more complicated fabrication scheme. TLC plates with different geometries are microfabricated, where plates with narrower channels show longer run times (lower mobile phase velocities), and plates with narrower features appear to give higher efficiencies.

---

*This chapter has been submitted to (David S. Jensen, Supriya S. Kanyal, Andrew Miles, Robert C. Davis, Richard R. Vanfleet, Michael A. Vail, Andrew E. Dadson, and Matthew R. Linford) *J.Vac. Sci. Technol., B.* for review.

6.2. Introduction

Recently a publication on the microfabrication of TLC plates through the growth of patterned carbon nanotube (CNT) forests, their infiltration with silicon, and the simultaneous removal of the CNTs and conversion of the silicon to SiO_2 through high temperature air oxidation of the devices.[1] The resulting TLC plates showed reasonably good efficiencies (75,000 theoretical plates per meter, N/m) and fast run times. However, the oxidation of the silicon led to a volume expansion in the devices that distorted the features and complicated the chromatography. Distorted features would be expected to unfavorably raise the A term in the van Deemter equation, which is an important determinant of efficiency in chromatographic separations.[2, 3] In addition, controlling this distortion would probably be difficult in a manufacturing environment. Irregular solvent fronts due to constricted/distorted channels, which complicated the chromatography, were also observed on some of the TLC plates made with this method.

A second report[4] represented an effort to fix the problems noted above. In this study microfabricated TLC plates were prepared via a fast, conformal, pseudo atomic layer deposition (ψ-ALD) of SiO_2 onto carbon/alumina primed CNTs.[5] Priming of the CNTs appeared to be necessary for conformal ALD because of the low number of reactive sites on them. The resulting TLC plates did not show the volume expansion/distortion previously observed. After formation of a bonded layer using an aminosilane, higher efficiencies/lower plate heights than before (ca. 100,000 – 270,000 N/m, H_{obs} of ca. 1.6 – 7.7 μm), were observed. Nevertheless, the addition of two extra steps into the fabrication process was less than desirable, and there were disadvantages to both steps. The deposition temperature of the carbon was relatively high (900 °C), which would limit possible substrates, and ca. 100 ALD cycles of trimethylaluminum (TMA) and water were required for the Al_2O_3 priming layer.

Here is reported an improved and less complicated microfabrication of carbon nanotube (CNT) templated thin layer chromatography (TLC) plates. This simplification comes by using of ozone as a priming layer for the CNTs, which replaces the previous chemical vapor deposition of carbon and ALD of alumina as priming steps. Ozonation of the CNTs is straightforward. It simply consists of passing the gaseous reagent over the patterned CNT forests. The amount of surface oxygen, which increases with exposure to ozone and then plateaus, was monitored by X-ray photoelectron spectroscopy (XPS). Direct, conformal deposition of SiO_2 via ψ-ALD takes place on the O_3-primed CNTs. As was done previously, a bonded phase was prepared on this surface from 3-aminopropyltriethoxysilane to hide any aluminum (TMA is used to catalyze the ψ-ALD) and/or highly acidic silanols.[4] Using this improved process, we also microfabricate a few TLC plates with different hedge and channel widths.[1, 4] As expected, thinner channels show longer run times (slow down the mobile phase), and thinner features appear to lead to higher separation efficiencies.

Various groups have previously deposited different materials onto CNTs by ALD.[6-9] For example, to increase film conformality, George and coworkers primed CNTs with numerous alternating cycles of NO_2 and trimethylaluminum prior to ALD of Al_2O_3.[6] In our previous report,[4] carbon appeared to have been effective as an adhesion promoter/priming layer for CNTs because it increased the surface concentration of oxygen (presumably at defect/layer termination sites) from a concentration too low to measure by X-ray photoelectron spectroscopy (XPS) to ca. 1 at.%.[4] Accordingly, an even greater increase in the surface concentration of oxygen via ozonation might allow even more efficient ψ-ALD depositions of SiO_2. Indeed, ozone has previously been used to oxidize both single walled (SW) and multiwalled (MW) CNTs as confirmed by surface area measurements[10] and infrared spectroscopy.[11] Tang and coworkers used ozone to treat MWCNTs to increase their dispersibility in epoxide matrices.[12] Lu and coworkers used theoretical calculations to determine the energy barrier for ozonation of SWCNTs.[13] However, to date we are unaware of any report of the treatment/oxidation of CNTs with ozone for subsequent ALD.

This study is part of a continued effort on the part of various research groups to make new materials for thin layer chromatography. Merck introduced (but has subsequently withdrawn) the UTLC (ultrathin layer chromatography) plate, which was based on monolithic silica.[14-16] Recently, this concept was further investigated by Frolova et al. via a sol-gel synthesis.[17, 18] a variety of other authors created new TLC plates based on polymer monoliths,[19-21] Clark et al. has prepared them from electrospun polymers,[22, 23] and Bezuidenhout et al. has made them using glancing-angle deposition (GLAD).[24]

6.3 Experimental

6.3.1 Microfabrication and Ozone Treatment

Our microfabrication process, up to and including CNT growth, was reported by Jensen et al.[4] To increase the surface oxygen content of CNT forests for atomic layer deposition (ALD), a mild, room temperature treatment with ozone was performed. CNTs were ozonated with an Atlas 30 Ozone Generator (Absolute Ozone, Edmonton, Alberta) at an O_2 flow rate of ca. 6.7×10^{-6} m^3/s with the current set at 45%. Under these conditions ca. 4.4 g/h of ozone is produced. X-ray photoelectron spectroscopy (XPS), which was performed as described previously,[4] was used to determine the extent of oxidation of the CNTs as a function of time. Patterned CNT forests, which were to be used as templates for TLC plates, were loaded into a 1 in. OD fused silica tube that was purged with oxygen for 1 min, exposed to a flow of ozone for 45 min, and finally purged with oxygen for 1 min before removal. The exposure times recorded herein do not include this extra 1 min purge time. Plates prepared from four different masks were used in this study (see Table 6.1). In all cases, a general zig-zag pattern of features was used (see Scheme 6.1). All plates had 90° angles.

6.3.2 Atomic Layer deposition and CNT Removal

6.3.2.1 Pseudo Atomic Layer Deposition (ψ-ALD)

ψ-ALD of SiO_2 was performed using a Cambridge Fiji F200 system (Cambridge Nanotechnology, Cambridge, MA) with trimethylaluminum (97%, Sigma-Aldrich) and tris(*tert*-butoxy)silanol (99.999%, Sigma-Aldrich) as half reactants that were cycled in an ABAB type fashion. The deposition took place at 235 °C. Ten AB cycles that yielded ca. 7 nm SiO_2/cycle were performed to produce the SiO_2 films. This deposition rate is lower than was previously reported;[4] the deposition rate (nm/cycle) depended on the amount of precursor [tris(*tert-butoxy*)silanol] present in the reservoir of the deposition system, which varied between runs and was difficult to control. In spite of this difference in deposition rate, the same overall tube diameters (ca. 100 - 120 nm) and smooth features/morphologies, as determined by SEM, were obtained in this and the previous study,[4] and they appeared to have essentially the same, smooth morphology by SEM when deposited on well-primed CNTs. Film thicknesses were also monitored via spectroscopic ellipsometry (M-2000D, J.A. Woollam Co., Lincoln, NE) using witness silicon wafers.

Table 6.1 Feature dimensions, as entered into the CAD (computer-aided design) drawing program, of TLC plates microfabricated for this study. ‘(c)’ and ‘(a)’ are indicated in Scheme 6.1.

Plate Type	Hedge Width (c)	Channel Width (a)
I	3 µm	4.24 µm
II	3 µm	4.95 µm
III	3 µm	5.65 µm
IV	4 µm	4.95 µm

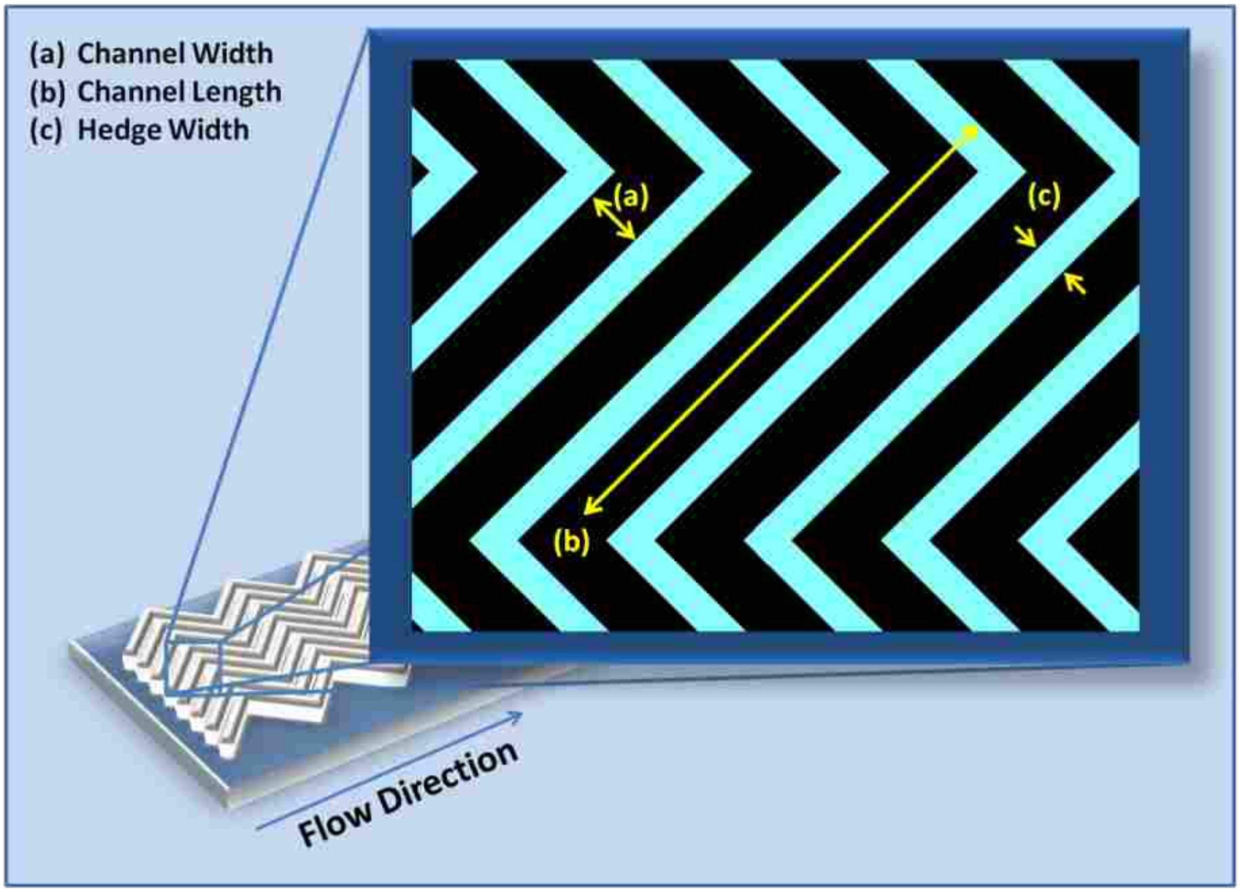

Scheme 6.1. Zig-zag geometry of microfabricated TLC plates. Plates differed in their channel and hedge widths. Dimensions of (a) and (c) given in Table 6.1. The hedge length (b) is 50 μm.

6.3.2.3 Removal of CNTs

CNTs were removed by air oxidation. Silica-coated CNTs were placed in a preheated (200 °C) bench top furnace (Thermolyne 6000 Furnace, Dubuque, IA) and heated to 600 °C at 1 °C/min. The material was held at this temperature for 17.33 h, for a total processing time of 24 h. The furnace was then cooled to 200 °C before removal of the samples.

6.3.3. Surface modification

6.3.3.1. Rehydration of SiO_2

Because the SiO_2 was subjected to temperatures above 200 °C, the surface needed to be repopulated with silanols.[25, 26] Accordingly, samples were immersed in a pH 10 NH_4OH etching solution for 18 h at room temperature, after which they were rinsed with deionized water to neutrality.[26]

6.3.3.2 Amino-functionalization[27]

TLC plates were coated with a ca. 1.5 nm film of 3-aminopropyltriethoxysilane (APTES) (≥ 98%, Sigma-Aldrich) as described previously.[4]

6.3.4. Chromatography

6.3.4.1 Separation of Fluorescent Dyes

A solution of two fluorescent dyes (sulfohrodamine B and rhodamine 6G) was prepared by dissolving the analytes in methanol at concentrations of ca. 10^{-7} M. A 1 µL volume of this solution was applied as a 3 mm x 0.7-0.8 mm band near the bottom of the TLC plates using a Linomat 5 spotter (CAMAG, Muttenz, Switzerland). The band was applied 5 mm from the bottom of the plate. The plate was then placed in a 10 x 10 cm twin trough chamber (CAMAG, Muttenz, Switzerland) and pre-equilibrated with the vapors of the developing solvent: 70:30:1 IPA/MeOH/LiCl (v/v/w) for 10 min. After pre-equilibration, 3 mL of the developing solvent was introduced at the bottom of the plate to commence chromatography. The immersion line was 2 mm above the bottom edge of the plate. The TLC plate was developed over a 30 mm distance from the application origin.

6.3.5. Visualization of Separated Dyes and Calculation of R_F, N, and H_{obs}

For detection of the fluorescent dyes, the TLC plate was exposed to short wavelength UV light (254 nm) (Model UVG-11 Mineralight Lamp, Ultra-Violet Products, San Gabriel, CA). TLC plates were imaged using a digital camera (Canon PowerShot S95, Canon USA, Lake Success, NY), and images were processed using ImageJ (ImageJ 1.42q, National Institutes of Health, USA).

Retention factors (R_F) were calculated using the following equation:

$$\boldsymbol{R_{\mathrm{F}}} = \frac{Z_o}{Z_f} \qquad (2)$$

where Z_o is the analyte migration distance from the application origin and Z_f is the distance the solvent front has traveled, also from the application origin. Chromatographic efficiencies were determined by the number of theoretical plates (N) according to:

$$\mathbf{N} = 16\left(\frac{Z_f R_{\mathrm{F}}}{W}\right)^2 \qquad (3)$$

where W is the width of the chromatographic band.[28]

Because of the changing mobile phase velocity in TLC, observed plate heights (H_{obs}) are a better way of reporting chromatographic efficiency:[29-33]

$$\boldsymbol{H_{obs}} = \frac{\sigma_{chrom}^2}{R_{\mathrm{F}}(Z_f - Z_o)} \qquad (4)$$

The value of σ^2_{chrom} in this equation is calculated from

$$\sigma^2_{\mathrm{obs}} = \sigma^2_{\mathrm{chrom}} + \sigma^2_{\mathrm{SA}} + \sigma^2_{\mathrm{INS}} \tag{5}$$

where σ^2_{obs} is the observed variance of the band after elution, σ^2_{SA} is the variance of the band at the spot application, and σ^2_{INS} is the variance of the densitometric measurement (a densitometer was not used, so $\sigma^2_{INS} = 0$ in Equation 5).[29, 32, 34] The value of σ^2_{SA} was determined from the initial width of the spot at application (0.7 mm), which was taken, as before,[4] as $5\sigma_{\mathrm{SA}}$, i.e., $\sigma^2_{SA} = 0.019_6$ mm^2 in our calculations. The widths of the bands after chromatography are similarly taken, also as before, as $5\sigma_{\mathrm{chrom}}$. Of course we recognize that the R_{F} values in this study are high and as such they do not fully represent the chromatographic abilities of the material – in general highest efficiencies are obtained at lower R_{F} values than those reported herein, although focusing of bands near the solvent front also occurs, which can artificially raise their efficiencies.[29] However, because chromatography often requires extensive method development to find conditions to separate sample mixtures efficiently and in desired R_{F} ranges, a large number of TLC plates would probably be required for such efforts. As discussed herein, our current microfabrication scheme is tedious, and we were unable to prepare enough TLC plates for thorough method development. Increased production of our TLC plates is one of our active aims. Nevertheless, the results reported herein do provide a measure of the quality of our plates, which appears to be high, and are, of course, comparable to the results from our previous study.

6.3.6. Microscopy

SEM images were captured with an FEI Helios Nanolab 600 (Hillsboro, OR).

6.4. Results and Discussion

6.4.1. Ozone Priming of CNTs for ψ-ALD Deposition and Microfabrication of TLC Plates.

Mild oxidation of CNTs was monitored as a function of exposure time to ozone on unpatterned CNT forests by X-ray photoelectron spectroscopy (XPS). XPS is a widely used and sensitive analytical technique for determining surface elemental compositions and oxidation states. Unpatterned CNT forests were used to ensure that no oxygen or silicon signals from the Si/SiO_2 substrate would complicate the XP spectra. Only carbon was observed in the XPS survey spectra of untreated CNTs,[35, 36] and the survey spectra of O_3-treated CNTs showed only carbon and oxygen. Unfortunately, it was difficult to control the concentration of ozone delivered by our ozone generator, although its concentration did appear to remain constant once it was operating. Accordingly, two experiments were performed on different days in which a series of unpatterned CNT forests were exposed to O_3 for different amounts of time. The percentages of oxygen on these materials were then measured by XPS (see Figure 6.1). At short times, the amount of oxygen increased quickly with time, and the surface concentration of oxygen then plateaued after about 20 min. Both sets of data were fit to a rising exponential function of the form $a(1 - e^{-t/\tau})$, but the fits were mediocre (R^2 values of 0.886 and 0.869). At this point, it seemed reasonable to account for the extra exposure time to O_3 that the CNTs experienced while the reaction tube was flushed with oxygen. Accordingly, the data were fitted to a function of the form $a(1 - e^{-t/\tau}) + b$. This function is not constrained to pass through the origin and contains an offset. The R^2 values for this function were much more acceptable (R^2 values of 0.977 and 0.965) (see fits in Figure 6.1).

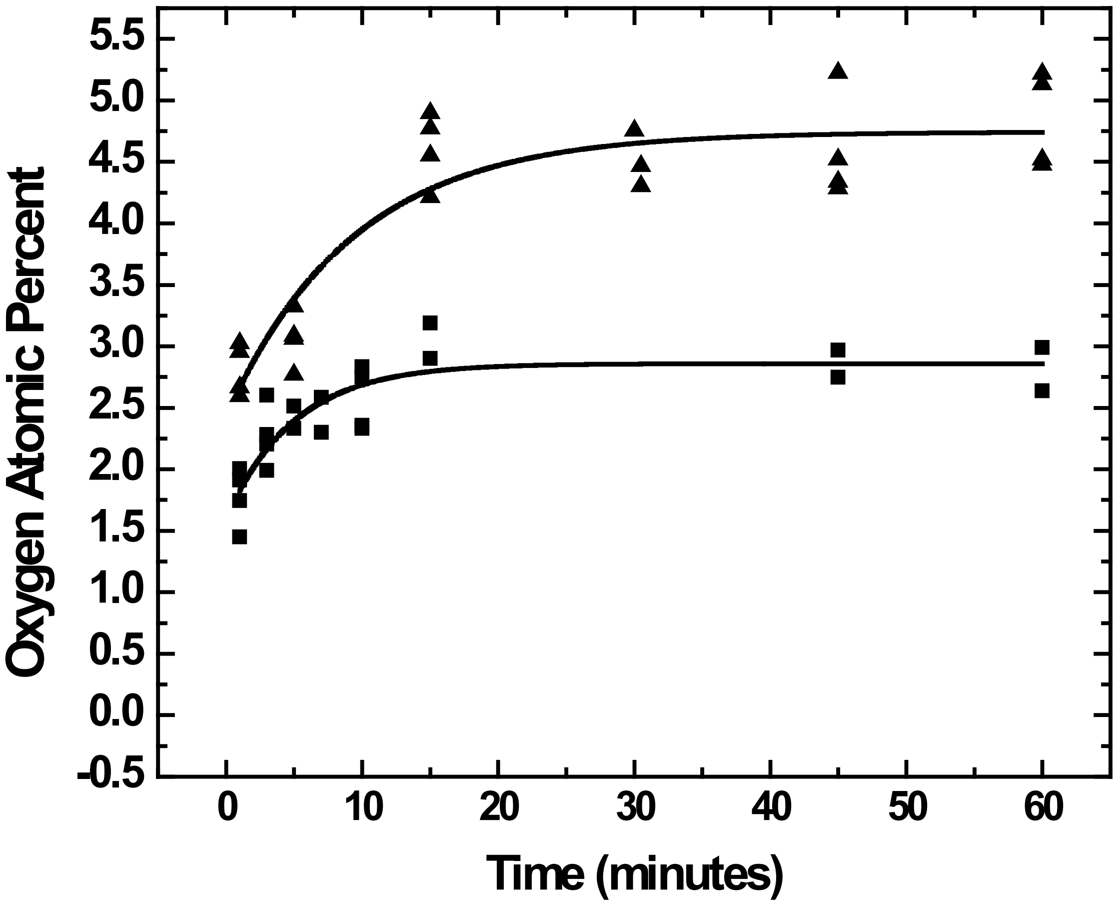

Figure 6.1 Atom % oxygen as a function of exposure time to ozone, as measured by XPS. The two different experiments are represented as either squares or diamonds. For the squares, R^2 = 0.977, a = 1.26, and b = 1.60. For the diamonds, R^2 = 0.9646, a = 2.31, and b = 2.43.

As shown in Figure 6.1, even a few minutes of exposure to ozone raised the surface concentration of oxygen on the CNTs to 2 – 3 atom% (at.%). This amount of oxygen is well above the ca. 0.8 at.% level introduced by our previous deposition of carbon by CVD, and which was believed to increase the number of nucleation sites on the CNTs – it appears that that the current ozonation of CNTs similarly increases the number of nucleation sites on this material.[4] Note that even though carbon (with 0.8 at.% oxygen) improved the ψ-ALD growth of SiO_2 onto CNTs, it was not entirely adequate as pearl-like (defective) features were still seen.[4] To determine the amount of oxygen needed for good SiO_2 coating by ψ-ALD, SiO_2 was deposited on CNT forests with a range of at.% values of oxygen, as previously measured by XPS. The resulting plates were evaluated by SEM for structural integrity and by a water immersion stability test (poor quality plates disintegrate in water).[4] From this study we determined that (i) ca. 2 at.% oxygen, with no other priming, was sufficient for reasonable and conformal ψ-ALD SiO_2 growth on CNTs, and (ii) above this threshold all ψ-ALD depositions of SiO_2 appear to be equally effective, i.e., no pearl-like features were present and plates were stable to immersion in water. To move to a region on the curves in Figure 6.1 that would clearly give at least 2 at.% oxygen, all growth experiments reported herein are based on a somewhat longer, but thorough, 45 min ozone exposure. This time of ozonation consistently led stable TLC plates that passed the water immersion test and gave good chromatographic results. Figure 6.2 is a representative SEM image of a CNT forest after adequate ozone treatment and ψ-ALD deposition of SiO_2, which shows the high degree of conformality of this process. Note that no pearl-like features are present in this image.

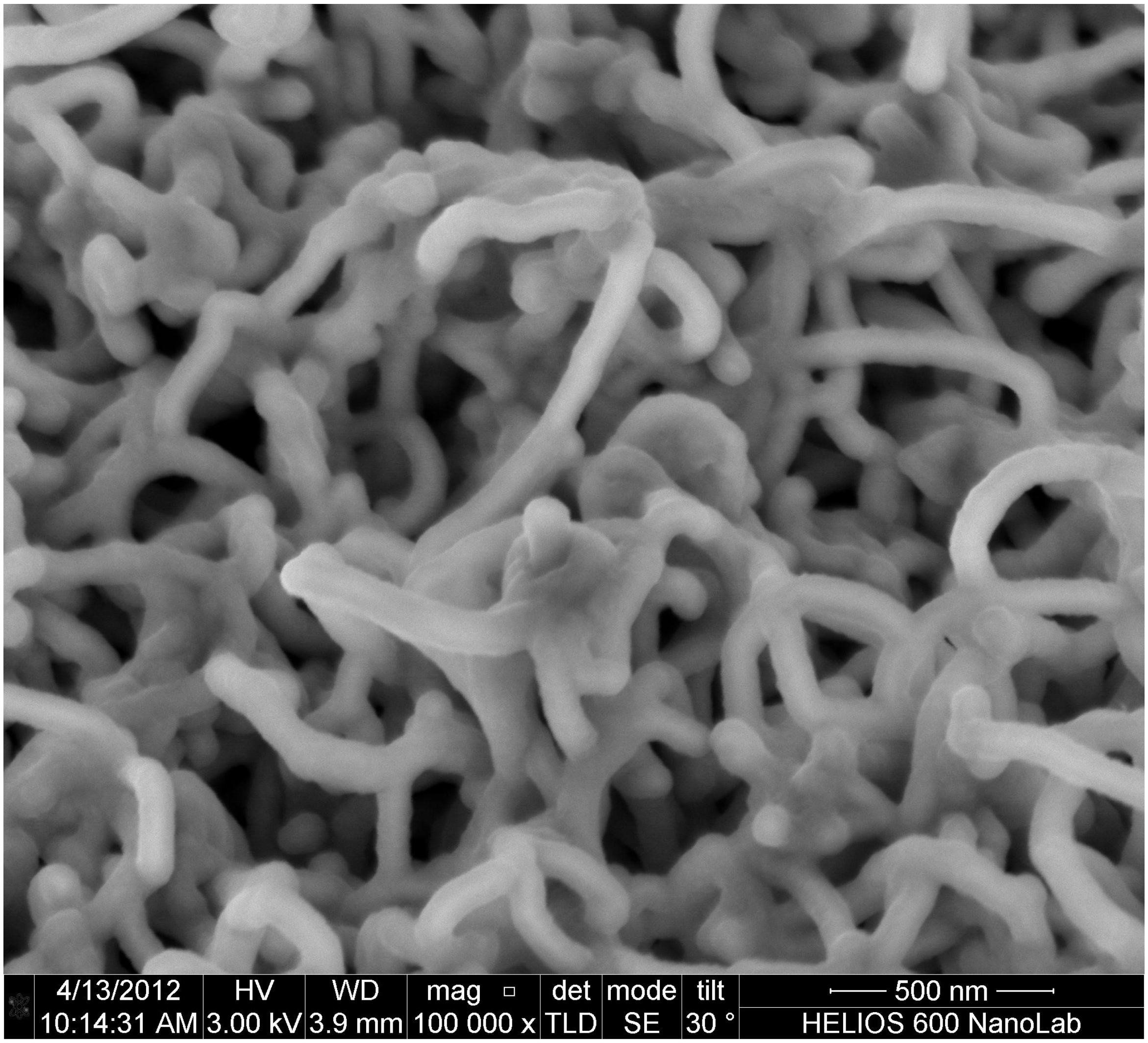

Figure 6.2 Top view of an ozone-primed CNT forest coated with SiO_2 by ψ-ALD.

6.4.2. Examples of Chromatography on Ozone-Primed Microfabricated TLC Plates.

We previously showed that the SiO_2 deposited by ψ-ALD onto primed CNTs contained strongly adsorbing sites that appeared to be present as a result of the TMA used in the deposition.[4] However, a thin film (ca. 1.5 nm) of 3-aminopropyltriethoxysilane (APTES) as a bonded phase on this material allowed good chromatography to take place. Accordingly, APTES was again used to cover/passivate the SiO_2 surface of the plates used in this study. To benchmark this study to our previous work[4] a separation of biological dyes was performed. The efficiencies of plates fabricated using the procedures described herein were higher than before, i.e., H_{obs} was often below the ca. 1.6 – 7.7 µm (above ca. 85,000 – 270,000 N/m) values obtained with our previous method. Figure 6.3 shows two separations of two fluorescent dyes on two APTES-coated plates with different geometries. In these separations, the separation distance was 30 mm and the development times were 2 min 20 s (Figure 6.3a) and 2 min and 45 s (Figure 6.3b). In Figure 6.3a the unretained compound had an H_{obs} of -0.6 µm (1,865,000 N/m), the H_{obs} for the band with an R_F of 0.93 was 0.3 µm (520,000 N/m), and the band with an R_F of 0.80 had an efficiency of 8.8 µm (80,000 N/m). In Figure 6.3b the unretained compound had an H_{obs} of -0.2 µm (830,000 N/m), the H_{obs} for the band with an R_F of 0.92 was 3.2 µm (164,000 N/m), and the band with an R_F of 0.85 had an efficiency of H_{obs} of 7.4 µm (87,000 N/m). For unretained compounds (R_F = 1), H_{obs} is hypothetical and represents the sample moving with the solvent front and not interacting with the stationary phase. It can be taken as the upper limit of chromatographic efficiency of the system.[29] As such, and because σ^2_{chrom} in Equation 5 is adjusted with σ^2_{SA}, the unretained chromatographic band has a zero or negative H_{obs} because the band is focused by the solvent front, i.e., the width of the band after development is smaller than the spot application width. Unfortunately, it is not possible to compare the H_{obs} values herein with any from the previous work[4] because no such unretained bands were observed. Table 6.2 gives the results of the separations on all the TLC plates we microfabricated. It is noteworthy that H_{obs} values in the range of 0.3 to 15.4 µm (58,000 – 520,000 N/m) are consistently obtained for the analytes. A reduction to lowered H_{obs} can be attribute in this work due to an improvement over the previous work,[4] which may be due to the simplification of the microfabrication scheme, i.e., with fewer fabrication steps on fewer pieces of equipment there is less heterogeneity introduced into the plates.

6.4.3. Effects of Channel and Hedge Width on Separations

The data in Table 6.2 provide an interesting opportunity to compare the development times of TLC plates with different channel widths. According to theory, the mobile phase velocity should decrease (increased development time) as channel width decreases.[30] Figure 6.4 is a plot of all the development times for all the plates we microfabricated vs. the channel widths of the different plates. While there is limited statistical data in this study, it does strongly suggest that development times increase with decreasing channel width as per the theory. From this limited data set the relationship appears linear. This is the first time we have reported a study of this important property of our TLC plates. To fully determine how development time depends on channel width, a more extensive study would be needed. Using our current research-directed production methods, it is relatively difficult for us to microfabricate our TLC plates. The work requires multiple pieces of equipment at two academic institutions, and has several limiting bottlenecks in the production process. Thus, it remains challenging for us to create a larger data set of chromatographic values.

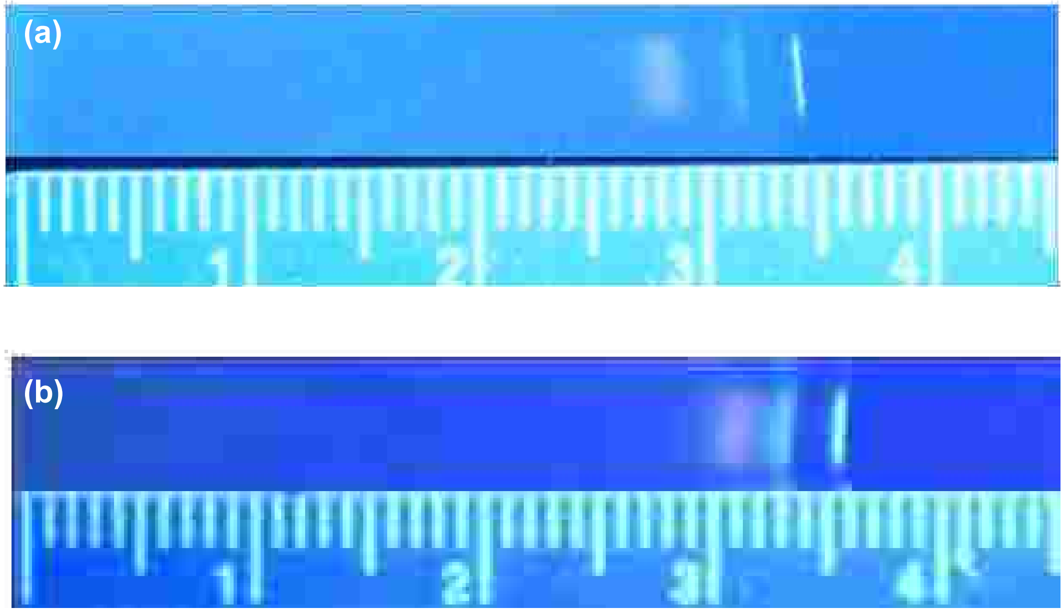

Figure 6.3 Separation of two fluorescent dyes (sulforhodamine B and rhodamine 6G) on (a) a Type II plate, and (b) a Type IV plate (see Table 6.1 for details of plate geometries). The developing solvent for these separations was 70:30:1 IPA/MeOH/LiCl. Separation distances were 30 mm. Development times, R_F values, and efficiencies are in the text.

Table 6.2 R_F values, chromatographic efficiencies (H_{obs} values in μm), and development times for TLC plates microfabricated with different geometries (Type I-IV plates, see Table 6.1). All development distances were 30 mm. Two of the images corresponding to these separations are shown in the text.

Type I		Type I		Type II	
R_F	Plate Height (μm)	R_F	Plate Height (μm)	R_F	Plate Height (μm)
1.00	-0.3	1.00	-0.5	1.00	-0.5
0.89	2.3	0.90	0.4	0.91	1.8
0.75	10.5	0.77	6.9	0.80	8.5
Development Time		Development Time		Development Time	
2 min 55 s		3 min 01 s		2 min 18 s	

Type II (Fig. 3a)		Type II		Type III	
R_F	Plate Height (μm)	R_F	Plate Height (μm)	R_F	Plate Height (μm)
1.00	-0.6	1.00	-0.3	1.00	-0.4
0.93	0.3	0.90	1.1	0.89	5.5
0.80	8.8	0.80	7.2	0.73	13.8
Development Time		Development Time		Development Time	
2 min 26 s		2 min 20 s		2 min 11 s	

Type IV		Type IV (Fig. 3b)	
R_F	Plate Height (μm)	R_F	Plate Height (μm)
1.00	-0.2	1.00	-0.2
0.93	2.1	0.92	3.2
0.85	6.8	0.85	7.4
Development Time		Development Time	
2 min 45 s		2 min 45 s	

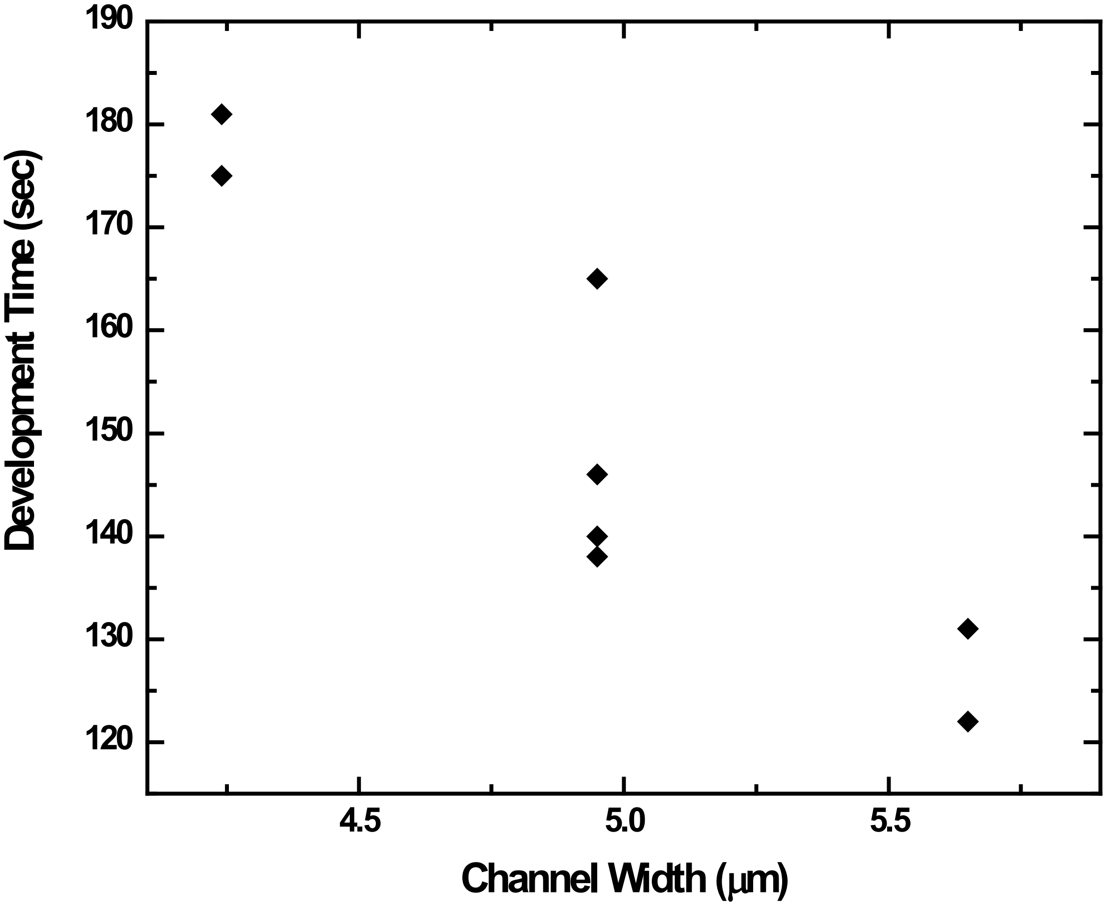

Figure 6.4 Development time vs. channel width for microfabricated TLC plates.

Additionally, the limited chromatographic efficiencies presented in Table 6.2 suggest, or are at least not inconsistent with the notion, that larger chromatographic features give larger values of H_{obs}, i.e., poorer efficiencies. This result is also chromatographically reasonable, and we hope to follow up on this issue as well in the future.

6.5. Conclusions

Oxidation of carbon nanotube (CNT) forests using ozone effectively primes them for subsequent deposition of SiO_2 by ψ-ALD. Ozonation is a relatively simple process that replaces two more complicated steps in our previous microfabrication of TLC plates.[4] The resulting TLC plates perform very well chromatographically – we show plates with higher efficiencies than any we have prepared to date, and a maximum efficiency for an unretained compound of -0.6 μm (1,865,000 N/m). Furthermore, the presented channel width study demonstrates, as expected, that the mobile phase velocity is higher on plates with wider channels. A limited study of channel and hedge width is consistent with wider hedges and channels resulting in less efficient separations.

6.6. Acknowledgments

We thank Diamond Analytics, a US Synthetic Corp. company (Orem, UT), for funding this study. Author contributions: D.J. Concieved the idea of ozone priming CNTs, did the ALD, chromatography and microscopy. S.K. and A.M. fabricated the devices up to and including CNT growth. R.D., R.V., M.V. and A.D. helped direct the research. M.L. was the principle investigator of the project. The manuscript was written by D.J. and M.L.

6.7. References

1. Song, J.; Jensen, D. S.; Hutchison, D. N.; Turner, B.; Wood, T.; Dadson, A.; Vail, M. A.; Linford, M. R.; Vanfleet, R. R.; Davis, R. C., *Adv. Funct. Mater.* **2011,** *21* (6), 1132-1139.

2. Billen, J.; Desmet, G., *J. Chromatogr. A* **2007,** *1168* (1-2), 73-99.

3. John H, K., *J. Chromatogr. A* **1999,** *831* (1), 3-15.

4. Jensen, D. S.; Kanyal, S. S.; Gupta, V.; Vail, M. A.; Dadson, A. E.; Engelhardt, H.; Vanfleet, R.; Davis, R. C.; Linford, M. R., *J. Chromatogr. A* **2012**.

5. Hausmann, D.; Becker, J.; Wang, S.; Gordon, R. G., *Science* **2002,** *298* (5592), 402-406.

6. Cavanagh, A. S.; Wilson, C. A.; Weimer, A. W.; George, S. M., *Nanotechnol.* **2009,** *20* (25), 255602.

7. Herrmann, C. F.; Fabreguette, F. H.; Finch, D. S.; Geiss, R.; George, S. M., *Appl. Phys. Lett.* **2005,** *87* (12), 2053358-2053360.

8. Farmer, D. B.; Gordon, R. G., *Electrochem. Solid-State Lett.* **2005,** *8* (4), G89-G91.

9. Farmer, D. B.; Gordon, R. G., *Nano Lett.* **2006,** *6* (4), 699-703.

10. Byl, O.; Liu, J.; Yates, J. T., *Langmuir* **2005,** *21* (9), 4200-4204.

11. Mawhinney, D. B.; Naumenko, V.; Kuznetsova, A.; Yates, J. T.; Liu, J.; Smalley, R. E., *Journal of the American Chemical Society* **2000,** *122* (10), 2383-2384.

12. Tang, L.-c.; Zhang, H.; Han, J.-h.; Wu, X.-p.; Zhang, Z., *Composites Science and Technology* **2011,** *72* (1), 7-13.

13. Lu, X.; Zhang, L.; Xu, X.; Wang, N.; Zhang, Q., *J. Phys. Chem. B* **2002,** *106* (9), 2136-2139.

14. Hauck, H. E.; Schulz, M., *J. Chromatogr. Sci.* **2002,** *40* (10), 550-552.

15. Hauck, H.; Schulz, M., *Chromatographia* **2003,** *57* (0), S313-S315.

16. Hauck, H.; Bund, O.; Fischer, W.; Schulz, M., *J. Planar Chromatogr.--Mod. TLC* **2001,** *14* (4), 234-236.

17. Frolova, A. M.; Chukhlieb, M. A.; Drobot, A. V.; Kryshtal, A. P.; Loginova, L. P.; Boichenko, A. P., *Open Surf. Sci. J.* **2009,** *1*, 40-45.

18. Frolova, A. M.; Konovalova, O. Y.; Loginova, L. P.; Bulgakova, A. V.; Boichenko, A. P., *J. Sep. Sci* **2011,** *34* (16-17), 2352-2361.

19. Urbanova, I.; Svec, F., *J. Sep. Sci.* **2011,** *34* (16-17), 2345-2351.

20. Han, Y.; Levkin, P.; Abarientos, I.; Liu, H.; Svec, F.; Fréchet, J. M. J., *Anal. Chem.* **2010,** *82* (6), 2520-2528.

21. Bakry, R.; Bonn, G. K.; Mair, D.; Svec, F., *Anal. Chem.* **2006,** *79* (2), 486-493.

22. Clark, J. E.; Olesik, S. V., *J. Chromatogr., A* **2010,** *1217* (27), 4655-4662.

23. Clark, J. E.; Olesik, S. V., *Anal. Chem.* **2009,** *81* (10), 4121-4129.

24. Bezuidenhout, L. W.; Brett, M. J., *J. Chromatogr., A* **2008,** *1183* (1–2), 179-185.

25. Bergna, H. E.; Roberts, W. O., *Colloidal silica: fundamentals and applications*. Taylor & Francis Group: Boca Raton, 2006; Vol. 131.

26. Köhler, J.; Kirkland, J. J., *J. Chromatogr. A* **1987,** *385* (0), 125-150.

27. Zhang, F.; Sautter, K.; Larsen, A. M.; Findley, D. A.; Davis, R. C.; Samha, H.; Linford, M. R., *Langmuir* **2010,** *26* (18), 14648-14654.

28. Poole, C. F.; Poole, S. K., *Anal. Chem.* **1989,** *61* (22), 1257A-1269A.

29. Poole, S. K.; Poole, C. F., *J. Chromatogr. A* **2011,** *1218* (19), 2648-2660.

30. Poole, C. F., *The Essence of Chromatography*. 2003.

31. Bertsch, W.; Hara, S.; Kaiser, R. E.; Zlatkis, A., *Instrumental HPTLC*. Huethig, 1980.

32. Spangenberg, B.; Poole, C. F.; Wiens, C., *Quantitative Thin-Layer Chromatography: A Practical Survey*. Springer: New York, 2011.

33. Prosek, M.; Golc-Wondra, A.; Vovk, I., *J. Planar Chromatogr.* **2001,** *14*, 100.

34. Poole, C. F., *J. Planar Chromatogr.* **1988,** *1*, 373.

35. Jensen, D. S.; Kanyal, S. S.; Engelhard, M.; Linford, M. R., *Submitted to Surf. Sci. Spectra*

2012, - (-), -.

36. Jensen, D. S.; Kanyal, S. S.; Handcock, J. M.; Vail, M. A.; Dadson, A. E.; Shutthanandan, V.; Zhu, Z.; Vanfleet, R.; Engelhard, M.; Linford, M. R., *Submitted to Surf. Interface Anal.* **2012,** - (-),

Chapter 7: Multi-Instrument Characterization of the Surfaces and Materials in Micro-fabricated, Carbon Nanotube-Templated Thin Layer Chromatography Plates. An Analogy to 'The Blind Men and the Elephant'*

7.1 Abstract

Herein apply a suite of analytical tools was used to characterize materials created in the production of microfabricated thin layer chromatography plates. Techniques used include XPS, valence band spectroscopy, ToF-SIMS in both positive and negative ion modes, RBS, and helium ion microscopy (HIM). Materials characterized include: the Si(100) substrate with native oxide: Si/SiO_2, alumina (35 nm) deposited as a diffusion barrier on the Si/SiO_2: Si/SiO_2/Al_2O_3, iron (6 nm) thermally evaporated on the Al_2O_3: Si/SiO_2/Al_2O_3/Fe, the iron film annealed in H_2 to make Fe catalyst nanoparticles: Si/SiO_2/Al_2O_3/Fe(NP), and carbon nanotubes (CNTs) grown from the Fe nanoparticles: Si/SiO_2/Al_2O_3/Fe(NP)/CNT. The Fe thin films and nanoparticles are found in an oxidized state. Some of the analyses of the CNTs/CNT forests reported appear to be unique: the CNT forest appears to exhibit an interesting 'channeling' phenomenon by RBS, we observe an odd-even effect in the ToF-SIMS spectra of C_n^- species for n = 1 – 6, with ions at even n showing greater intensity than their neighboring odd n signals and ions with $n \geq 6$ showing a steady decrease in intensity, and valence band characterization of CNTs using X-radiation is reported. The information obtained from the combination of the different analytical tools provides a more complete understanding of our materials than a single technique, which is analogous to the story of 'The Blind Men and the Elephant'. The raw XPS and ToF-SIMS spectra from this study will be submitted to Surface Science Spectra for archiving.

*This chapter is reproduced with permission from (David S. Jensen, Vipul Gupta, Rebecca E. Olsen, Alex T. Miller, Robert C. Davis, Daniel Ess, Zihua Zhu, Michael A. Vail, Andrew Dadson, Matthew R. Linford) *J. Chromatogr., A.* **2011**, *1218* (46), 8362-8369. Copyright 2011 Elsevier B.V.

7.2. Introduction

Multi-Instrument Characterization of Materials

Clearly many researchers recognize the importance of employing multiple analytical techniques to characterize surfaces and materials.[1] However, to better understand the degree to which this message is being put into practice, we selected 13 papers from nine research groups on the topic of surface modification of hydrogen-terminated, porous, and scribed silicon with carbon-carbon double bond containing reagents.[2-14] This is an area in which one of us (MRL) has published.[14-21] All of the functionalized surfaces/materials synthesized in these studies are expected to exhibit considerable complexity.

Table 7.1 lists the techniques that were used to analyze these new materials and the number of papers that reported the use of each technique. It comes as little surprise that XPS and FTIR were first followed by wetting, ellipsometry, and SEM. Some of the techniques are also fairly specialized and would not apply to many materials. Nevertheless, the key messages for this work are that (i) half of the papers in this admittedly incomplete survey of the materials literature characterized their *new* materials using three techniques or fewer (one paper used only one analytical technique and two used only two), and (ii) not one of these techniques, as powerful as they are, provides a complete picture of the complexity of these materials. Thus, this glance at the literature suggests that the message of more thorough materials analysis through a broader use of analytical tools could be applied to a greater extent. Note also that the average number of techniques applied per paper drops from 3.5 to 3.2 when the 2 papers from our research group are omitted. This view of things is also consistent with our experience with materials synthesis and characterization: it is not terribly uncommon to find reports in the literature that employ only one or two analytical methods to characterize new materials.

Table 7.1 Number of uses of various characterization techniques in 13 studies on the functionalization of silicon with carbon-carbon double bond containing reagents.

Technique	Number of Times Employed in 13 Studies
XPS	9
FTIR	9
Wetting	5
Ellipsometry	5
SEM	5
AFM	3
ToF-SIMS	3
Photoluminescence	3
HREELS	1
X-ray Reflectivity	1
Photoconductivity Decay	1
Total Number of Uses of These Methods	45
Average Number of Techniques Employed Per Paper	3.5

Herein a focus on the synergistic nature of the data obtained from multiple materials analytical techniques, where the information gleaned from the combination of techniques is clearly greater than that from an individual method. Recently, we recognized an analogy between probing materials with different analytical techniques and the proverbial story of *The Blind Men and the Elephant*.[22] In this old parable from India each member of a group of blind men approaches and then touches a different part of an elephant: the tail, flank, leg, ear, tusk, and trunk. Having experienced the animal in different ways, they then argue whether the elephant is like a rope, wall, pillar, fan, spear, or thick tree branch, respectively. Obviously the combined information from the blind men provides a much more complete view of the elephant than any one experience.

Analytical Techniques Used in this Work

Herein the following suite of analytical tools was used to characterize the series of materials created in the production of microfabricated thin layer chromatography (TLC) plates:[23,24]

X-ray photoelectron spectroscopy (XPS) probes ca. 10 nm into materials, where the typical mean free path of a photoelectron in a typical solid is ca. 3 nm. XPS is a core electron spectroscopy. Survey (wide) scans reveal the elements present in samples.[25] Oxidation state information is obtained from narrow scans. XPS is sensitive to ca. 0.1 – 1% of a monolayer and is quantitative to semi-quantitative. Other information is sometimes available, e.g., angle resolved XPS can give film thicknesses and analysis of complete line shapes provides information about surface morphology.[26-29] Auger, plasmon loss, and $\pi \rightarrow \pi^*$ signals may be present.

Valence band (VB) spectroscopy probes the valence bands of materials. While these spectra may be complex, they provide unique signatures for materials and can be sensitive to their chemical states. Metals and insulators are quite easily distinguished. VB spectra may be collected using the X-radiation from X-ray photoelectron spectrometers.

Static time-of-flight secondary ion mass spectrometry (ToF-SIMS) is sensitive to the outer few nanometers of materials.[30] Surface sensitivity and yield of large organic ions are increased by the use of cluster ions, e.g., Bi_3^{2+}, as opposed to monatomic, e.g., Ga^+, primary ions. In general, ToF-SIMS provides more *chemical* information about surfaces, especially organic surfaces, than XPS, yielding characteristic positive and negative secondary ions. Detection limits are often much lower than for XPS, especially for easily ionized species, e.g., metals in positive ion mode and highly electronegative species in negative ion mode. ToF-SIMS suffers from a strong matrix effect and quantitation is often difficult. It can be an effective imaging and depth profiling tool.

Rutherford backscattering spectroscopy (RBS) uses an energetic ion beam (1 – 3 MeV, typically He^+) to probe tens to hundreds of nanometers into samples. Energies and intensities of backscattered ions give the identities and concentrations, respectively, of elements. It shows relatively low sensitivity for lighter elements and for ultrathin films. This technique is particularly effective for films of heavier atoms on substrates of lighter atoms.

Helium ion microscopy (HIM) uses energetic helium ions as the imaging particles. It has a resolution advantage over scanning electron microscopy (SEM) because of the shorter de Broglie wavelength of helium compared to that of electrons; diffraction effects are negligible, increasing the resolving power of the technique.[31]

Microfabrication of Thin Layer Chromatography Plates

Recently a microfabrication of a new type of thin layer chromatography (TLC) plate based on patterned, carbon nanotube templates has been demonstrated.[23, 24] It is believed that these devices will offer the end user faster separations at higher resolution (efficiency), and with better reproducibility. To produce these plates, a thin film of alumina (35 nm) is first deposited on a silicon wafer. A thin (6 nm) film of iron is then thermally evaporated onto the alumina, and the iron is annealed in H_2 to make Fe catalyst nanoparticles.[7-9] The alumina acts as a barrier layer to prevent iron silicide formation, which represents a poisoning of the iron catalyst.[32-34] Carbon nanotubes (CNTs) are grown from the Fe nanoparticles, and the resulting CNT forest provides a template for deposition of an inorganic material upon which chromatography is performed.[24, 35, 36] The sp^2 carbon in the CNTs is quite inert, so it is advantageous to improve adhesion to them by priming/activating them. Which has been previously done[23] by chemical vapor deposition (CVD) of carbon, followed by atomic layer deposition (ALD) of alumina.[10-12] The primed CNTs are then coated with a relatively thick layer of SiO_2 via a pseudo (ψ) ALD process.[37] In this paper a multi-technique characterization of the basic, initial layers needed for this micrfabrication: Si/SiO_2, $Si/SiO_2/Al_2O_3$, $Si/SiO_2/Al_2O_3/Fe$, $Si/SiO_2/Al_2O_3/Fe(NP)$, and $Si/SiO_2/Al_2O_3/Fe(NP)/CNT$ is presented.

7.3. Experimental

Materials were fabricated according to our previous reports.[23] Accordingly, Si(100) wafers (University Wafers, South Boston, MA, dopant free) were coated with a thin film (35 nm) of Al_2O_3 via e-beam evaporation (Benton Vacuum E-beam Evaporator, Moorestown, NJ). Onto the Al_2O_3 film, Fe (6 nm) was deposited via thermal evaporation (cryopumped, home-built apparatus), where Fe is the catalytic material for CNT growth.[24] The Fe is annealed in H_2 at 750 °C to create Fe nanoparticles,[38-40] and the CNTs are grown from the Fe nanoparticles at 750 °C with argon, hydrogen and ethylene as process gases.

X-ray photoelectron spectroscopy (XPS) and valence band spectroscopy (VBS) were performed on bare Si (100) wafers, 35 nm films of Al_2O_3, Fe films, H_2-annealed Fe, and CNTs. This work was performed at the Pacific Northwest National Laboratory (PNNL) in the Environmental Molecular Sciences Laboratory (EMSL) using a Physical Electronics Quantera Scanning X-ray Microprobe. This system uses a focused, monochromatic Al Kα X-ray (1486.7 eV) source for excitation, a spherical section analyzer, and a 32 element multichannel detection system. A 98 W X-ray beam focused to 100 μm (diameter) was rastered over a 1.3 mm x 0.1 mm rectangle on the sample. The X-ray beam is at normal incidence to the sample and the photoelectron detector is at 45° off-normal. High energy resolution spectra were collected using a pass-energy of 69.0 eV with a step size of 0.125 eV. For the Ag $3d_{5/2}$ line, these conditions produced a FWHM of 1.2 eV. All samples were analyzed as received. All XPS spectra were charge referenced to the maximum in the carbon C 1s narrow scan, taken as 285.0 eV.

Static time-of-flight secondary ion mass spectrometry (ToF-SIMS) was performed on bare Si (100) wafers, 35 nm films of Al_2O_3, Fe films, H_2-annealed Fe films, and CNTs. These analyses were performed at EMSL/PNNL using an ION-TOF V instrument (Münster, Germany) with a 50 keV Bi_3^{2+} cluster ion source, 10kHz, and a sample area of 200 μm^2. All samples were analyzed as received. The ratios of the F^- signals to the highest signal in the spectrum reported in the Discussion are the averages from two spots on the same sample. The standard deviations for these numbers are equal to or less than 0.001.

Rutherford backscattering spectroscopy (RBS) was performed at EMSL/PNNL on bare Si(100) wafers, 35 nm films of Al_2O_3, Fe films, H_2-annealed Fe films, and CNT forests. All samples were analyzed as received. For RBS measurements, a 2.0 MeV Helium ion beam was used and the backscattered He^+ ions from the targets were collected at a scattering angle of 96°. RBS experimental data were then fitted to a theoretical model using the SIMNRA simulation code. This code utilizes known RBS cross-sections and experimental parameters.

Helium ion microscopy (HIM) was performed on a Zeiss Orion Plus Helium Ion Microscope (Oberkochen, Germany) at EMSL/PNNL on Fe, H_2-annealed Fe, and CNT forests. HIM is very similar to SEM, but it uses He ions as a probing beam compared to electrons. The incident He^+ beam was set at normal direction and energized to 25 keV. The secondary electrons generated from the sample surface during the He ion-sample interaction were collected using a Everhart and Thornley (ET) detector.

7.4. Results

The characterization of the materials used to prepare our new microfabricated TLC plates is organized below according to material and not analytical technique.

7.4.1. The Si/SiO_2 Substrate

The XPS survey spectrum of the silicon wafer (Figure 7.1a) shows the expected silicon (2p and 2s) and oxygen (1s, 2s, and Auger) signals. The rise in the baseline from *ca.* 100 – 200 eV is due to inelastically scattered electrons. Small amounts of three surface contaminants: carbon, fluorine, and nitrogen, are present. Adventitious hydrocarbon is found on almost all samples so the presence of a small C 1s signal as a single peak (no sign of chemically shifted carbon) is reasonable. A correspondingly small carbon Auger signal is also present. Etches containing ammonia and HF are common in the semiconductor industry, which may explain the presence of N and F. A narrow scan of the Si 2p region (Figure 7.1a) reveals two peaks centered at 100.0 eV and 103.9 eV that correspond to bulk silicon and the thin silicon dioxide upper layer, respectively. The thickness of the native oxide (SiO_2), t_{ox}, was estimated from the two Si 2p signals using the following equation.[41, 42]

$$t_{ox} = \lambda_{SiO_2} sin\theta ln\left\{\left[\left({}^{1}/_{\beta}\right)\left(I_{SiO_2}/I_{Si}\right)\right] + 1\right\} \qquad (1)$$

where λ_{SiO2} is the inelastic mean free path (IMFP or attenuation length) of the Si 2p electrons in SiO_2, θ is the photoelectron take-off angle of the analyzer, $\beta = I_{SiO_2}^{\infty}/I_{Si}^{\infty}$ (I is the 2p intensity for infinitely thick SiO_2 and Si materials), and I_{SiO_2}/I_{Si} is the ratio of peak areas from the unknown film. Values of the IMFP for SiO_2 and β were taken as 2.7 ± 0.2 nm and 0.83, respectively,[43] which gave an SiO_2 thickness of 1.18 ± 0.09 nm (n = 4, i.e., average of four measurements). The valence band spectrum (VBS) of our Si/SiO_2 substrate (see Figure 7.1a) is similar to literature VB spectra of silicon wafers with ca. 1 nm of SiO_2.[44-48]

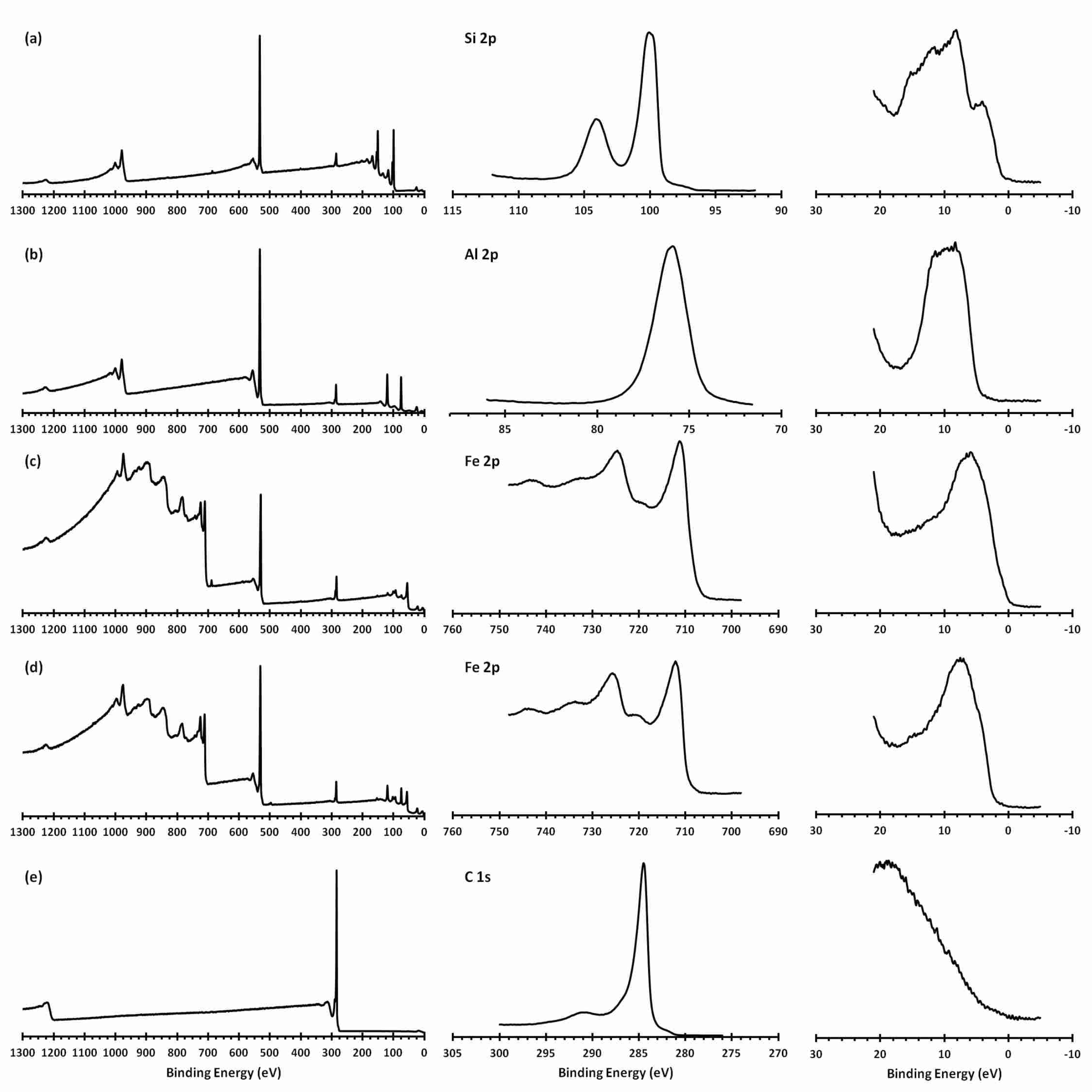

Figure 7.1 Left: XPS survey scans. Middle: Narrow scans of selected regions from the survey spectra. Right: Valence band spectra. Materials include: (a) Si (100) wafer, (b) e-beam evaporated Al_2O_3 (35 nm) on SiO_2, (c) thermally evaporated Fe (6 nm), (d) 6 nm Fe thermally annealed in H_2, and (e) CNT forest. Key peaks (peak positions taken from the survey spectra) in each survey spectrum include: (a) 25 eV O 2s, 99 eV Si 2p, 150 eV Si 2s, 285 eV C 1s, 532.5 eV O1s, F 1s 687 eV, 979 eV O KLL, and 1225 eV C KLL. (b) 24 eV O 2s, 74.5 eV Al 2p, 119 eV Al 2s, 285 eV C 1s, 531.5 eV O1s, 978.5 eV O KLL, and 1223.5 eV C KLL. (c) 22.5 eV O 2s, 56 eV Fe 3p, 75 eV Al 2p, 93.5 eV Fe 3s, 101 eV Si 2p, 119.5 eV Al 2s, 152.5 eV Si 2s, 285 eV C 1s, 530 eV O1s, 689.5 eV F 1s, 711 eV Fe $2p_{1/2}$, 725 eV Fe $2p_{3/2}$, 788.5, 845.5 and 897.5 eV Fe LMM, 975 eV O KLL, and 1224.5 eV C KLL. (d) 22.5 eV O 2s, 56 eV Fe 3p, 74 eV Al 2p, 94 eV Fe 3s, 99.5 eV Si 2p, 119 eV Al 2s, 153 eV Si 2s, 285 eV C 1s, 530.5 eV O1s, 711 eV Fe $2p_{1/2}$, 724.5 eV Fe $2p_{3/2}$, 783.5, 843 and 897 eV Fe LMM, 975 eV O KLL, and 1226 eV C KLL. (e) 285 eV C1s, and 1222 eV C KLL.

Rutherford backscattering (RBS) of the silicon wafer showed a single step towards lower channel number (energy) (see Table 7.2 and Figure 7.2). The signal at the step edge represents unattenuated, backscattered He^+ from the silicon-air interface. The signal at increasingly lower channel numbers (energy) corresponds to He^+ backscattered (and attenuated) from increasingly deep within the material. RBS is usually insensitive to ultrathin (ca. 1 nm) light element films, and the oxygen signal from the SiO_2 is not apparent. The detection of a small amount of oxygen is further complicated because it is lighter than Si and so will fall on the silicon step, creating a small signal on a large background. Thus, RBS can only confirm the presence of silicon on the Si/SiO_2 substrate. However, its usefulness will become apparent for the Al_2O_3, Fe, and CNT films.

For greater surface sensitivity and increased chemical information, time-of-flight secondary ion mass spectrometry (ToF-SIMS) was used. The positive ion spectrum showed a series of mass fragments separated by ca. 14 amu, as is expected from hydrocarbons, i.e., CH_x^+, $C_2H_x^+$, $C_3H_x^+$, $C_4H_x^+$, etc. These signals are consistent with the adventitious carbon predicted by the XPS analysis. A noticeable peak corresponding to ammonium, NH_4^+, is also present. This signal can also be related back to the XPS spectrum, which showed a small nitrogen peak (ca. 0.5 at.%). SIMS also helps us understand what is not present on these surfaces. For example, it is clear that the adventitious hydrocarbon is not rich in aromatic (benzyl) units, which would produce the tropylium ion at m/z 91 (this signal is not strong). The sample was also free of contamination from aluminum (Al^+), calcium (Ca^+), and iron (Fe^+), while sodium (Na^+) and a trace of potassium (K^+) were present. Finally, the positive ion spectrum showed the expected $^{28}Si^+$, $^{29}Si^+$, and $^{30}Si^+$ signals in their expected isotopic ratios.

Table 7.2 RBS values for the spectra presented in Figure 7.2.

sample #			
		Thickness (1 x 10^{15} atoms/cm^2)	Composition (atomic %)
3	Si	100000	Si: 100 %
6	Al_2O_3	200	Al: 40% O: 60%
	Si	100000	Si: 100 %
9	Fe Film	36	Fe: 45% O: 55%
	Al_2O_3	200	Al: 40% O: 60% Fe: 0.1%
	Si/SiO_2	2	Si: 34% O: 66%
	Si	100000	Si: 100%
12	H_2 Annealed Fe	36	Fe: 45% O: 50% Cl: 3% P: 2%
	Al_2O_3	200	Al: 37% O: 60.09% Fe: 0.1% Si: 2%
	SiO_2	10	Si: 34% O: 66%
	Si	100000	Si: 100%

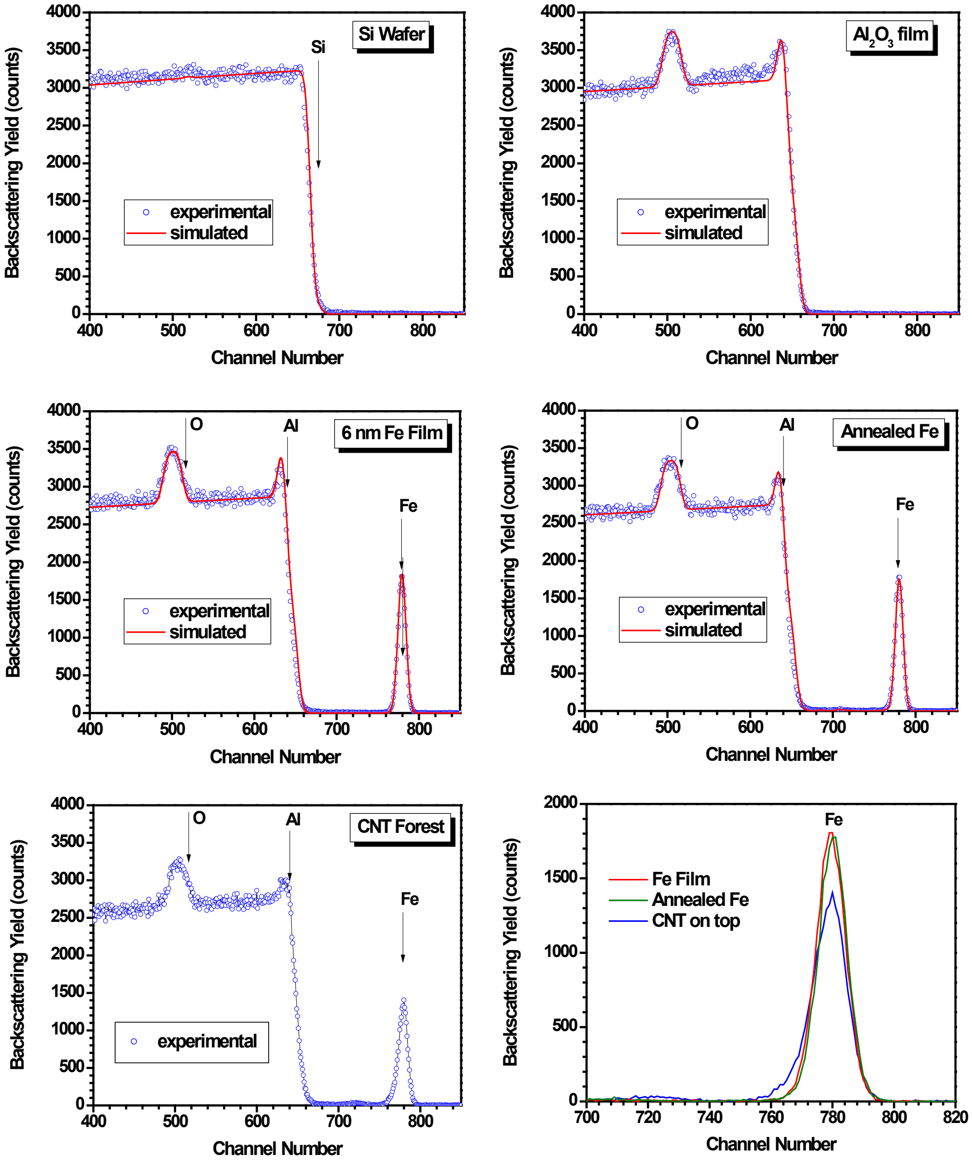

Figure 7.2 RBS spectra (from left to right, top to bottom): Si wafer, Al_2O_3 film (35 nm), 6 nm Fe film, annealed Fe film, and CNT forest. The silicon edge is located at ca. channel number 650. The last spectrum (bottom right) is an overlay of the Fe peak from Fe film, Fe H_2 annealed material, and Fe from CNT forest.

Negative ion SIMS spectra typically show fewer peaks, making them easier to interpret but often not as rich in information. The negative ion SIMS spectrum of Si/SiO_2 showed a small F^- signal, although small F^- peaks are commonly observed on many samples. The negative ion spectrum also exhibited the following silicon-containing anions: SiO_2^-, SiO_2H^-, SiO_3^-, and SiO_3H^-, which are typical of silicon oxide surfaces.[49]

7.4.2 Al_2O_3 on Si/SiO_2

Although a metal catalyst, which in our case is iron nanoparticles, is necessary for CNT growth, CNT growth does not occur if the Fe catalyst is poisoned with Si.[32-34] Accordingly, a barrier layer of Al_2O_3 (35 nm) was deposited on the Si/SiO_2.[24] The XP survey spectrum of the Al_2O_3 film shows that the film is comprised of Al, O, and C (Figure 7.1b). Since the alumina film is relatively thick, (i) XPS cannot be used to determine its thickness, as was done for the SiO_2 film, and (ii) no signal from the Si/SiO_2 substrate is present. The Al 2p peak position at 75.4 eV indicates that the aluminum is oxidized.[25, 50, 51] The O 1s signal consists of a single peak at 531.6 eV. The Al/O ratio was ca. 0.40 and not the 0.67 value that would be expected for Al_2O_3. However, this is not surprising because (i) the C 1s narrow scan shows some oxidized carbon and (ii) it is not uncommon for air-exposed surfaces to have some adsorbed hydroxyls. Interestingly, RBS (see below), which is much less surface sensitive/more sensitive to the bulk of the material, shows the appropriate Al:O ratio. The valence band spectrum of this Al_2O_3 film is in reasonable agreement with literature spectra for this material.[50-53]

RBS of the Al_2O_3 on Si/SiO_2 film showed an aluminum signal at the silicon edge (see Figure 7.2). The closeness of these two signals is not unexpected as Al and Si are neighbors in the periodic table. An oxygen signal at channel number ca. 500 is now obvious – the Al_2O_3 film is thick enough to produce a substantial oxygen peak. Quantitative analysis (see Table 7.2) shows the two expected layers: the Si substrate with an overlayer composed of Al and O in a 2:3 atomic ratio. Positive ion ToF-SIMS showed a strong Al^+ signal along with the expected series of peaks attributable to hydrocarbon surface contamination. Negative ion ToF-SIMS showed a strong AlO^- peak. In agreement with the XPS result, essentially no Si^+ is present in the positive ion spectrum.

7.4.3 Fe on $Si/SiO_2/Al_2O_3$

XPS confirms the expected presence of iron in the 6 nm Fe layer deposited on the Al_2O_3 diffusion barrier (see Figure 7.1c). However, while the Fe should have been deposited in a reduced state, no metallic iron signal at ca. 707 eV is observed, i.e., the film had been exposed to the air and the Fe $2p_{3/2}$ signal is at 711.2 eV.[54-56] The strong O 1s signal is consistent with the oxidized state of the iron. The splitting between the $2p_{3/2}$ and $2p_{1/2}$ peaks (delta eV) is also indicative of an oxidized material. Delta eV for our Fe films is 13.4 eV, which is closer to the values for oxidized iron (13.5 - 13.6 eV) than for metallic iron (13.0 eV).[25, 57, 58] In addition, the Fe $2p_{3/2}$ and Fe $2p_{1/2}$ peaks show shake-up satellites that are observed in most forms of oxidized iron.[57, 59] Unfortunately, while it is apparent that the iron is oxidized, and while it appears that our film is in a +3 oxidation state, there is enough ambiguity in the literature to make it difficult to definitively state whether our iron is in a +2 or +3 oxidation state.[55, 57, 60]

Small Al and Si signals are also present in this film. Because of the thinness of the Fe film it comes as little surprise that the small Al signals would be present. Possible sources of the Si signal could be silicon diffusing through the Al_2O_3 during the Fe deposition (this seems unlikely), Si contamination in the Fe target, or polydimethylsiloxane (PDMS) contamination.[61]

ToF-SIMS, which is more surface sensitive than XPS, shows only very small Si^+ and Al^+ peaks, which is consistent with an Fe layer over the Al_2O_3 film – the Al_2O_3 is not very accessible to the primary ions. SIMS is extremely sensitive to PDMS contamination,[61] but neither the m/z 73 ($Si(CH_3)_3^+$) nor 147 ($(CH_3)_3SiOSi(CH_3)_2^+$) peak from PDMS is present to any significant extent. This issue of surface contamination will be further addressed in the Discussion below.

A narrow scan of the O 1s region shows an asymmetric O 1s peak that suggests at least two chemical states for the oxygen (see Figure 7.3). Similar O 1s narrow scans have been reported in the XPS of oxidized iron, where the lower binding energy peak has been attributed to lattice oxygen (O^{2-}) and the higher binding energy peak to chemisorbed OH^- groups, e.g., Fe-OH moieties.[62-64] Given the small size of the Al signals in the unannealed Fe film, it seems likely that oxygen from Al_2O_3 makes only a relatively small contribution to the O 1s envelop, i.e., the assignments of O^{2-} and Fe-OH for the chemical states of oxygen appear reasonable.

Comparison of the valence band spectrum of the 6 nm Fe film with literature reports showed good agreement for oxidized, and not metallic, iron, i.e., if the film had been metallic it would have shown a sharper peak close to 0 eV (see Figure 7.1d).[54, 55] RBS of the film shows that the expected components of the stack are present in their expected order: Si (substrate), followed by Al and O, and Fe, with the signal from the heavier Fe atoms well separated from the others (see Figure 7.2 and Table 7.2).

ToF-SIMS showed the expected hydrocarbon contamination and sizeable signals due to $^{56}Fe^+$ (the largest peak in the spectrum) and $FeOH^+$. A tiny signal attributable to Al^+ was observed. Peak areas for these species are given in Table 7.3. Helium ion microscopy (HIM) and ToF-SIMS showed the expected results. HIM revealed a smooth, featureless layer (see Figure 7.4).

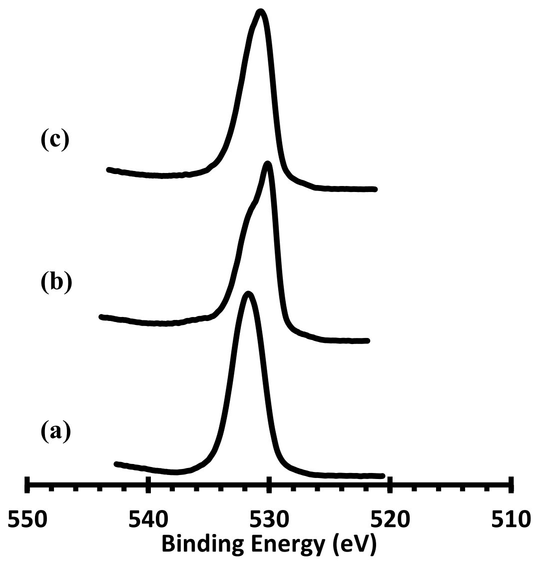

Figure 7.3 XPS O 1s narrow scans of (a) the 35 nm Al_2O_3 film on Si/SiO_2, (b) the 6 nm iron film on $Si/SiO_2/Al_2O_3$, and (c) the film from (b) after annealing in H_2. Both iron films/materials were exposed to the air before analysis.

Table 7.3 Comparison of various ToF-SIMS peak areas for the Fe film before and after annealing in H_2.

Species	Fe Film	Fe Annealed Material
Al^+	3105	45213
Fe^+	141395	62086
$FeOH^+$	27572	12887
AlO^-	0	4826

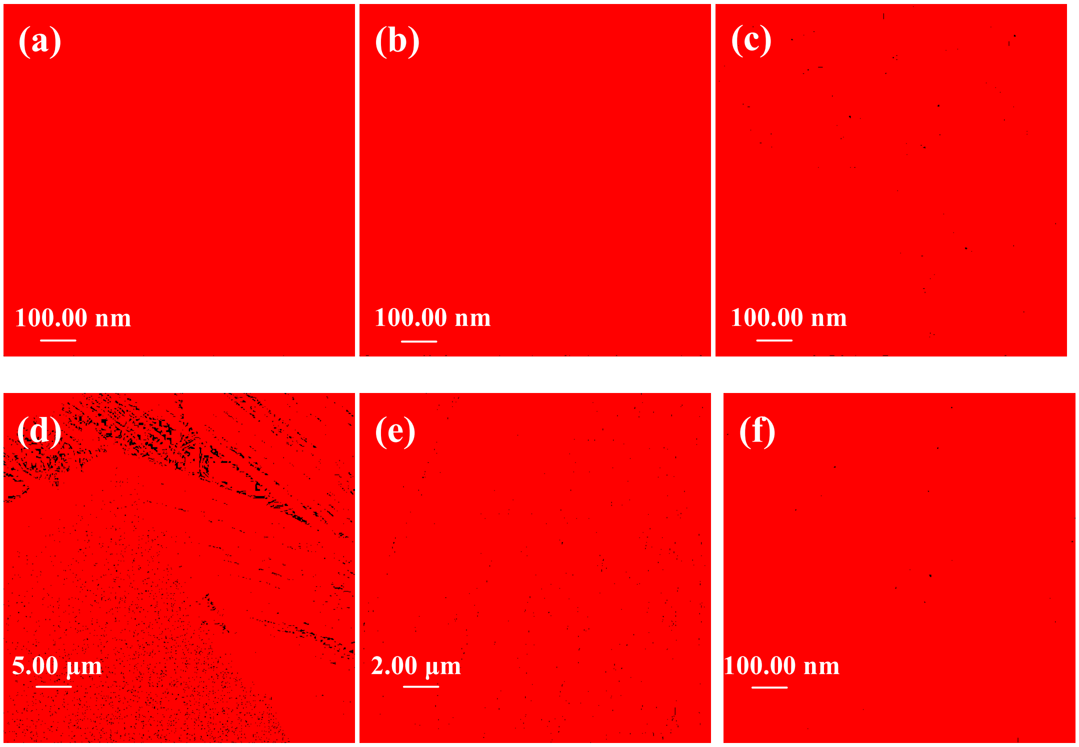

Figure 7.4 HIM micrographs of (a) unannealed iron film, (b) thermally annealed iron film, (c) top view of the CNT forest, (d) view of a break in the CNT forest showing its top and side, (e) side view of the vertically aligned CNT forest, (f) close view of vertically aligned CNT forest.

7.4.4 Annealed Iron Film

To grow CNTs from a metal catalyst the film was annealed at 750 °C in H_2. Annealing under H_2 reduces the iron oxide to elemental, metallic Fe so that CNT growth can occur.[65] This process causes the Fe film to dewet from the surface and create nanoparticles due to a surface free energy mismatch between the Al_2O_3 and Fe.[38, 39, 66, 67] Like the spectrum of the unannealed Fe film, the XP spectrum of the Fe nanoparticles is quite complex, although the only major difference between these spectra is that the annealed film shows considerably larger Al peaks (2s and 2p) (Figure 7.1e). This increase in the Al signal is attributed to exposure of the underlying Al_2O_3 film upon creation of Fe nanoparticles. The Fe 2p narrow scan from the annealed film is very similar to the spectrum of the unannealed film. The Fe $2p_{3/2}$ and $2p_{1/2}$ peaks are at 710.8 and 724.5 eV in the narrow scan, respectively, giving a delta eV value of 13.7 eV. These peak positions, the value of delta eV, and the absence of any sign of reduced iron are again consistent with a fully oxidized material. These results are reasonable – if a smooth Fe film would completely oxidize in the air, then Fe nanoparticles with much greater surface area should only be more susceptible to oxidation.

The O 1s narrow scan is now changed from the unannealed film (Figure 7.3), showing more signal at higher binding energy. This may be due to an increased concentration of Fe-OH in the material. However, it is more likely that this change is due to a greater contribution from the O 1s signal from the exposed Al_2O_3, c.f., the ratio of O and Al signals in the survey scan of the Al_2O_3 film in Figure 7.3. The satellite signals around the Fe 2p peaks are more intense in the annealed than unannealed film. The literature suggests that chemical/oxidation state changes in iron change the intensity of the satellite signals, i.e., this result suggests at least some chemical differences between the oxidized, unannealed film and the oxidized nanoparticle layer.[56] The valence band spectrum for the annealed Fe sample has features similar to the valence band spectrum of the thermally evaporated Fe film, indicating again that the film is oxidized, although the peak from the annealed Fe sample is shifted to higher binding energies. As was the case for the O 1s signal, we attribute this shift to a greater contribution from the more exposed Al_2O_3 film.

RBS of the H_2-annealed Fe film showed the expected elements in their expected layer structure: Si, SiO_2, Al_2O_3, FeO, with trace amounts of Cl and P in the Fe film (see Figure 7.2 and Table 7.2). Differences between this spectrum and the previous spectrum of the unannealed Fe are that the SiO_2 film appears a little thicker, the Al_2O_3 now shows small amounts of Si and Fe, and the annealed Fe layer shows some contamination. The additional thickness of the SiO_2 film and the presence of Si and Fe in the Al_2O_3 are probably due to interdiffusion of the elements during annealing and/or a small degree of oxidation of the silicon substrate. The source of the Cl and P contaminants is uncertain.

In contrast to the featureless HIM image of the unannealed Fe film, the annealed film shows considerable texture in the form of the expected array of nanoparticles that are essential for CNT growth.[24, 38-40] ToF-SIMS characterization of the H_2 annealed Fe film/nanoparticles. showed many of the same ions as the Fe film (see previous section). However, the intensities of the peaks changed in a manner that is consistent with greater exposure of the Al_2O_3 underlayer.[66] In particular, Table 7.2 shows that after annealing the Al^+ and AlO^- signals increase dramatically and the Fe^+ and $FeOH^+$ decrease, although these latter two signals remain significant.

7.4.5 Carbon Nanotubes

Carbon nanotubes (CNTs) were catalytically grown from H_2-annealed Fe. The XPS survey spectrum of CNTs shows that the material is 100% carbon. Narrow scans of the C 1s region showed two peaks. The first asymmetrical peak at ca. 285 eV is the carbon 1s peak, and the second signal at ca. 291 eV is the $\pi \rightarrow \pi^*$ transition or shake-up peak. Both of these features are common in graphitic carbon[68] and CNTs.[68-71] The valence band (VB) region consists of a signal that increases steadily with increasing binding energy to ca. 20 eV. While there are examples in the literature of UPS spectra of CNTs (taken with UV light), we have struggled to find any valence band spectrum of CNTs obtained with X-radiation.

Interestingly, RBS of the CNT forest did not show any carbon. Using the thickness of our multiwalled CNT film (ca. 50 μm) and its approximate density (0.009 g/cm^3)[40, 72] we calculated the thickness of a film of graphite (ρ = 2.27 g/cm^3) containing the same number of carbon atoms as our CNT forest. The thickness of the resulting film should be ca. 200 nm, which in spite of the fact that carbon is a light element should be easily seen by RBS. We conclude that there is something of a channeling phenomenon taking place within our CNT forests. While some of the He^+ ions may be stopped, many are able to enter and exit the film as they pass between the vertically aligned CNTs. This hypothesis is consistent with the Fe peaks from the Fe, Fe(NP), and Fe(CNT) films (see Figure 7.2). While the peaks from the Fe and Fe(NP) films are very similar, the Fe(CNT) peak is reduced in height and shows a small tail to lower channel number (energy). HIM clearly showed the vertical alignment of the CNTs in the forest and intertwining of the CNTs at the top of the forest (see Figure 7.4), which have also been reported in the literature.[40, 73, 74]

ToF-SIMS of the CNTs showed a number of carbon-containing moieties. The most intense peak in the positive ion spectrum was C^+. Hydrocarbon fragments were also observed, suggesting adventitious hydrocarbon contamination. The negative ion spectrum contains a series of significant signals of the type C_n^- for n = 1 … 12 and beyond. For n = 1 to 6, the fragments with odd numbers of carbons are less intense than their neighboring fragments with even numbers of carbons, i.e., there is an even-odd effect.[75] Beyond n = 6 there appears to be a steady decrease in the intensities of the fragments.

7.5. Discussion

7.5.1. In accord with our hypothesis that multiple techniques would yield more information than one or two techniques:

XPS survey scans showed atomic compositions of the materials, e.g., that the only element detectable by XPS for the CNTs was carbon. Narrow scans showed chemical state information, e.g., that the Al and Fe were in oxidized states.

By comparison to literature spectra, valence band spectra confirmed the chemical states of the materials, e.g., that the Al and Fe were in an oxidized state and not metallic. Both positive and negative ion ToF-SIMS showed ions characteristic of the materials. RBS probed deeply into the materials and confirmed the layered nature of the structures. HIM provided high resolution images of the unannealed Fe, annealed Fe, and CNT forests. It was particularly useful for showing the morphologies of the latter two materials. It is interesting to note the complementary nature of these methods. Each provided information that the others could not. Of course part of this complementarity comes from their different probe depths.

7.5.2. The following are technical aspects of special interest:

The extremely small, essentially nonexistant, C signal in the RBS spectrum of the CNT forest suggesting a form of 'channeling' of the ions through the CNT forest. This phenomenon does not appear to have been previously reported, although it has been suggested that the *interiors* of CNTs could be used as ion guides.[76, 77]

The odd-even effect for the ToF-SIMS C_n^- peaks for n = 1 ... 6 and the steady decrease in intensity for the $n \geq 6$ peaks. While negative ion SIMS of CNTs has been reported,[78] there does not appear to have been any recognition or discussion of this effect.

The valence band spectrum of CNTs taken with X-radiation (Al Kα) does not appear to have been reported.

Although not entirely surprising, it was important to show the complete oxidation of our Fe film and nanoparticles, i.e., no metallic iron was present. This oxidation should not be an issue for our CNT growth during which the Fe film is reduced at elevated temperature under H_2, and then C_2H_4 and H_2 are flowed over the nanoparticles to allow CNT growth, i.e., the nanoparticles remain under a reducing environment from the time they are created until they have served their purpose.

7.5.3 Small signals from surface contaminants

An issue raised in this work is that of the small fluorine signals in two of the XPS spectra: the Si/SiO_2 and $Si/SiO_2/Al_2O_3/Fe$ (unannealed) materials, the Si signal in the unannealed Fe film, and the Cl and P signals in the RBS spectrum of the H_2-annealed Fe film. To better understand the possible source of the fluorine signals we checked the negative ion ToF-SIMS spectra of all the materials, expecting to see higher F^- signals from the two contaminated films. No such correlation existed. The ratios of the F^- signal to the largest signal in that spectrum, which in all cases was H^-, except for the CNT material in which it was C_2^-, were Si/SiO_2 (0.024), $Si/SiO_2/Al_2O_3$ (0.020), $Si/SiO_2/Al_2O_3/Fe$ (0.006), $Si/SiO_2/Al_2O_3/Fe(NP)$ (0.126), and $Si/SiO_2/Al_2O_3/Fe(NP)/CNT$ (0.013). In other words, there was no correlation between the XPS and SIMS signals, and the surface that showed the greatest degree of F^- contamination by SIMS (the $Si/SiO_2/Al_2O_3/Fe(NP)$ surface) showed none in the XPS survey scan. Had fluorine been seen in only one instrument it might have suspected that that instrument was the source of the contamination. However, an advantage of multiple instruments and the fact that no sample shows substantial fluorine by both techniques suggests that neither the synthesis of the materials nor the analytical chambers is the source of the contamination. A similar result was obtained for the Si contamination in the unannealed Fe film – silicon was seen by XPS but only at a very low level by SIMS. Similarly, XPS of the H_2-annealed Fe film did not show the Cl and P signals that were suggested in the RBS spectrum of this material. Finally, it is noted that XPS and SIMS do appear to confirm that the Si/SiO_2 surface is contaminated with a nitrogen-containing species, showing N 1s and NH_4^+ signals, respectively.

7.5.4 Other methods of increasing the amount of information from one's analyses: data mining.

While very important for materials analysis, using more analytical techniques is not the only way to increase the amount of useful information one has about one's materials. Various data analysis tools can also provide valuable insight. For example, we have previously referenced some of the work of Tougaard.[26-29] In addition, while the set of samples under consideration here did not lend itself to this type of analysis, the high degree of correlation that often exists between many of the ions in SIMS spectra has allowed the effective application of various chemometric methods to SIMS data, especially when series of similar samples are under consideration.[49, 61, 79-81]

7.5.5. This manuscript ends by reminding the reader of the following compelling reasons for employing multiple techniques in surface analysis.

The more techniques applied to the characterization of a material or interface, the lower the chance there will be a fatal or lurking flaw in its future fabrication and/or performance.

If a material's synthesis ceases to work in a production setting, the complete, previously performed characterization of the material can help significantly in troubleshooting.

It is not always clear in advance which techniques will provide the greatest amount of information about a material – by applying multiple tools one will better understand how to undertake future materials characterization.

With a deeper understanding of a material one can better relate its performance to its more fundamental properties, and this information can then be used to improve material/device performance.

More extensive materials characterization reduces the likelihood that the effects observed in a synthesis are due to impurities in a starting material. Thus, one's explanation of one's results has a higher chance of being correct, and one is less susceptible to process failure if the supplier of a starting material is changed.[1]

By employing multiple techniques it is less likely that artifacts will be interpreted as true signals from one's samples – note the case of the F^- contamination above.

7.6. Acknowledgments

We thank Diamond Analytics, a US Synthetic company (Orem, UT), for funding this study. Part of this research was performed at EMSL, a national scientific user facility sponsored by the Department of Energy's Office of Biological and Environmental Research and located at Pacific Northwest National Laboratory.

Author contributions: D.J. arragned, organized, plotted and analyzed the data from the multiple characterization tools. S.K. fabricated the devices up to and including CNT growth. J.H. helped with analyses. M.V., A.D., and R.V. helped direct the research. M.E. did XPS analyses. V.S. did both RBS and HIM. Z.Z. did the ToF-SIMS. M.L. recognized the odd-even and channeling effects. M.L. was the principle investigator of the project. The manuscript was written by D.J. and M.L.

7.7. Data Archiving

The original XPS and ToF-SIMS spectra for the materials studied herein will be submitted to Surface Science Spectra, an AVS journal published by the Society through the American Institute of Physics.

7.8. References

1. Wolf, L. K., *C&E News* **2012,** *90* (22), 48-50.

2. Dutta, S.; Perring, M.; Barrett, S.; Mitchell, M.; Kenis, P. J. A.; Bowden, N. B., *Langmuir* **2006,** *22* (5), 2146-2155.

3. Perring, M.; Dutta, S.; Arafat, S.; Mitchell, M.; Kenis, P. J. A.; Bowden, N. B., *Langmuir* **2005,** *21* (23), 10537-10544.

4. Yam, C. M.; Cai, C., *J. Colloid Interface Sci.* **2006,** *301* (2), 441-445.

5. Ciampi, S.; Böcking, T.; Kilian, K. A.; Harper, J. B.; Gooding, J. J., *Langmuir* **2008,** *24* (11), 5888-5892.

6. Wickard, T. D.; Nelsen, E.; Madaan, N.; ten Brummelhuis, N.; Diehl, C.; Schlaad, H.; Davis, R. C.; Linford, M. R., *Langmuir* **2009,** *26* (3), 1923-1928.

7. Yamada, T.; Shirasaka, K.; Noto, M.; Kato, H. S.; Kawai, M., *J. Phys. Chem. B* **2006,** *110* (14), 7357-7366.

8. Fellah, S.; Amiar, A.; Ozanam, F.; Chazalviel, J. N.; Vigneron, J.; Etcheberry, A.; Stchakovsky, M., *J. Phys. Chem. B* **2007,** *111* (6), 1310-1317.

9. Juang, A.; Scherman, O. A.; Grubbs, R. H.; Lewis, N. S., *Langmuir* **2001,** *17* (5), 1321-1323.

10. Plass, K. E.; Liu, X.; Brunschwig, B. S.; Lewis, N. S., *Chem. Mater.* **2008,** *20* (6), 2228-2233.

11. Gurtner, C.; Wun, A. W.; Sailor, M. J., *Angew. Chem., Int. Ed.* **1999,** *38* (13-14), 1966-1968.

12. Schmeltzer, J. M.; Porter, L. A.; Stewart, M. P.; Buriak, J. M., *Langmuir* **2002,** *18* (8), 2971-2974.

13. Stewart, M. P.; Buriak, J. M., *J. Am. Chem. Soc.* **2001,** *123* (32), 7821-7830.

14. Yang, L.; Lua, Y.-Y.; Tan, M.; Scherman, O. A.; Grubbs, R. H.; Harb, J. N.; Davis, R. C.; Linford, M. R., *Chem. Mater.* **2007,** *19* (7), 1671-1678.

15. Linford, M. R.; Fenter, P.; Eisenberger, P. M.; Chidsey, C. E. D., *J. Am. Chem. Soc.* **1995,** *117* (11), 3145-3155.

16. Yang, L.; Lua, Y.-Y.; Lee, M. V.; Linford, M. R., *Acc. Chem. Res.* **2005,** *38* (12), 933-942.

17. Shirahata, N.; Linford, M. R.; Furumi, S.; Pei, L.; Sakka, Y.; Gates, R. J.; Asplund, M. C., *Chem. Comm.* **2009,** (31), 4684-4686.

18. Lee, M. V.; Lee, J. R. I.; Brehmer, D. E.; Linford, M. R.; Willey, T. M., *Langmuir* **2009,** *26* (3), 1512-1515.

19. Linford, M. R.; Chidsey, C. E. D., *J. Am. Chem. Soc.* **1993,** *115* (26), 12631-12632.

20. Sieval, A. B.; Demirel, A. L.; Nissink, J. W. M.; Linford, M. R.; van der Maas, J. H.; de Jeu, W. H.; Zuilhof, H.; Sudhölter, E. J. R., *Langmuir* **1998,** *14* (7), 1759-1768.

21. Lua, Y.-Y.; Lee, M. V.; Fillmore, W. J. J.; Matheson, R.; Sathyapalan, A.; Asplund, M. C.; Fleming, S. A.; Linford, M. R., *Angew. Chem., Int. Ed.* **2003,** *42* (34), 4046-4049.

22. Linford, M. R.; Copeland, S.; Dadson, A. E.; Davis, R. C.; Jensen, D. S.; Olsen, R.; Saini, G.; Shutthanandan, V.; Song, J.; Vail, M. A.; Vanfleet, R.; Wiest, L. A.; Wyman, R. D.; Yang, L., *Microsc. Microanal.* **2010,** *16* (S2), 410-411.

23. Jensen, D. S.; Kanyal, S. S.; Gupta, V.; Vail, M. A.; Dadson, A. E.; Engelhard, M.; Vanfleet, R.; Davis, R. C.; Linford, M. R., *J. Chromatogr., A* **2012,** *1257* (0), 195-203.

24. Song, J.; Jensen, D. S.; Hutchison, D. N.; Turner, B.; Wood, T.; Dadson, A.; Vail, M. A.; Linford, M. R.; Vanfleet, R. R.; Davis, R. C., *Adv. Funct. Mater.* **2011,** *21* (6), 1132-1139.

25. Moulder, J. F.; Stickle, W. F.; P.E., S.; Bomber, K. D., *Handbook of X-ray Photoelectron Spectroscopy*. Physical Electronics, Inc.: Eden Prairie, 1995.

26. Tougaard, S.; Jansson, C., *Surf. Interface Anal.* **1993,** *20* (13), 1013-1046.

27. Tougaard, S., *Surf. Interface Anal.* **1998,** *26* (4), 249-269.

28. Tougaard, S., *Surf. Interface Anal.* **1997,** *25* (3), 137-154.

29. Tougaard, S., *J. Vac. Sci. Technol., A* **1996,** *14* (3), 1415-1423.

30. *ToF-SIMS: Surface Analysis by Mass Spectrometry*. IM Publications and SurfaceSpectra Limited: West Sussex and Manchester, 2001.

31. Ward, B.; Notte, J. A.; Economou, N. P., *Photonics Spectra* **2007,** *August*.

32. Homma, Y.; Kobayashi, Y.; Ogino, T.; Takagi, D.; Ito, R.; Jung, Y. J.; Ajayan, P. M., *J. Phys. Chem. B* **2003,** *107* (44), 12161-12164.

33. Ci, L.; Ryu, Z.; Jin-Phillipp, N. Y.; Rühle, M., *Diamond Relat. Mater.* **2007,** *16* (3), 531-536.

34. Chang, W.-T., *J. Mater. Sci.: Mater. Electron.* **2010,** *21* (1), 16-19.

35. Kanyal, S. S.; Jensen, D. S.; Miles, A. J.; Dadson, A. E.; Vail, M. A.; Scorza, F.; Shutthanandan, V.; Vanfleet, R.; Davis, R. C.; Linford, M. R., *J. Chromatogr., A* **2012,** *Submitted for Review*.

36. Jensen, D. S.; Kanyal, S. S.; Gupta, V.; Vail, M. A.; Dadson, A. E.; Engelhardt, H.; Vanfleet, R.; Davis, R. C.; Linford, M. R., *J. Chromatogr. A* **2012**.

37. Hausmann, D.; Becker, J.; Wang, S.; Gordon, R. G., *Science* **2002,** *298* (5592), 402-406.

38. Mattevi, C.; Wirth, C. T.; Hofmann, S.; Blume, R.; Cantoro, M.; Ducati, C.; Cepek, C.; Knop-Gericke, A.; Milne, S.; Castellarin-Cudia, C.; Dolafi, S.; Goldoni, A.; Schloegl, R.; Robertson, J., *J. Phys. Chem. C* **2008,** *112* (32), 12207-12213.

39. Esconjauregui, S.; Fouquet, M.; Bayer, B. C.; Ducati, C.; Smajda, R.; Hofmann, S.; Robertson, J., *ACS Nano* **2010,** *4* (12), 7431-7436.

40. Hutchison, D. N.; Morrill, N. B.; Aten, Q.; Turner, B. W.; Jensen, B. D.; Howell, L. L.; Vanfleet, R. R.; Davis, R. C., *J. Microelectromech. Syst.* **2010,** *19* (1), 75-82.

41. Strohmeier, B. R., *Surf. Interface Anal.* **1990,** *15* (1), 51-56.

42. Carlson, T. A.; McGuire, G. E., *J. Electron Spectrosc. Relat. Phenom.* **1972,** *1* (2), 161-168.

43. Shallenberger, J. R.; Cole, D. A.; Novak, S. W.; Moore, R. L.; Edgell, M. J.; Smith, S. P.; Hitzman, C. J.; Kirchhoff, J. F.; Principe, E.; Biswas, S.; Bleiler, R. J.; Nieveen, W.; Jones, K. In *Oxide thickness determination by XPS, AES, SIMS, RBS and TEM*, Ion Implantation Technology Proceedings, 1998 International Conference on, 1999; 1999; pp 79-82 vol.1.

44. van der Heide, P. A. W.; Azzarello, F. V., *Surf. Sci.* **2003,** *531* (3), L369-L377.

45. Hirose, K.; Nohira, H.; Azuma, K.; Hattori, T., *Prog. Surf. Sci.* **2007,** *82* (1), 3-54.

46. Hirose, K.; Nohira, H.; Koike, T.; Sakano, K.; Hattori, T., *Phys. Rev. B* **1999,** *59* (8), 5617-5621.

47. Hirose, K.; Sakano, K.; Nohira, H.; Hattori, T., *Phys. Rev. B* **2001,** *64* (15), 155325.

48. Zatsepin, D. A.; Mack, P.; Wright, A. E.; Schmidt, B.; Fitting, H. J., *Phys. Status Solidi A* **2011,** *208* (7), 1658-1661.

49. Yang, L.; Lua, Y.-Y.; Jiang, G.; Tyler, B. J.; Linford, M. R., *Anal. Chem.* **2005,** *77* (14), 4654-4661.

50. Rotole, J. A.; Sherwood, P. M. A. In *Valence band x-ray photoelectron spectroscopic studies to distinguish between oxidized aluminum species*, Baltimore, Maryland (USA), AVS: Baltimore, Maryland (USA), 1999; pp 1091-1096.

51. Rotole, J. A.; Sherwood, P. M. A., *Fresenius J. Anal. Chem.* **2001,** *369* (3), 342-350.

52. Thomas, S.; Sherwood, P. M. A., *Anal. Chem.* **1992,** *64* (21), 2488-2495.

53. Snijders, P. C.; Jeurgens, L. P. H.; Sloof, W. G., *Surf. Sci.* **2002,** *496* (1–2), 97-109.

54. Xue, M.; Wang, S.; Wu, K.; Guo, J.; Guo, Q., *Langmuir* **2010,** *27* (1), 11-14.

55. Temesghen, W. T.; Sherwood, P. S., *Anal. Bioanal. Chem.* **2002,** *373* (7), 601-608.

56. Fujii, T.; Alders, D.; Voogt, F. C.; Hibma, T.; Thole, B. T.; Sawatzky, G. A., *Surf. Sci.* **1996,** *366* (3), 579-586.

57. Yamashita, T.; Hayes, P., *Appl. Surf. Sci.* **2008,** *254* (8), 2441-2449.

58. Mansour, A. N.; Brizzolara, R. A., *Surf. Sci. Spectra* **1996,** *4* (2), 175-179.

59. Xia, W.; Su, D.; Birkner, A.; Ruppel, L.; Wang, Y.; Wöll, C.; Qian, J.; Liang, C.; Marginean, G.; Brandl, W.; Muhler, M., *Chem. Mater.* **2005,** *17* (23), 5737-5742.

60. Corneille, J. S.; He, J.-W.; Goodman, D. W., *Surf. Sci.* **1995,** *338* (1–3), 211-224.

61. Yang, L.; Shirahata, N.; Saini, G.; Zhang, F.; Pei, L.; Asplund, M. C.; Kurth, D. G.; Ariga, K.; Sautter, K.; Nakanishi, T.; Smentkowski, V.; Linford, M. R., *Langmuir* **2009,** *25* (10), 5674-5683.

62. Shustak, G.; Domb, A. J.; Mandler, D., *Langmuir* **2004,** *20* (18), 7499-7506.

63. Jovancicevic, V.; Kainthla, R. C.; Tang, Z.; Yang, B.; Bockris, J. O. M., *Langmuir* **1987,** *3* (3), 388-395.

64. McIntyre, N. S.; Zetaruk, D. G., *Anal. Chem.* **1977,** *49* (11), 1521-1529.

65. Tiernan, M. J.; Barnes, P. A.; Parkes, G. M. B., *J. Phys. Chem. B* **2000,** *105* (1), 220-228.

66. Amama, P. B.; Pint, C. L.; Kim, S. M.; McJilton, L.; Eyink, K. G.; Stach, E. A.; Hauge, R. H.; Maruyama, B., *ACS Nano* **2010,** *4* (2), 895-904.

67. Quintana, C.; Menéndez, J. L.; Huttel, Y.; Lancin, M.; Navarro, E.; Cebollada, A., *Thin Solid Films* **2003,** *434* (1–2), 228-238.

68. Henriette, E.-S., *Carbon* **2004,** *42* (8–9), 1713-1721.

69. Okpalugo, T. I. T.; Papakonstantinou, P.; Murphy, H.; McLaughlin, J.; Brown, N. M. D., *Carbon* **2005,** *43* (1), 153-161.

70. Yang, D.-Q.; Rochette, J.-F.; Sacher, E., *J. Phys. Chem. B* **2005,** *109* (16), 7788-7794.

71. Yang, D.-Q.; Rochette, J.-F.; Sacher, E., *J. Phys. Chem. B* **2005,** *109* (10), 4481-4484.

72. Hutchison, D. N. VERTICALLY ALIGNED CARBON NANOTUBES AS A FRAMEWORK FOR MICROFABRICATION OF HIGH ASPECT RATIO MEMS. Brigham Young University, Provo, 2008.

73. Zhang, W. D.; Thong, J. T. L.; Tjiu, W. C.; Gan, L. M., *Diamond Relat. Mater.* **2002,** *11* (9), 1638-1642.

74. Moulton, K.; Morrill, N. B.; Konneker, A. M.; Jensen, B. D.; Vanfleet, R. R.; Allred, D. D.; Davis, R. C., *J. Micromech. Microeng.* **2012,** *22* (5), 055004.

75. Kanyal, S. S.; Jensen, D. S.; Zhu, Z., *Surf. Sci. Spectra* **2012,** *In review* (-), -.

76. Zhao, D.; Song, Y.-H.; Wang, Y.-N., *Chin. Phys. Lett.* **2008,** *25* (7), 2588.

77. Lysova, I.; Sabirov, A.; Stepanov, A., *J. Surf. Invest.: X-Ray, Synchrotron Neutron Tech.* **2010,** *4* (2), 335-337.

78. He, P.; Lian, J.; Shi, D.; Mast, D.; van Ooij, W. J.; Schulz, M. In *Coating of Ultrathin Polymer Films on Carbon Nanotubes by a Plasma Treatment*, MRS Proceedings, 2002; pp I3-.19.

79. Muramoto, S.; Graham, D. J.; Wagner, M. S.; Lee, T. G.; Moon, D. W.; Castner, D. G., *J. Phys. Chem. C* **2011,** *115* (49), 24247-24255.

80. Graham, D. J.; Wagner, M. S.; Castner, D. G., *App. Surf. Sci.* **2006,** *252* (19), 6860-6868.

81. Zhang, F.; Gates, R. J.; Smentkowski, V. S.; Natarajan, S.; Gale, B. K.; Watt, R. K.; Asplund, M. C.; Linford, M. R., *J. Am. Chem. Soc.* **2007,** *129* (30), 9252-9253.

Chapter 8: Improvements in the Chromatographic Properties of Porous Graphitic Carbon by Surface Passivation with Di-*tert*-Amylperoxide[*]

8.1. Abstract

Porous graphitic carbon (PGC) particles were functionalized in situ in packed beds at elevated temperature with neat di-*tert*-amylperoxide (DTAP) in a column oven. The performance of these particles for high performance liquid chromatography (HPLC) was assayed before and after functionalization with the following analytes: benzene, toluene, ethyl benzene, *n*-propyl benzene, *n*-butyl benzene, *p*-xylene, phenol, 4-methylphenol, phenetole, 3,5-xylenol, and anisole. After the first functionalization, the retention factors, *k*, of these compounds decreased by about 5% and the number of theoretical plates (N) increased by ca. 15%. These values of *k* then remained roughly constant after a second functionalization but a further increase in N was noticed. In addition, after each of the functionalizations, the peak asymmetries decreased by ca. 15%, for a total of ca. 30%. In fact, this functionalization process with DTPA resulted in a minimal reduction in *k*, therefore, the functionalization process could be better termed as a surface passivation of PGC. The columns were then subjected twice to methanol at 100°C for 5 h at 1 mL/min. After these stability tests, the values of *k* remained roughly constant, the number of plates increased, which is favorable, and the asymmetries rose and then declined, where they remained below the initial values for the unfunctionalized columns. Functionalized and unfunctionalized particles were characterized by scanning electron microscopy and BET measurements, which showed no difference between the functionalized and unfunctionalized materials, and X-ray photoelectron spectroscopy and time-of-flight secondary ion mass spectrometry (ToF-SIMS), where ToF-SIMS suggested some chemical differences between the functionalized and unfunctionalized materials. In particular ToF-SIMS suggested that the

expected five-carbon fragments from DTAP exist at higher concentrations on DTAP-functionalized PGC. First principle calculations on model graphitic surfaces suggest that the first addition of a DTAP radical to the surface proceeds in an approximately isothermal or slightly favorable fashion, but that subsequent DTAP additions are then increasingly thermodynamically favorable. Thus, this analysis suggests that the direct functionalization of PGC with DTAP is plausible. Chemometric analyses of the chromatographic and ToF-SIMS data are also presented.

8.2. Introduction

Porous graphitic carbon (PGC) is an important alternative to silica-based supports for liquid chromatography (LC).[1] PGC has two considerable advantages over silica. The first is stability, both at extremes of pH (from 10 M HCl to 10 M NaOH) and at elevated temperatures.[1] For example, recent studies show low column bleed from PGC when it is subjected to pure aqueous mobile phases at temperatures as high as 200 °C.[2] For this reason it is often preferred over silica-based materials in elevated temperature LC.[2-3] The second advantage is its unique selectivity, where the retention mechanism of PGC is quite different from that of silica-based C_{18} columns because PGC shows a 'polar retention effect on graphite' (PREG), a result of charge-induced dipoles on the graphitic surface.[1, 4] That is, with conventional silica-C_{18} reversed phase (RP) columns an increase in an analyte's polarity usually reduces retention. However, with PGC, analytes with increased polarity can often be retained and separated. Another retention phenomenon of PGC is an increase in retention of *non*-polar compounds compared to silica C_{18} columns. Because it is planar, PGC also shows shape selectivity – it can often separate structurally related compounds, *e.g.*, geometric and diastereoisomers, which may be harder to separate with silica C_{18} columns.

Perhaps the only disadvantage of PGC is that it has been a challenge to functionalize. Knox et al. successfully coated PGC with polyethyleneimine (PEI), where they also showed further cross-linking of the immobilized PEI. The resulting PEI-coated PGC was suitable for ion-chromatography but not for RP-LC.[5] Polyethylene glycol coated PGC also has been used for supercritical fluid chromatography, showing good peak shapes along with interesting selectivity.[6] Knox et al. further demonstrated that enantiomeric separations could be performed by adsorbing either L- or D-isomers of *N*-(2-naphthanlene-sulphonyl)-phenylalanine onto PGC.[7] Nahashima et al. coated PGC with cetyltrimethylammonium ions for ion chromatography.[8] Chambers et al. showed that other cationic surfactants could be adsorbed onto the surface of PGC for anion-exchange chromatography.[9] A number of additional adsorbates that can similarly modify PGC are mentioned in the paper of West et al.[10] Hamisch et al. were able to chemically modify the surface of PGC using diazonium salts and then use the modified surface for separation of phenolic compounds.[11] Wildgoose et al. were able to chemically modify both graphitic powder and carbon nanotubes with diazonium salts.[12]

In this contribution the radical functionalization of PGC in packed beds using a neat, commercially available peroxide: di-*tert*-amylperoxide (DTAP, $(CH_3CH_2C(CH_2)_2O)_2$) is explored. This manuscript represents a search of more than two years for a way to improve the properties of PGC. During most of this time, and up to this most recent discovery, all of the attempts to modify PGC degraded its chromatographic properties. These failed attempts used various reagents that produce radical moieties upon exposure to heat: pentafluoroiodobenzene, 1-iodoperfluoroctane, azobisisobutyronitrile (AIBN), and 2,2'-azobis(2-methylpropane). Upon heating, DTAP decomposes into two peroxy radicals of the form $CH_3CH_2C(CH_2)_2O•$, which are believed to add to the π network of PGC particles, onto previously adsorbed DTAP fragments, and perhaps to other chemical groups that may be at the PGC surface. Our research group has previously explored the use of DTAP for surface functionalization of hydrogen- and deuterium-terminated diamond, which were treated with either neat DTAP[13] or a mixture of DTAP and styrene.[14] In both cases, the resulting materials were used for solid-phase extraction. A variety of radical-based reactions have also been demonstrated for the functionalization of other allotropes of carbon, including carbon nanotubes and fullerenes. Wang et al. used azo(bisisobutyronitrile) to functionalize single-walled nanotubes (SWNTs) by opening the π-bonds of the SWNTs.[15] Nakamura et al. successfully modified SWNTs without disturbing their electronic behavior through photolysis of perfluoroazooctane.[16] Fafan et al. were able to surface modify Buckminsterfullerenes with either fluoroalkyl iodides or fluorodiacyl peroxides.[17] These methods resulted in the surface functionalization of polyaromatic systems that resemble the π network of graphite.

After treatment with DTAP, the chromatographic properties of PGC are changed. Plate numbers from peaks of various analytes increase, their asymmetries decrease, and their retention factors also decrease somewhat. Functionalized particles are characterized with a suite of techniques. ToF-SIMS, in particular, suggests chemical differences between the functionalized and unfunctionalized materials. First principle calculations suggest that the first addition of a radical fragment of DTAP to the surface is approximately thermoneutral, but that subsequent additions of these radicals are increasingly favorable.

8.3. Experimental

8.3.1. Reagents and Materials

Reagents included: di-*tert*-amyl peroxide (Luperox® DTAP® 97% Sigma-Aldrich), water (18 MΩ resistance, filtered using a Milli-Q Water System, Millipore, Billerica, MA), methanol (HPLC grade, Fisher Scientific, Fair Lawn, NJ), and a Benzenoid Hydrocarbon Kit (Sigma Aldrich) containing the following analytes: benzene, toluene, ethyl benzene, *n*-propyl benzene, *n*-butyl benzene, *p*-xylene, phenol, 4-methylphenol, phenetole, 3,5-xylenol, and anisole. Hypercarb™ columns (50 x 2.1 mm) containing metal, not PEEK (to avoid possible polymerization of DTAP onto PEEK[13]), frits were packed with 5 µm diameter particles provided by ThermoFisher, Runcorn UK. Loose 5 µm Hypercarb™ particles were packed in-house (at BYU) using a Chrom Tech Pack in the Box system (Apple Valley, MN). The particles packed at BYU were used for SEM, BET, XPS, and ToF-SIMS analyses.

8.3.2. Chromatography

HPLC was performed using a Waters binary HPLC pump (Model No. 1525) equipped with a 5 µL sample injection loop. Detection was with a dual wavelength detector (Model No. 2487). The columns were thermostated at 30 ± 0.5°C using a column oven (Model Number 5CH), all from Waters Corporation, Milford, MA. The LC system was fitted with a 17 bar backpressure regulator.

8.3.3. Surface Measurements

X-ray photoelectron spectroscopy (XPS) was performed with a Surface Science SSX-100 X-ray photoelectron spectrometer (serviced by Service Physics, Bend, OR) with a monochromatic Al K_α source, a hemispherical analyzer, and a take-off angle of 35°. Survey scans as well as narrow scans were recorded with 800 µm × 800 µm spots. For XPS analysis the graphite powders were pressed into conductive double-sticky tape adhered to silicon wafers. SEM imaging was done on a Philips XL30 S-FEG. Surface area measurements were performed with a Micromeritics TriStar II instrument taking Brunauer−Emmett−Teller (BET) isotherm measurements from N_2 adsorption at 77 K. The samples were degassed at 200°C for 12 h prior to data collection. Static time-of-flight secondary ion mass spectrometry (ToF-SIMS) was performed at the Pacific Northwest National Laboratory using an IONTOF V instrument (Münster, Germany) with a 25 keV Bi^{3+} cluster ion source and sample area of 200 μm^2. For ToF-SIMS analysis the graphite powders were mounted onto conductive double-sticky tape adhered to silicon wafers.

8.3.4. First Principles Simulations on Graphite, Student's t-test, and Chemometrics Data Analysis

Restricted and unrestricted M06-2X density functional calculations were carried out in Jaguar 7.7 with the 6-311++G(d,p) basis set on (U)B3LYP/6-31G(d,p) optimized structures. All stationary points were confirmed to be minima by computing the full Hessian using Gaussian 03. To determine statistical differences between the functionalized and unfunctionalized materials a one-tailed Student's t-test at a 95% confidence interval was used. Since most of the chromatographic peaks were asymmetric we used the following equation to calculate N:[18]

$$N = \frac{47.1(\frac{t_r}{w_{10\%}})^2}{(\frac{B}{A})_{10\%} + 1.25}$$

where $(B/A)_{10\%}$ is the asymmetry factor at 10%, t_r is the retention time, and $w_{10\%}$ is the width at 10% peak height. Chemometric data analyses were performed using the PLS_Toolbox (Version 6.0) from Eigenvector Research (Wenatchee, WA).

8.3.5 In situ Functionalization of PGC

A new, 50 x 2.1 mm ID column packed with 5 µm PGC particles was flushed with a minimum of 30 column volumes of degassed methanol, followed by 20 column volumes of DTAP, all at room temperature. The column oven (Polaratherm Series 9000, Selerity, SLC, UT) was then set at 145˚C and held at that temperature for 1 h while pumping DTAP through the column at 0.1 mL/min. This corresponded to ca. 35 column volumes of DTAP. The DTAP was sparged with helium throughout both the initial flushing and functionalization steps. After functionalization the column was brought to room temperature and then flushed with a minimum of 350 column volumes of methanol. After chromatographic evaluation, the column was subjected to a second modification with DTAP that was identical to the first. This double functionalization was performed on three separate 50 x 2.1 mm columns. Each column was chromatographically tested prior to functionalization and after the first and second functionalizations.

8.3.6. HPLC

All separations were isocratic with a 40:60 H_2O/methanol mobile phase at a flow rate of 0.5 mL/min. No effort was made to optimize the flow rate. The solvents, including methanol, were sparged with helium using a home built sparging apparatus. The LC system was fitted with a 17 bar (250 psi) backpressure regulator and the total backpressure during chromatography was approximately 240 bar (3200 psi). The column was thermostated at 30.0°C and the UV detector was set at 254 nm. Each analyte was dissolved in methanol. Acetone was added as the dead time marker. Each analyte was injected manually in replicates of four – no mixtures of analytes were used.

8.3.7. Stability Test

One of the columns, which had been doubly functionalized with DTAP, was subjected to two separate elevated temperature tests in which the mobile phase was 100% methanol and the flow rate was 1.0 mL/min at 100°C. Each stability test was performed for 5 h after which the column was cooled and chromatographic characterization was performed.

8.4. Results and Discussion

8.4.1. Chromatographic Performance of Functionalized Porous Graphitic Carbon (PGC)

Chromatographic evaluation on three separate PGC columns was performed before functionalization and then after each of two functionalizations with di-*tert*-amylperoxide (DTAP) to determine if any change in the retention factor (*k*), number of theoretical plates (N), and/or asymmetry ($\text{asymm.}_{10\%}$) was achieved (Table 8.1). After the second functionalization with DTAP, and the subsequent characterization of the columns, one of the columns was subjected to two separate elevated temperature tests for 5 h, each at 100˚C, under a steady flow of methanol (1 mL/min).

Table 8.1 Average values of the retention factor (*k*), number of theoretical plates (*N*), and tailing factor (10% asymmetry) from four injections of each analyte on three separate columns before and after functionalization.

Average									
Values	Prefunctionalization								
Analytes (n=12)	*k*			N			Asymmetry (10%)		
benzene	0.751	±	0.016	173	±	15	1.945	±	0.085
toluene	2.876	±	0.022	271	±	13	3.262	±	0.097
ethyl benzene	3.912	±	0.027	259	±	39	3.643	±	0.143
proply benzene	8.312	±	0.065	80	±	8	7.607	±	0.426
butyl benzene	21.131	±	0.436	72	±	17	7.383	±	1.284
p-xylene	11.337	±	0.242	139	±	12	5.724	±	0.294
phenol	0.865	±	0.016	177	±	8	1.983	±	0.044
4-methyl phenol	3.294	±	0.056	272	±	21	3.058	±	0.116
phenetole	7.538	±	0.107	297	±	23	4.128	±	0.198
xylenol	9.400	±	0.247	190	±	12	4.971	±	0.185
anisole	3.123	±	0.070	308	±	15	3.013	±	0.069

Average									
Values	1st Functionalization								
Analytes (n=12)	*k*			N			Asymmetry (10%)		
benzene	0.722	±	0.011	160	±	7	2.040	±	0.052
toluene	2.737	±	0.013	216	±	12	3.090	±	0.074
ethyl benzene	3.788	±	0.024	254	±	19	2.961	±	0.112
proply benzene	8.119	±	0.106	202	±	16	4.627	±	0.205
butyl benzene	19.956	±	0.199	96	±	27	5.095	±	0.590
p-xylene	10.667	±	0.093	188	±	12	4.484	±	0.232
phenol	0.760	±	0.025	186	±	10	1.801	±	0.076
4-methyl phenol	2.872	±	0.017	340	±	10	2.536	±	0.085
phenetole	7.633	±	0.056	350	±	117	3.295	±	0.450
xylenol	8.224	±	0.041	213	±	12	5.907	±	0.299
anisole	2.888	±	0.030	318	±	20	2.410	±	0.077

Average									
Values	2nd Functionalization								
Analytes (n=12)	*k*			N			Asymmetry (10%)		
benzene	0.730	±	0.013	162	±	7	1.966	±	0.043
toluene	2.697	±	0.136	292	±	39	2.506	±	0.143
ethyl benzene	3.761	±	0.057	341	±	23	2.395	±	0.086
proply benzene	8.103	±	0.068	280	±	23	3.668	±	0.089
butyl benzene	19.794	±	0.092	135	±	26	3.463	±	0.532
p-xylene	10.632	±	0.117	230	±	37	3.377	±	0.348
phenol	0.755	±	0.021	190	±	9	1.746	±	0.035
4-methyl phenol	2.860	±	0.128	350	±	12	2.240	±	0.038
phenetole	7.525	±	0.071	406	±	50	2.467	±	0.127
xylenol	7.984	±	0.046	228	±	17	4.026	±	0.268
anisole	2.850	±	0.023	347	±	14	2.242	±	0.082

Table 8.1 shows that after the first functionalization, all of the retention factors decrease somewhat (on average ca. -7%), the number of theoretical plates for the analytes increases by ca. 20%, and the chromatographic peaks generally become more symmetric (ca. -20% decrease in asymm.$_{10\%}$). Overall, improvements are again observed with the second functionalization, in which the retention values and N remain roughly constant, and the peak asymmetries continue to improve for a total improvement ofca. -35%. Thus it appears that functionalization of PGC with DTAP leads to a relatively small decrease in *k* with noticeable improvements in both N and asymmetry (Figure 8.1). These improvements in asymmetry may be a result of a decreased number of strongly adsorbing sites on the PGC after chemisorption or reaction with DTAP fragments. Thus, these results imply that the most strongly adsoptive sites on PGC are also the most reactive with DTAP.

To understand whether the changes in *k*, N, and the asymm.$_{10\%}$ are statistically different after the two functionalizations, Student's t-test was used by averaging values from three separate PGC columns that were functionalized with DTAP (see Table 8.2).

The t-test shows a clear change in the value of *k* for all the analytes after the first functionalization. This difference continues after the second functionalization for all the values of *k* but one (phenetole) compared to the values of the raw material. After the second functionalization, just over half the analytes undergo a statistically significant change in *k* compared to the first functionalization. Five of eleven analytes show an increase in N after one functionalization with DTAP, and nine out of eleven after two such functionalizations. Clearly, some of the analytes undergo larger changes in retention than others after DTAP functionalization of PGC. Presumably, this is because the new chemical moieties at the PGC surface interact more strongly with some analytes than others. Nevertheless, the fact that very large changes in retention are not observed leads us to believe that the PREG effect remains at largely operational. Finally, all but one analyte shows a decrease in asymmetry for both the first and second functionalizations compared to the unfunctionalized material.

In spite of the fact that many of the changes in k are statistically significant after functionalization (see Table 8.3), Table 8.1 shows that these changes are not large. In addition, because the retention factors for all the analytes tend to decrease uniformly and in the same direction, overall there is little change in selectivity. This is not necessarily bad; one of the main selling points of PGC is its unique selectivity. Table 8.4 shows the selectivities of four alkyl benzenes relative to benzene, and two aryl-alkyl ethers relative to phenol before and then after the two functionalizations. Plots of log k vs calculated dipole moment (see Figure 8.2) for the various analytes on the unfunctionalized and functionalized materials show no correlation between the variables, with all R^2 values less than 0.04. The primary gains of this functionalization appear to be in the improvements in numbers of plates and better peak asymmetries.

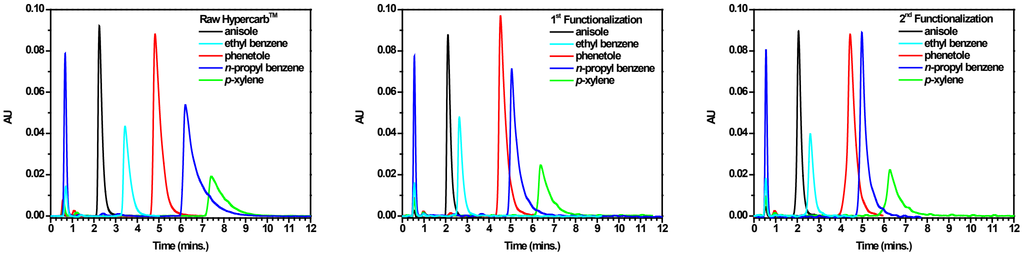

Figure 8.1 Representative composite chromatograms (each compound was injected separately) for the raw Hypercarb™ (PGC), 1st functionalization of PGC with DTAP, and 2ndfunctionalization of PGC with DTAP.

Table 8.2 Chromatographic data for each of the two elevated temperature stress tests.

Column				**Column**			
0600560T	**1st Elevated Temperature Test**			**0600560T**	**2nd Elevated Temperature Test**		
Analytes (n=4)	***k***	***NTP***	**Asymmetry10%**	**Analytes (n=4)**	***k***	***NTP***	**Asymmetry10%**
benzene	0.728 ± 0.003	217 ± 10	1.651 ± 0.022	benzene	0.699 ± 0.005	210 ± 6	1.643 ± 0.022
toluene	2.746 ± 0.025	653 ± 16	2.330 ± 0.043	toluene	2.623 ± 0.003	618 ± 18	2.333 ± 0.022
ethyl benzene	3.765 ± 0.040	779 ± 56	2.407 ± 0.066	ethyl benzene	3.631 ± 0.004	765 ± 47	2.313 ± 0.072
proply benzene	8.114 ± 0.012	1659 ± 66	2.945 ± 0.111	proply benzene	7.897 ± 0.037	1993 ± 223	2.643 ± 0.035
butyl benzene	19.413 ± 0.128	927 ± 62	3.920 ± 0.313	butyl benzene	18.800 ± 0.117	1292 ± 65	3.204 ± 0.255
p-xylene	10.422 ± 0.063	1186 ± 158	2.566 ± 0.151	p-xylene	10.350 ± 0.085	1300 ± 106	2.346 ± 0.049
phenol	0.754 ± 0.004	212 ± 2	1.411 ± 0.009	phenol	0.760 ± 0.005	212 ± 6	1.391 ± 0.016
4-methyl phenol	2.830 ± 0.011	554 ± 27	1.837 ± 0.020	4-methyl phenol	2.813 ± 0.007	556 ± 6	1.853 ± 0.025
phenetole	7.961 ± 0.031	1438 ± 144	1.898 ± 0.088	phenetole	7.730 ± 0.064	1523 ± 80	1.829 ± 0.023
xylenol	8.909 ± 0.028	1359 ± 75	1.554 ± 0.051	xylenol	8.835 ± 0.030	1348 ± 49	1.548 ± 0.041
anisole	2.804 ± 0.005	708 ± 30	2.109 ± 0.003	anisole	2.766 ± 0.009	695 ± 13	1.966 ± 0.021

Table 8.3 Average percent differences of the retention factor (*k*), number of theoretical plates (*N*), and tailing factor (10% asymmetry for four injections of each analyte on three separate columns before and after functionalization.

Percent Difference between 1st Funct. and Unfunct.				Percent Difference between 2st Funct. and Unfunct.				Percent Difference Between 1st Funct. and 2nd Funct.			
	k	*N*	**Asymmetry10%**		*k*	*N*	**Asymmetry10%**		*k*	*N*	**Asymmetry10%**
benzene	-4.0	-7.8	4.7	benzene	-2.9	-6.6	1.0	benzene	1.2	1.2	-3.7
toluene	-5.0	-22.5	-5.4	toluene	-6.4	7.6	-26.2	toluene	-1.5	30.0	-20.9
ethyl benzene	-3.2	-1.9	-20.6	ethyl benzene	-3.9	27.3	-41.3	ethyl benzene	-0.7	29.1	-21.1
proply benzene	-2.3	86.2	-48.7	proply benzene	-2.5	110.9	-69.9	proply benzene	-0.2	32.5	-23.1
butyl benzene	-5.7	28.4	-36.7	butyl benzene	-6.5	61.1	-72.3	butyl benzene	-0.8	34.2	-38.1
p-xylene	-6.1	29.9	-24.3	p-xylene	-6.4	48.9	-51.6	p-xylene	-0.3	19.7	-28.2
phenol	-12.9	4.8	-9.6	phenol	-13.5	6.8	-12.7	phenol	-0.6	2.1	-3.1
4-methyl phenol	-13.7	22.1	-18.6	4-methyl phenol	-14.1	25.2	-30.9	4-methyl phenol	-0.4	3.1	-12.4
phenetole	1.3	16.3	-22.4	phenetole	-0.2	30.9	-50.4	phenetole	-1.4	14.8	-28.8
xylenol	-13.3	11.7	17.2	xylenol	-16.3	18.2	-21.0	xylenol	-3.0	6.5	-37.9
anisole	-7.8	3.1	-22.2	anisole	-9.1	11.9	-29.3	anisole	-1.3	8.8	-7.2

Table 8.4 Selectivity of various analytes, including selectivity of four alkyl benzenes vs. benzene and two aryl-alkyl ethers vs. phenol.

	Unfunctionalized	1st functionalized	2nd functionalized
	benzene selectivity		
toluene	3.8	3.8	3.7
ethyl benzene	5.2	5.2	5.2
propyl benzene	11.1	11.2	11.1
butyl benzene	28.1	27.6	27.1
	phenol selectivity		
anisole	3.6	3.8	3.8
phenetole	8.7	10.0	10.0

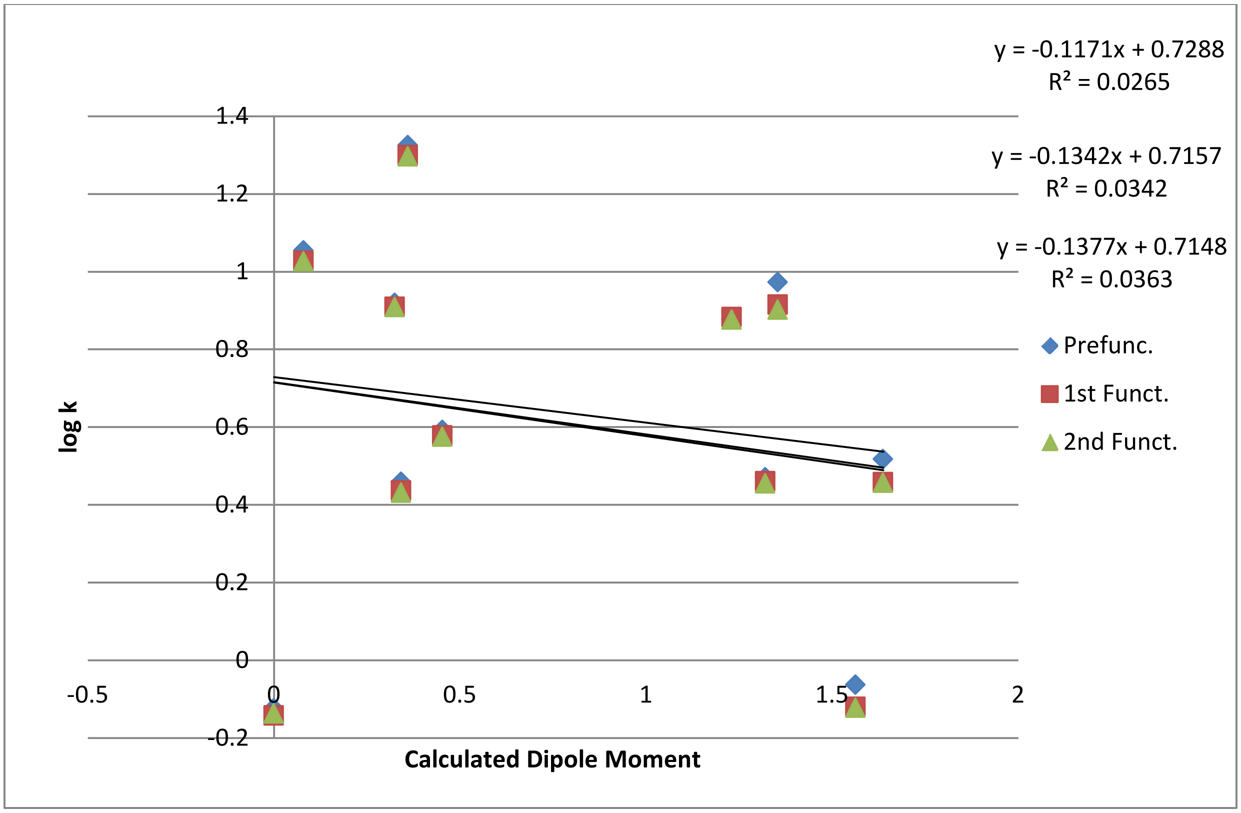

Figure 8.2 Calculated dipole moment vs log *k* for all tested analytes on functionalized and unfunctionalized materials. There appears to be no correlation between retention factor and dipole moment.

8.4.2. Stability Studies

Arguably, the first stability test performed on DTAP functionalized columns was the extensive rinsing of the columns with at least 350 column volumes of methanol after each of the first and second functionalizations. This stability test is consistent with the coating/functionalization produced by heating PGC in the presence of DTAP being stable against large quantities of a typical mobile phase for PGC ; all indications point to a change in PGC that is stable around room temperature to extensive washing with methanol and multiple injections. After the second functionalization with DTAP, and the subsequent characterization of the columns, one of the columns was subjected to two separate elevated temperature tests for 5 h, each at 100˚C, under a steady flow of methanol (1 mL/min). After each of these stability tests, the columns were characterized with the same set of analytes as before. As shown by the changes in *k,* N, and $\text{asymm.}_{10\%}$ (see Table 5) (i) the retention factors generally decrease by a small amount, where most of them undergo a statistically significant change, (ii) in general N decreases somewhat after the first stability test, and increases after the second stability test, where the changes between the second functionalization the first stability test collectively show the most statistical differences, and (iii) the asymmetry increases after the first stability test, and then drops after the second, where it is significant that asymmetries remain lower than for the unfunctionalized PGC, and again most of these difference are statistically significant.

Table 8.5 Average percent differences (bottom row) of *k*, *N*, and asymmetry$_{10\%}$ for multiple injections on a single column after a first and second elevated temperature test (MeOH at 100°C for 5 h at 1 mL/min) compared to PGC that was twice functionalized with DTAP. Also given is the percent difference in *k*, N, and TF$_{10\%}$ between unfunctionalized PGC that was subjected to two stability tests. Included above is a table of a Student’s t-test to indicate statistical differences between data sets.

Percent Difference Between 2nd Functionalized. and 1st Temp. Test				Percent Difference Between 1st Temperature Test				Percent Difference Between Raw PGC			
and 1st Temperature Test				and 2nd Temperature Test				and 2nd Temperature Test			
	k	*N*	**Asymmetry10%**		*k*	*N*	**Asymmetry10%**		*k*	*N*	**Asymmetry10%**
benzene	0.3	-18.8	15.5	benzene	-4.0	-2.2	-1.7	benzene	-7.0	-8.6	7.7
toluene	5.3	-70.8	46.1	toluene	-4.6	5.0	-5.3	toluene	-9.5	-40.0	6.5
ethyl benzene	0.3	-80.6	48.7	ethyl benzene	-3.6	8.1	-5.7	ethyl benzene	-8.4	-25.0	0.3
proply benzene	-0.9	-59.0	26.3	proply benzene	-2.7	33.3	-13.7	proply benzene	-6.5	92.8	-43.0
butyl benzene	-2.4	-71.2	27.2	butyl benzene	-3.2	42.4	-17.3	butyl benzene	-14.5	22.5	-0.5
p-xylene	-2.7	-26.2	3.0	p-xylene	-0.7	32.4	-13.1	p-xylene	-9.5	34.4	-9.0
phenol	-1.7	-6.0	-2.2	phenol	0.8	1.9	-2.3	phenol	-12.2	-4.2	-12.5
4-methyl phenol	-1.6	-15.5	10.8	4-methyl phenol	-0.6	-1.7	1.6	4-methyl phenol	-16.1	-4.1	-4.2
phenetole	8.6	16.2	-14.6	phenetole	-2.9	18.5	-4.1	phenetole	1.1	52.3	-31.7
xylenol	8.3	100.6	-57.4	xylenol	-0.8	2.3	0.7	xylenol	-6.4	109.7	-66.9
anisole	-2.7	-41.3	40.1	anisole	-1.4	13.1	-10.3	anisole	-12.8	-9.2	-3.4

	Change in *k*			Change in *N*			Asymmetry10%		
	2nd Funt and 1st Heat	1st and 2nd Heat	Raw and 2nd Heat	2nd Funt and 1st Heat	1st and 2nd Heat	Raw and 2nd Heat	2nd Funt and 1st Heat	1st and 2nd Heat	Raw and 2nd Heat
benzene	-	+	+	+	-	-	+	-	-
toluene	-	+	+	+	+	+	+	+	+
ethyl benzene	-	+	+	+	+	-	+	+	+
proply benzene	+	+	+	+	+	+	+	+	+
butyl benzene	+	+	+	+	+	-	+	+	+
p-xylene	+	-	+	+	+	-	-	+	+
phenol	+	-	+	+	-	+	+	+	+
4-methyl phenol	+	+	+	+	-	+	+	-	+
phenetole	+	+	+	-	-	-	+	-	+
xylenol	+	+	+	+	-	-	+	-	+
anisole	+	+	+	+	+	+	+	+	+

8.4.3. Data Analysis by Principal Components Analysis (PCA) and Cluster Analysis

The Student's t-test is a valuable way of comparing pairs of averages. However, it does not see beyond two averages; it does not give a complete picture of the differences/similarities between columns, as there are many metrics used to characterize each of them under each set of conditions. In our case, each PGC column, under each set of conditions is characterized by the values of k, N, and asymm.$_{10\%}$ from 11 analytes for a total of 33 measurements. Hence, to better compare and understand the data, two multivariate data analysis tools: principal components analysis (PCA) and cluster analysis, were applied to the data. The data matrix for this analysis consisted of the data from each PGC column (the 11 k values, followed by the 11 N values, followed by the 11 asymm.$_{10\%}$ values from the 11 analytes) from the three PGC columns before functionalization (Points 1 – 3), after the first functionalization (Points 4 – 6), after the second functionalization (Points 7 – 9), and after the first (Point 10) and second (Point 11) 5 h methanol stability tests. Because of the difference in magnitude and units of k, N, and asymm.$_{10\%}$ the most appropriate preprocessing method for this data seemed to be autoscaling with no prior data normalization.

The principal components analysis of the data suggested that either three or five principal components (PCs) would best describe the data. The software recommended three PCs, and we took this recommendation, where three PCs account for 81.37% of the variation in the data. This recommendation is consistent with the scree test,[19] i.e., there is a change in slope between the third and fourth PCs in the plot of Eigenvalues vs. PC (see Figure 8.3).

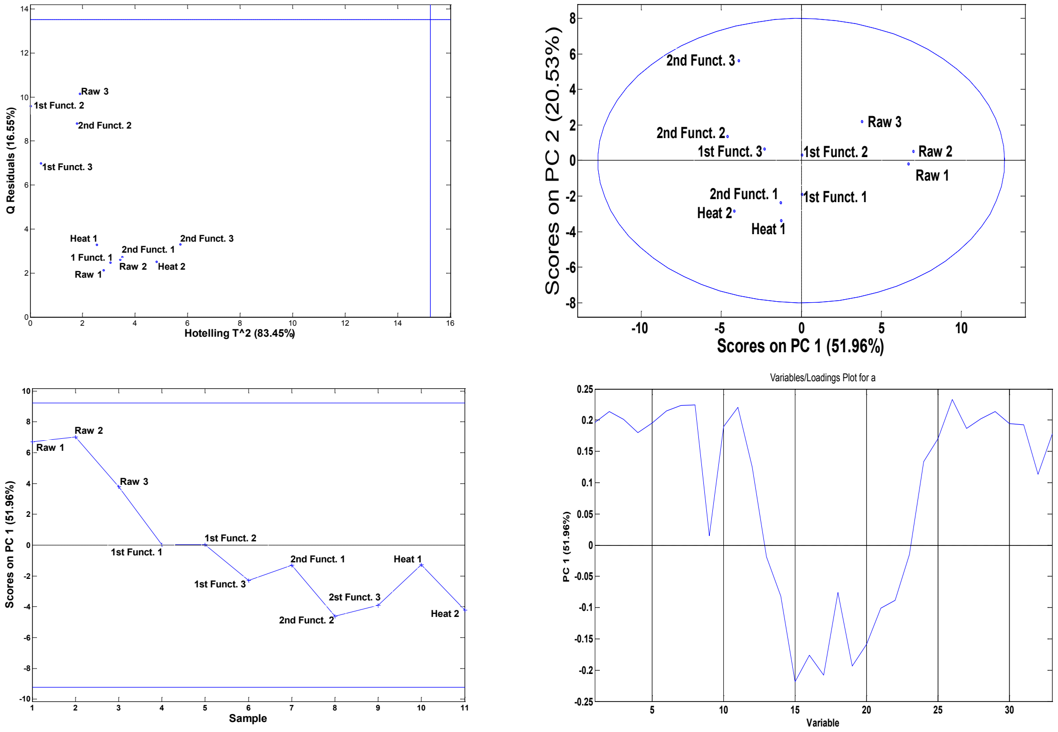

Figure 8.3 Principal components analysis of data from three unfunctionalized columns (Unfunct. 1 – Unfunct. 3), the same three columns after a first DTAP functionalization (1st Funct. 1 – 1st Funct. 3), the same three columns after a second DTAP functionalization (2nd Funct. 1 – 2nd Funct. 3), and two sequential 100°C MeOH stability tests on one of the columns (Heat 1 and Heat 2). Shown are plots of Q Residuals vs. Hotelling T^2 (the dashed lines show 95% confidence limits), Scores on PC2 vs. PC1, and Scores on PC1 vs. sample, Loadings on PC1 vs. Variable. For the loadings plot, variables 1-11 are the values of *k*, variables 12 - 22 are the values of N, and variables 23 - 33 are the values of $TF_{10\%}$.

The plot of Q Residuals vs. Hotelling T^2 (see Figure 8.3) indicates that there are no outliers in the data. The plot of the scores on PC1 vs. sample suggests that Samples 1 – 3 (the unfunctionalized PGC) are different from the remaining samples. The plot of the loadings on PC1 vs. variable shows that samples with high scores on PC1 (the unfunctionalized materials) generally have higher values of *k* (variables 1 – 11), lower values of N (variables 12 – 22), and higher values of $\text{asymm.}_{10\%}$ (variables 23 – 33). These features are consistent with the chromatographic properties of unfunctionalized PGC. The plot of scores on PC1 vs. scores on PC2 also suggests that samples 1, 2, and 3 (the unfunctionalized material) are different from the remaining samples. A cluster analysis (see Figure 8.4) clearly shows that Samples 1 – 3 are different from the other samples. Perhaps the most reasonable conclusion to draw from the PCA/cluster analyses is that there are two main groupings in the data: the unfunctionalized material and the functionalized material. An implication of this statement is that once functionalized, the columns do not change in a large way, showing good chemical resistance to subsequent functionalization, solvent, and temperature.

8.4.4. Materials Analysis

Surface/materials analysis was performed on PGC particles before and after functionalization with DTAP. Given that heated DTAP has shown some ability to add to itself on a surface, i.e., polymerize,[13] it was first necessary to determine whether any polymer was created or deposited in the interstitial volumes of PGC particles. Figure 8.5 is an scanning electron micrograph of PGC particles before and after the two DTAP functionalizations.

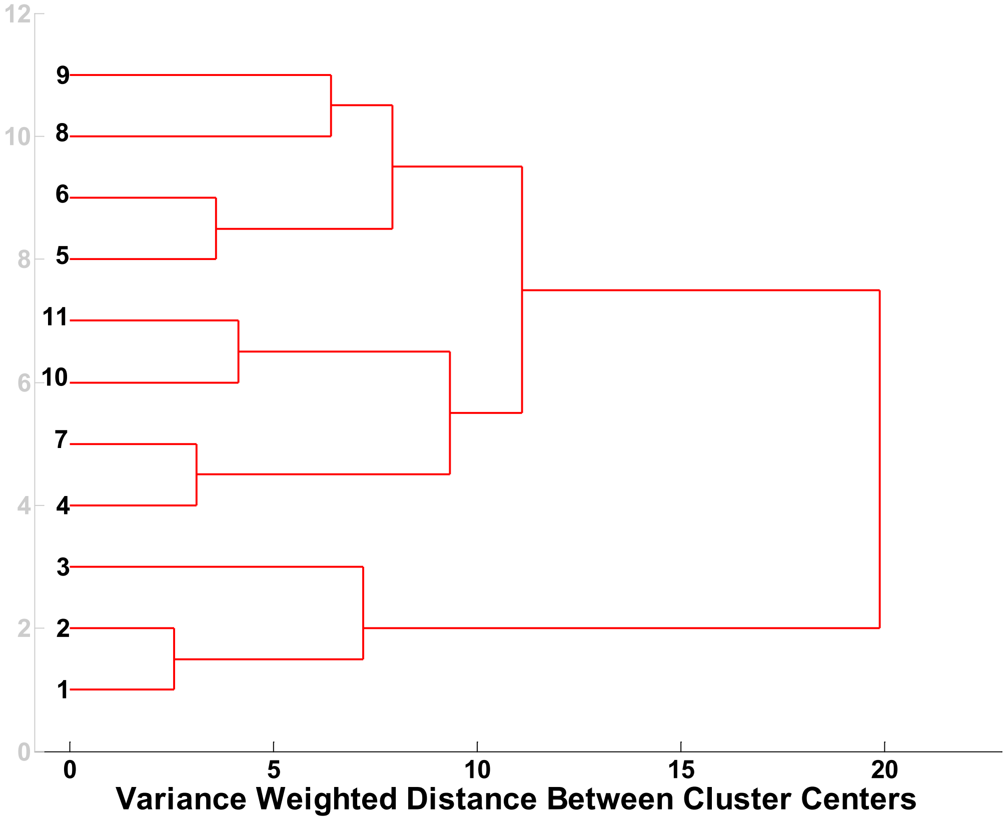

Figure 8.4 Dendrogram produced by a cluster analysis of the same data matrix used for the PCA analysis in Figure 8.3. Samples 1 – 3 (unfunctionalized PCG) and Samples 4 – 11 (the functionalized material) are clearly separated.

The important result of this analysis is that at both high and low magnifications we find no noticeable difference between the unfunctionalized and functionalized particles- *differences indicative of gross polymerization of DTAP would manifest themselves as distortions in the image due to charging of the polymer and/or as visible clogging of the pores*. Since PGC is highly conductive and no image distortions are observed, these results suggest that functionalization with DTAP occurs in a uniform manner that does not clog the pores of the material or lead to an excessively thick film.

As an additional probe of the degree of coating/functionalization of the PGC particles, BET surface area measurements were performed. The resulting surface area, pore volume, and pore diameter for unfunctionalized PGC were 158 m^2/g, 0.81 cm^3/g, and 110 Å, respectively, and for doubly functionalized PGC were 160 m^2/g, 0.82 cm^3/g, and 110 Å, respectively.

In our experience the uncertainty in this measurement is in the final digit. One analysis was performed of each material. Clearly, this analysis shows that functionalization with DTAP does not alter the surface area, pore volume, and pore diameter of PGC. Both functionalized and unfunctionalized PGC particles were also characterized by X-ray photoelectron spectroscopy (XPS). It was anticipated that chemical analysis of the functionalized materials might be challenging because the functionalization of PGC with DTAP represents the deposition of a material composed of carbon, hydrogen, and oxygen onto a material of similar composition. XPS probes the upper ca. 10 nm of materials and is sensitive to all elements except H and He. In the analysis of PGC particles before and after functionalization with DTAP, XPS survey scans showed that both materials are mostly carbon and that no elements besides carbon and oxygen are present (see Figure 8.6).

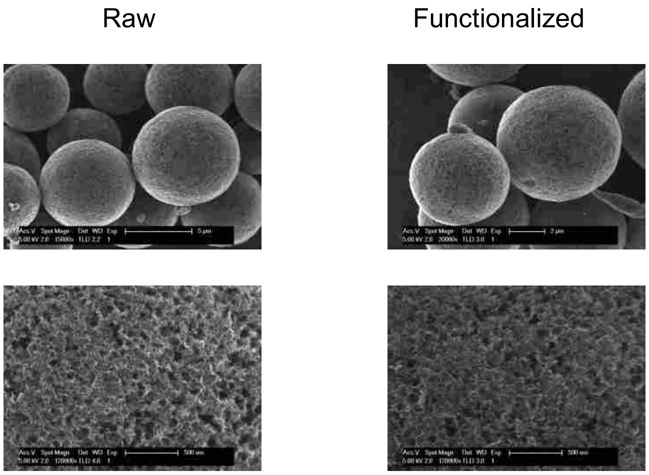

Figure 8.5 SEM images of the raw (prefunctionalized) PGC (left images) and PGC functionalized twice with DTAP (right images).

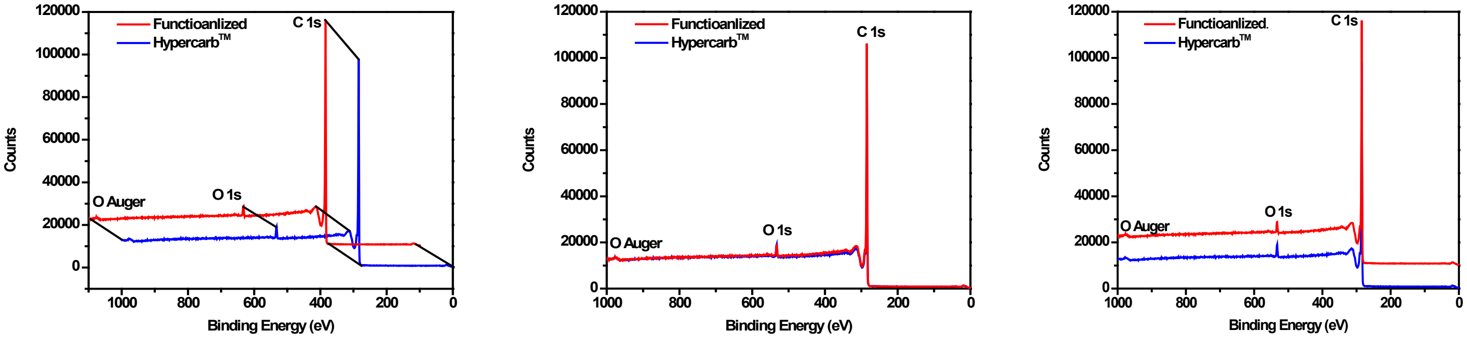

Figure 8.6 Three views of the same two XPS survey scans of PGC, and PGC functionalized twice with DTAP. The spectra show only carbon and oxygen.

XPS analysis of the PGC samples before and after functionalization could be performed without employing charge compensation. An absence of charging was expected for the unfunctionalized particles, as they are made of graphitic carbon, and should be conductive. For the functionalized particles, this lack of surface charging is, like the SEM results, consistent with deposition of a very thin film of DTAP of molecular dimensions on the surfaces of the particles. Both functionalized and unfunctionalized PGC particles were further characterized by time-of-flight secondary ion mass spectrometry (ToF-SIMS), a form of surface mass spectrometry. ToF-SIMS provides chemical information about the upper ca. 3 nm of a material, and is sensitive to all elements, generally giving the analyst a semiquantitative measure of surface chemistry. Because SIMS spectra are generally quite complex, typically containing large numbers of peaks, chemometrics methods are regularly applied to SIMS data. PCA, which is essentially a pattern recognition technique, is one of the most commonly used. Accordingly, 20 peaks were selected from the positive and negative ion SIMS spectra from samples of functionalized and unfunctionalized PGC (see Figure 8.7).

Significantly, the biplot (the plot of both loading and scores on PC1 and PC2) shows that the functionalized samples are richer in the heavier hydrocarbon fragments, and in particular in the five-carbon fragments that are expected from chemisorbed DTAP fragments – note the positions in the plot of $C_5H_{11}^+$ and other related five and four carbon fragments. Indeed, the cation $C_5H_{11}^+$would be expected from chemisorbed $–OC(CH_3)_2CH_2CH_3$ because it is bonded to oxygen, an electron withdrawing element, and scission of the C-O bond would lead to formation of a stable, tertiary cation. Another interesting result of this analysis is that the O^- and OH^- peaks appear far to the right in the biplot, i.e., these species are more prevalent on the unfunctionalized samples, even though there is oxygen in the DTAP. These results would be consistent with

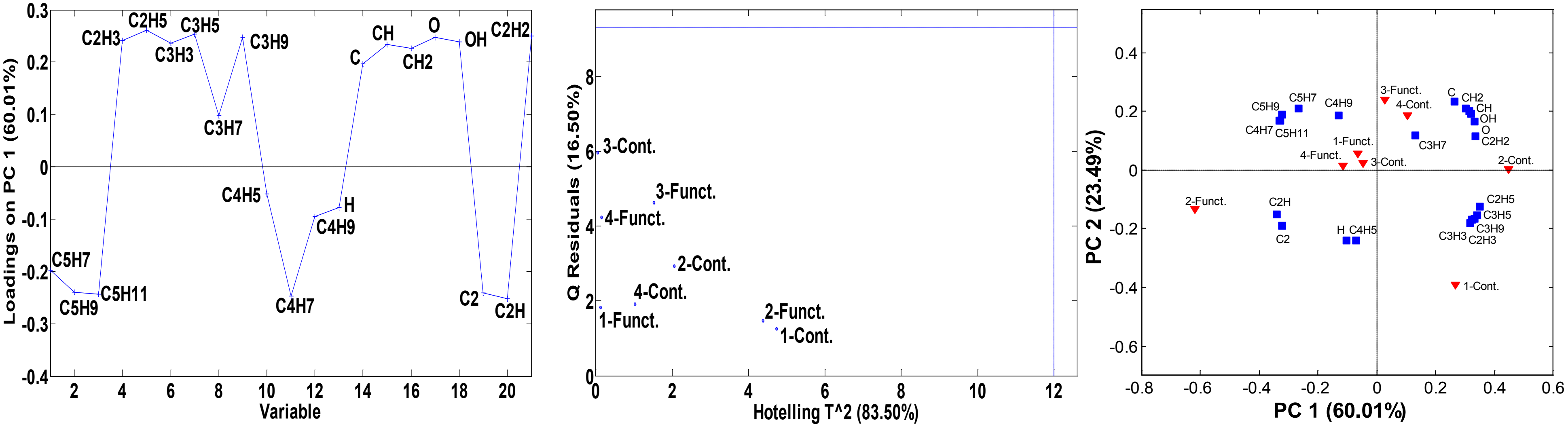

Figure 8.7 Results of a principal components analysis of ToF-SIMS data from functionalized and unfunctionalized PGC. Shown are scores on PC1 vs. Sample, a plot of Q Residuals vs. Hotelling T^2 (the dashed lines show 95% confidence limits), and a biplot of scores and loadings on PC1 and PC2. 'Cont.' stands for control (unfunctionalized material) and 'Funct.' stands for doubly functionalized material.

functionalization of PGC with DTAP to remove or cover strongly adsorbing sites, where these sites may contain oxygen and lead to peak asymmetry in chromatography.

8.4.5. First Principle Calculations on Model Surfaces

To investigate the thermodynamics of C-O covalent bond formation between graphite and the $C_5H_{11}O$ radical quantum mechanical calculations in the form of density functional theory was utilized. Restricted and unrestricted M06-2X density functional calculations[20-22] were carried out in Jaguar 7.7[23] with the 6-311++G(d,p) basis set on (U)B3LYP/6-31G(d,p) optimized structures. All stationary points were confirmed to be minima by computing the full Hessian using Gaussian 03.[24] Graphite was modeled in two ways: (1) a 5 by 4 grid of graphene hexagonal carbon rings capped with hydrogen ($C_{58}H_{20}$) and (2) as circumcoronene ($C_{54}H_{18}$).[25-26] (For the $C_{58}H_{20}$ model cluster the B3LYP energy solution has an unrestricted solution 5 kcal/mol lower than the restricted solution. In contrast, the $C_{54}H_{18}$ cluster model has a stable B3LYP energy solution.) Figure 8.8a shows the optimized $C_{58}H_{20}$ cluster model and Figure 8.8b shows the optimized structures for addition of a single $C_5H_{11}O$ radical species at the C1 and C5 carbon centers. C1 and C5 carbon atoms are closest to the center of this cluster model and likely best mimic bulk graphene properties.

The M06-2X density functional approximation predicts $C_5H_{11}O$ radical addition to be exothermic by -13 to -19 kcal/mol. Upon C-O (1.49Å) covalent bond formation the C1 and C5 carbon centers become sp^3 hybridized and tetrahedral resulting in slight deformation of the graphene sheet with a carbon surface internal dihedral angle of 30º. There is a kinetic barrier for $C_5H_{11}O$ radical addition. A potential energy scan of the forming C-O bond from 3.0Å to 1.6Å shows a peak at 2.0Å that approximates the transition structure. The barrier for this process is estimated to be ca. 13 kcal/mol.

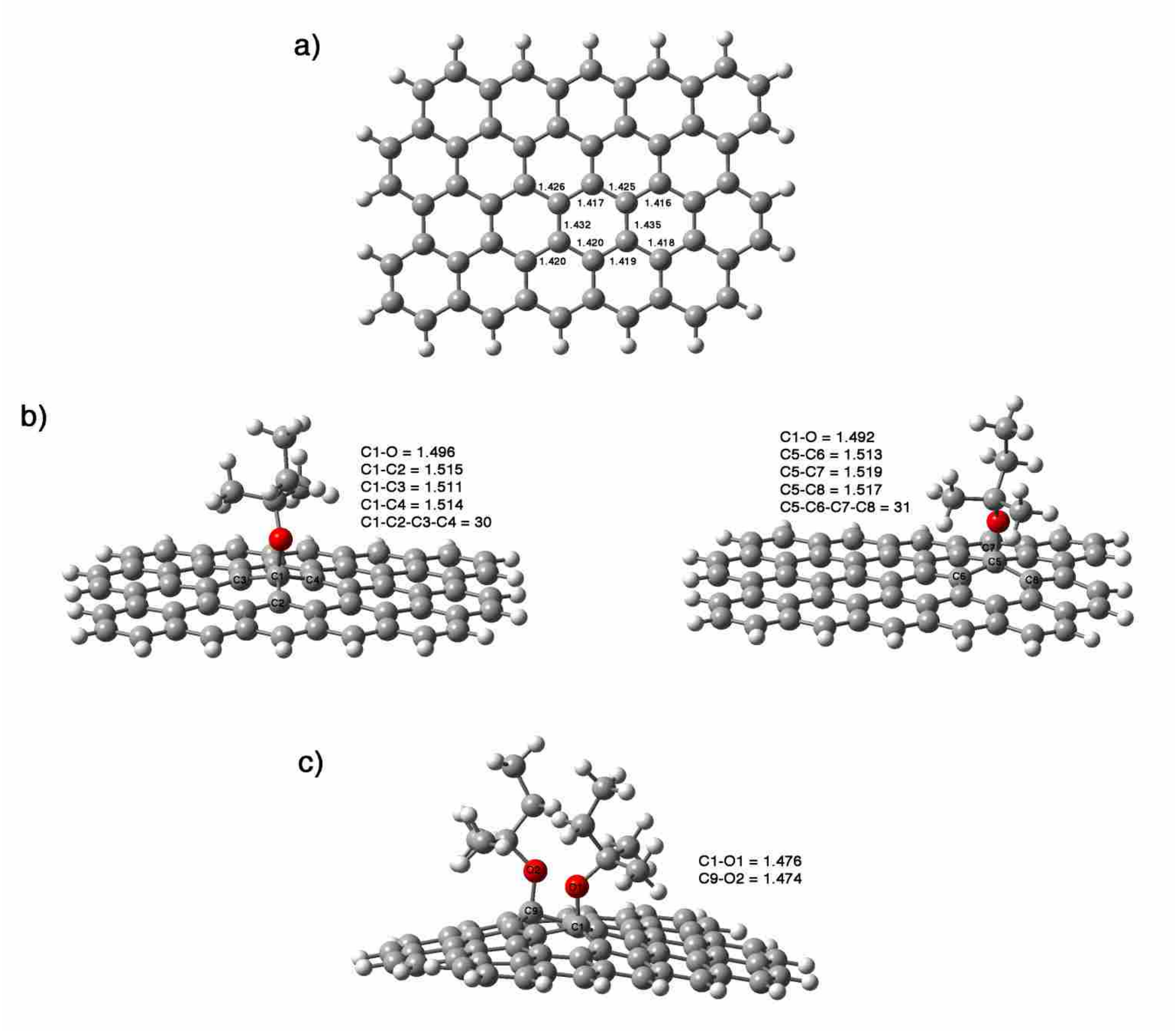

Figure 8.8 a) $C_{58}H_{20}$ hydrogen-capped graphite cluster model, b) single C-O bond formation, and c) double C-O bond formation.

Figure 8.8c shows the optimized structure for addition of a second $C_5H_{11}O$ radical unit with a 1,4-carbon atom relationship. Attempted optimization of $C_5H_{11}O$ radical addition to adjacent carbons (1,2-addition) resulted in the formation of only one C-O covalent bond and dissociation of one of the $C_5H_{11}O$ radicals due to steric repulsions. The formation of the second C-O bond is favorable by –22 kcal/mol. However, these thermodynamic values are relative to $C_5H_{11}O$ radicals. The thermodynamics of $(C_5H_{11}O)_2$ addition to give the structure in Figure 8.3c is close to thermal neutral due to the energy required to break the relatively weak O-O bond. The thermodynamics for $C_5H_{11}O$ radical addition depend upon the graphene model used. For example, the $C_{54}H_{18}$ circumcoronene cluster model (see Figure 8.9) shows a much less exothermic addition of the $C_5H_{11}O$ radical. Addition of two $C_5H_{11}O$ radical species to this surface results in an exothermic reaction of only -6 kcal/mol (Figure 10 8b). Comparison of this structure to $(C_5H_{11}O)_2$ and circumcoronene shows that this process would be thermodynamically unfavorable.

Although functionalization of $C_{58}H_{20}$ with one unit of $(C_5H_{11}O)_2$ is only slightly favorable, increasing the number of covalent C-OR surface functionalizations leads to more favorable thermodynamics. Figure 8.10 plots the M06-2X C-OR bond energies ($R = CH_3$) for addition to the $C_{58}H_{20}$ cluster model. Addition of one to four C-OR bonds leads to bond energies less than 20 kcal/mol. However, as the surface becomes more saturated the bond energies increase up to 35 kcal/mol. The increase in bond energy as the surface becomes more saturated is likely the result of decreased π conjugation stabilization throughout the surface. In a real material that contains defects, such as PGC, the process should be even more thermodynamically favorable – the degree of π conjugation stabilization for the material would be expected to be less significant.

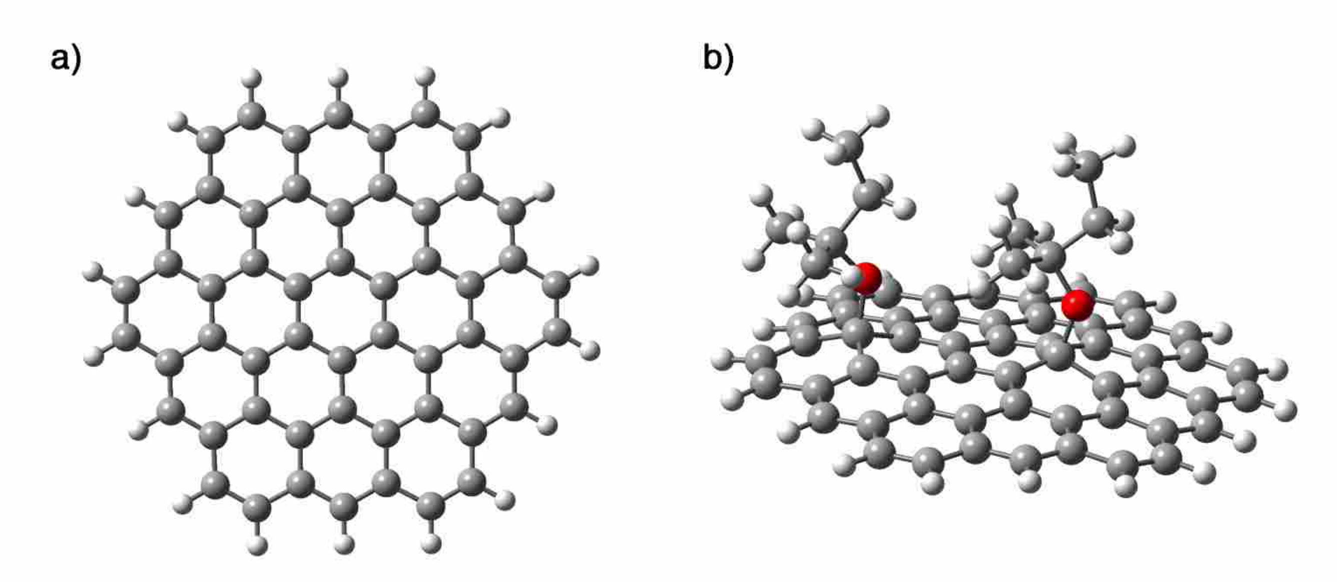

Figure 8.9 a) Circumcoronene ($C_{54}H_{18}$) model, b) $C_5H_{11}O$ radical addition.

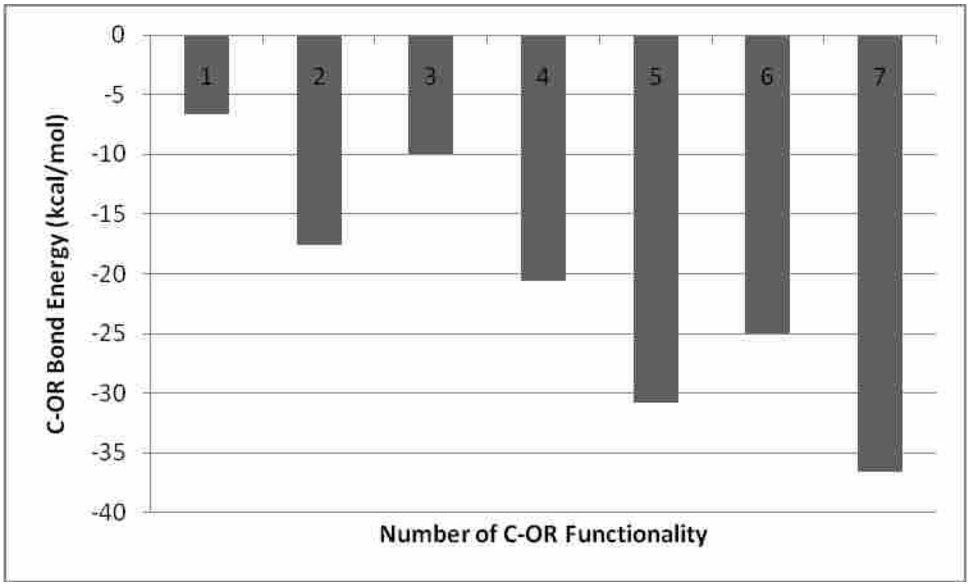

Figure 8.10 Plot of increasing number of C-OR for (R = CH_3) bonds formed on the $C_{58}H_{20}$ surface vs. C-OR bond energy.

8.5. Conclusions

It has been shown that the functionalization of porous graphitic carbon particles with neat, heated di-*tert*-amylperoxide influences its chromatographic properties. The performance of the particles for liquid chromatography was assayed before and after functionalization and stability tests. After two functionalizations, retention factors of test analytes decreased slightly, their numbers of theoretical plates increased, and their asymmetries decreased. The performance of the particles was still improved over the unfunctionalized material after two elevated temperature stability tests. A chemometrics analysis of the chromatographic data appeared to be consistent with these results. Scanning electron microscopy and BET suggested no substantial difference in morphology or surface area between the functionalized and unfunctionalized particles. A principal components analysis of time-of-flight secondary ion mass spectrometry data suggested that the surface chemistry was changed after functionalization, where signals from five carbon fragments were stronger on the functionalized material. First principle calculations showed that addition of the first alkoxy radical to the PGC surface might be thermal neutral or perhaps somewhat unfavorable. However, the thermodynamics of adsorption would become increasingly favorable with increased material derivatization.

It appears that DTAP functionalization did not significantly change the retention mechanism/selectivity of PGC, while in general it did lead to improvements in N and $\text{asymm.}_{10\%}$. Thus, DTAP may play the role of reacting with/covering any highly adsorptive sites on PGC that cause gross tailing. Hence, this functionalization might be considered a surface passivation of highly adsorptive sites in rather than a more traditional functionalization that might be aimed at entirely changing the chemistry, and therefore selectivity, of the stationary phase.[27]

8.6. Acknowledgments

We thank Diamond Analytics, a US Synthetic company (Orem, UT), for funding this study. Part of this research was performed at EMSL, a national scientific user facility sponsored by the Department of Energy's Office of Biological and Environmental Research and located at Pacific Northwest National Laboratory.

Author contributions: D.J. and M.L. conceived the idea of using DTAP. D.J. and V.G. did chromatographic testing. R.O. did BET surface area measurements. D.J. did XPS and Z.Z. did ToF-SIMS analyses. A.M. and D.E. did first principle calculations. R.D., M.A., and A.D., helped direct the research. M.L. was the principle investigator of the project. The manuscript was written by D.J. and M.L.

8.7. References

1. Pereira, L., *J. Liq. Chromatogr. Relat. Technol.* 2008, *31* (11), 1687 - 1731.

2. Teutenberg, T.; Tuerk, J.; Holzhauser, M.; Kiffmeyer, T. K., *J. Chromatogr., A* 2006, *1119* (1-2), 197-201.

3. Teutenberg, T.; Tuerk, J.; Holzhauser, M.; Giegold, S., *J. Sep. Sci.* 2007, *30* (8), 1101-1114.

4. Knox, J.; Ross, P., Carbon-based packing materials for liquid chromatography: Structure, performance and retention mechanisms. In *Advances in Chromatography*, Grushka, E., Ed. 1997; Vol. 37, pp 73-119.

5. Knox, J.; Wan, Q., *Chromatographia* 1996, *42* (1), 83-88.

6. Schoenmakers, P. J.; Uunk, L. G. M.; Janssen, H.-G., *J. Chromatogr., A* 1990, *506*, 563-578.

7. Knox, J. H.; Wan, Q.-H., *Chromatographia* 1995, *40* (1-2), 9-14.

8. Nagashima, H.; Okamoto, T., *J. Chromatogr., A* 1999, *855* (1), 261-266.

9. Chambers, S. D.; Lucy, C. A., *J. Chromatogr., A* 2007, *1176* (1-2), 178-184.

10. West, C.; Elfakir, C.; Lafosse, M., *J. Chromatogr., A* 2010, *1217* (19), 3201-3216.

11. Harnisch, J. A.; Gazda, D. B.; Anderegg, J. W.; Porter, M. D., *Anal. Chem.* 2001, *73* (16), 3954-3959.

12. Wildgoose, G. G.; Lawrence, N. S.; Leventis, H. C.; Jiang, L.; Jones, T. G. J.; Compton, R. G., *J. Mater. Chem.* 2005, *15* (9), 953-959.

13. Yang, L.; Vail, M. A.; Dadson, A.; Lee, M. L.; Asplund, M. C.; Linford, M. R., *Chem. Mater.* 2009, *21* (19), 4359-4365.

14. Yang, L.; Jensen, D. S.; Vail, M. A.; Dadson, A.; Linford, M. R., *J. Chromatogr., A* 2010, *1217* (49), 7621-7629.

15. Wang, X.; Li, S.; Xu, Y.; Wan, L.; You, H.; Li, Q.; Wang, S., *Appl. Surf. Sci.* 2007, *253* (18), 7435-7437.

16. Nakamura, T.; Ishihara, M.; Ohana, T.; Tanaka, A.; Koga, Y., *Diamond Relat. Mater. 13* (11-12), 1971-1974.

17. Fagan, P. J.; Krusic, P. J.; McEwen, C. N.; Lazar, J.; Parkert, D. H.; Herron, N.; Wasserman, E., *Science* 1993, *262* (5132), 404-407.

18. Foley, J. P.; Dorsey, J. G., *Anal. Chem.* 1983, *55* (4), 730-737.

19. Otto, M., *Chemometrics: Statistics and Computer Application in Analytical Chemistry*. 2nd ed.; Wiley-VCH: 2007.

20. Becke, A. D., *J.Chem. Phys.* 1993, *98* (7), 5648-5652.

21. Lee, C.; Yang, W.; Parr, R. G., *Phys. Rev. B* 1988, *37* (2), 785.

22. Zhao, Y.; Truhlar, D., *Theor. Chem. Acc.* 2008, *120* (1), 215-241.

23. Esconjauregui, S.; Fouquet, M.; Bayer, B. C.; Ducati, C.; Smajda, R.; Hofmann, S.; Robertson, J., *ACS Nano* 2010, *4* (12), 7431-7436.

24. M. J. Frisch; G. W. Trucks; H. B. Schlegel, G. E. S., M. A. Rob, J. R. Cheeseman, J. A. Montgomery Jr., T. Vreven, K. N. Kudin, J. C. Burant, J. M. Millam, S. S. Iyengar, J. Tomasi, V. Barone, B. Mennucci, M. Cossi, G. Scalmani, N. Rega, G. A. Petersson, H. Nakatsuji, M. Hada, M. Ehara, K. Toyota, R. Fukuda, J. Hasegawa, M. Ishida, T. Nakajima, Y. Honda, O. Kitao, H. Nakai, M. Klene, X. Li, J. E. Knox, H. P. Hratchian, J. B. Cross, V. Bakken, C. Adamo, J. Jaramillo, R. Gomperts, R. E. Stratmann, O. Yazyev, A. J. Austin, R. Cammi, C. Pomelli, J. W. Ochterski, P. Y. Ayala, K. Morokuma, G. A. Voth, P. Salvador, J. J. Dannenberg, V. G. Zakrzewski, S. Dapprich, A. D. Daniels, M. C. Strain, O. Farkas, D. K. Malick, A. D. Rabuck, K. Raghavachari, J. B. Foresman, J. V. Ortiz, Q. Cui, A. G. Baboul, S. Clifford, J. Cioslowski, B. B. Stefanov, G. Liu, A. Liashenko, P. Piskorz, I. Komaromi, R. L. Martin, D. J. Fox, T. Keith, M. A. Al-Laham, C. Y. Peng, A. Nanayakkara, M. Challacombe, P. M. W. Gill, B. Johnson, W. Chen, M. W. Wong, C. Gonzalez, and J. A. Pople, *Gaussian 03*, Revision D.01; Gaussian, Inc.: Wallingford, 2004.

25. Xu, S.; Irle, S.; Musaev, D. G.; Lin, M. C., *J. Phys. Chem. A* 2005, *109* (42), 9563-9572.

26. Montoya, A.; Truong, T. N.; Sarofim, A. F., *J. Phys. Chem. A* 2000, *104* (26), 6108-6110.

27. Srinivasan, G.; Kyrlidis, A.; McNeff, C.; Müller, K., *J. Chromatogr. A* 2005, *1081* (2), 132-139.

Chapter 9: XPS of Silicon (100)/SiO_2*

9.1. Abstract

Silicon (100) substrates are ubiquitous in microfabrication and, accordingly, their surface characteristics are important. Herein, we report the analysis of Si (100) via X-ray photoelectron spectroscopy (XPS) using monochromatic Al Kα radiation. Survey scans show that the material is primarily silicon and oxygen with small amounts of carbon, nitrogen, and fluorine contamination. The Si 2p region shows two peaks that correspond to elemental silicon and silicon dioxide. Using these peaks the thickness of the native oxide (SiO_2) is estimated using the equation of Strohmeier.[1] The oxygen peak is symmetric. These silicon wafers are used as the substrate for subsequent growth of templated carbon nanotubes in the preparation of microfabricated thin layer chromatography plates.[2-4]

9.2. Introduction

Silicon wafers, especially of the (100) orientation are widely used in microfabrication and in academic research. Accordingly, the surface characteristics of Si (100) are important. Here XPS was used to characterize the upper ca. 10 nm of this material. The present spectra are from a study by Jensen et al., the entirety of the study can be found in Ref 5.[5] The Si (100) sample was analyzed as received from the vendor, without any cleaning. The survey scan shows that the material is primarily silicon and oxygen (Figure 9.1). The narrow scan of the silicon 2p region contains two peaks (Figure 9.2) at 100.1 eV and 104.1 eV that correspond to elemental silicon and silicon dioxide, respectively, where the upper portion of the material is the native oxide layer. The thickness of the oxide layer calculated to be 1.18 ± 0.09 nm (average and standard

---

*This chapter has been submitted to *Surf. Sci. Spectra* for review (David S. Jensen, Supriya S. Kanyal, Michael A. Vail, Andrew E. Dadson, Mark Engelhard, and Matthew R. Linford)

deviation of two measurement on two different of two different pieces of silicon) using an equation developed by Strohmeier[1, 6] and Carlson.[7]

$$t_{ox} = \lambda_{SiO_2} sin\theta \; ln\left\{\left[\left({}^{1}/_{\beta}\right)\left(I_{SiO_2}/I_{Si}\right)\right] + 1\right\}$$

Where λ_{SiO2} is the inelastic mean free path (IMFP or attenuation length) of the Si 2p electrons in SiO_2, θ is the photoelectron take-off angle of the analyzer, $\beta = I^{\infty}_{SiO_2}/I^{\infty}_{Si}$ (I^{∞} corresponds to the Si 2p intensity for infinitely thick SiO_2 and Si as noted in its subscript), and the I_{SiO_2}/I_{Si} term is the ratio of peak areas from the unknown film. The IMFP for Si 2p photoelectrons in SiO_2 was taken as 2.7 ± 0.2 nm and the value used for β was 0.83.[8]

The valence band portion of the spectrum from ca. 0 – 25 eV is similar to the valence band spectra of other silicon wafers with ca. 1 nm of native oxide (Figure 9.3).[9-13] The oxygen peak is symmetric and centered at 533.3 eV (Figure 9.4). The survey spectra show surface contamination by fluorine, adventitious carbon, and nitrogen.

Si (100) wafers are used as the substrate for templated carbon nanotube (CNT) forests as part of a preparation of microfabricated thin-layer chromatography plates.[2-4] Indeed, submissions to Surface Science Spectra have been made on the XPS and SIMS characterization of the key materials in this microfabrication, Si/SiO_2 (the current submission and one on ToF-SIMS[14]) an alumina barrier layer on the Si/SiO_2 substrate,[15, 16] the Fe film on the alumina layer,[17, 18] the Fe film after annealing in H_2 to create Fe nanoparticles,[19, 20] and the carbon nanotube forest grown on the Fe nanoparticles.[21, 22]

9.3. Instrumental Parameters

XPS and valence band spectroscopy were performed on as received bare Si (100) wafers. This work was performed at the Pacific Northwest National Laboratory (PNNL) in the

Environmental Molecular Sciences Laboratory (EMSL) using a Physical Electronics Quantera Scanning X-ray Microprobe. This system uses a focused, monochromatic Al Kα X-ray (1486.7 eV) source for excitation, a spherical section analyzer, and a 32 element multichannel detection system. A 98 W X-ray beam focused to 100 μm (diameter) was rastered over a 1.3 mm x 0.1 mm rectangle on the sample. The X-ray beam is at normal incidence to the sample and the photoelectron detector is at 45° off-normal. High energy resolution spectra were collected using a pass-energy of 69.0 eV with a step size of 0.125 eV. For the Ag $3d_{5/2}$ line, these conditions produced a FWHM of 1.2 eV. All samples were analyzed as received. All XPS spectra were charge referenced to the maximum in the carbon C 1s narrow scan, taken as 285.0 eV.

9.4. Acknowledgments

We thank Diamond Analytics, a US Synthetic company (Orem, UT), for funding this study. Part of this research was performed at EMSL, a national scientific user facility sponsored by the Department of Energy's Office of Biological and Environmental Research and located at Pacific Northwest National Laboratory.

Author contributions: D.J., M.E. and M.L. did data analysis. M.E. acquired XPS spectra. S.K. fabricated the materials. M.L. was the principle investigator of the project. The manuscript was written by D.J. and M.L.

9.5. References

1. Strohmeier, B. R., *Surf. Interface Anal.* **1990,** *15* (1), 51-56.

2. Song, J.; Jensen, D. S.; Hutchison, D. N.; Turner, B.; Wood, T.; Dadson, A.; Vail, M. A.; Linford, M. R.; Vanfleet, R. R.; Davis, R. C., *Adv. Funct. Mater.* **2011,** *21* (6), 1132-1139.

3. Jensen, D. S.; Kanyal, S. S.; Gupta, V.; Vail, M. A.; Dadson, A. E.; Engelhard, M.; Vanfleet, R.; Davis, R. C.; Linford, M. R., *J. Chromatogr., A* **2012,** *1257* (0), 195-203.

4. Jensen, D. S.; Kanyal, S. S.; Miles, A. J.; Davis, R. C.; Vanfleet, R.; Vail, M. A.; Dadson, A. E.; Linford, M. R., *Submitted to J. Vac. Sci. Technol., B* **2012,** - (-), -.

5. Jensen, D. S.; Kanyal, S. S.; Handcock, J. M.; Vail, M. A.; Dadson, A. E.; Shutthanandan, V.; Zhu, Z.; Vanfleet, R.; Engelhard, M.; Linford, M. R., *Submitted to Surf. Interface Anal.* **2012,** - (-), -.

6. Lu, Z. H.; McCaffrey, J. P.; Brar, B.; Wilk, G. D.; Wallace, R. M.; Feldman, L. C.; Tay, S. P., *Appl. Phys. Lett* **1997,** *71* (19), 2764-2766.

7. Carlson, T. A.; McGuire, G. E., *J. Electron Spectrosc. Relat. Phenom.* **1972,** *1* (2), 161-168.

8. Shallenberger, J. R.; Cole, D. A.; Novak, S. W.; Moore, R. L.; Edgell, M. J.; Smith, S. P.; Hitzman, C. J.; Kirchhoff, J. F.; Principe, E.; Biswas, S.; Bleiler, R. J.; Nieveen, W.; Jones, K. In *Oxide thickness determination by XPS, AES, SIMS, RBS and TEM*, Ion Implantation Technology Proceedings, 1998 International Conference on, 1999; 1999; pp 79-82 vol.1.

9. Zatsepin, D. A.; Mack, P.; Wright, A. E.; Schmidt, B.; Fitting, H. J., *Phys. Status Solidi A* **2011,** *208* (7), 1658-1661.

10. van der Heide, P. A. W.; Azzarello, F. V., *Surf. Sci.* **2003,** *531* (3), L369-L377.

11. Hirose, K.; Nohira, H.; Azuma, K.; Hattori, T., *Prog. Surf. Sci.* **2007,** *82* (1), 3-54.

12. Hirose, K.; Nohira, H.; Koike, T.; Sakano, K.; Hattori, T., *Phys. Rev. B* **1999,** *59* (8), 5617-5621.

13. Hirose, K.; Sakano, K.; Nohira, H.; Hattori, T., *Phys. Rev. B* **2001,** *64* (15), 155325.

14. Kanyal, S. S.; Jensen, D. S.; Zhu, Z.; Linford, M. R., *Submitted to Surf. Sci. Spectra*

2012, - (-), -.

15. Jensen, D. S.; Kanyal, S. S.; Engelhard, M.; Linford, M. R., *Submitted to Surf. Sci. Spectra* **2012,** - (-), -.

16. Kanyal, S. S.; Jensen, D. S.; Zhu, Z.; Linford, M. R., *Submitted to Surf. Sci. Spectra* **2012,** - (-), -.

17. Kanyal, S. S.; Jensen, D. S.; Zhu, Z.; Linford, M. R., *Submitted to Surf. Sci. Spectra* **2012,** - (-), -.

18. Jensen, D. S.; Kanyal, S. S.; Engelhard, M.; Linford, M. R., *Submitted to Surf. Sci. Spectra* **2012,** - (-), -.

19. Kanyal, S. S.; Jensen, D. S.; Zhu, Z.; Linford, M. R., *Submitted to Surf. Sci. Spectra* **2012,** - (-), -.

20. Jensen, D. S.; Kanyal, S. S.; Engelhard, M.; Linford, M. R., *Submitted to Surf. Sci. Spectra* **2012,** - (-), -.

21. Jensen, D. S.; Kanyal, S. S.; Engelhard, M.; Linford, M. R., *Submitted to Surf. Sci. Spectra* **2012,** - (-), -.

22. Kanyal, S. S.; Jensen, D. S.; Zhu, Z.; Linford, M. R., *Submitted to Surf. Sci. Spectra* **2012,** - (-), -.

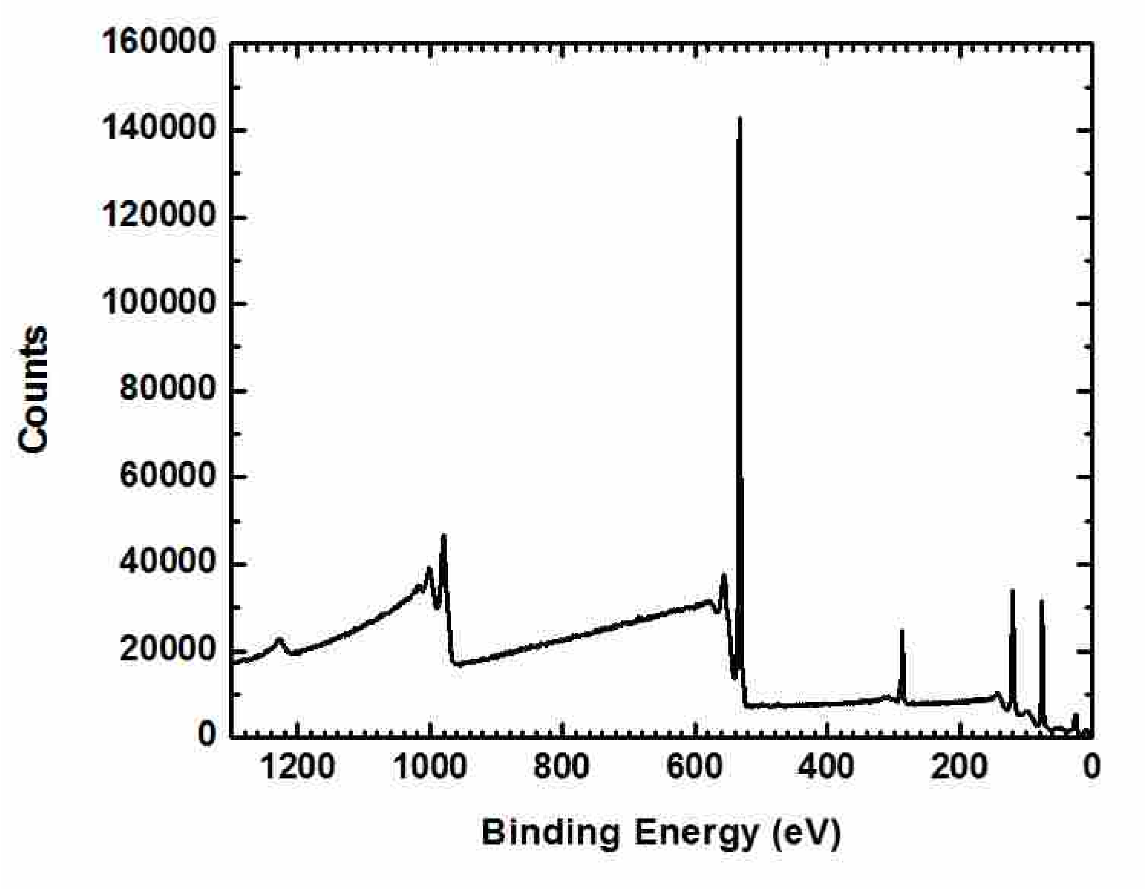

Figure 9.11 Survey scan of Si (100) wafer. O 2s (ca. 30 eV), Si 2p (ca 99 eV), 2s (ca. 150 eV), C 1s (ca. 285 eV), O 1s (ca. 530 eV), F 1s (ca. 690 eV), O KLL (ca. 975 eV), and C KVV (ca. 1230 eV).

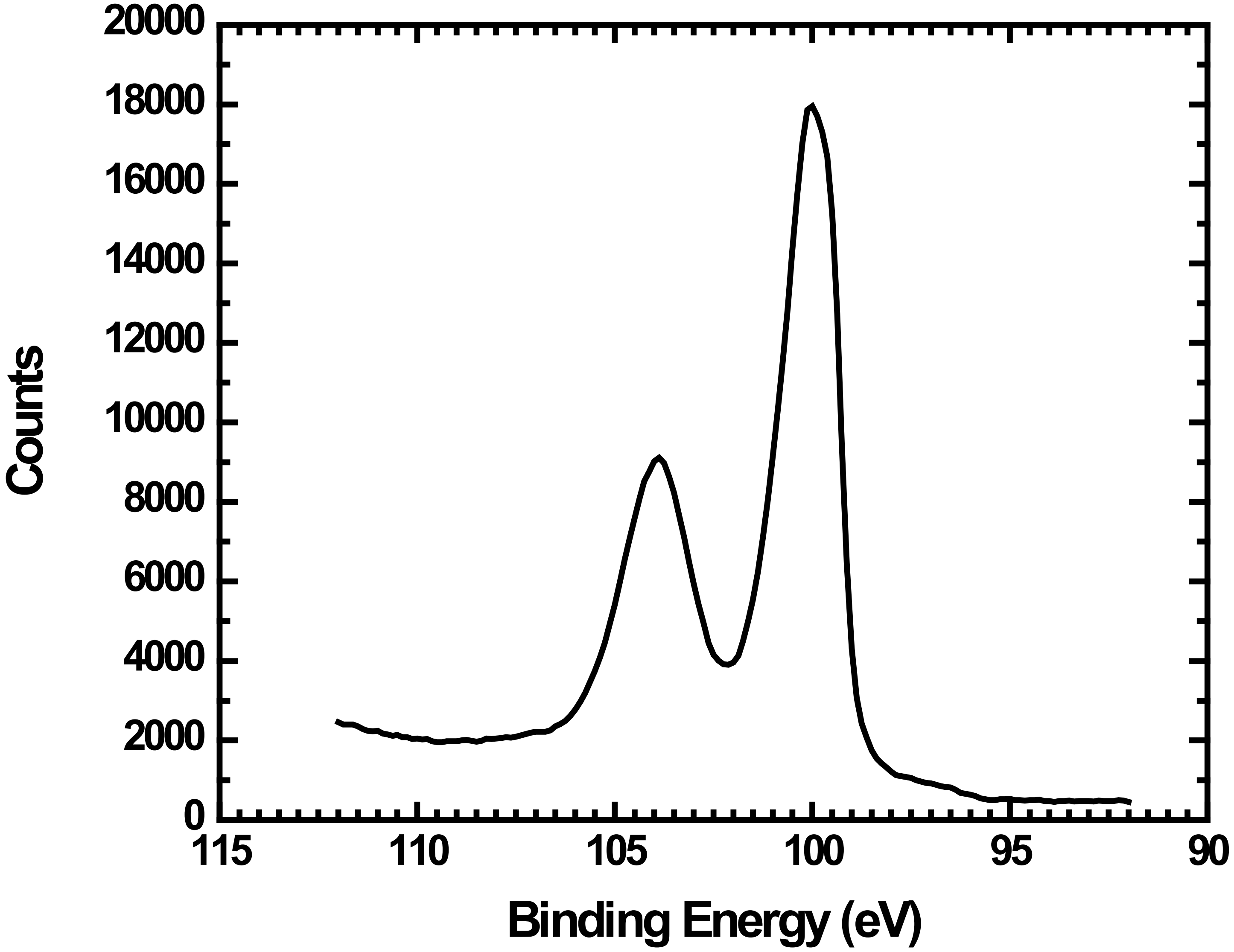

Figure 9.12 Si 2p narrow scan of Si (100) wafer. The spectrum shows peaks due to elemental Si (ca. 99 eV) and oxidized Si (ca. 104 eV).

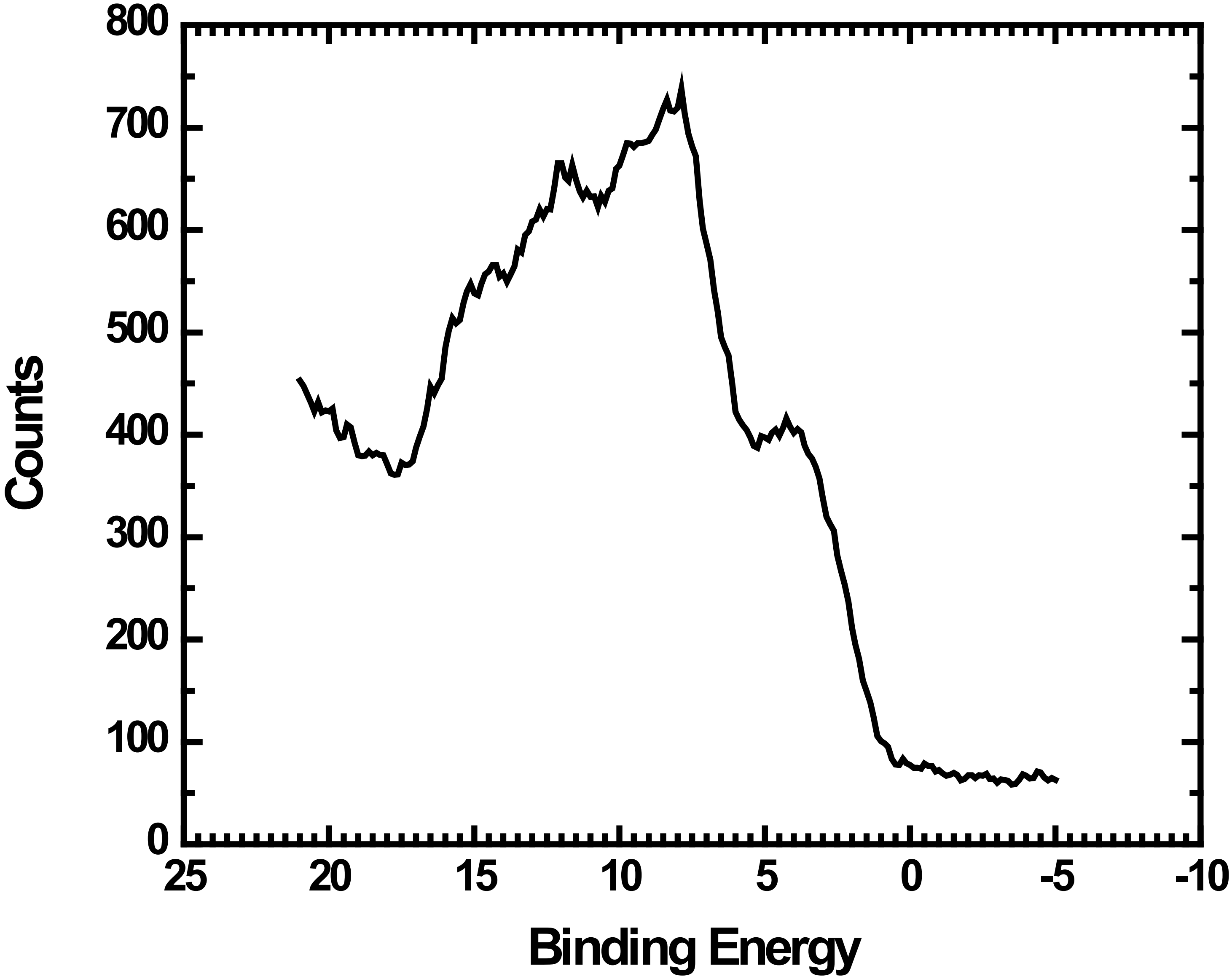

Figure 9.13 Valence band spectrum of Si (100) wafer.

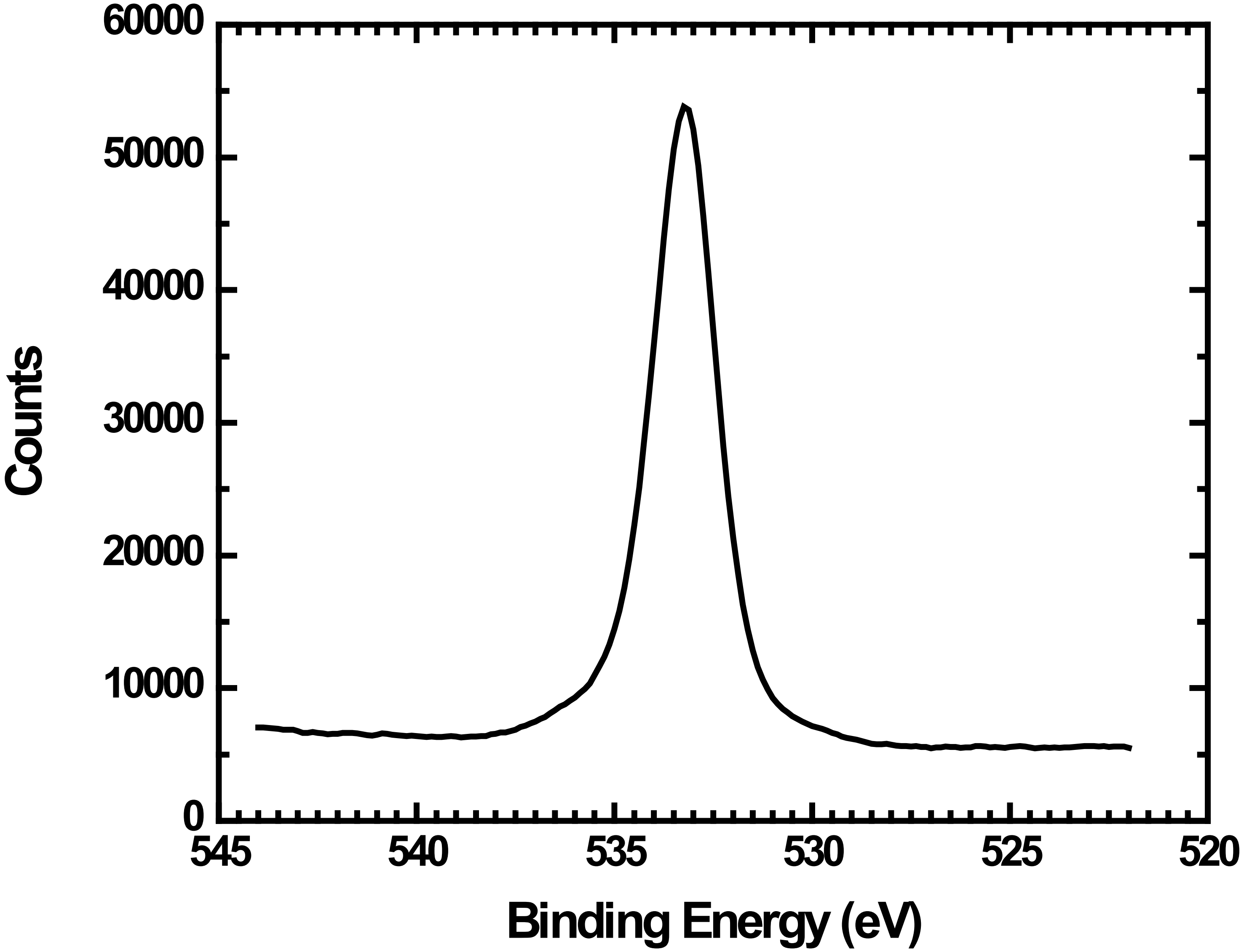

Figure 9.14 O 1s narrow scan of Si (100) wafer.

Chapter 10: XPS of Al_2O_3 e-Beam Evaporated onto Silicon (100)/SiO_2*

10.1. Abstract

We report the XPS characterization of a thin film of Al_2O_3 (35 nm) deposited via e-beam evaporated onto silicon (100). The film was characterized with monochromatic Al Kα radiation. An XPS survey scan, an Al 2p narrow scan, and the valence band were used to characterize the material. The Al_2O_3 thin film is used as a diffusion barrier layer for templated carbon nanotube (CNT) growth in the preparation of microfabricated thin layer chromatography plates.[1-3]

10.2. Introduction

The Al_2O_3 film, deposited by e-beam evaporation is used as a diffusion barrier layer for the catalytic growth from iron nanoparticles of templated carbon nanotube (CNT) forests in the preparation of microfabricated thin layer chromatography plates.[1-3] The present spectra are from a study by Jensen et al., the entirety of the study can be found in Ref 4.[4] The characteristics of the deposited Al_2O_3 barrier films are important because the ability to catalytically grow CNTs is dependent upon the catalyst, Fe, not being poisoned by silicide formation.[5-7] Accordingly, we have used XPS to characterize the thin (35) Al_2O_3 barrier film. The survey spectrum (Figure 10.1) shows that the material is composed of Al, O, and C, where C is presumably adventitious contamination (Figure 10.1). The narrow scans of Al 2p and O 1s give an Al/O atom% ratio of 0.41 which is not the expected value of 0.67 for Al_2O_3. A possible reason for this discrepancy (i) the C 1s narrow scan shows an oxidized carbon peak and (ii) it is common for the Al_2O_3 film after exposure to air to have some adsorbed hydroxyls. The narrow Al 2p scan (Figure 10.2) shows a peak at 75.9 eV (Figure 10.3), indicating that the aluminum is oxidized. The narrow scan of the O 1s region shows a symmetric peak centered at 533.1 eV (Figure 10.3). The valence

---

*This chapter has been submitted to *Surf. Sci. Spectra* for review (David S. Jensen, Supriya S. Kanyal, Michael A. Vail, Andrew E. Dadson, Mark Engelhard, and Matthew R. Linford)

band spectrum is in reasonable agreement with the valance band spectra of alumina found in the literature (Figure 10.4).[8-11]

The Al_2O_3 layer described herein is an essential part of the materials deposited in the preparation of microfabricated thin layer chromatography (TLC) plates.[1-3] Indeed, submissions to Surface Science Spectra have been made on the XPS and SIMS characterization of the key materials in this microfabrication, including the silicon substrate,[12, 13] an alumina barrier layer on the Si/SiO_2 substrate (the current submission and one on ToF-SIMS[14]), the Fe film on the alumina layer,[15, 16] the Fe film after annealing in H_2 to create Fe nanoparticles,[17, 18] and the carbon nanotube forest grown on the Fe nanoparticles.[19, 20]

10.3. Instrumental Parameters

XPS and valence band spectroscopy were performed on an as received bare Si (100) wafers coated with thin film of e-beam evaporated Al_2O_3 (35 nm). This work was performed at the Pacific Northwest National Laboratory (PNNL) in the Environmental Molecular Sciences Laboratory (EMSL) using a Physical Electronics Quantera Scanning X-ray Microprobe. This system uses a focused, monochromatic Al Kα X-ray (1486.7 eV) source for excitation, a spherical section analyzer, and a 32 element multichannel detection system. A 98 W X-ray beam focused to 100 μm (diameter) was rastered over a 1.3 mm x 0.1 mm rectangle on the sample. The X-ray beam is at normal incidence to the sample and the photoelectron detector is at 45° off-normal. High energy resolution spectra were collected using a pass-energy of 69.0 eV with a step size of 0.125 eV. For the Ag $3d_{5/2}$ line, these conditions produced a FWHM of 1.2 eV. All samples were analyzed as received. All XPS spectra were charge referenced to the maximum in the carbon C 1s narrow scan, taken as 285.0 eV.

10.4. Acknowledgments

We thank Diamond Analytics, a US Synthetic company (Orem, UT), for funding this study. Part of this research was performed at EMSL, a national scientific user facility sponsored by the Department of Energy's Office of Biological and Environmental Research and located at Pacific Northwest National Laboratory.

Author contributions: D.J., M.E. and M.L. did data analysis. M.E. acquired XPS spectra. S.K. fabricated the materials. M.L. was the principle investigator of the project. The manuscript was written by D.J. and M.L.

10.5. References

1. Song, J.; Jensen, D. S.; Hutchison, D. N.; Turner, B.; Wood, T.; Dadson, A.; Vail, M. A.; Linford, M. R.; Vanfleet, R. R.; Davis, R. C., *Adv. Funct. Mater.* **2011,** *21* (6), 1132-1139.

2. Jensen, D. S.; Kanyal, S. S.; Miles, A. J.; Davis, R. C.; Vanfleet, R.; Vail, M. A.; Dadson, A. E.; Linford, M. R., *Submitted to J. Vac. Sci. Technol., B* **2012,** - (-), -.

3. Jensen, D. S.; Kanyal, S. S.; Gupta, V.; Vail, M. A.; Dadson, A. E.; Engelhard, M.; Vanfleet, R.; Davis, R. C.; Linford, M. R., *J. Chromatogr., A* **2012,** *1257* (0), 195-203.

4. Jensen, D. S.; Kanyal, S. S.; Handcock, J. M.; Vail, M. A.; Dadson, A. E.; Shutthanandan, V.; Zhu, Z.; Vanfleet, R.; Engelhard, M.; Linford, M. R., *Submitted to Surf. Interface Anal.* **2012,** - (-), -.

5. Homma, Y.; Kobayashi, Y.; Ogino, T.; Takagi, D.; Ito, R.; Jung, Y. J.; Ajayan, P. M., *J. Phys. Chem. B* **2003,** *107* (44), 12161-12164.

6. Ci, L.; Ryu, Z.; Jin-Phillipp, N. Y.; Rühle, M., *Diamond Relat. Mater.* **2007,** *16* (3), 531-536.

7. Chang, W.-T., *J. Mater. Sci.: Mater. Electron.* **2010,** *21* (1), 16-19.

8. Thomas, S.; Sherwood, P. M. A., *Anal. Chem.* **1992,** *64* (21), 2488-2495.

9. Rotole, J. A.; Sherwood, P. M. A. In *Valence band x-ray photoelectron spectroscopic studies to distinguish between oxidized aluminum species*, Baltimore, Maryland (USA), AVS: Baltimore, Maryland (USA), 1999; pp 1091-1096.

10. Rotole, J. A.; Sherwood, P. M. A., *Fresenius J. Anal. Chem.* **2001,** *369* (3), 342-350.

11. Snijders, P. C.; Jeurgens, L. P. H.; Sloof, W. G., *Surf. Sci.* **2002,** *496* (1–2), 97-109.

12. Jensen, D. S.; Kanyal, S. S.; Engelhardt, H.; Linford, M. R., *Submitted to Surf. Sci. Spectra*

2012, - (-), -.

13. Kanyal, S. S.; Jensen, D. S.; Zhu, Z.; Linford, M. R., *Submitted to Surf. Sci. Spectra*

2012, - (-), -.

14. Kanyal, S. S.; Jensen, D. S.; Zhu, Z.; Linford, M. R., *Submitted to Surf. Sci. Spectra*

2012, - (-), -.

15. Jensen, D. S.; Kanyal, S. S.; Engelhard, M.; Linford, M. R., *Submitted to Surf. Sci. Spectra*

2012, - (-), -.

16. Kanyal, S. S.; Jensen, D. S.; Zhu, Z.; Linford, M. R., *Submitted to Surf. Sci. Spectra*

2012, - (-), -.

17. Jensen, D. S.; Kanyal, S. S.; Engelhard, M.; Linford, M. R., *Submitted to Surf. Sci. Spectra*

2012, - (-), -.

18. Kanyal, S. S.; Jensen, D. S.; Zhu, Z.; Linford, M. R., *Submitted to Surf. Sci. Spectra*

2012, - (-), -.

19. Jensen, D. S.; Kanyal, S. S.; Engelhard, M.; Linford, M. R., *Submitted to Surf. Sci. Spectra*

2012, - (-), -.

20. Kanyal, S. S.; Jensen, D. S.; Zhu, Z.; Linford, M. R., *Submitted to Surf. Sci. Spectra*

2012, - (-), -.

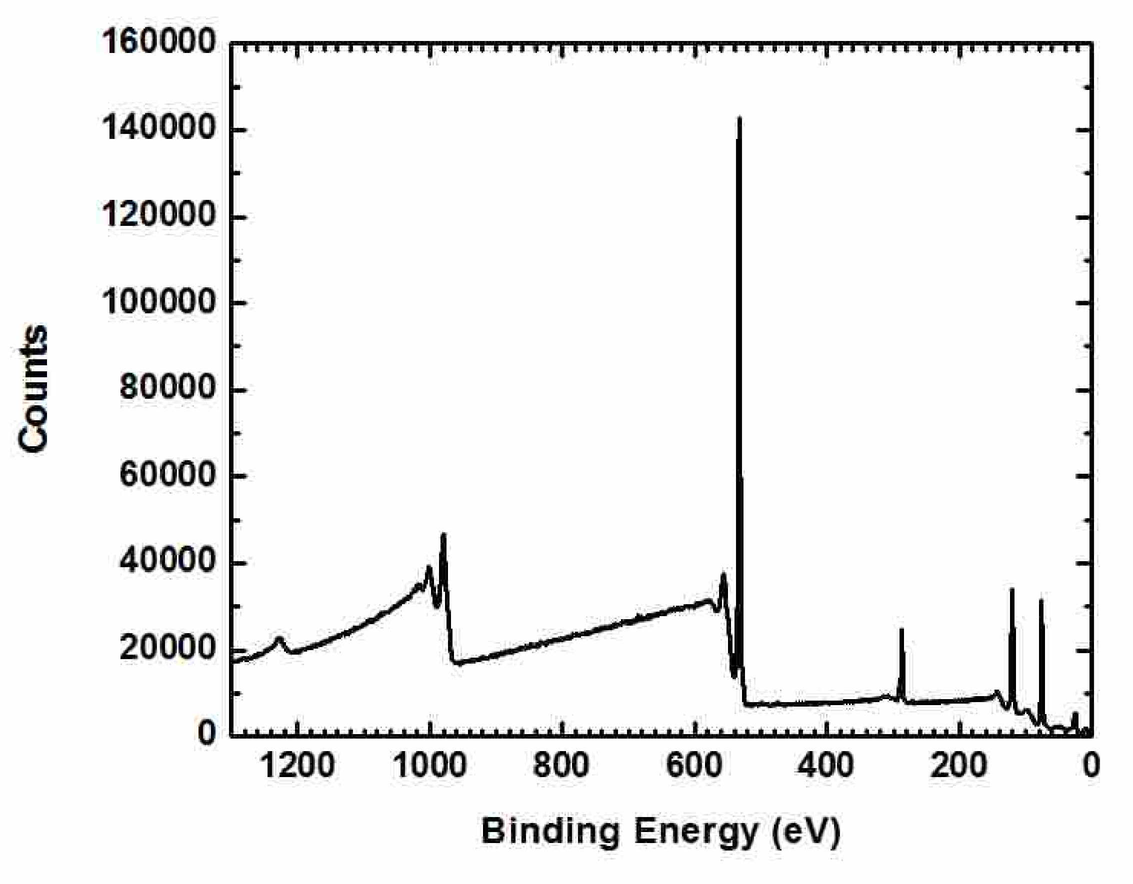

Figure 10.1 Survey spectrum of thermally evaporated Al_2O_3 thin film (35 nm) on a Si (100) wafer. The spectrum shows O 2s (ca. 30 eV), Al 2p (ca. 77 eV), Al 2s (ca. 120 eV), C 1s (ca. 285 eV), O 1s (ca. 530), O KLL (ca. 980 eV) and, C KLL (ca. 1230 eV) signals.

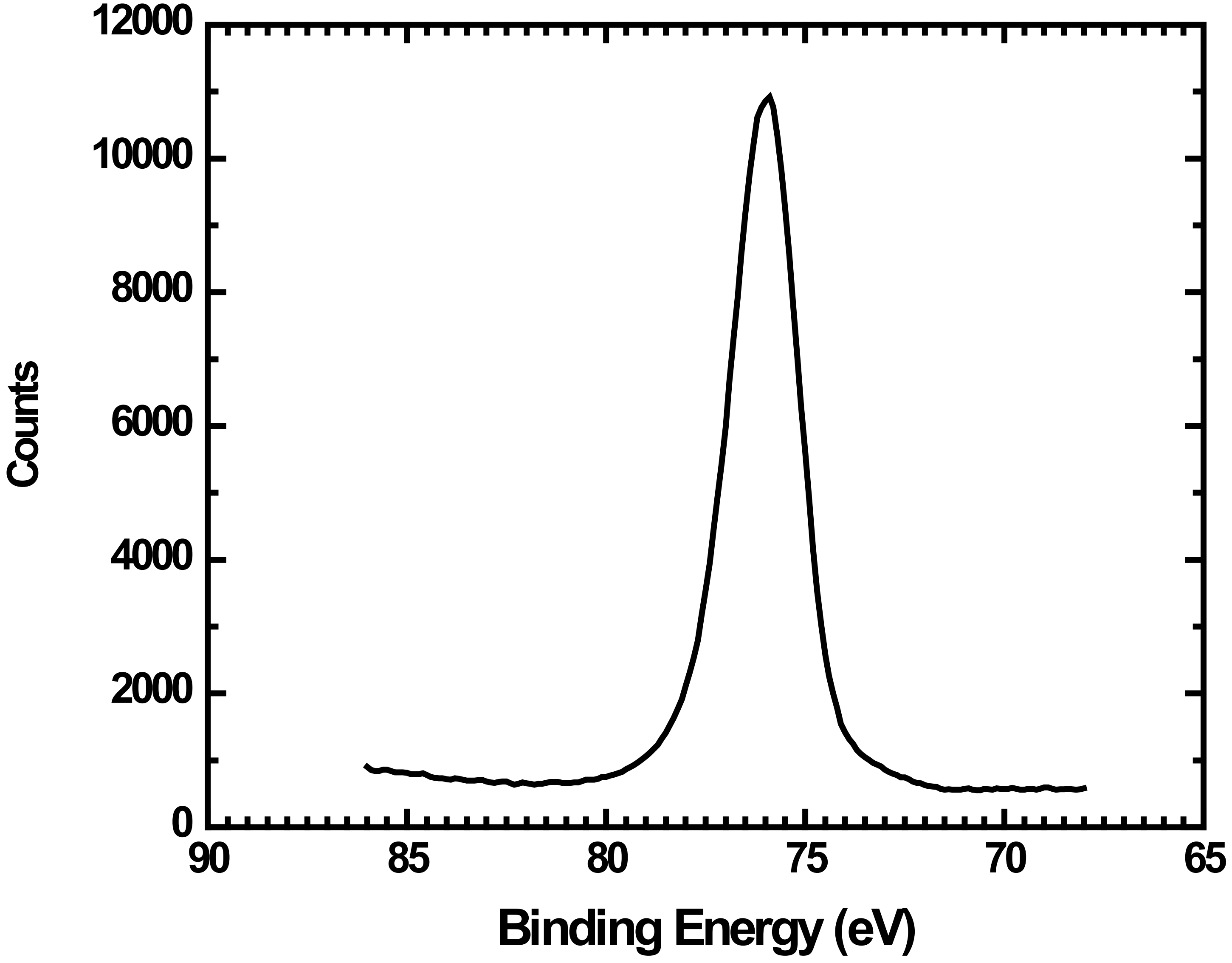

Figure 10.2 Narrow scan of the Al 2p peak of thermally evaporated Al_2O_3 (35 nm) on a Si (100) wafer.

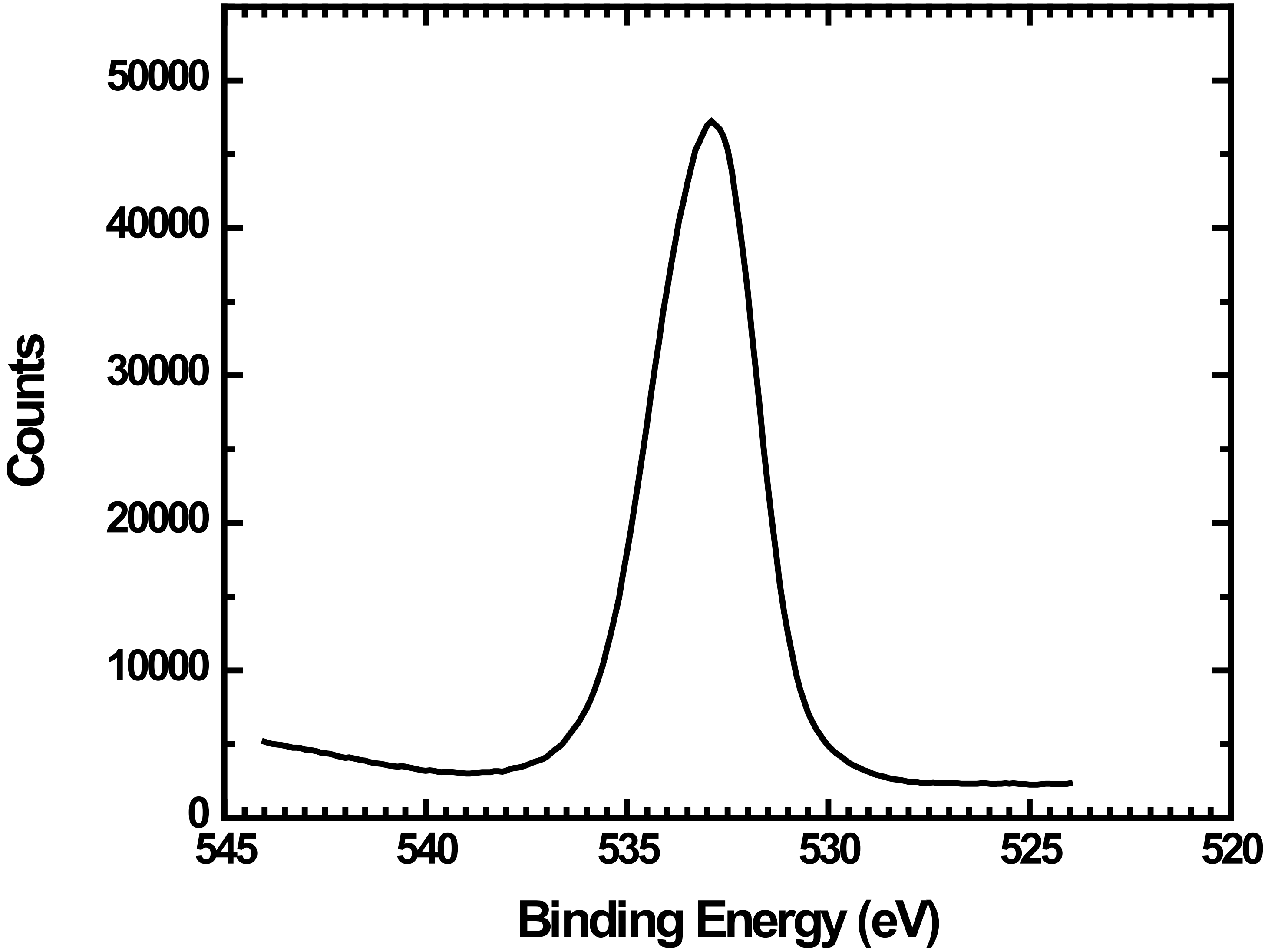

Figure 10.3 O 1s narrow scan of thermally evaporated Al_2O_3 (35 nm) on a Si (100) wafer.

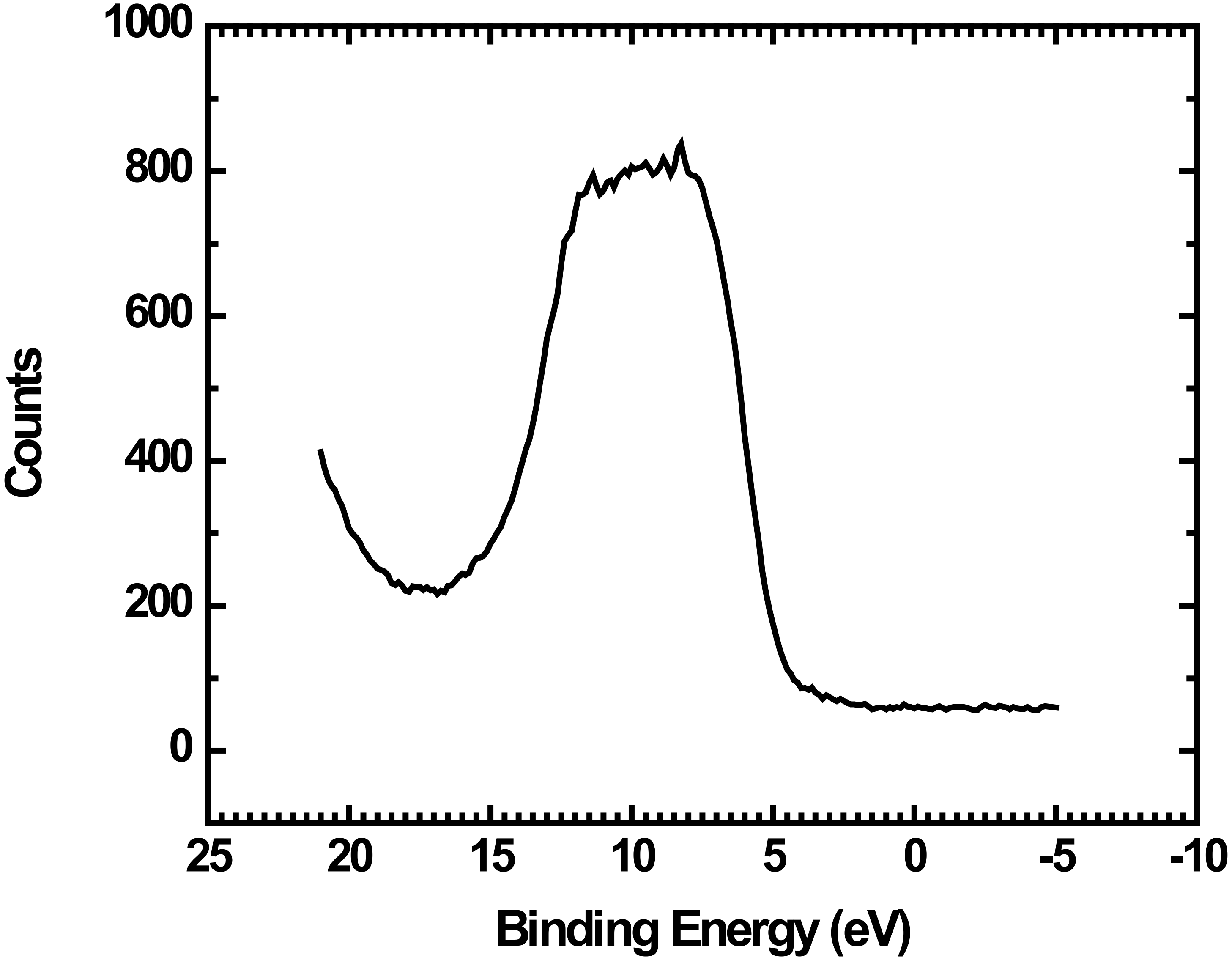

Figure 10.4 Valence band spectrum of thermally evaporated Al_2O_3 (35 nm) on a Si (100) wafer.

Chapter 11: XPS of Thermally Evaporated Iron on an Alumina Barrier Layer*

11.1. Abstract

We report the XPS characterization using Al Kα X-rays of a thermally evaporated iron thin film (6 nm) deposited on an $Si/SiO_2/Al_2O_3$ substrate. An XPS survey spectrum, narrow Fe 2p scan, narrow O 1s, and valence band scan are shown.

11.2. Introduction

A thin film of metallic iron (6 nm) was deposited on an alumina diffusion barrier via thermal evaporation. The iron film is ultimately used as a catalyst for carbon nanotube (CNT) growth. The present spectra are from a study by Jensen et al., and the entirety of the study can be found in Ref 1.[1] Because the iron film is thinner than the probe depth of XPS the underlying alumina layer is detected, and, the photoelectron features of iron and aluminum are present in the survey spectrum (Figure 11.1). The Fe 2p region shows the expected spin-orbit splitting, i.e., the iron $2p_{1/2}$ and $2p_{3/2}$ states (Figure 11.2), where, no metallic iron peak at ca. 707 eV is present.[2] The fact that the iron is not in a reduced state is consistent with the exposure of the film to air after deposition. The Fe $2p_{3/2}$ and $2p_{1/2}$ peaks appear at 710.6 and 724.0 eV. Shake-up peaks appear in the Fe narrow scan, which again indicates that the Fe is in an oxidized state.[3-7]

A large O 1s signal is present. The narrow scan of the O 1s region shows two states for oxygen (Figure 11.3). The lower binding energy peak is attributed to O^{2-} (lattice oxygen) and the higher binding energy peak to chemisorbed OH^- groups, ie., Fe-OH moieties.[2, 8] Comparison of the valence band spectrum to literature spectra also indicates that the material is oxidized (Figure 11.4).[9, 10]

*This chapter has been submitted to *Surf. Sci. Spectra* for review (David S. Jensen, Supriya S. Kanyal, Michael A. Vail, Andrew E. Dadson, Mark Engelhard, and Matthew R. Linford)

The Fe layer described herein is an essential part of the materials deposited in the preparation of microfabricated thin layer chromatography (TLC) plates.[11-13] Indeed, submissions to Surface Science Spectra have been made on the XPS and SIMS characterization of the key materials in this microfabrication, including the silicon substrate,[14, 15] an alumina barrier layer on the Si/SiO_2 substrate,[16, 17] the Fe film on the alumina layer (the current submission and one onm ToF-SIMS[18]), the Fe film after annealing in H_2 to create Fe nanoparticles,[19, 20] and the carbon nanotube forest grown on the Fe nanoparticles.[21, 22]

11.3. Instrumental Parameters

XPS and valence band spectroscopy were performed on an as received bare Si (100) wafers, coated with a thin films of e-beam evaporated Al_2O_3 and thermally evaporated Fe (6 nm). This work was performed at the Pacific Northwest National Laboratory (PNNL) in the Environmental Molecular Sciences Laboratory (EMSL) using a Physical Electronics Quantera Scanning X-ray Microprobe. This system uses a focused, monochromatic Al Kα X-ray (1486.7 eV) source for excitation, a spherical section analyzer, and a 32 element multichannel detection system. A 98 W X-ray beam focused to 100 μm (diameter) was rastered over a 1.3 mm x 0.1 mm rectangle on the sample. The X-ray beam is at normal incidence to the sample and the photoelectron detector is at 45° off-normal. High energy resolution spectra were collected using a pass-energy of 69.0 eV with a step size of 0.125 eV. For the Ag $3d_{5/2}$ line, these conditions produced a FWHM of 1.2 eV. All samples were analyzed as received. All XPS spectra were charge referenced to the maximum in the carbon C 1s narrow scan, taken as 285.0 eV.

11.4. Acknowledgments

We thank Diamond Analytics, a US Synthetic company (Orem, UT), for funding this study. Part of this research was performed at EMSL, a national scientific user facility sponsored by the Department of Energy's Office of Biological and Environmental Research and located at Pacific Northwest National Laboratory.

Author contributions: D.J., M.E. and M.L. did data analysis. M.E. acquired XPS spectra. S.K. fabricated the materials. M.L. was the principle investigator of the project. The manuscript was written by D.J. and M.L.

11.5. Reference

1. Jensen, D. S.; Kanyal, S. S.; Handcock, J. M.; Vail, M. A.; Dadson, A. E.; Shutthanandan, V.; Zhu, Z.; Vanfleet, R.; Engelhard, M.; Linford, M. R., *Submitted to Surf. Interface Anal.* **2012,** - (-), -.

2. Shustak, G.; Domb, A. J.; Mandler, D., *Langmuir* **2004,** *20* (18), 7499-7506.

3. Fujii, T.; de Groot, F. M. F.; Sawatzky, G. A.; Voogt, F. C.; Hibma, T.; Okada, K., *Phys. Rev. B* **1999,** *59* (4), 3195-3202.

4. Fujii, T.; Alders, D.; Voogt, F. C.; Hibma, T.; Thole, B. T.; Sawatzky, G. A., *Surf. Sci.* **1996,** *366* (3), 579-586.

5. Okada, K.; Kotani, A., *J. Phys. Soc. Jpn.* **1992,** *62*, 4619-4637.

6. Bocquet, A. E.; Mizokawa, T.; Saitoh, T.; Namatame, H.; Fujimori, A., *Phys. Rev. B* **1992,** *46* (7), 3771-3784.

7. Uozumi, T.; Okada, K.; Kotani, A.; Zimmermann, R.; Steiner, P.; Hüfner, S.; Tezuka, Y.; Shin, S., *J. Electron Spectrosc. Relat. Phenom.* **1997,** *83* (1), 9-20.

8. Jovancicevic, V.; Kainthla, R. C.; Tang, Z.; Yang, B.; Bockris, J. O. M., *Langmuir* **1987,** *3* (3), 388-395.

9. Temesghen, W. T.; Sherwood, P. S., *Anal. Bioanal. Chem.* **2002,** *373* (7), 601-608.

10. Xue, M.; Wang, S.; Wu, K.; Guo, J.; Guo, Q., *Langmuir* **2010,** *27* (1), 11-14.

11. Jensen, D. S.; Kanyal, S. S.; Gupta, V.; Vail, M. A.; Dadson, A. E.; Engelhard, M.; Vanfleet, R.; Davis, R. C.; Linford, M. R., *J. Chromatogr., A* **2012,** *1257* (0), 195-203.

12. Jensen, D. S.; Kanyal, S. S.; Miles, A. J.; Davis, R. C.; Vanfleet, R.; Vail, M. A.; Dadson, A. E.; Linford, M. R., *Submitted to J. Vac. Sci. Technol., B* **2012,** - (-), -.

13. Song, J.; Jensen, D. S.; Hutchison, D. N.; Turner, B.; Wood, T.; Dadson, A.; Vail, M. A.; Linford, M. R.; Vanfleet, R. R.; Davis, R. C., *Adv. Funct. Mater.* **2011,** *21* (6), 1132-1139.

14. Jensen, D. S.; Kanyal, S. S.; Engelhardt, H.; Linford, M. R., *Submitted to Surf. Sci. Spectra*

2012, - (-), -.

15. Kanyal, S. S.; Jensen, D. S.; Zhu, Z.; Linford, M. R., *Submitted to Surf. Sci. Spectra*

2012, - (-), -.

16. Jensen, D. S.; Kanyal, S. S.; Engelhard, M.; Linford, M. R., *Submitted to Surf. Sci. Spectra* **2012,** - (-), -.

17. Kanyal, S. S.; Jensen, D. S.; Zhu, Z.; Linford, M. R., *Submitted to Surf. Sci. Spectra*

2012, - (-), -.

18. Kanyal, S. S.; Jensen, D. S.; Zhu, Z.; Linford, M. R., *Submitted to Surf. Sci. Spectra*

2012, - (-), -.

19. Jensen, D. S.; Kanyal, S. S.; Engelhard, M.; Linford, M. R., *Submitted to Surf. Sci. Spectra*

2012, - (-), -.

20. Kanyal, S. S.; Jensen, D. S.; Zhu, Z.; Linford, M. R., *Submitted to Surf. Sci. Spectra* **2012,** - (-), -.

21. Jensen, D. S.; Kanyal, S. S.; Engelhard, M.; Linford, M. R., *Submitted to Surf. Sci. Spectra* **2012,** - (-), -.

22. Kanyal, S. S.; Jensen, D. S.; Zhu, Z.; Linford, M. R., *Submitted to Surf. Sci. Spectra* **2012,** - (-), -.

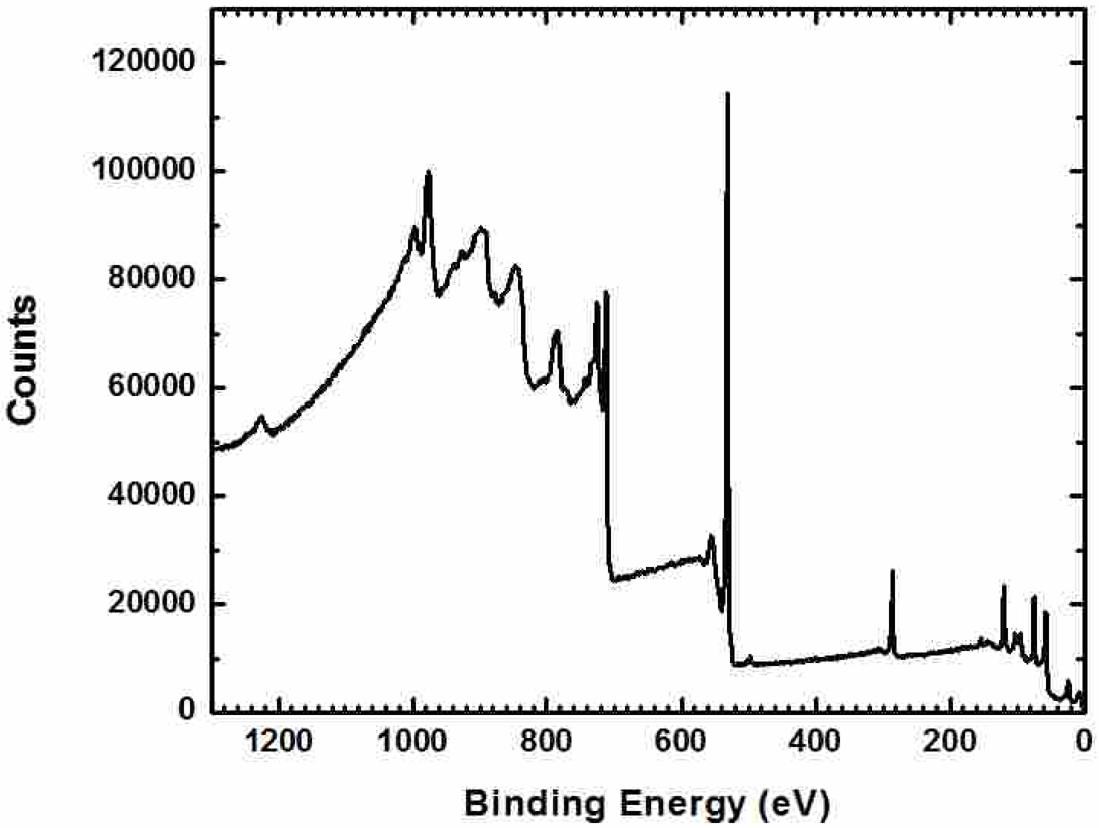

Figure 11.1 Survey scan of the thin Fe film (ca. 6 nm) on a thin layer of Al_2O_3 (35 nm). Peaks present: Al 2s (ca. 120 eV), Al 2p (ca. 75 eV), C 1s (ca. 285 eV), C KVV (ca. 1230 eV), Fe $2p_{3/2}$ (ca. 710 eV), Fe $2p_{1/2}$ (ca. 725 eV), Fe 3p (ca. 58 eV), Fe 3s (ca. 95 eV), O 2s (ca. 30 eV), O 1s (ca. 530 eV), O KLL (ca. 975 eV), Si 2p (ca 104 eV), and Si 2s (ca. 154 eV).

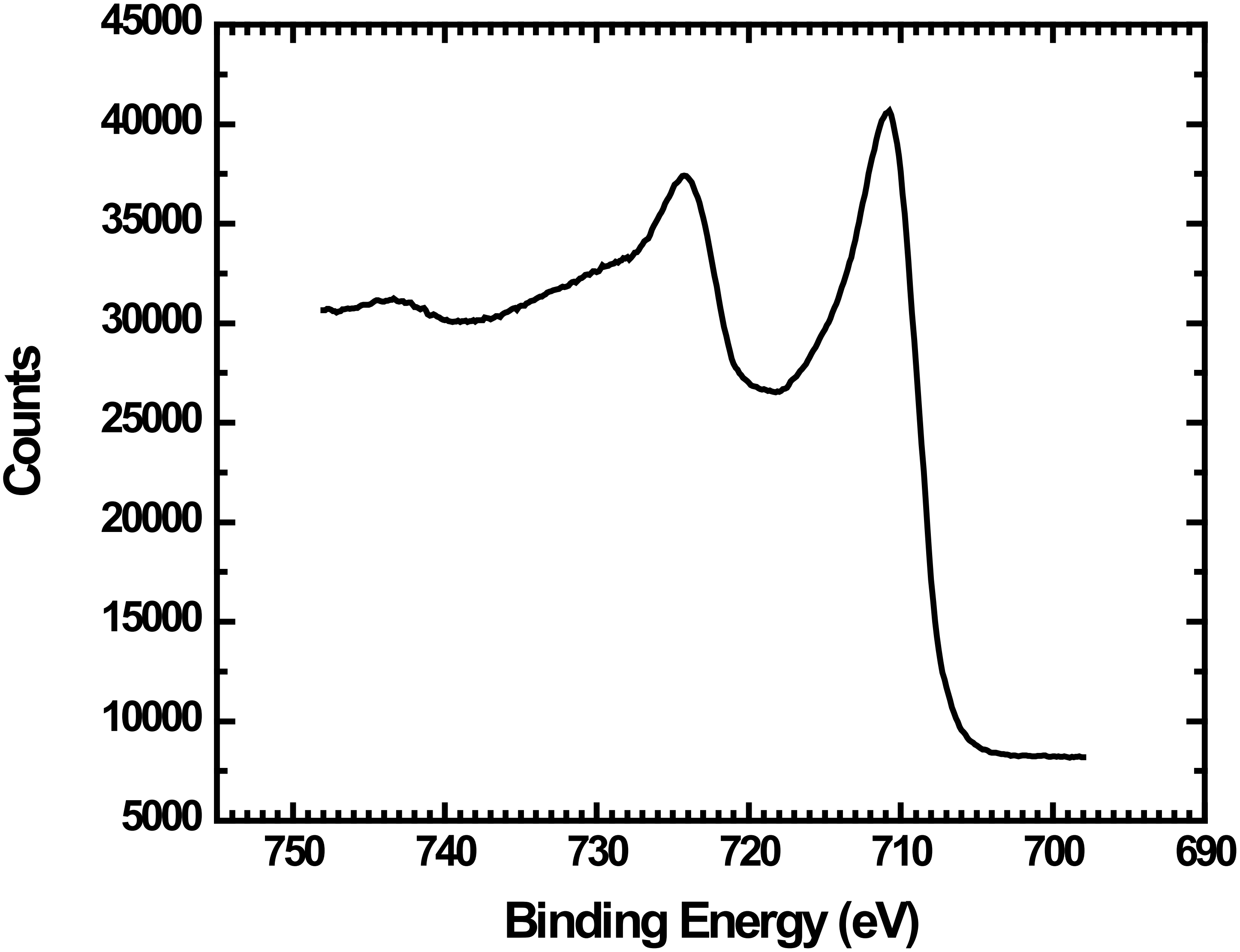

Figure 11.2 Narrow scan of the Fe thin film (ca. 6 nm). The Fe $2p_{3/2}$ and Fe $2p_{3/2}$ are at 711.2 and 724.6 eV, respectively.

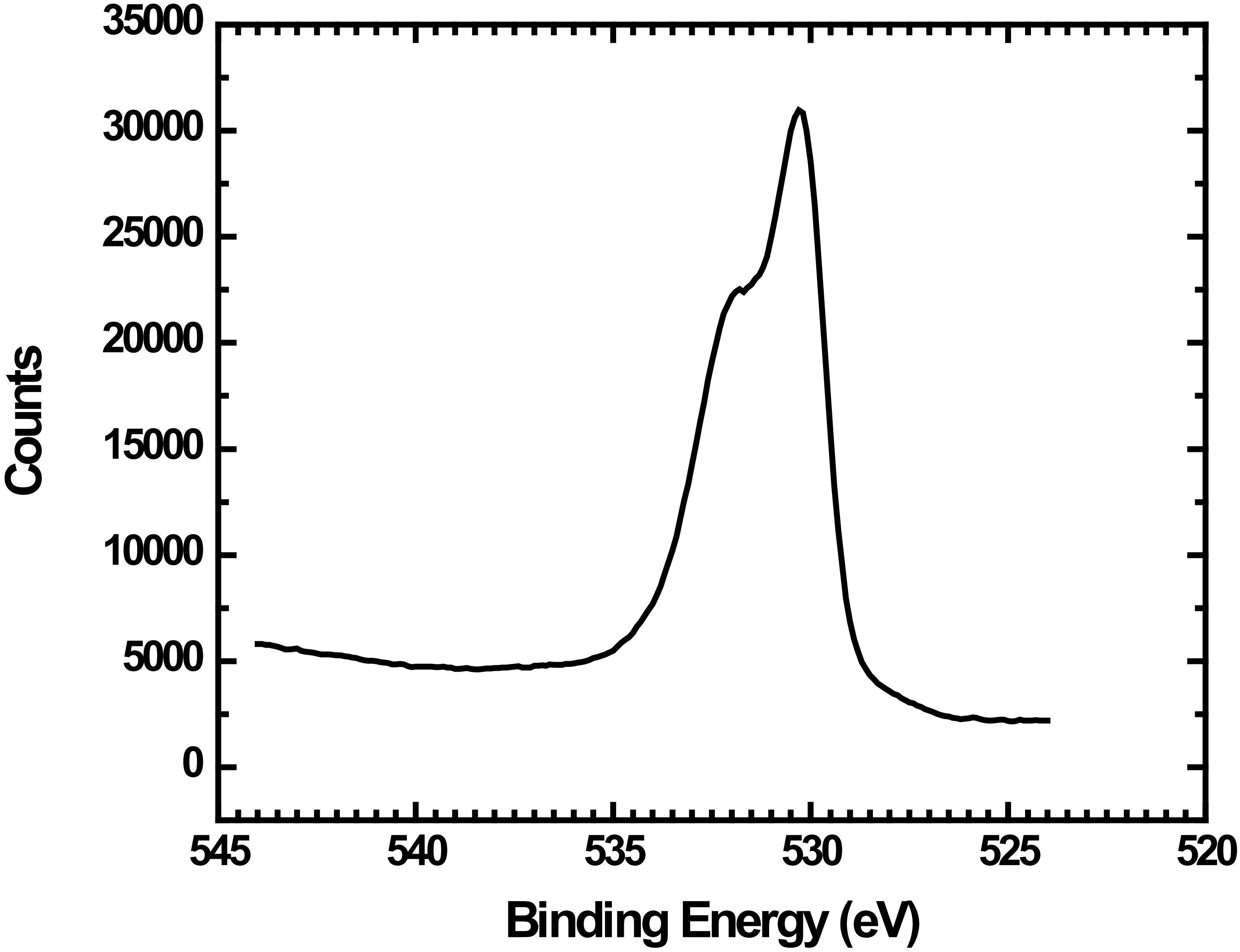

Figure 11.3 O 1s narrow scan.

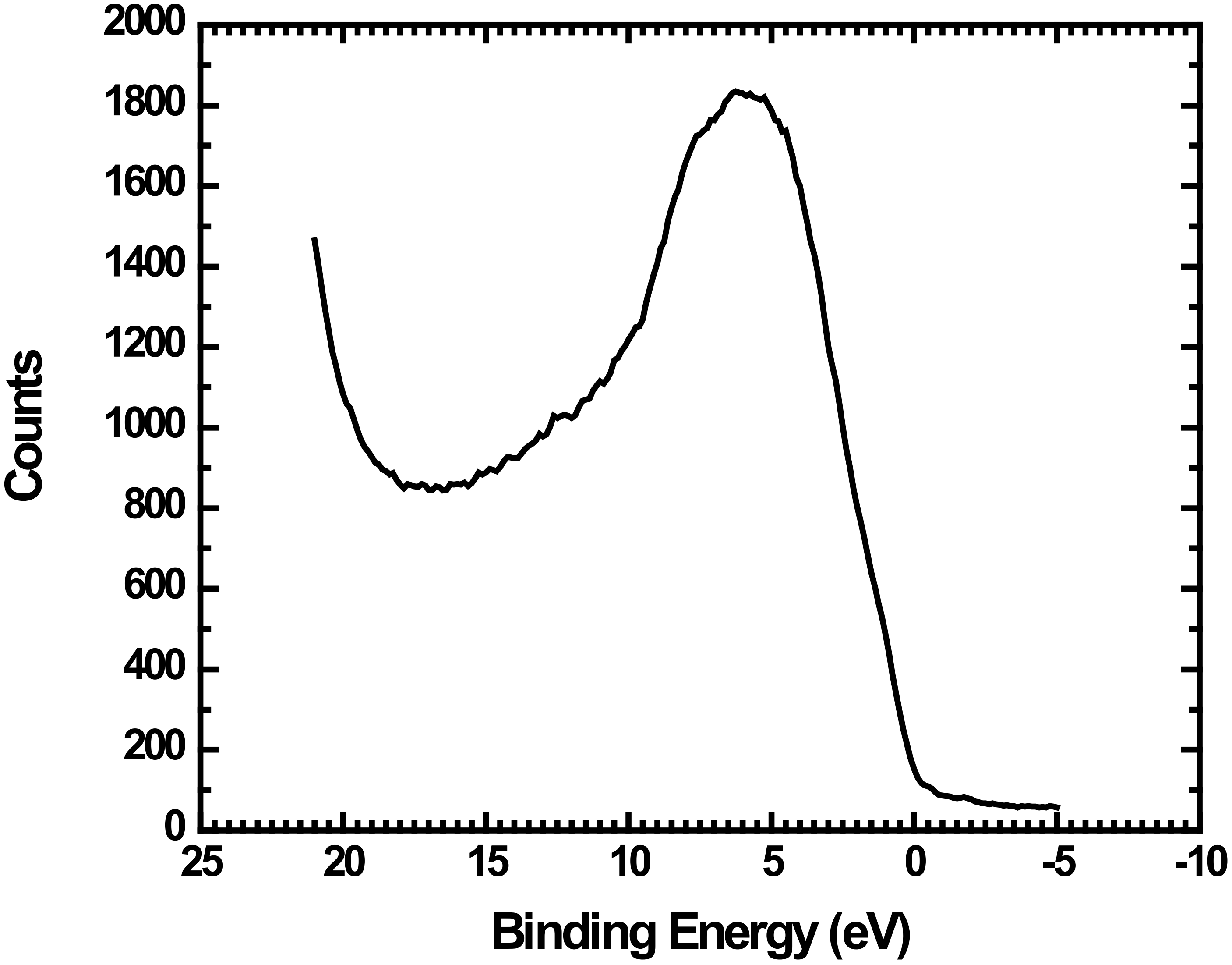

Figure 11.4 Valence band spectrum.

Chapter 12: XPS of a Thermally Annealed Iron Thin Film on an Alumina Barrier Layer*

12.1. Abstract

Herein the characterization of an Fe thin film on Al_2O_3 after thermal annealing under H_2 using Al Kα X-rays was done. The XPS survey spectrum, narrow Fe 2p scan and valence band regions are presented. The survey spectrum shows aluminum signals due to exposure of the underlying Al_2O_3 film during Fe nanoparticle formation.

12.2. Introduction

A thin film of iron (6 nm) was thermally evaporated onto a thin layer of alumina (35 nm) and then thermally annealed to create iron nanoparticles. The present spectra are from a study by Jensen et al., the entirety of the study can be found in Ref 1.[1] Thermal annealing of the thin iron film dewets it from the surface due to a surface free energy mismatch between the iron and alumina films, which causes spontaneous formation of iron nanoparticles.[2-5] The resulting iron nanoparticles can be used to grow carbon nanotubes.[6-8] During annealing in H_2 the Fe is reduced and the underlying alumina is exposed.[9] Accordingly, a larger than expected signal from aluminum is seen in the survey spectrum (Figure 12.1). However, after exposure to air XPS shows that the material is oxidized (Figure 12.2).

The Fe 2p region shows the Fe $2p_{1/2}$ and $2p_{3/2}$ signals,[10] with no peak corresponding to metallic iron at ca. 707 eV.[11] The Fe 2p narrow scan also shows shake-up satellites, which are also consistent with an oxidized material.[12-19]

Compared to the signal in the unannealed Fe film, the O 1s narrow scan (Figure 12.3) shows a greater contribution at higher energy from what appears to be the Al_2O_3

---

*This chapter has been submitted to *Surf. Sci. Spectra* for review (David S. Jensen, Supriya S. Kanyal, Michael A. Vail, Andrew E. Dadson, Mark Engelhard, and Matthew R. Linford)

underlayer.Comparison of the valence band (Figure 12.4) of the annealed iron film with literature spectra suggests that the material is oxidized.[20, 21]

The annealed Fe layer described herein is an essential part of the materials deposited in the preparation of microfabricated thin layer chromatography (TLC) plates.[6-8] Indeed, submissions to Surface Science Spectra have been made on the XPS and SIMS characterization of the key materials in this microfabrication, including the silicon substrate,[22, 23] an alumina barrier layer on the Si/SiO_2 substrate,[24, 25] the Fe film on the alumina layer,[26, 27] the Fe film after annealing in H_2 to create Fe nanoparticles (the current submission and one on ToF-SIMS[28]) and the carbon nanotube forest grown on the Fe nanoparticles.[29, 30]

12.3. Instrumental Parameters

XPS and valence band spectroscopy were performed on an as received bare Si (100) wafers coated with a thin film of Al_2O_3, onto which a thin film of thermally evaporated Fe (6 nm) was thermally annealed in H_2. This work was performed at the Pacific Northwest National Laboratory (PNNL) in the Environmental Molecular Sciences Laboratory (EMSL) using a Physical Electronics Quantera Scanning X-ray Microprobe. This system uses a focused, monochromatic Al Kα X-ray (1486.7 eV) source for excitation, a spherical section analyzer, and a 32 element multichannel detection system. A 98 W X-ray beam focused to 100 μm (diameter) was rastered over a 1.3 mm x 0.1 mm rectangle on the sample. The X-ray beam is at normal incidence to the sample and the photoelectron detector is at 45° off-normal. High energy resolution spectra were collected using a pass-energy of 69.0 eV with a step size of 0.125 eV. For the Ag $3d_{5/2}$ line, these conditions produced a FWHM of 1.2 eV. All samples were analyzed as received. All XPS spectra were charge referenced to the maximum in the carbon C 1s narrow scan, taken as 285.0 eV.

12.4. Acknowledgments

We thank Diamond Analytics, a US Synthetic company (Orem, UT), for funding this study. Part of this research was performed at EMSL, a national scientific user facility sponsored by the Department of Energy's Office of Biological and Environmental Research and located at Pacific Northwest National Laboratory.

Author contributions: D.J., M.E. and M.L. did data analysis. M.E. acquired XPS spectra. S.K. fabricated the materials. M.L. was the principle investigator of the project. The manuscript was written by D.J. and M.L.

12.5. References

1. Jensen, D. S.; Kanyal, S. S.; Handcock, J. M.; Vail, M. A.; Dadson, A. E.; Shutthanandan, V.; Zhu, Z.; Vanfleet, R.; Engelhard, M.; Linford, M. R., *Submitted to Surf. Interface Anal.* **2012,** - (-), -.

2. Mattevi, C.; Wirth, C. T.; Hofmann, S.; Blume, R.; Cantoro, M.; Ducati, C.; Cepek, C.; Knop-Gericke, A.; Milne, S.; Castellarin-Cudia, C.; Dolafi, S.; Goldoni, A.; Schloegl, R.; Robertson, J., *J. Phys. Chem. C* **2008,** *112* (32), 12207-12213.

3. Esconjauregui, S.; Fouquet, M.; Bayer, B. C.; Ducati, C.; Smajda, R.; Hofmann, S.; Robertson, J., *ACS Nano* **2010,** *4* (12), 7431-7436.

4. Amama, P. B.; Pint, C. L.; Kim, S. M.; McJilton, L.; Eyink, K. G.; Stach, E. A.; Hauge, R. H.; Maruyama, B., *ACS Nano* **2010,** *4* (2), 895-904.

5. Quintana, C.; Menéndez, J. L.; Huttel, Y.; Lancin, M.; Navarro, E.; Cebollada, A., *Thin Solid Films* **2003,** *434* (1–2), 228-238.

6. Song, J.; Jensen, D. S.; Hutchison, D. N.; Turner, B.; Wood, T.; Dadson, A.; Vail, M. A.; Linford, M. R.; Vanfleet, R. R.; Davis, R. C., *Adv. Funct. Mater.* **2011,** *21* (6), 1132-1139.

7. Jensen, D. S.; Kanyal, S. S.; Gupta, V.; Vail, M. A.; Dadson, A. E.; Engelhard, M.; Vanfleet, R.; Davis, R. C.; Linford, M. R., *J. Chromatogr., A* **2012,** *1257* (0), 195-203.

8. Jensen, D. S.; Kanyal, S. S.; Miles, A. J.; Davis, R. C.; Vanfleet, R.; Vail, M. A.; Dadson, A. E.; Linford, M. R., *Submitted to J. Vac. Sci. Technol., B* **2012,** - (-), -.

9. Tiernan, M. J.; Barnes, P. A.; Parkes, G. M. B., *J. Phys. Chem. B* **2000,** *105* (1), 220-228.

10. Cornell, R. M.; Schwertmann, U., *The Iron Oxides: Structure, Properties, Reactions, Occurences and Uses*. 2nd ed.; Wiley-VCH: Weinheim, 2003.

11. Shustak, G.; Domb, A. J.; Mandler, D., *Langmuir* **2004,** *20* (18), 7499-7506.

12. Fujii, T.; de Groot, F. M. F.; Sawatzky, G. A.; Voogt, F. C.; Hibma, T.; Okada, K., *Phys. Rev. B* **1999,** *59* (4), 3195-3202.

13. Fujii, T.; Alders, D.; Voogt, F. C.; Hibma, T.; Thole, B. T.; Sawatzky, G. A., *Surf. Sci.* **1996,** *366* (3), 579-586.

14. Okada, K.; Kotani, A., *J. Phys. Soc. Jpn.* **1992,** *62*, 4619-4637.

15. Bocquet, A. E.; Mizokawa, T.; Saitoh, T.; Namatame, H.; Fujimori, A., *Phys. Rev. B* **1992,** *46* (7), 3771-3784.

16. Gweon, G.-H.; Park, J.-G.; Oh, S. J., *Phys. Rev. B* **1993,** *48* (11), 7825-7835.

17. Uozumi, T.; Okada, K.; Kotani, A.; Zimmermann, R.; Steiner, P.; Hüfner, S.; Tezuka, Y.; Shin, S., *J. Electron Spectrosc. Relat. Phenom.* **1997,** *83* (1), 9-20.

18. Muhler, M.; Schlögl, R.; Ertl, G., *J. Catal.* **1992,** *138* (2), 413-444.

19. Schedel-Niedrig, T.; Weiss, W.; Schlögl, R., *Phys. ReV. B* **1995,** *52* (24), 17449-17460.

20. Temesghen, W. T.; Sherwood, P. S., *Anal. Bioanal. Chem.* **2002,** *373* (7), 601-608.

21. Xue, M.; Wang, S.; Wu, K.; Guo, J.; Guo, Q., *Langmuir* **2010,** *27* (1), 11-14.

22. Jensen, D. S.; Kanyal, S. S.; Engelhardt, H.; Linford, M. R., *Submitted to Surf. Sci. Spectra* **2012,** - (-), -.

23. Kanyal, S. S.; Jensen, D. S.; Zhu, Z.; Linford, M. R., *Submitted to Surf. Sci. Spectra* **2012,** - (-), -.

24. Jensen, D. S.; Kanyal, S. S.; Engelhard, M.; Linford, M. R., *Submitted to Surf. Sci. Spectra* **2012,** - (-), -.

25. Kanyal, S. S.; Jensen, D. S.; Zhu, Z.; Linford, M. R., *Submitted to Surf. Sci. Spectra* **2012,** - (-), -.

26. Jensen, D. S.; Kanyal, S. S.; Engelhard, M.; Linford, M. R., *Submitted to Surf. Sci. Spectra* **2012,** - (-), -.

27. Kanyal, S. S.; Jensen, D. S.; Zhu, Z.; Linford, M. R., *Submitted to Surf. Sci. Spectra* **2012,** - (-), -.

28. Kanyal, S. S.; Jensen, D. S.; Zhu, Z.; Linford, M. R., *Submitted to Surf. Sci. Spectra* **2012,** - (-), -.

29. Jensen, D. S.; Kanyal, S. S.; Engelhard, M.; Linford, M. R., *Submitted to Surf. Sci. Spectra* **2012,** - (-), -.

30. Kanyal, S. S.; Jensen, D. S.; Zhu, Z.; Linford, M. R., *Submitted to Surf. Sci. Spectra* **2012,** - (-), -.

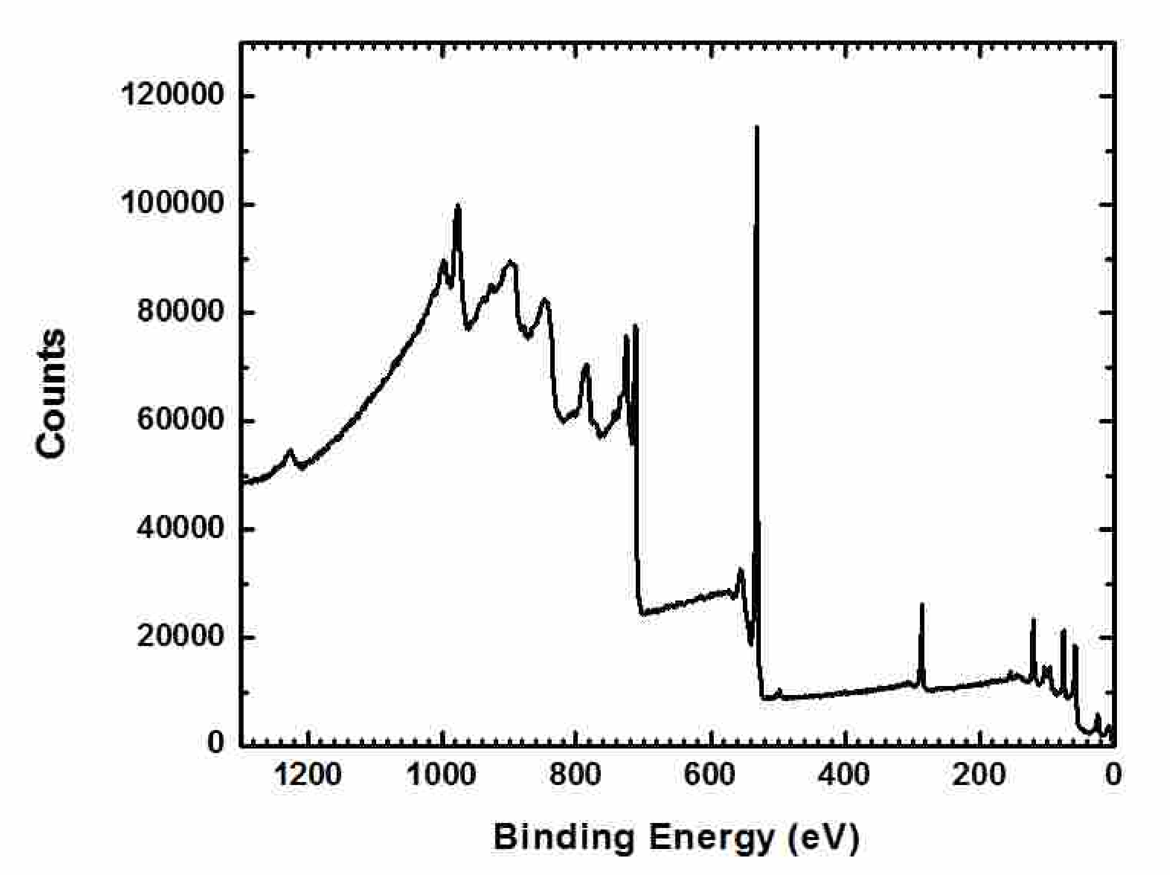

Figure 12.1 Survey scan of H_2 annealed Fe thin film, i.e., Fe nanoparticles on a thin film of Al_2O_3 (35 nm). Peaks present: O 2s (ca. 30 eV), Fe 3p (ca. 58 eV), Al 2p (ca. 75 eV), Fe 3s (ca. 95 eV), Si 2p (ca 104 eV), Al 2s (ca. 120 eV), Si 2s (ca. 154 eV), C 1s (ca. 285 eV), O 1s (ca. 530 eV), F 1s (ca. 690 eV), Fe $2p_{3/2}$ (ca. 710 eV), Fe $2p_{1/2}$ (ca. 725 eV), O KLL (ca. 975 eV), and C KVV (ca. 1230 eV).

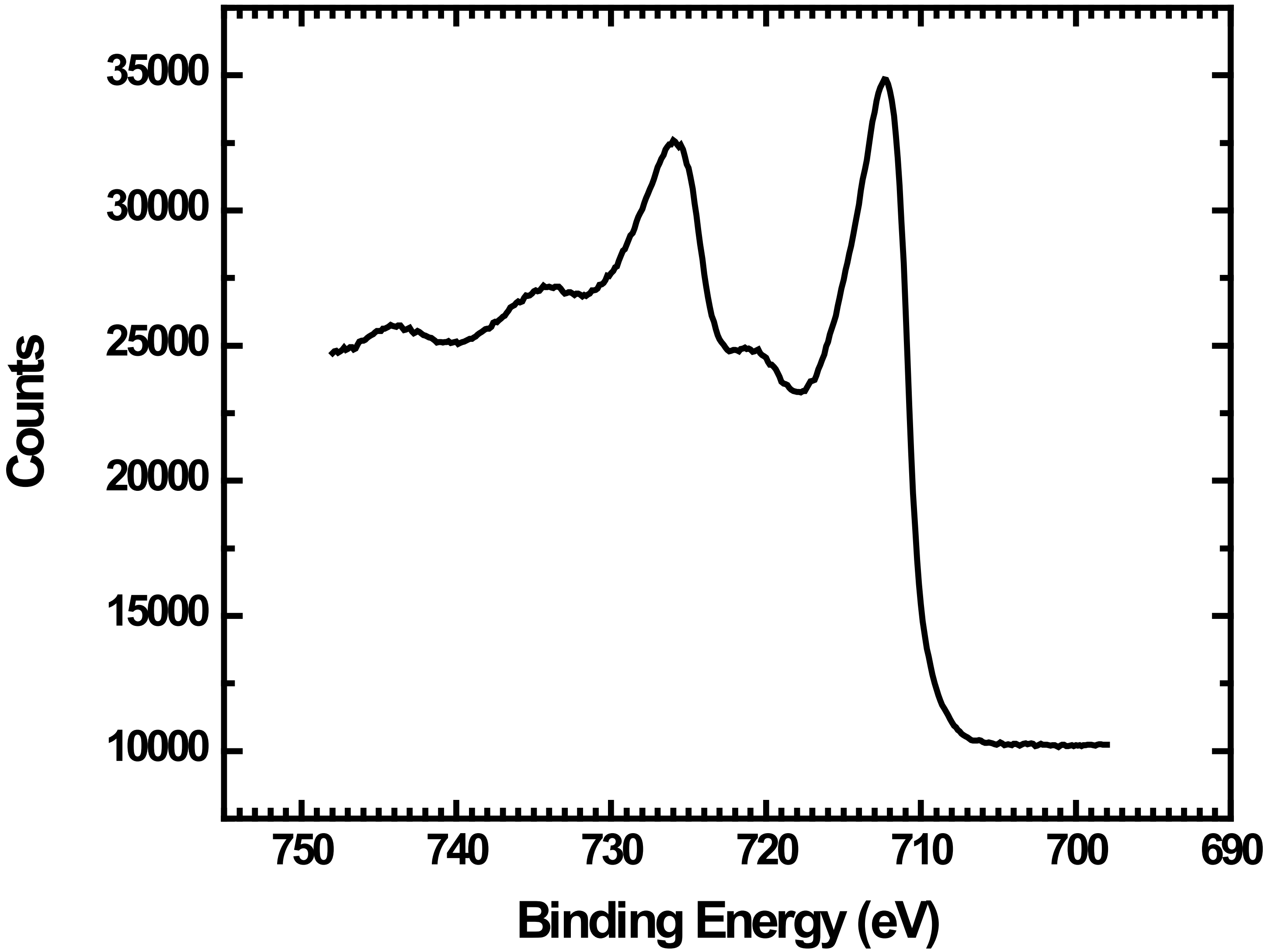

Figure 12.2 Fe 2p narrow scan of an annealed Fe thin film/nanoparticles. Fe $2p_{3/2}$ located ca. 711.2 eV and Fe $2p_{3/2}$ located 724.6 eV.

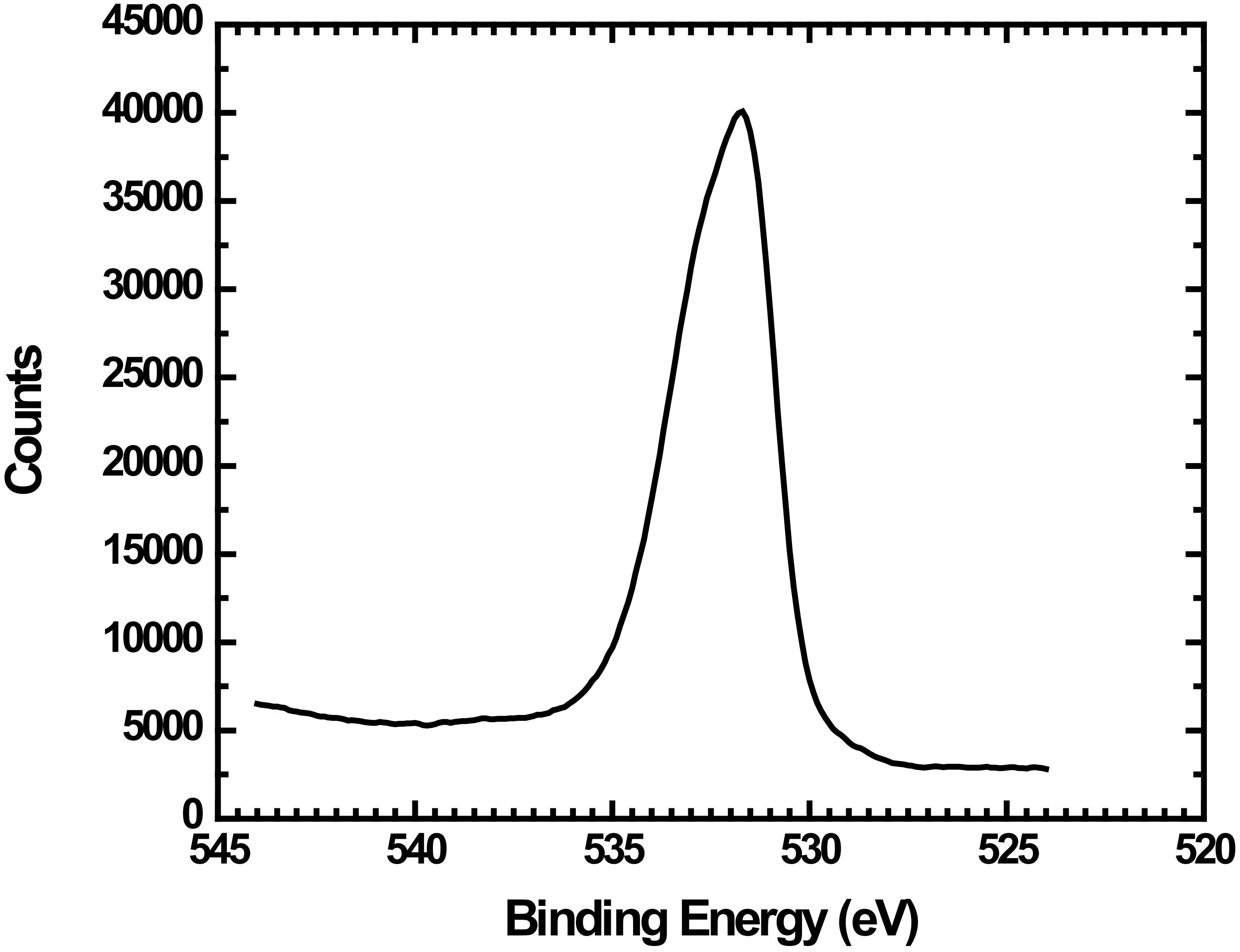

Figure 12.3 O 1s narrow scan of Fe nanoparticles.

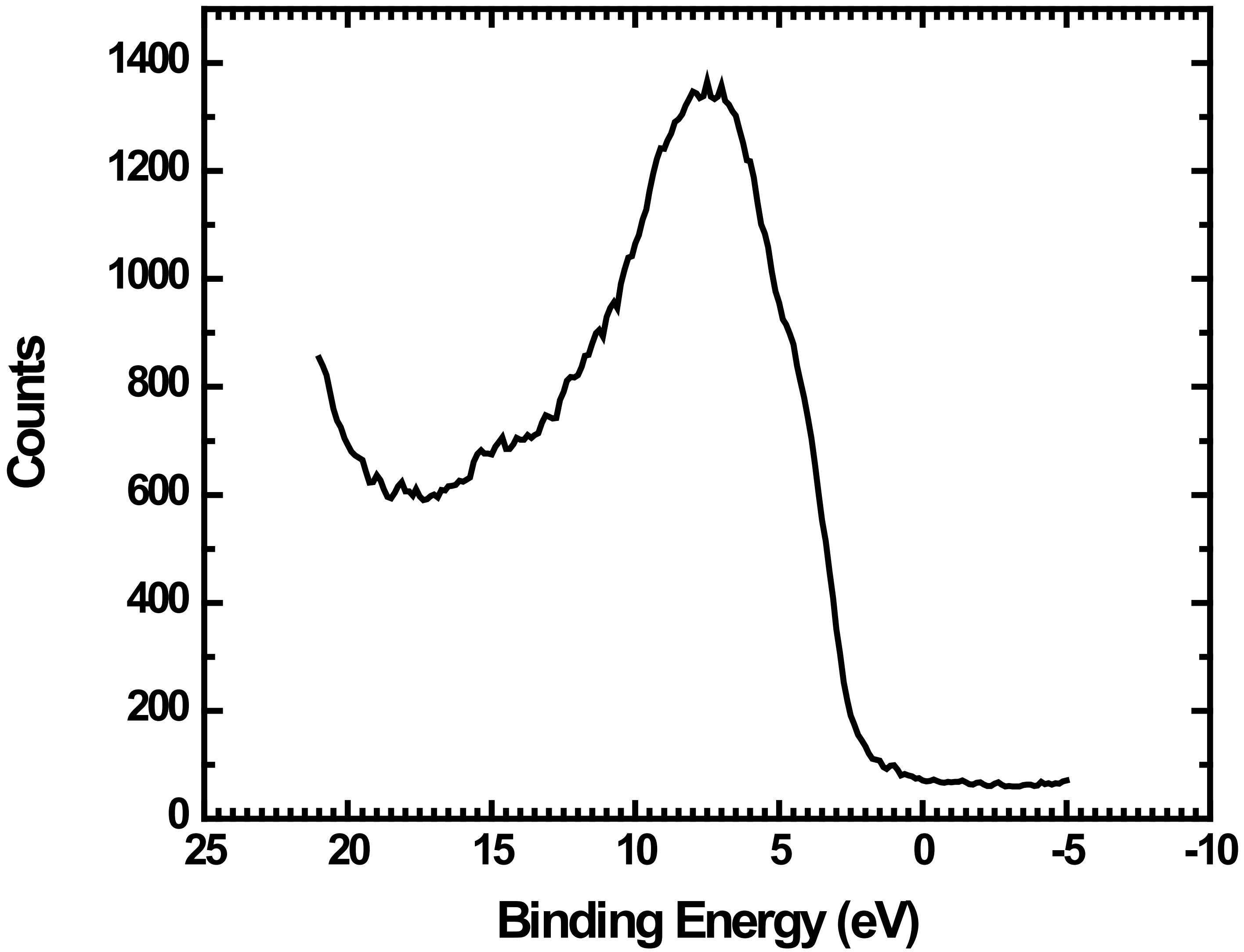

Figure 12.4 Narrow scan of the valence band of Fe nanoparticles.

Chapter 13: XPS of a Multiwalled Carbon Nanotube Forest Grown via Chemical Vapor Deposition from Iron Catalyst Nanoparticles

13.1. Abstract

Carbon nanotubes (CNTs) have unique chemical and physical properties. Herein, an XPS analysis of a forest of multiwalled CNTs using monochromatic Al Kα radiation is reported. Survey scans show only one element: carbon. The carbon 1s peak is centered 284.5 eV. The C 1s envelope also shows the expected $\pi \rightarrow \pi^*$ shake-up peak at ca. 291 eV. The valence band and carbon KVV Auger signals are also presented. When patterned, the CNT forests can be used as a template for subsequent deposition of metal oxides to make thin layer chromatography plates.[1-3]

13.2. Introduction

The physical and chemical properties of carbon nanotubes (CNTs) are unique. Individual CNTs have remarkably high aspect ratios, are extremely strong, and can have metallic or semiconducting properties.[4, 5] Herein XPS was used to characterize multiwalled CNT forests that were grown via chemical vapor deposition using iron nanoparticle catalysts with ethylene and hydrogen as precursors.[1-3] The present spectra are from a study by Jensen et al., and the entirety of the study can be found in Ref 6.[6] The survey scan shows only carbon: the C 1s peak at ca. 284.5 eV, and the C KVV Auger signal at ca. 1230 eV (Figure 13.1). The narrow C 1s scan shows the expected shake-up peak ($\pi \rightarrow \pi^*$ transition) at ca. 291 eV (Figure 13.2).[7-10] The valence band (VB) region (-5 – 20 eV) is also shown, and consists of a signal that increases steadily with increasing binding energy to ca. 20 eV (Figure 13.3). The carbon KVV Auger signal is also shown (Figure 13.4).

The CNT forests described herein is an essential part of the materials deposited in the preparation of microfabricated thin layer chromatography (TLC) plates.[1-3] Indeed, submissions to Surface Science Spectra have been made on the XPS and SIMS characterization of the key materials in this microfabrication, including the silicon substrate,[11, 12] an alumina barrier layer on the Si/SiO_2 substrate,[13, 14] the Fe film on the alumina layer,[15, 16] the Fe film after annealing in H_2 to create Fe nanoparticles,[17, 18] and the carbon nanotube forest grown on the Fe nanoparticles (the current submission and one on ToF-SIMS[19]).

13.3. Instrumental Parameters

XPS and valence band spectroscopy were performed on an as received CNT forest. This work was performed at the Pacific Northwest National Laboratory (PNNL) in the Environmental Molecular Sciences Laboratory (EMSL) using a Physical Electronics Quantera Scanning X-ray Microprobe. This system uses a focused, monochromatic Al Kα X-ray (1486.7 eV) source for excitation, a spherical section analyzer, and a 32 element multichannel detection system. A 98 W X-ray beam focused to 100 μm (diameter) was rastered over a 1.3 mm x 0.1 mm rectangle on the sample. The X-ray beam is at normal incidence to the sample and the photoelectron detector is at 45° off-normal. High energy resolution spectra were collected using a pass-energy of 69.0 eV with a step size of 0.125 eV. For the Ag $3d_{5/2}$ line, these conditions produced a FWHM of 1.2 eV. All samples were analyzed as received. All XPS spectra were charge referenced to the maximum in the carbon C 1s narrow scan, taken as 285.0 eV.

13.4. Acknowledgments

We thank Diamond Analytics, a US Synthetic company (Orem, UT), for funding this study. Part of this research was performed at EMSL, a national scientific user facility sponsored by the Department of Energy's Office of Biological and Environmental Research and located at Pacific Northwest National Laboratory.

Author contributions: D.J., M.E. and M.L. did data analysis. M.E. acquired XPS spectra. S.K. fabricated the materials. M.L. was the principle investigator of the project. The manuscript was written by D.J. and M.L.

13.5. References

1. Song, J.; Jensen, D. S.; Hutchison, D. N.; Turner, B.; Wood, T.; Dadson, A.; Vail, M. A.; Linford, M. R.; Vanfleet, R. R.; Davis, R. C., *Adv. Funct. Mater.* **2011,** *21* (6), 1132-1139.

2. Jensen, D. S.; Kanyal, S. S.; Miles, A. J.; Davis, R. C.; Vanfleet, R.; Vail, M. A.; Dadson, A. E.; Linford, M. R., *Submitted to J. Vac. Sci. Technol., B* **2012,** - (-), -.

3. Jensen, D. S.; Kanyal, S. S.; Gupta, V.; Vail, M. A.; Dadson, A. E.; Engelhard, M.; Vanfleet, R.; Davis, R. C.; Linford, M. R., *J. Chromatogr., A* **2012,** *1257* (0), 195-203.

4. Valcárcel, M.; Cárdenas, S.; Simonet, B. M., *Anal. Chem.* **2007,** *79* (13), 4788-4797.

5. Merkoçi, A., *Microchim. Acta* **2006,** *152* (3), 157-174.

6. Jensen, D. S.; Kanyal, S. S.; Handcock, J. M.; Vail, M. A.; Dadson, A. E.; Shutthanandan, V.; Zhu, Z.; Vanfleet, R.; Engelhard, M.; Linford, M. R., *Submitted to Surf. Interface Anal.* **2012,** - (-), -.

7. Okpalugo, T. I. T.; Papakonstantinou, P.; Murphy, H.; McLaughlin, J.; Brown, N. M. D., *Carbon* **2005,** *43* (1), 153-161.

8. Yang, D.-Q.; Rochette, J.-F.; Sacher, E., *J. Phys. Chem. B* **2005,** *109* (16), 7788-7794.

9. Yang, D.-Q.; Rochette, J.-F.; Sacher, E., *The Journal of Physical Chemistry B* **2005,** *109* (10), 4481-4484.

10. Yang, D.-Q.; Rochette, J.-F.; Sacher, E., *J. Phys. Chem. B* **2005,** *109* (10), 4481-4484.

11. Jensen, D. S.; Kanyal, S. S.; Engelhardt, H.; Linford, M. R., *Submitted to Surf. Sci. Spectra* **2012,** - (-), -.

12. Kanyal, S. S.; Jensen, D. S.; Zhu, Z.; Linford, M. R., *Submitted to Surf. Sci. Spectra* **2012,** - (-), -.

13. Jensen, D. S.; Kanyal, S. S.; Engelhard, M.; Linford, M. R., *Submitted to Surf. Sci. Spectra* **2012,** - (-), -.

14. Kanyal, S. S.; Jensen, D. S.; Zhu, Z.; Linford, M. R., *Submitted to Surf. Sci. Spectra* **2012,** - (-), -.

15. Jensen, D. S.; Kanyal, S. S.; Engelhard, M.; Linford, M. R., *Submitted to Surf. Sci. Spectra* **2012,** - (-), -.

16. Kanyal, S. S.; Jensen, D. S.; Zhu, Z.; Linford, M. R., *Submitted to Surf. Sci. Spectra* **2012,** - (-), -.

17. Jensen, D. S.; Kanyal, S. S.; Engelhard, M.; Linford, M. R., *Submitted to Surf. Sci. Spectra* **2012,** - (-), -.

18. Kanyal, S. S.; Jensen, D. S.; Zhu, Z.; Linford, M. R., *Submitted to Surf. Sci. Spectra* **2012,** - (-), -.

19. Kanyal, S. S.; Jensen, D. S.; Zhu, Z.; Linford, M. R., *Submitted to Surf. Sci. Spectra* **2012,** - (-), -.

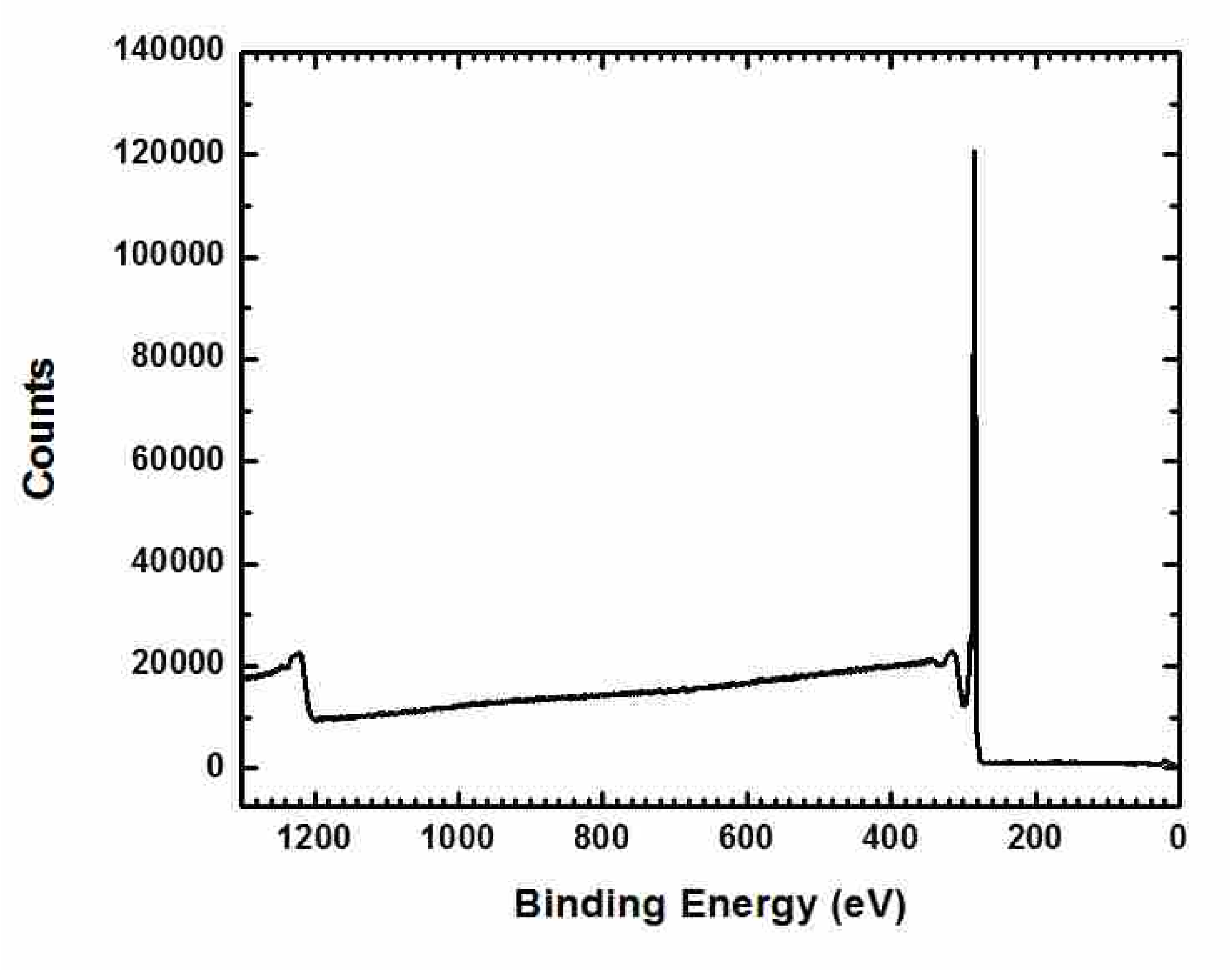

Figure 13.1 Survey spectrum of a multiwalled carbon nanotube forest. The peak at ca. 285 eV is the C 1s signal, and that at ca. 1230 is the carbon KVV Auger peak.

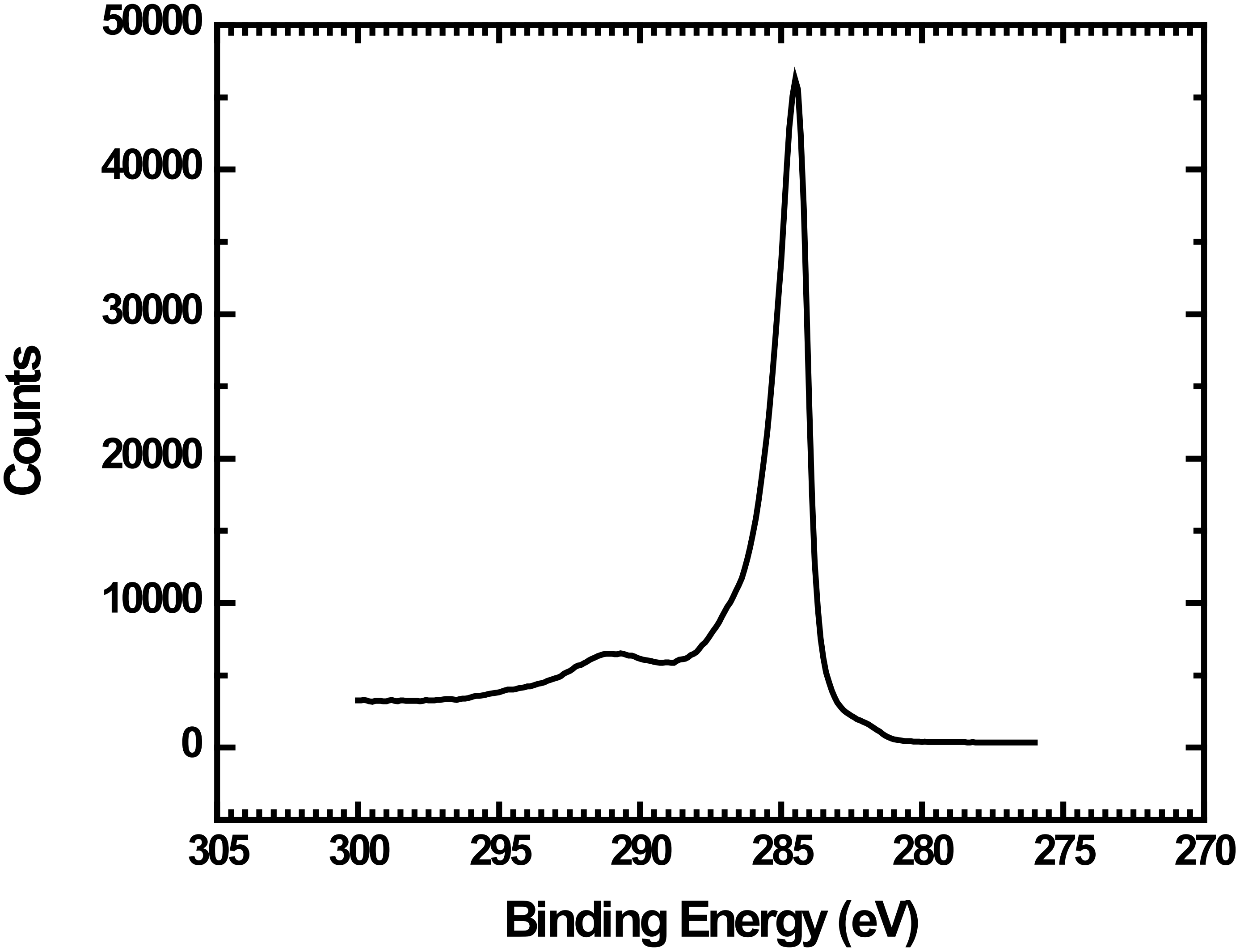

Figure 13.2 Narrow scan of the C 1s region. There are two distinct peaks, one at ca. 284.5 eV (the C 1s signal), and the other at ca. 291 eV, which is the shake-up peak ($\pi \rightarrow \pi^*$ transition in aromatic carbon systems).

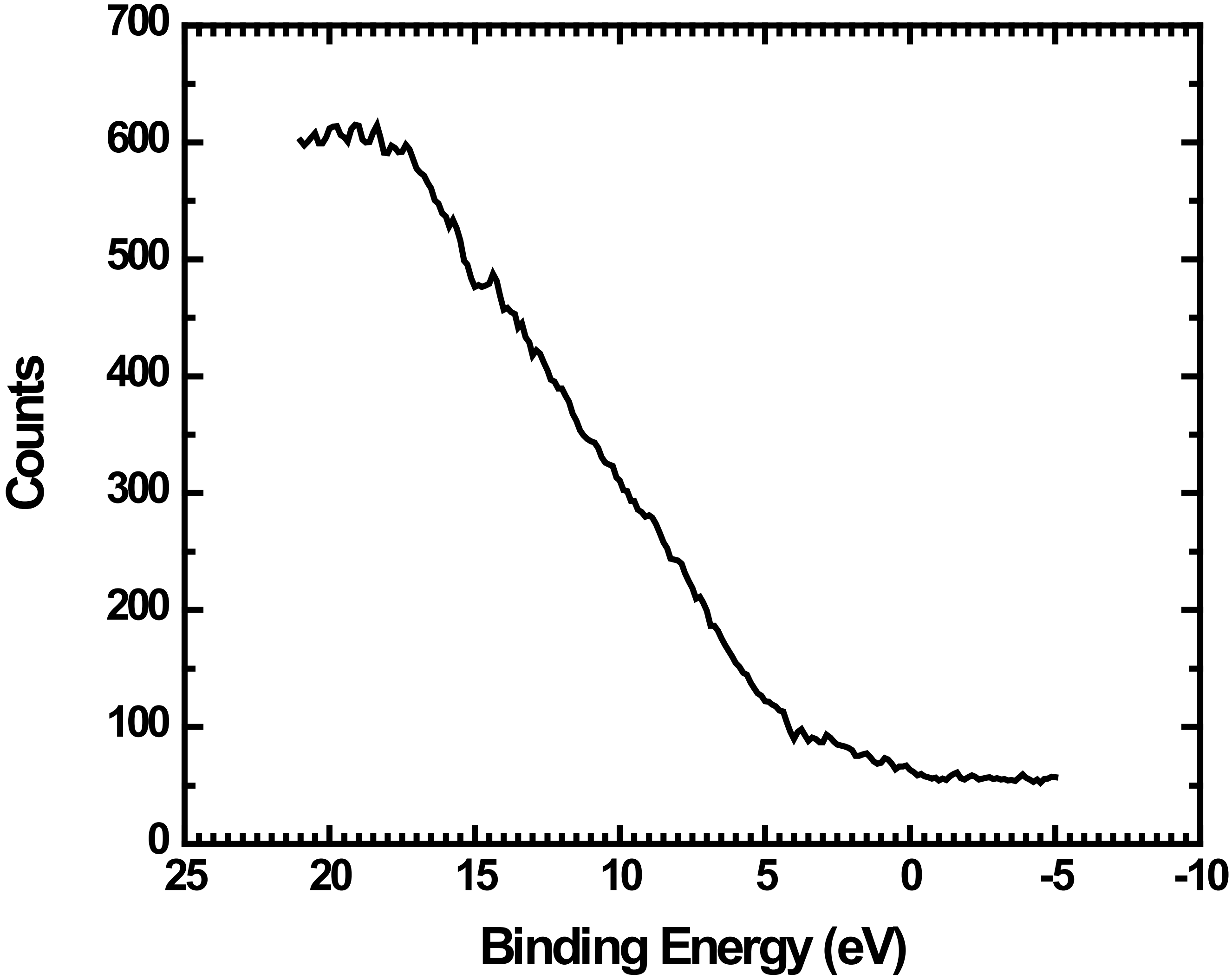

Figure 13.3 Valence band spectrum of a multiwalled CNT forest. Photoelectron emission steadily increases with increasing binding energy up to ca. 20 eV.

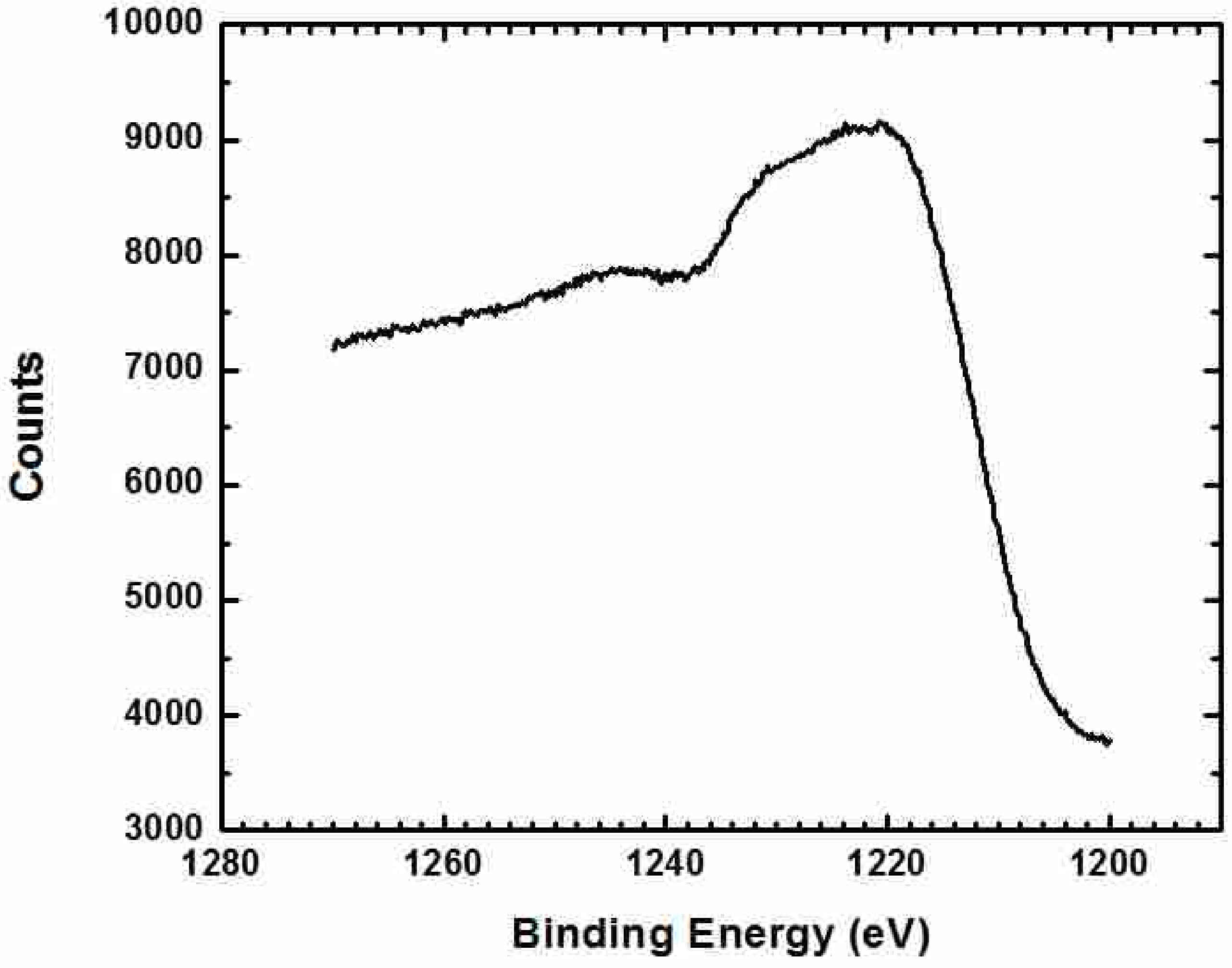

Figure 13.4 Narrow scan of the carbon KVV Auger signal.

Chapter 14: Conclusions

14.1. Conclusions

In my graduate work I mainly focused on developing and characterizing materials used to microfabricated carbon nanotube (CNT) templated thin layer chromatography (TLC) plates. These efforts included deposition/priming of CNTs with chemical vapor deposited (CVD) carbon and atomic layer deposited (ALD) alumina. This process readied the CNTs for conformal ALD-like deposition of silica. After functionalizing with 3-aminopropyltriethoxysilane, the TLC plates were used to separate a few biological dyes with improved efficiencies over commercially available products. Nevertheless, the process of coating CNTs with a priming material was cumbersome, so, ozone was used to ready CNTs for ALD deposition. That is, lightly oxidizing CNTs with ozone allowed CNTs to be coated with a conformal film of silica. This method decreased the number of processing steps, which increased the performance of the TLC plates.

Characterization of the thin films/CNTs used in the microfabrication process was done using X-ray photoelectron spectroscopy (XPS), time-of-flight secondary ion mass spectrometry (ToF-SIMS), Rutherford backscattering spectroscopy (RBS), and helium ion microscopy (HIM). Use of these surface sensitive techniques allowed for important characterization. That is, the information gathered from this study can be used to help troubleshoot the process if it were to go awry.

A small portion of my graduate studies was spent functionalizing porous graphitic carbon (PGC) for use in liquid chromatography. Di-*tert*-amylperoxide was used as the functionalizing agent. After functionalization, the chromatographic properties of PGC were enhanced, resulting in reduce tailing effects with an ultimate improvement in plate counts.

14.2. Recommendations for Future Work

The objective of my graduate research was to produce microfabricated CNT templated TLC plates and demonstrate their application in TLC. Such materials were repeatedly produced and showed impressive chromatographic properties. Although the materials were made out of silica, they contained a small amount of metal from the ALD-like deposition of silica, and as such APTES was used to passivate the surface. Future work should focus on using a metal-free source of silica and further separations under normal phase mode.

The migration speeds of these microfabricated TLC plates were rather fast. As such, if a less viscous mobile phase were used chromatography would suffer due to mass transfer issues. A geometry optimization study, which would include reducing the channel size, should be done to reduce the migration speed. I would expect such a study to improve the final chromatography. Additionally, a reduction in the hedge width of the TLC plate material should increase the performance of these plates.

Because these TLC plates are based on templated CNT forest, and the porosity results from such, the analyte loading capacity is somewhat limited. The current surface area of the material is ca. 10 m^2/g. It would be advantageous to find ways to improve the surface area of these materials.

Finally, silicon wafers are expensive, and as such, a more suitable/economical substrate needs to be found.